Understanding Haemodynamics in Neurodegenerative Disease

Richard J. Dury
The University of Nottingham

Thesis submitted to the University of Nottingham
for the degree of Doctor of Philosophy

Abstract

In this thesis, the haemodynamic, functional and structural changes in Alzheimer's Disease, Huntington's Disease and Multiple Sclerosis are assessed at 7T. Across all chapters, there is a focus on the use of Arterial Spin Labelling (ASL) to provide haemodynamic measures of perfusion (or cerebral blood flow) and transit time (TT) to provide a useful marker of disease. Arterial Spin Labelling (ASL) has the advantage that it is a non-invasive method to measure perfusion using magnetic resonance imaging (MRI). Clinically, perfusion is assessed using contrast-enhanced techniques which requires the intravenous administration of an exogenous gadolinium-based contrast agent, such as Prohance^{TM} and Gadovist^{TM}. Contrast-enhanced techniques typically provide higher SNR than ASL methods, however the non-invasive nature of ASL makes it a safe method suited for repeated measures in any subjects, including those with poor renal clearance. Additionally, gadolinium contrast agents have been shown to accumulate in neuronal tissue, and until the clinical significance of this is determined, contrast-enhanced scans should be performed with caution.

In Chapter 5, arterial spin labelling is used to assess cerebral perfusion in a patient group with Alzheimer's Disease (AD) and compared with an age-matched healthy control group (HC). Functional MRI (fMRI) is used to assess functional connectivity within the default mode network (DMN) and measures compared between the AD and HC group. In addition, high resolution structural data is acquired to assess the effects of atrophy in AD. Results demonstrate a significant decrease in grey matter perfusion and a significant increase in grey matter transit time in the AD group compared the HC group. A trend showing a decrease in functional connectivity in the DMN was found in the AD group as compared to the HC group. As expected, significant grey matter loss and cortical thinning were observed in the AD group compared to the HC group.

Secondly, haemodynamic and vascular changes in a Huntington's Disease (HD) patient group are assessed and compared with healthy age matched controls (HC). Phase contrast angiography is used to assess vessel density and vessel radius distributions between the two groups. Structural data was also acquired to assess grey matter volume and cortical thickness differences between the two groups. A

significant reduction in perfusion was found in grey matter, putamen and the caudate in the HD group compared to the HC group. The ASL transit time was found to be significantly increased in the caudate and putamen in the HD group compared to the HC group. Phase contrast angiography data showed an increase in the frequency of smaller vessels (0.15-0.35mm) in the HD group compared to the HC group, whereas larger vessels appeared more frequently in the HC group. A significant reduction in grey matter volume was also observed in the HD group compared to the HC group, which manifested as thinning of the cortical ribbon.

In the final study of this thesis, high spatial resolution arterial spin labelling is used to assess perfusion inside cortical lesions and compare with perfusion in surrounding normal appearing grey matter in a Multiple Sclerosis (MS) patient group. Grey matter perfusion as a function of distance from the cortical lesions was also assessed. It was found that cortical lesions have reduced perfusion compared to surrounding normal appearing grey matter. Perfusion increased and stabilised immediately outside of the cortical lesion itself, suggesting that the perfusion deficit observed is highly spatially localised.

List of Abbreviations

A

AβP	Amyloid-β Plaques
aCBV	Arterial Cerebral Blood Volume
AD	Alzheimer's Disease
ADC	Analogue to Digital Converter
AIF	Arterial Input Function
AP	Anterior-Posterior
APP	Amyloid Precursor Protein
ASL	Arterial Spin Labelling

B

BASIL	Bayesian Inference for Arterial Spin Labelling MRI
BBB	Blood-Brain Barrier
BOLD	Blood Oxygenation Level Dependent
BS	Background Suppression
bSSFP	Balanced Steady-State Free Precession

C

CASL	Continuous Arterial Spin Labelling
CAT	Computer Anatomy Toolbox
CBF	Cerebral Blood Flow
CBV	Cerebral Blood Volume
CKD	Chronic Kidney Disease
CL	Cortical Lesion
$CMRO_2$	Cerebral Metabolic Rate of Oxygen
CNR	Contrast to Noise Ratio
CNS	Central Nervous System
CPMG	Carr-Purcell-Meiboom-Gill
CSF	Cerebral Spinal Fluid
CT	Cortical Thickness

D

DAC	Digital to Analogue Converter
DCE	Dynamic Contrast Enhanced
DIR	Double Inversion Recovery
DMN	Default Mode Network
DR	Dual Regression
DSC	Dynamic Susceptibility Contrast

E

EDSS	Expanded Disability Status Scale
EDT	Euclidean Distance Transform
EPI	Echo Planar Imaging
EVI	Echo Volumar Imaging

F

FA	Flip angle
FAIR	Flow Alternating Inversion Recovery
FAST	FMRIB's Automated Segmentation Tool with FSL
FH	Foot-Head
FID	Free Induction Decay
FIESTA	Fast Imaging Employing Steady-State Acquisition
FLIRT	FMRIB's Linear Image Registration Tool with FSL
fMRI	Functional Magnetic Resonance Imaging
FMRIB	Oxford Centre for Functional MRI of the Brain
FOV	Field of View
FSL	FMRIB Software Library
FSS	Functional Systems Scores

G

GM	Grey Matter
GRASE	Gradient Echo And Spin Echo

H

HC	Healthy Controls
HD	Huntington's Disease

HRF	Haemodynamic Response Function
HTT	Huntingtin Gene

I

ICA	Idependent Component Analysis
IPL	Inferior Parietal Lobe
IR	Inversion Recovery
ITS-FAIR	Inflow Turbo Sampling - Flow Alternating Inversion Recovery
iVASO	Inflow-based vascular-space-occupancy

L

LR	Left-Right
LUT	Look-Up Table

M

MB	Multiband
MCI	Mild Cognitive Impairment
MCFLIRT	FMRIB's Linear Image Registration Tool for Motion Correction
MELODIC	Multivariate Exploratory Linear Optimized Decomposition into Independent Components
MFIS	Modified Fatigue Impact Scale
MIPAV	Medical Image Processing, Analysis and Visualization
MMSE	Mini-Mental State Examination
MNI	Montreal Neurological Institute
mPFC	Medial Prefrontal Cortex
MRI	Magnetic Resonance Imaging
MRA	Magnetic Resonance Angiography
MS	Multiple Sclerosis
mT	milli Tesla
MT	Magnetisation Transfer
MTT	Mean Transit Time

N

NAGM	Normal Appearing Grey Matter

NFT	Neurofibrilary Tangles
NMR	Nuclear Magnetic Resonance
NPI	Null Point Imaging

O

OEF	Oxygen Extraction Fraction

P

PASL	Pulse Arterial Spin Labelling
PCA	Phase Contrast Angiography
PCASL	Pseudo-Continuous Arterial Spin Labelling
PCC	Posterior Cingulate Cortex
PET	Positron Emission Tomography
PICORE	Proximal Inversion Controlling for Off-Resonant Effects
PLD	Post Label Delay
PNS	Peripheral Nerve Stimulation
PP-MS	Primary-Progressive Multiple Sclerosis
PR-MS	Primary-Relapsing Multiple Sclerosis
PSIR	Phase Sensitive Inversion Recovery
PWI	Perfusion Weighted Image

R

REC	Research Ethics Committee
RF	Radiofrequency
RR-MS	Relapsing-Remitting Multiple Sclerosis
RS	Resting State

S

SAR	Specific Absorption Rate
SENSE	Sensitivity Encoding
SMS	Simultaneous Multi-Slice
SNR	Signal-to-Noise Ratio
SP-MS	Secondary-Progressive Multiple Sclerosis
SPECT	Single-Photon Emission Computed Tomography

SPM	Statistical Parametric Mapping
SPMIC	Sir Peter Mansfield Imaging Centre
STAR	Signal Targeting with Alternating Radiofrequency
SUSAN	Smoothing over Univalue Segment Assimilating Nucleus

T

T	Tesla
TE	Echo Time
TFE	Turbo Field Echo
TIV	Total Intracranial Volume
TOF	Time of Flight
TR	Repetition Time
TrueFISP	True fast imaging with steady state precession

V

VBM	Voxel-Based Morphometry

W

WET	Water suppression Enhanced through T1 effects
WM	White Matter

Contents

1 Introduction **1**

1.1 Alzheimer's Disease . . . 2
1.2 Huntington's Disease . . . 2
1.3 Multiple Sclerosis . . . 3

2 Nuclear Magnetic Resonance **4**

2.1 Outline . . . 4
2.2 Classical Spin . . . 4
2.3 Nuclear Spin . . . 6
2.4 Magnetisation . . . 8
2.5 Excitation . . . 10
2.6 Bloch Equations . . . 10
2.7 Relaxation . . . 12
2.7.1 Longitudinal T_1 Relaxation . . . 12
2.7.2 Transverse T_2/T_2^* Relaxation . . . 13
2.8 Signal Detection . . . 14
2.9 Measuring T_1 and T_2 relaxation . . . 16
2.9.1 Measuring T_1 relaxation . . . 17
2.9.2 Measuring T_2 relaxation . . . 18
2.10 Summary . . . 19

3 Magnetic Resonance Imaging **21**

3.1 Outline . . . 21
3.2 Spatial Encoding . . . 21
3.2.1 Slice Selection . . . 22
3.2.2 Frequency Encoding . . . 25
3.2.3 Phase Encoding . . . 26
3.3 k-Space . . . 28
3.4 Imaging Techniques . . . 29
3.4.1 Spin Warp . . . 30
3.4.2 Balanced Steady-State Free Precession . . . 31
3.4.3 2D Echo-planar imaging . . . 35
3.4.4 EVI and 3D Echo Planar Imaging . . . 36
3.5 Faster coverage of k-space . . . 38
3.5.1 Partial Fourier . . . 38
3.5.2 SENSE . . . 39
3.6 Hardware . . . 41

3.6.1 Static magnetic field . . . 41
3.6.2 Gradient Coils . . . 42
3.6.3 Shimming Coils . . . 43
3.6.4 Radiofrequency Coils . . . 43
3.6.5 Overview . . . 43
3.7 Safety . . . 45
3.7.1 Static field . . . 46
3.7.2 Gradients . . . 46
3.7.3 Radiofrequency Pulses . . . 46
3.8 Summary . . . 47

4 Functional Brain Imaging **48**
4.1 Functional Brain Measures . . . 49
4.2 Arterial Spin Labelling . . . 51
4.2.1 Introduction . . . 51
4.2.2 Labelling Schemes . . . 52
4.2.3 Acquisition . . . 56
4.2.4 Improving SNR . . . 58
4.2.5 Quantification . . . 63
4.2.6 Pre-processing . . . 72
4.2.7 Applications . . . 77
4.3 Dynamic Susceptibility Contrast . . . 78
4.3.1 Introduction . . . 78
4.3.2 Theory . . . 80
4.3.3 Applications . . . 81
4.4 Magnetic Resonance Angiography . . . 82
4.4.1 Time of Flight (TOF) . . . 82
4.4.2 Phase contrast angiography . . . 84
4.4.3 Applications . . . 86
4.5 Functional MRI . . . 88
4.5.1 Theory . . . 88
4.5.2 Applications . . . 90
4.5.3 Resting State Networks . . . 90
4.6 Summary . . . 92

5 Alzheimer's Disease **93**
5.1 Outline . . . 93
5.2 Introduction . . . 93
5.2.1 Pathology . . . 94

5.2.2 Use MRI in Alzheimer's Disease . . . 95
5.2.3 Overview of structural changes in Alzheimer's Disease . . . 96
5.2.4 Overview of ASL perfusion studies in Alzheimer's Disease . 97
5.2.5 Overview of DMN studies in Alzheimer's Disease . . . 98
5.3 Aims and Objectives . . . 99
5.4 Methods . . . 99
5.4.1 Participants . . . 99
5.4.2 MR Acqusition . . . 99
5.4.3 Data processing . . . 104
5.5 Results . . . 112
5.5.1 Volunteers . . . 112
5.5.2 Clinical Scores . . . 112
5.5.3 Perfusion as assessed by Arterial Spin Labelling . . . 113
5.5.4 Structural . . . 118
5.5.5 Clinical scores and Structural Correlation . . . 121
5.5.6 fMRI Network Analysis . . . 122
5.5.7 Perfusion and Structural Correlation . . . 122
5.5.8 Perfusion and fMRI correlation . . . 123
5.6 Discussion . . . 125
5.6.1 Clinical Scores . . . 125
5.6.2 Arterial Spin Labelling . . . 125
5.6.3 Structural Measures . . . 127
5.6.4 fMRI . . . 128
5.7 Conclusion . . . 129

6 Huntington's Disease 130
6.1 Outline . . . 130
6.2 Introduction . . . 130
6.2.1 Pathology . . . 131
6.2.2 Overview of structural changes in Huntington's Disease . . 132
6.2.3 Overview of perfusion studies in Huntington's Disease . . . 133
6.2.4 Overview of vascular changes in Hutnington's Disease . . . 134
6.3 Aims and Objectives . . . 135
6.4 Methods . . . 136
6.4.1 Participants . . . 136
6.4.2 MR Acquisition . . . 136
6.4.3 Data Processing . . . 140
6.5 Results . . . 147

6.5.1 Volunteers . . . 147
6.5.2 Structural . . . 147
6.5.3 Arterial Spin Labelling . . . 150
6.5.4 Phase contrast angiography . . . 154
6.6 Discussion . . . 157
6.7 Conclusion . . . 161

7 Assessment of cortical lesion perfusion in MS using high resolution ASL at 7T 162

7.1 Outline . . . 162
7.2 Introduction . . . 162
7.2.1 Pathology . . . 162
7.2.2 Types of MS . . . 164
7.2.3 Symptoms . . . 165
7.2.4 Treatment . . . 166
7.2.5 Overview of Cortical Lesions in MS . . . 166
7.3 Aims and Objectives . . . 169
7.4 Methods . . . 170
7.4.1 Participants . . . 170
7.4.2 MR Acquisition . . . 171
7.4.3 Data processing . . . 173
7.5 Results . . . 179
7.5.1 Cortical Lesion Identification . . . 179
7.5.2 Cortical Lesions Perfusion . . . 180
7.5.3 Cortical Lesions Perfusion correlation with clinical scores . 181
7.6 Discussion . . . 182
7.7 Conclusion . . . 185

8 Conclusion 186

References 189

1 Introduction

Nuclear magnetic resonance (NMR) is the phenomenon by which atomic nuclei in a magnetic field absorb and re-emit electromagnetic radiation. It was 36 years between the discovery of NMR by Isidor Rabi in 1936 [1], and its extension to magnetic resonance imaging (MRI) by Paul Lauterbur and Peter Mansfield in the 1970s [2, 3]. Lauterbur and Mansfield's contributions not only demonstrated that imaging biological material was possible, but also that it could be extended for clinical use. In 1981 the first commercial MRI scanner was installed, and by 2013 an estimated 26,000 were in use worldwide performing over 77 million scans annually [4]. In 2003, the Nobel Prize in Physiology or Medicine was jointly awarded to Sir Peter Mansfield and Paul Lauterbur 'for their discoveries concerning Magnetic Resonance Imaging (MRI)'.

The last 35 years of research and development in MRI have continued to improve the capabilities of MR imaging. The first human MR scanner was able to achieve a field strength of 0.05 T, however this has since significantly increased with clinical MR systems now at 1.5 and 3 T. A number of 7 T systems worldwide are being used for research [5], however only recently has the first human 7 T MR system secured CE marking approval for clinical use. The next increase in field strength will likely be seen in 2018, when an 11.75 T human MR scanner will be put to field at Neurospin, France. This increase in field strength has led to both improved image quality due to increased signal to noise ratio and higher spatial resolution, and allowed scans to become quicker, both of which are important properties.

MRI has had a major clinical impact in the field of neurodegenerative diseases. For example it has improved the chance of early detection in Alzheimer's Disease [6], increased the sensitivity of diagnosing Multiple Sclerosis [7], and improved the quality of treatment for many diseases as repeated check-up scans are much safer than X-rays and computed tomography (CT). Not only has MRI improved the clinical care of neurodegenerative diseases, it has informed the methodology and led the direction of many research studies into better understanding these neurodegenerative diseases.

The advances in MRI over the years have allowed dynamic processes of the

body to be investigated. One of the first examples of this is functional MRI (fMRI). This uses the blood-oxygen-level dependent (BOLD) contrast which was discovered in 1990 by *Ogawa et al., (1990)* [8], and is able to identify regions of the brain working together driven by similar blood flow patterns. The interest in the quantitative assessment of perfusion has led to the further development of techniques such as phase contrast angiography (PCA), dynamic susceptibility contrast (DSC) and arterial spin labelling (ASL).

The work presented in this thesis is concerned with investigating cerebral haemodynamics using MRI in three neurodegenerative diseases; *Alzheimer's Disease*, *Huntington's Disease* and *Multiple Sclerosis*.

1.1 Alzheimer's Disease

Alzheimer's Disease (AD) is a chronic and progressive neurodegenerative disease that accounts for 50-60% of dementia cases overall [9]. Common symptoms of AD are short-term memory loss, language problems and disorientation which are known to become more severe as the disease progresses. Cortical perfusion is known to be impaired in Alzheimer's Disease [10–24], as is the functional connectivity between areas of the default mode network (DMN) [25–31]. In Chapter 5, the reported reduction in cortical perfusion was assessed in Alzheimer's Disease patients compared to age-matched healthy controls using arterial spin labelling (ASL). fMRI was also performed to quantify the change in the strength of connectivity between the areas of the DMN. This study aimed to investigate the relationship between cerebral perfusion and strength of connectivity between the areas of the DMN, an issue which has not yet been addressed. These measures were also correlated with structural changes associated with AD.

1.2 Huntington's Disease

Huntington's Disease (HD) is an autosomal dominant neurodegenerative disease, causing progressive mobility problems and cognitive decline [32]. HD is characterised by a loss of neurons in the basal ganglia and severe atrophy of the caudate and putamen. Previous studies have also reported a reduction in cerebral perfusion in HD patients compared to healthy controls using both

SPECT [33–35] and ASL [36, 37]. Vascular abnormalities are also present, with studies indicating increased vessel density in mice with HD compared to control mice [38–40]. The full extent of vascular abnormalities of the human brain in HD has currently only been investigated in post-mortem studies. Chapter 6 describes a study in which vascular abnormalities associated with HD were assessed *in-vivo* using high spatial resolution phase contrast angiography (PCA) at 7T using a novel image processing algorithm. Cerebral perfusion abnormalities in HD are assessed using arterial spin labelling, with the caudate and putamen being used as regions of interest.

1.3 Multiple Sclerosis

Multiple Sclerosis (MS) is an autoimmune disease in which leakage of the blood-brain barrier (BBB) allows lymphocytes to demylinate the central nervous system (CNS), commonly causing cognitive impairment, fatigue and ataxia. This cognitive impairment has been strongly correlated with the presence of lesions within the cortical ribbon [41], which has prompted studies assessing their physiological properties. The perfusion within these cortical lesions has been shown to be reduced compared to normal appearing grey matter (NAGM) using dynamic susceptibility contrast (DSC) [42, 43]. In Chapter 7, a cross-sectional study is described where perfusion within cortical lesions was compared to NAGM using high spatial resolution ASL. Perfusion as a function of distance from the centre of the cortical lesion was also assessed to determine if perfusion deficits are localised.

Funding Bodies

This work was funded by the Medical Research Council and The University of Nottingham.

2 Nuclear Magnetic Resonance

2.1 Outline

This chapter discusses the principles of nuclear magnetic resonance using both classical and quantum mechanical descriptions. Also described is the behaviour of an ensemble of nuclei creating a classical macroscopic magnetisation. The principles of manipulating this magnetisation using radiofrequency pulses and the behaviour of the magnetisation returning to equilibrium after a perturbation is described. Excitation and relaxation are described mathematically using Bloch equations and the physics of measuring magnetisation is explained. Finally, two common NMR experiments which are used to measure the longitudinal and transverse relaxation times of a sample are described.

2.2 Classical Spin

The term 'spin' or 'nuclear spin' refers to the spin angular momentum of a nucleus. A nucleus with spin can be modelled classically as a sphere spinning on a symmetrical axis with uniformly distributed mass and charge. Suppose this sphere has a radius r, a mass m, and is rotating with an angular velocity $\underline{\omega}$, the angular momentum $\underline{L}$ is found to be

$$\underline{L} = \frac{2}{5} m r^2 \underline{\omega} \tag{2.1}$$

where the direction of $\underline{L}$ is parallel to the spinning axis. Suppose this sphere has a total charge q distributed uniformly over its volume. The rotating sphere can be seen as a current loop which will therefore produce a magnetic field described by the 'magnetic moment', $\underline{\mu}$. This effect is illustrated by Figure 2.1. The magnetic moment is derived to be

$$\underline{\mu} = \frac{q}{2m} \underline{L} \tag{2.2}$$

This equation holds for all nuclei where mass and charge are distributed in the same way. The coefficient which relates the magnetic moment to the angular momentum $(q/2m)$ is known as the 'gyromagnetic ratio', denoted as γ.

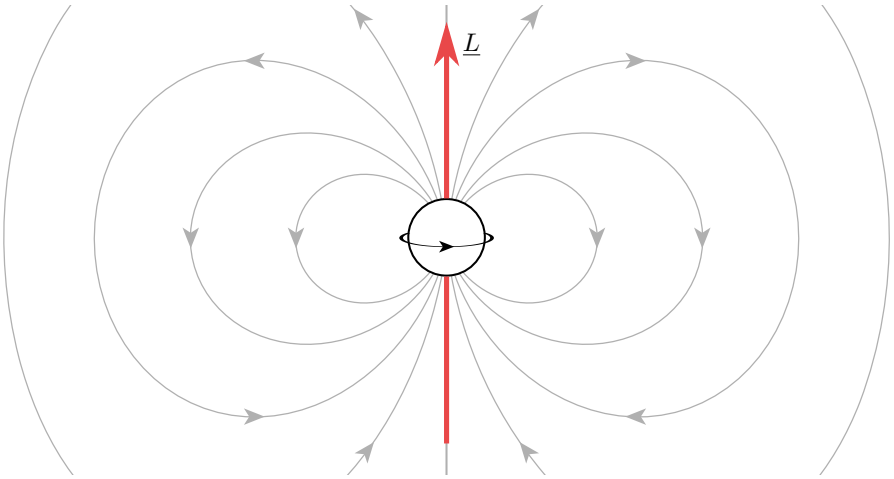


Figure 2.1: The effect of a spinning charged sphere. The red arrow shows the direction of the magnetic moment and the grey lines indicate the magnetic field lines.

The interaction between this model of a nucleus and an external magnetic field can be understood using a classical description. Just as linear momentum is changed through the application of a force, the angular momentum is changed through the application of a 'torque'. A charge moving through a magnetic field will experience the 'Lorentz force' acting perpendicular to both velocity and magnetic field. Similarly, a charged sphere spinning in a magnetic field will experience a 'torque'. Torque is given by

$$\underline{\tau} = \frac{\mathrm{d}}{\mathrm{d}t}\underline{L} = \underline{\mu} \times \underline{B_0} \tag{2.3}$$

Equations 2.2 and 2.3 can be combined to describe how the magnetic moment $\underline{\mu}$ changes when exposed to an external magnetic field, B_0.

$$\frac{\mathrm{d}\underline{\mu}}{\mathrm{d}t} = \underline{\mu} \times \gamma\underline{B_0} \tag{2.4}$$

The vectors in Equation 2.4 are illustrated in in Figure 2.2 which shows that if the magnitude of the magnetic moment is constant, as is the case for real nuclei, then only the direction of the magnetic moment can change. This equation also implies that the change in direction of the magnetic moment must always be perpendicular to the magnetic field and the magnetic moment itself. This constant rotation of the magnetic moment around the external magnetic field is known as 'precession'. The frequency of the precession is given by γB_0, known as the 'Larmor frequency' denoted as ω_0. The Larmor frequency is therefore

linearly proportional to the gyromagnetic ratio and external magnetic field strength.

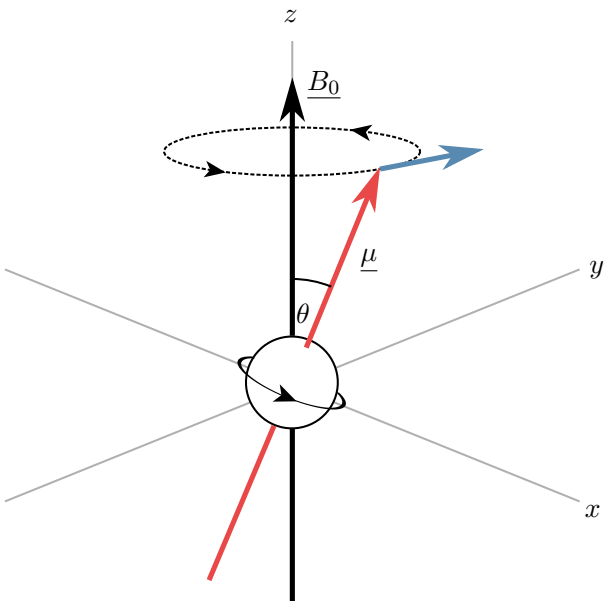


Figure 2.2: The evolution of a charged spinning sphere when exposed to an external magnetic field. A magnetic field is applied in the $+z$ direction (black arrow) which causes the magnetic moment, $\underline{\mu}$ (red arrow) to precess. The change in direction of the magnetic moment (blue arrow) is always perpendicular to both the magnetic moment and the magnetic field.

The angle between the magnetic field and the magnetic moment (θ) is not affected by the precessional motion and the angle will remain constant if unperturbed. The angle determines the potential energy of the system such that

$$E = -\underline{\mu} \cdot \underline{B_0} = -\mu B_0 \cos\theta \tag{2.5}$$

Classically, θ can take any value between 0 and π radians, implying a continuous range of energies between $-\mu B_0$ and $+\mu B_0$, with the potential energy minimised when $\underline{\mu}$ and $\underline{B_0}$ are parallel and maximised when these vectors are anti-parallel.

2.3 Nuclear Spin

Classically, the angular momentum of a spinning sphere can possess a continuous set of magnitudes and orientations. However, it is found that the

angular momentum of a nucleus only possesses a discrete set of magnitudes and orientations, known as the Zeeman Effect. Quantum mechanics is the branch of physics concerned with explaining such observations.

When describing the nuclear spin using quantum mechanics, the nucleus is assigned a value known as the 'quantum spin number', often denoted as I. For elementary particles such as protons, neutrons and electrons, the quantum spin number is 1/2. However, when protons and neutrons group to form a nucleus, the quantum spin number is determined by the number of constituents as demonstrated Table 2.1. All known isotopes are found to have a spin quantum number between 0 and 8, but calculating the exact value of I is not trivial.

Protons	Neutrons	I	Examples
Even	Even	0	^{12}C, ^{16}O, ^{32}S
Odd/Even	Even/Odd	Half-integer	^{1}H, ^{13}C, ^{15}N
Odd	Odd	Integer	^{2}H, ^{14}N, ^{56}Co

Table 2.1: The relationship between the number of protons and number of neutrons, and the quantum spin number, I.

The spin number I determines the discrete set of the magnitudes and orientations that the angular momentum can possess. A nucleus with a quantum spin number of I will have $2I + 1$ possible orientations. Each of these orientations is given a value (m_I) ranging from $-I$ to I in steps of 1 such that

$$m_I = (-I), (-I + 1), (-I + 2), ..., (I - 2), (I - 1), (I) \tag{2.6}$$

If a nucleus with a quantum spin number I were to have its z-component of angular momentum measured, it would yield one of $2I + 1$ possible magnitudes. The magnitude of the z-component of spin angular momentum is given by

$$L_z = m\hbar \tag{2.7}$$

In the case of ^{1}H, which has a quantum spin number of 1/2, there are 2 allowed values of angular momentum when placed in a magnetic field. These orientations

are often called 'spin-up' and 'spin-down', where 'spin-up' refers to the magnetic moment parallel to the magnetic field and 'spin-down' refers to the magnetic moment anti-parallel to the magnetic field. The 'spin-up' state is often given the subscript of '↑' and the 'spin-down' state is often given the subscript of '↓'. As MR imaging uses ^{1}H to create images, the remaining theory will be explained using the $I = 1/2$ case, known as the 'spin-1/2' case.

The z-component of the possible magnetic moments of a nucleus, μ_z, can be found using Equations 2.2 and 2.7

$$\mu_z = m\hbar\gamma \tag{2.8}$$

The potential energy, E, of the system when placed inside an external magnetic field (B_0) and orientated along the z-axis, is given by

$$E = -\mu_z B_0 = -m\hbar\gamma B_0 \tag{2.9}$$

When dealing with the spin-1/2 case, m can take values of $+1/2$ and $-1/2$. This leads to two possible potential energies for the 'spin-up' and 'spin-down' states of a nucleus, where

$$E_\downarrow = -\left(-\frac{1}{2}\right)\hbar\gamma B_0 = +\frac{1}{2}\hbar\gamma B_0 \tag{2.10}$$

$$E_\uparrow = -\left(+\frac{1}{2}\right)\hbar\gamma B_0 = -\frac{1}{2}\hbar\gamma B_0 \tag{2.11}$$

The energy difference, ΔE, between the two states is given by $\Delta E = \hbar\gamma B_0 = \hbar\omega_0$, and is proportional to the strength of the external magnetic field (Figure 2.3).

2.4 Magnetisation

The probability of finding a nucleus with a particular energy level is described by the Boltzmann distribution. For the spin-1/2 case, the probability of measuring the nucleus in a 'spin-up' or 'spin-down' state at thermal equilibrium is found to be

$$p_\downarrow = \frac{\exp(-E_\downarrow/k_B T)}{\exp(-E_\downarrow/k_B T) + \exp(-E_\uparrow/k_B T)} \tag{2.12}$$

$$p_\uparrow = \frac{\exp(-E_\uparrow/k_B T)}{\exp(-E_\downarrow/k_B T) + \exp(-E_\uparrow/k_B T)} \tag{2.13}$$

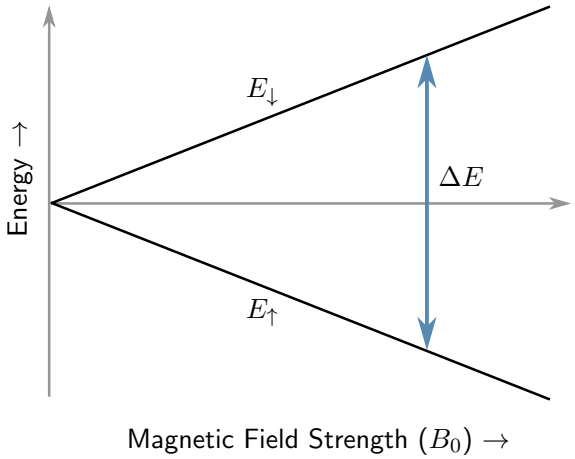


Figure 2.3: The energy difference (ΔE) between the spin-up ($E_\uparrow$) and spin-down ($E_\downarrow$) energy states as a function of magnetic field strength B_0.

where k_B is the Boltzmann constant and T is the temperature in Kelvin. Therefore in an ensemble of N nuclei, one would expect to measure $n_\downarrow = Np_\downarrow$ spin-down nuclei and $n_\uparrow = Np_\uparrow$ spin-up nuclei. The ratio between the two states is therefore $p_\downarrow/p_\uparrow$ which simplifies to

$$\frac{p_\downarrow}{p_\uparrow} = \frac{n_\downarrow}{n_\uparrow} = \exp(-\Delta E/k_B T) \tag{2.14}$$

In the absence of an external magnetic field ($B_0 = 0$) the spin-up and spin-down states have zero potential energy and therefore one would expect to measure an equal number of spin-up and spin-down states. When the system is exposed to a non-zero external magnetic field ($B_0 \neq 0$) at absolute zero ($T = 0$), one would expect to measure all the nuclei in the low energy spin-up state.

An unequal distribution of spin states in an ensemble will therefore create a net magnetisation. The phases of the precessing magnetic moments are randomly distributed, so the net magnetic field in the xy plane is zero. The z-component of magnetisation of a spin-1/2 system ($\underline{M_z}$) where $\underline{B_0} = B_0\hat{\underline{z}}$, at thermal equilibrium is given as

$$\underline{M_z} = \frac{N(\hbar\gamma)^2 B_0}{4k_B T}\hat{\underline{z}} \tag{2.15}$$

2.5 Excitation

The net magnetisation of a macroscopic sample of spins in thermal equilibrium, $\underline{M}$, is a static vector orientated parallel to B_0. The orientation of $\underline{M}$ can be manipulated with the application of a second magnetic field, known as 'excitation'. Excitation can be achieved with the application of a perpendicular magnetic field oscillating near the Larmor frequency, known as the B_1 field. As the Larmor frequency typically falls inside the radiofrequency band, it is commonly referred to as a radiofrequency (RF) field. The RF field tips the magnetisation $\underline{M}$ by applying a torque with the extent of the tip measured by the angle between $\underline{M}$ and $\underline{B_0}$, denoted as the flip angle θ.

Figure 2.4 illustrates the effect of the application of an RF field of flip angle of 90^o on M. Figure 2.4a illustrates the excitation when viewed from the 'laboratory frame'. Figure 2.4b illustrates the excitation from a reference frame rotating at the Larmor frequency, known as the 'rotating frame'. The rotating frame is given a new co-ordinate system (x', y', z) such that the two reference frames can be distinguished. The laboratory frame and the rotating frame are related by

$$
\begin{aligned}
x' &= x\cos(\omega_0 t) - y\sin(\omega_0 t) \\
y' &= x\sin(\omega_0 t) + y\cos(\omega_0 t) \\
z' &= z
\end{aligned}
$$

Three important features have been introduced by simplifying the laboratory frame to the rotating frame. Firstly, the effect of B_0 on M has been removed so no precession is observed. Secondly, B_1 does not appear to rotate at the Larmor frequency but instead remains in a fixed orientation. Finally, M appears to precess around B_1 with a frequency described by $\omega = \gamma B_1$. However, the z component of M and B_1 remains unaffected by the transformation.

2.6 Bloch Equations

The evolution of magnetisation of a sample of nuclei in a magnetic field exposed to an RF field was modelled by Felix Bloch in 1946. The Bloch equations are

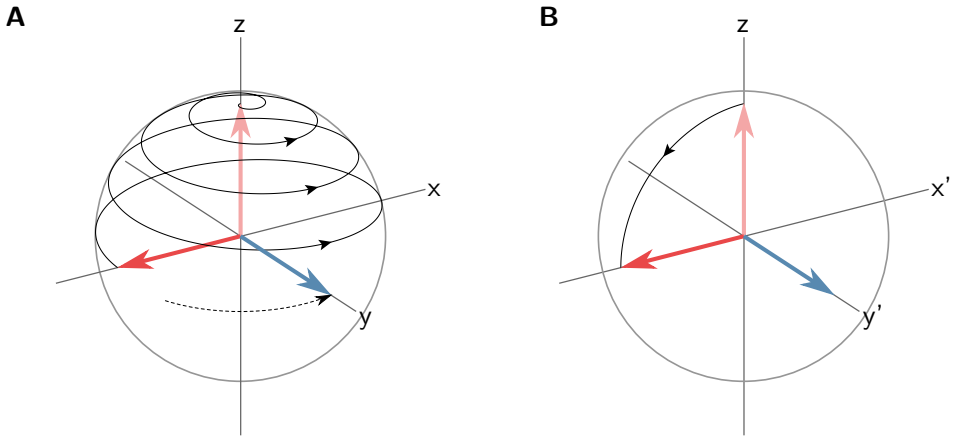


Figure 2.4: Excitation in (A) the laboratory reference frame, (B) the rotating reference frame. The solid red arrow indicates the final position of the magnetisation after excitation by B_1 (blue arrow). The black line represents the evolution of the magnetisation vector, and the dashed black line represents the evolution of the B_1 field.

three coupled differential equations which describe each component of the magnetisation in the laboratory reference frame, with B_0 in the $+z$ direction. These equations are

$$\frac{\mathrm{d}M_x(t)}{\mathrm{d}t} = \gamma\left[M_y(t)B_0 - M_z(t)B_{1y}(t)\right] - \frac{M_y(x)}{T_2} \tag{2.16}$$

$$\frac{\mathrm{d}M_y(t)}{\mathrm{d}t} = \gamma\left[M_z(t)B_{1x}(t) - M_x(t)B_0\right] - \frac{M_y(x)}{T_2} \tag{2.17}$$

$$\frac{\mathrm{d}M_z(t)}{\mathrm{d}t} = \gamma\left[M_x(t)B_{1y}(t) - M_y(t)B_{1x}(t)\right] - \frac{M_z(t) - M_0}{T_1} \tag{2.18}$$

where T_1 and T_2 are constants defining the longitudinal and transverse relaxation of the system (discussed in Section 2.7.1 and 2.7.2). The Bloch equations can be transformed into the rotating frame by substituting γB_0 with Ω, where Ω is the frequency difference between the Larmor frequency and the rotating frame. This implies that on-resonance ($\Omega = 0$), B_1 has the Larmor frequency component removed such that a B_1 field oscillating at the Larmor frequency appears static in the rotating frame. The Bloch equations for the rotating frame are given by

$$\frac{\mathrm{d}M_x(t)}{\mathrm{d}t} = \gamma\left[M'_y(t)\Omega - M'_z(t)B'_{1y}(t)\right] - \frac{M'_y(x)}{T_2} \tag{2.19}$$

$$\frac{\mathrm{d}M_y(t)}{\mathrm{d}t} = \gamma\left[M'_z(t)B'_{1x}(t) - M'_x(t)\Omega\right] - \frac{M'_y(x)}{T_2} \tag{2.20}$$

$$\frac{\mathrm{d}M_z(t)}{\mathrm{d}t} = \gamma\left[M'_x(t)B'_{1y}(t) - M'_y(t)B'_{1x}(t)\right] - \frac{M'_z(t) - M_0}{T_1} \tag{2.21}$$

2.7 Relaxation

Suppose an excitation occurs that tips $\underline{M}$ out of equilibrium and then the RF field is removed; $\underline{M}$ will then return towards thermal equilibrium and realign with the B_0 field, this is known as 'relaxation'.

Relaxation occurs due to energy loss of the individual spins which contribute to $\underline{M}$. The energy is transferred to other spins and to the environment. Two relaxation terms are introduced in order to describe this process; T_1 and T_2^*. T_1 is the time constant of the recovery of M_z towards M_0, and T_2^* is the time constant of the decay of the transverse components of $\underline{M}$ (M_{xy}) towards zero. Figure 2.5 shows the relaxation of a magnetisation vector in a magnetic field following a 90^o pulse.

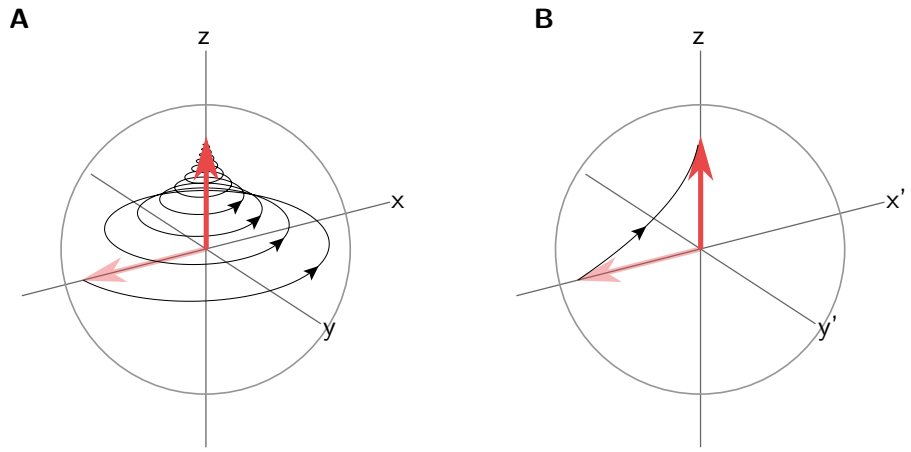


Figure 2.5: T_1 and T_2^* relaxation following a 90^o excitation in (A) the laboratory reference frame, (B) the rotating reference frame. The red arrow indicates the final magnetisation following relaxation and the black line indicates the path of the magnetisation during relaxation.

2.7.1 Longitudinal T_1 Relaxation

The rate of recovery of the M_z component back to thermal equilibrium (M_0) is defined by the longitudinal or spin-lattice time constant known as T_1. The evolution of M_z back to thermal equilibrium can be found by solving the Bloch equation to yield

$$M_z(t) = M_{z,t=0} \exp\left(-\frac{t}{T_1}\right) + M_0 \left[1 - \exp\left(-\frac{t}{T_1}\right)\right] \tag{2.22}$$

As M_z relaxes towards M_0, the potential energy of the system decreases. This implies that for T_1 relaxation to occur, energy must be transferred from the system to the environment, which happens in the form of collisions and rotations. The rate of longitudinal recovery is dependent on the 'molecular tumbling rate' of the sample, also termed the correlation time, τ_c. This describes the frequency at which the molecules in the sample vibrate, move or tumble. Energy is able to leave the system more readily when the system itself is tumbling at a frequency close to the Larmor frequency. This suggests that the closer the system's molecular tumbling rate is to the Larmor frequency, the more efficient and so shorter is the T_1 value.

2.7.2 Transverse T_2/T_2^* Relaxation

Transverse relaxation is the process whereby the xy-component of magnetisation decays back to equilibrium. Transverse relaxation can be described in terms of either T_2 or T_2^*, where T_2 describes the irreversible time variant effects which contribute to transverse relaxation.

There are two factors which contribute towards T_2, the first being T_1 contributions. During T_1 relaxation, energy is transferred to surrounding nuclei which causes their magnetic moments to be knocked into a random phase, decreasing the transverse magnetisation. This implies that any process that causes T_1 relaxation contributes towards T_2 relaxation, meaning that the T_1 relaxation time is always longer than T_2. Secondly, spin-spin interactions occur between nuclei. A lone nucleus will only be subject to the magnetic field of B_0 and therefore precess at the Larmor frequency. However in a sample of nuclei, magnetic fields interact with each other. If the field from one nucleus increases the local magnetic field surrounding a second nucleus for a finite time, then the precessional frequency will slightly increase. Similarly, if the field from one nucleus decreases the local magnetic field, the precessional frequency of the second will slightly decrease. This random and temporary effect causes the precessions of two nuclei to become dephased, resulting in the overall decay of M_{xy}.

T_2^* describes transverse decay when effects due to static (time invariant) field inhomogeneities are also considered along with T_2. Local static field inhomogeneities may be present causing a range of precessional frequencies. These can originate from inhomogeneities in the magnetic field, for example due to unwanted objects inside the magnetic field, air-tissue boundaries causing susceptibility gradients or change in blood oxygenation (BOLD). The spins will gradually fall out of phase causing M_{xy} to decay. The resultant T_2^* relaxation can be described by

$$\frac{1}{T_2^*} = \frac{1}{T_2} + \frac{1}{T_2'} \tag{2.23}$$

where T_2' is the transverse relaxation caused purely by the time invariant field inhomogeneities. The evolution of the M_{xy} component can be modelled using

$$M_{xy}(t) = M_{xy,t=0} \exp\left(-\frac{t}{T_2^*}\right) \tag{2.24}$$

2.8 Signal Detection

The magnetisation of a sample can be observed by detecting its precession. Faraday's Law of Induction describes that a changing magnetic field through a circuit will induce a voltage. Therefore placing a coil close to the precessing magnetisation will induce a signal which can be used to observe the magnetisation (Figure 2.6). The induced signal, S_{ind}, is described by the equation

$$S_{\text{ind}} = -\frac{d}{\mathrm{d}t}\underline{M} \cdot \underline{A} \tag{2.25}$$

where A is the vector area of the coil. The coil is positioned such that the vector area is perpendicular to the external magnetic field, such that only changes in transverse magnetisation are observed.

The induced signal following excitation can be modelled as

$$s_{\text{ind}} = M_0 \, sin(\theta) \, cos(\omega_L t) \exp\left(-\frac{t}{T_2^*}\right) \tag{2.26}$$

where M_0 is the magnitude of equilibrium magnetisation, θ is the angle between the magnetisation and the z-axis, ω_L is the precessional frequency of the sample and t is time after excitation (Figure 2.7A). By using phase sensitive detection to remove the frequency from the signal caused by precession, the magnetisation can be effectively observed in the rotating reference frame. This is achieved by first

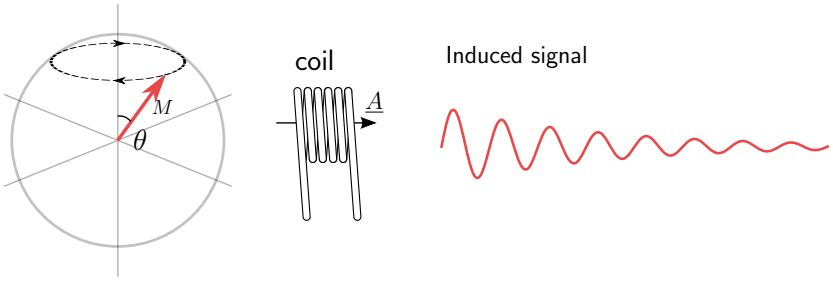


Figure 2.6: Received signal detected through a receive coil due to the precession of the macroscopic magnetisation. The red line represents the induced signal with relaxation. The amplitude of the induced signal is dependent on the angle θ between the magnetisation M and the xy plane.

multiplying the induced signal by a reference signal s_{ref} with a known frequency, ω_0 (Figure 2.7B) yielding

$$s = M_0\, sin(\theta)\cos(\omega_L t)\exp\left(-\frac{t}{T_2^*}\right)\cos(\omega_0 t) \tag{2.27}$$

Using the trigonometrical identity $\cos(\alpha)\cos(\beta) = \frac{1}{2}(\cos(\alpha+\beta)-\cos(\alpha-\beta))$, the signal can be written as the sum of two signals with frequencies of $(\omega_0+\omega_L)$ and $(\omega_0-\omega_L)$ (Figure 2.7C).

$$s = \frac{M_0}{2}\, sin(\theta)\exp\left(-\frac{t}{T_2^*}\right)[\cos((\omega_0+\omega_L)t)+\cos((\omega_0-\omega_L)t)] \tag{2.28}$$

The difference between the Larmor frequency and precessional frequency of the sample $(\omega_0-\omega_L)$ can be extracted from the signal s by integrating over small windows of δt. If δt is much larger than the time period of the high frequency component $(\omega_0+\omega_L)$, it will effectively average to zero. However, the lower frequency component $(\omega_0-\omega_L)$ will remain approximately unaffected (Figure 2.7D). This is known as 'low-pass filtering'. The integral can therefore be approximated as

$$S = \int_t^{t+\delta t} s(t)\mathrm{d}t \;\approx\; \frac{M_0}{2}\, sin(\theta)\exp\left(-\frac{t}{T_2^*}\right)\cos((\omega_L-\omega_0)t)\delta t \tag{2.29}$$

as seen in Figure 2.7D. The frequency of this signal will be the difference between the reference signal and the received signal. This can be identified by Fourier

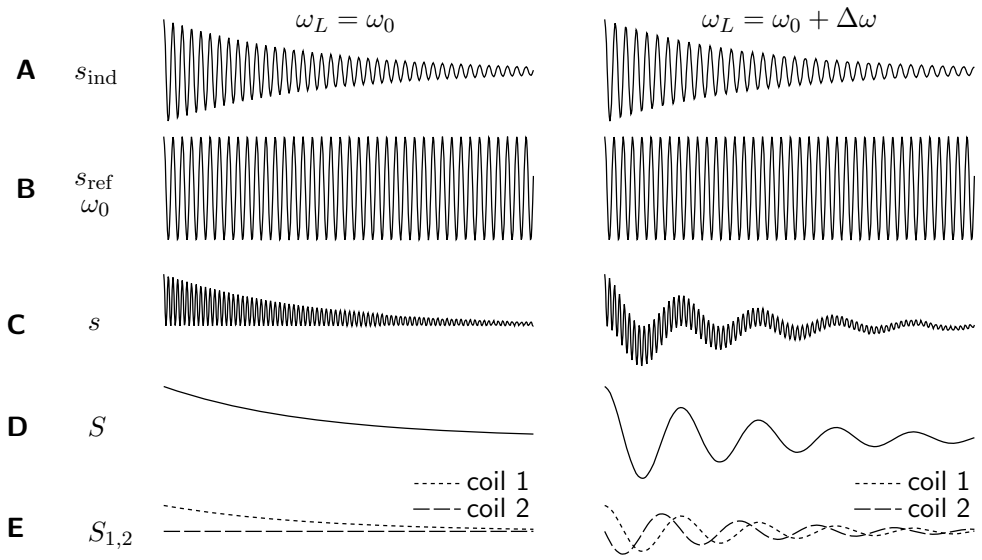


Figure 2.7: Signal processing steps of phase sensitive detection to convert the signal from the laboratory reference frame to the rotating reference frame. (A) Shows the detected FIDs where frequencies are ω_0 (left) and $\omega_0 + \Delta\omega$ (right). (B) A carrier signal oscillating at ω_0 is multiplied with the detected FID to produce the signal shown in *C*, labelled s. (D) By applying a low pass filter to *D*, the frequency difference can be extracted. (E) Detecting the resultant signal using two perpendicular coils allows the sign of the frequency difference to be determined.

transforming the signal. However, this method cannot distinguish between $+\Delta\omega$ and $-\Delta\omega$. To determine the sign of $\Delta\omega$, a second coil is placed at 90^o to the first coil. The induced signal in this coil receives the same signal except 90^o out of phase.This is known as quadrature phase sensitive detection and can be seen in Figure 2.7E, labelled as signals S_1 and S_2.

2.9 Measuring T_1 and T_2 relaxation

$T_1$and T_2 relaxations are interesting properties of a sample to measure and specific clinical applications are discussed in later chapters (Chapters 5, 6 and 7). By using a series of excitations and measuring the FID, these properties can be isolated and quantified.

2.9.1 Measuring T_1 relaxation

In order to measure the T_1 relaxation time of a sample, the evolution of the z component of magnetisation must be observed during its transition to equilibrium. This can achieved using an 'inversion recovery' sequence.

Starting with the magnetisation at equilibrium (M_0), a 180^o RF pulse is applied at time $t = 0$ which inverts the longitudinal magnetisation to $-M_0$ and the transverse magnetisation to 0. After a time period known as the 'inversion time' (TI), a 90^o pulse is applied to convert the longitudinal magnetisation at that time into transverse magnetisation such that it can be measured by the receive coil (Figure 2.8A), as described in Section 2.8. By measuring the magnetisation at many TIs, the longitudinal relaxation time can be derived by fitting the inversion recovery curve (Figure 2.8B).

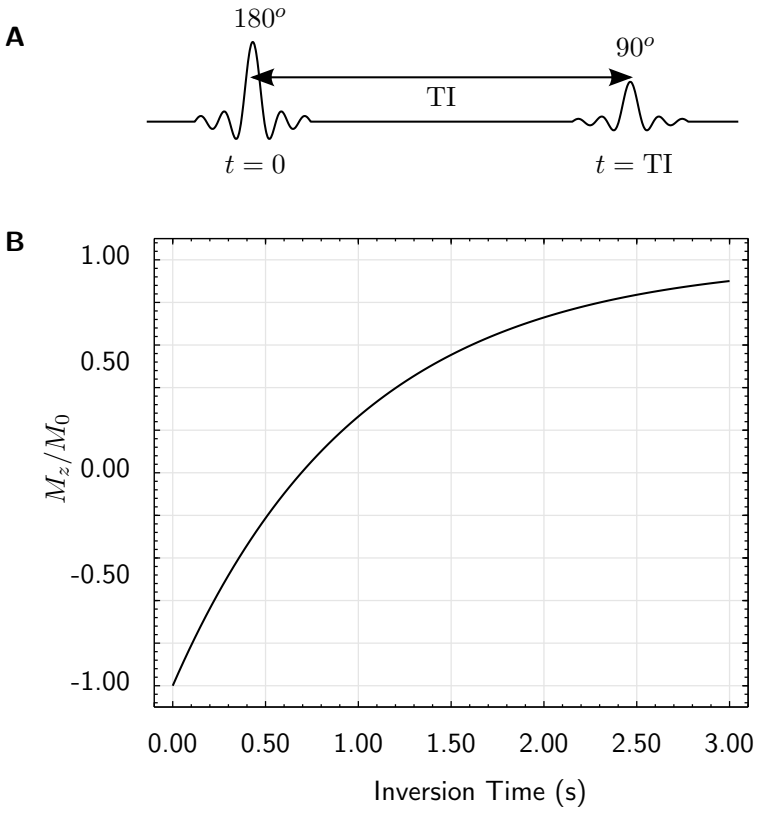


Figure 2.8: (A) Pulse sequence diagram of an inversion recovery sequence illustrating the timings of 180^o and 90^o pulses. (B) The simulated z-magnetisation for inversion recovery data collected as a function of inversion time (illustration shown for T_1=1.0s).

The evolution of the z-magnetisation after a 180^o inversion pulse can be modelled using the Bloch equations. After the initial inversion, the magnetisation only changes due to relaxation until the subsequent 90^o pulse ($B_1 = 0$). With the z-magnetisation initially being equal to $-M_0$ at time $t = 0$, the inversion recovery curve can derived as

$$M_z(t) = M_0 \left(1 - 2e^{-\frac{\mathrm{TI}}{T_1}}\right) \tag{2.30}$$

By fitting Equation 2.30 to the received signal across a number of inversion times, the T_1 of the sample can be quantified.

2.9.2 Measuring T_2 relaxation

T_2 relaxation is the component of transverse decay arising from T_1 effects and spin-spin interactions (described in Section 2.7.2). However, simply measuring the transverse decay following an RF pulse would give an estimate of T_2^*. In order to solely observe the effects of T_2, T_2' effects must be removed by rephasing these. This is achieved using a 'spin echo' sequence (Figure 2.9A).

Starting with the magnetisation at equilibrium (M_0), a 90^o pulse is applied to knock the longitudinal magnetisation into the transverse plane (Figure 2.9B-i). From here the transverse magnetisation decays at a rate defined by T_2^*. The spin-spin interactions cause small precessional variations in each of the spins contributing towards the magnetisation (Figure 2.9B-ii). After a delay equal to $TE/2$, a 180^o refocussing pulse is applied. This inverts the phases of each spin, however precession still occurs in the same direction (Figure 2.9B-iii). This will cause the decayed transverse magnetisation to refocus and produce a signal echo (Figure 2.9B-iv).

As T_2' is the dephasing of spins caused by static field inhomogeneities, the decay is completely reversed by the spin-echo sequence. However, T_2 relaxation cannot be reversed as it is governed by random time varying processes. Therefore, the magnitude of each echo is only affected by T_2 relaxation.

By performing the above sequence multiple times with increasing TEs, the peaks can be recorded and fitted to Equation 2.24 to compute T_2. Alternatively, this process can be accelerated whereby all peaks are measured from one pulse sequence using multiple 180^o pulses, this is known as a Carr Purcell Meiboom

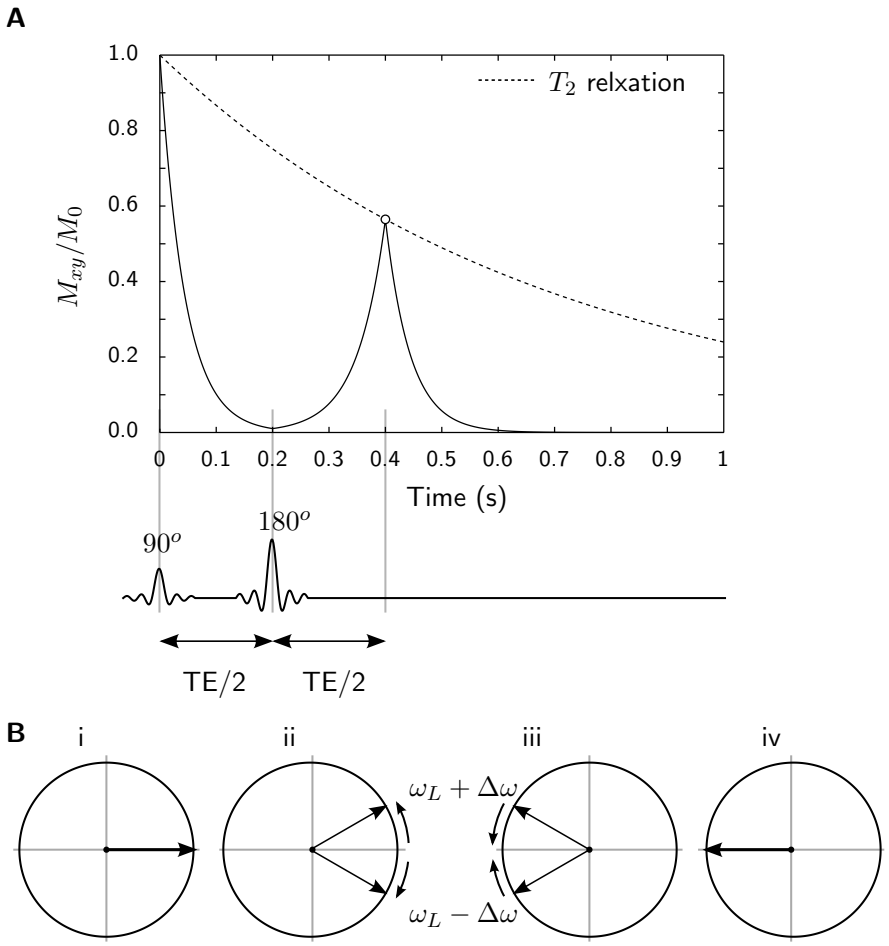


Figure 2.9: (A) Simulated spin-echo sequence ($T_2 = 0,7s, T_2' = 0.05s, TE = 0.4s$). The dashed line represents the relaxation due to T_2 and the solid line is the transverse magnetisation. A pulse sequence diagram is placed below showing timings of the pulses. (B) Evolution of spins following a 90^o pulse (i-ii), followed by a 180^o pulse (iii-iv). The time between i and iv is defined as the echo time TE.

Gill (CPMG) sequence (Figure 2.10).

2.10 Summary

This section has described the basic principles of Nuclear Magnetic Resonance. It has been shown that a spin system can be described using either a classical or quantum approach, and that nuclei with spin are necessary to perform NMR. Nuclei with spin can be manipulated using radiofrequency pulses, and their evolution can be modelled using the Bloch equations. The magnetisation will

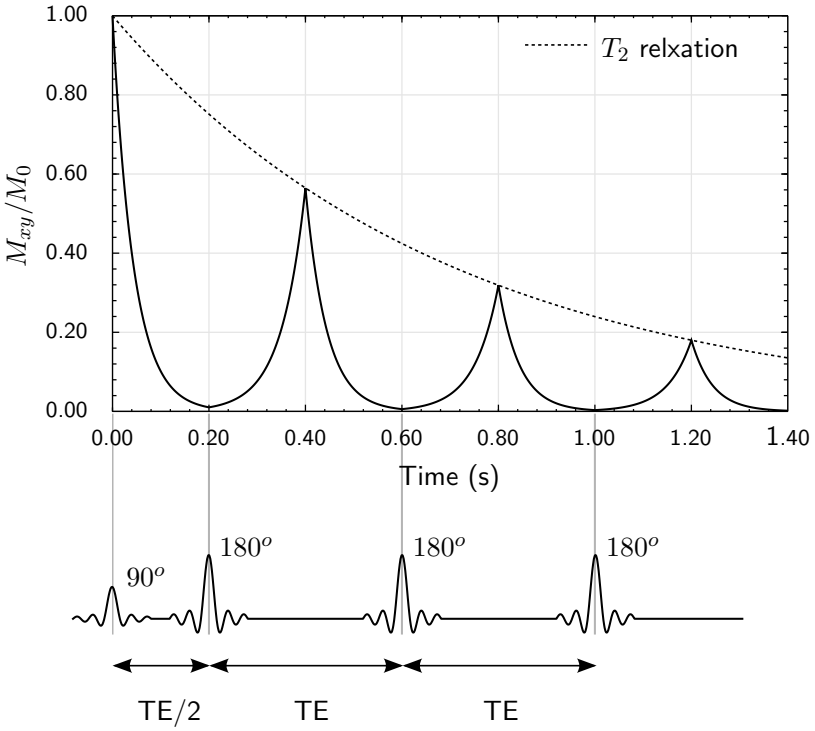


Figure 2.10: (A) Simulated CPMG sequence ($T_2 = 0,7s, T_2' = 0.05s, TE = 0.4s$). The dashed line represents the relaxation due to T_2 and the solid line is the transverse magnetisation following each RF pulse.

relax back to equilibrium with time constants T_1 and T_2, which describe the build up of longitudinal magnetisation in the direction of B_0 and the loss of transverse magnetisation. The inversion recovery sequence can be used to measure T_1 and the spin-echo sequence can be used to measure T_2.

3 Magnetic Resonance Imaging

3.1 Outline

This chapter describes how the NMR phenomenon is applied to image a sample *in-vivo*. The concept of spatially encoding signals from a sample in three dimensions is explained. The schemes used in order acquire sufficient data to image a sample are discussed, including various ways to decrease the time required for acquisition. Finally the hardware required to implement these concepts to image *in-vivo* is presented.

3.2 Spatial Encoding

The previous section described how to measure the magnetisation from an ensemble of spins. However, with a sufficiently large sample, it is desirable to be able to localise the magnetisation to small regions of interest. This can be achieved using the principles of imaging first described by Lauterbur in 1973 [2].

From the derivation of the classical spin in Section 2.2, it can be seen that the Larmor frequency of precession is dependent on the gyromagnetic ratio (γ) and the external magnetic field (B_0). By varying the magnetic field across the sample, the Larmor frequency becomes spatially dependent.

This is achieved by applying magnetic field gradients in addition to B_0. The applied magnetic field gradients, G, can be written as a tensor where

$$\underline{G} = \begin{bmatrix} \hat{i}\hat{i}\frac{\delta B_x}{\delta x} & \hat{i}\hat{j}\frac{\delta B_x}{\delta y} & \hat{i}\hat{k}\frac{\delta B_x}{\delta z} \\ \hat{j}\hat{i}\frac{\delta B_y}{\delta x} & \hat{j}\hat{j}\frac{\delta B_y}{\delta y} & \hat{j}\hat{k}\frac{\delta B_y}{\delta z} \\ \hat{k}\hat{i}\frac{\delta B_z}{\delta x} & \hat{k}\hat{j}\frac{\delta B_z}{\delta y} & \hat{k}\hat{k}\frac{\delta B_z}{\delta z} \end{bmatrix} \tag{3.1}$$

However, the direction of the magnetic field is fixed to the z-axis, such that B_x and B_y are effectively zero. Therefore the tensor can be reduced to

$$\underline{G} = \frac{\delta B_z}{\delta x}\underline{\hat{i}} + \frac{\delta B_z}{\delta y}\underline{\hat{j}} + \frac{\delta B_z}{\delta z}\underline{\hat{k}} \tag{3.2}$$

The external magnetic field, B_0, will always be orientated along the z axis, only the strength of the magnetic field is altered by the gradients (Figure 3.1). The

Larmor frequency can therefore be described by

$$\omega_L(\underline{r}) = \gamma(\underline{B_0} + \underline{G} \cdot \underline{r}) \tag{3.3}$$

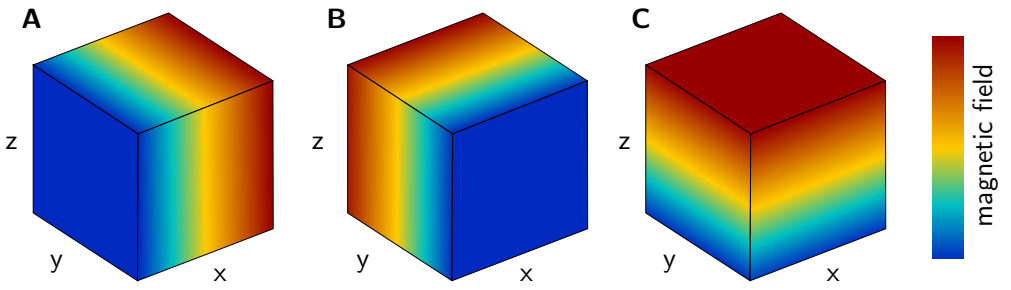


Figure 3.1: Magnetic field gradients applied in the (A) x-direction, (B) y-direction and (C) z-direction. The direction of the magnetic field does not change with the application of magnetic field gradients, only the strength changes.

This ability to spatially alter the Larmor frequency allows 3D samples to be imaged and is the basis of MR imaging.

3.2.1 Slice Selection

Isolating a cross section of a volume in a given direction (illustrated here along z) is known as 'slice selection'. Tailoring an RF pulse to excite the magnetisations of only a specific range of frequencies allows for only a cross section to be excited.

When applying an RF pulse to a sample, it is found that the excitation profile is approximately the Fourier transform of the pulse shape. This only applies to small flip angles as described by the small tip angle approximation. Therefore, the ideal excitation profile for slice selection is the 'top-hat' or 'box-car' shape, which saturates all spins within the slice and leaves all spins outside the slice unaltered. Therefore, an excitation RF pulse with magnitude evolving according to the *sinc* function is used (Figure 3.2). Furthermore, the non-linearities of the Bloch equations causes additional errors with large flip angles.

When a sinc pulse with an infinite number of lobes either side of the peak are Fourier transformed, this produces an ideal top-hat excitation profile because

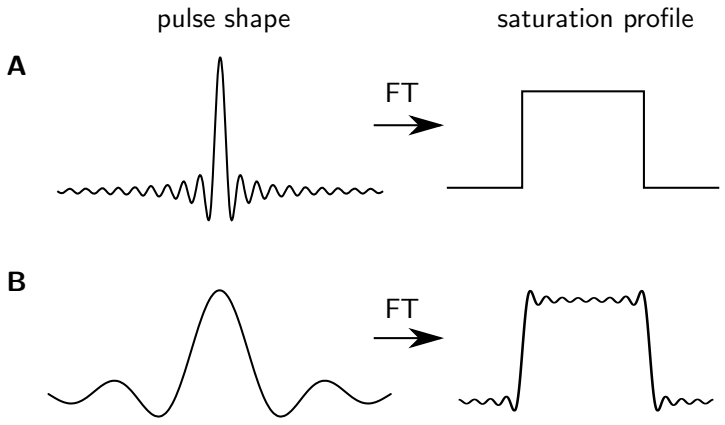


Figure 3.2: This diagram illustrates the saturation profile of a sample in response to a sinc pulse. (A) An ideal sinc pulse producing an ideal tophat. (B) a truncated sinc pulse producing an imperfect top hat.

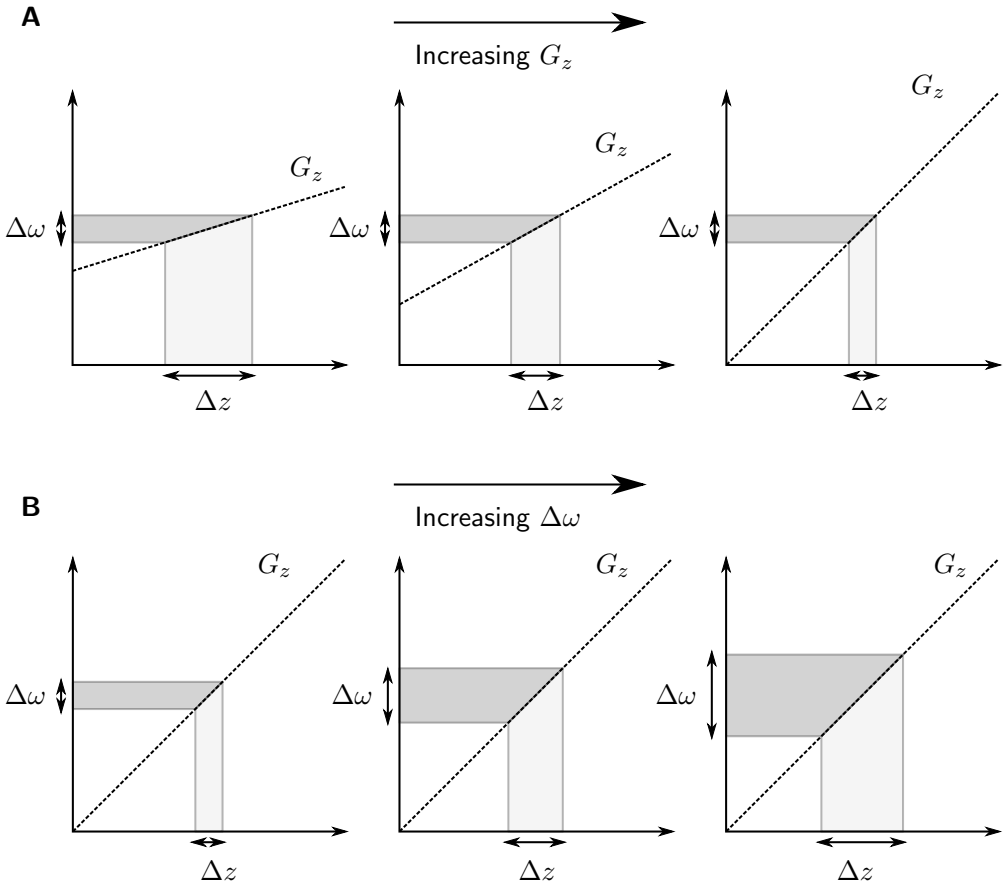


Figure 3.3: The effect of (A) gradient strength G_z and (B) bandwidth of the RF pulse on the slice thickness, Δz.

it contains the high frequency components necessary for a sharp profile (Figure 3.2.A). However, in practice the sinc pulse is truncated such that there are only a few lobes either side of the peak. This produces an imperfect top hat excitation profile, as it does not contain the high frequency components required for a sharp profile (Figure 3.2.B).

The slice thickness (ΔZ) is determined by two factors; the strength of the gradient in the z-direction (G_z) and the bandwidth of the RF pulse ($\Delta\omega$). The strength of the gradient determines the range of Larmor frequencies in the sample, while the bandwidth of the pulse determines the range of frequencies which are excited. These two factors are related to the slice thickness by

$$\Delta Z = \frac{\Delta\omega}{\gamma G_z} \tag{3.4}$$

A larger gradient means that the range of excitable frequencies occurs across a smaller distance, therefore decreasing the slice thickness (Figure 3.3.A). A larger bandwidth excites a wider range of frequencies corresponding to a wider space within the gradient field, therefore increasing the slice thickness (Figure 3.3.B).

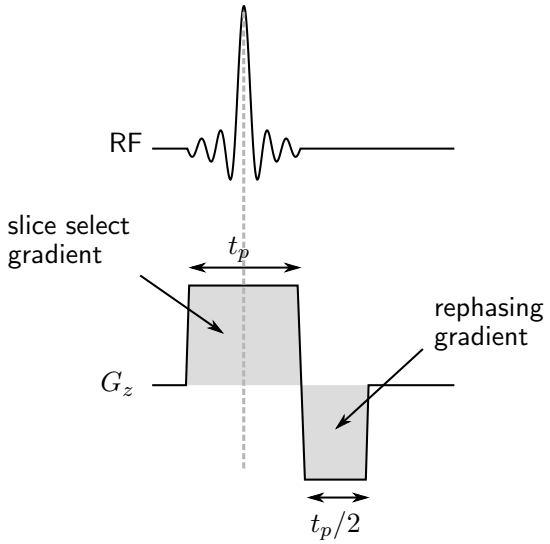


Figure 3.4: Illustration of the pulse sequence required for slice selection and to maximise the resulting signal, where t_p is the duration of the pulse.

The RF pulse and the gradient are applied at the same time to allow selective

excitation of the sample. Once the RF pulse been applied, the magnetic field gradient in the z-direction can be turned off as the necessary spins are excited. However, the application of a sinc pulse and magnetic field gradient will produce phase differences across the slice which will lead to a loss in transverse coherence and hence signal. By applying a gradient of an equal but opposite magnitude and half the duration, this dephasing can be reversed. (Figure 3.4).

3.2.2 Frequency Encoding

After exciting a slice, the magnetisation from this region can be detected and any manipulation of spins using magnetic field gradients only affects the spins in this slice. The next step is to spatially encode the slice, which again requires the application of magnetic field gradients.

Figure 3.5.A illustrates a 2D plane split into three columns labelled with their average spin densities (A, B and C). The spins in each column all precess at the same Larmor frequency. If the total signal from the slice is measured, it produces a sinusoid oscillating at a single frequency, ω_L. This signal can be written as

$$S = (A + B + C)\sin(\omega_L t) \tag{3.5}$$

From this equation, it is not possible to solve for the spin densities as the Fourier transform produces a single peak with an amplitude of $A + B + C$. In order to separate and solve these spin densities, a magnetic field gradient must be applied.

A magnetic field gradient is applied in the x-direction to linearly vary the Larmor frequency of the spins along this axis. Figure 3.5.B illustrates the same slice with a magnetic field gradient applied in the x-direction, causing a range of frequencies from ω_1 to ω_3. Assuming each column contains a discrete frequency, the total signal can now be written as

$$S = A\sin(\omega_1 t) + B\sin(\omega_2 t) + C\sin(\omega_3 t) \tag{3.6}$$

By Fourier transforming the signal described by Eq. 3.6, the contributions from each frequency can be resolved. The amplitudes of the peaks for each frequency component correspond to the spin densities, known as projection. By changing the direction of this magnetic field gradient, many projections at different angles

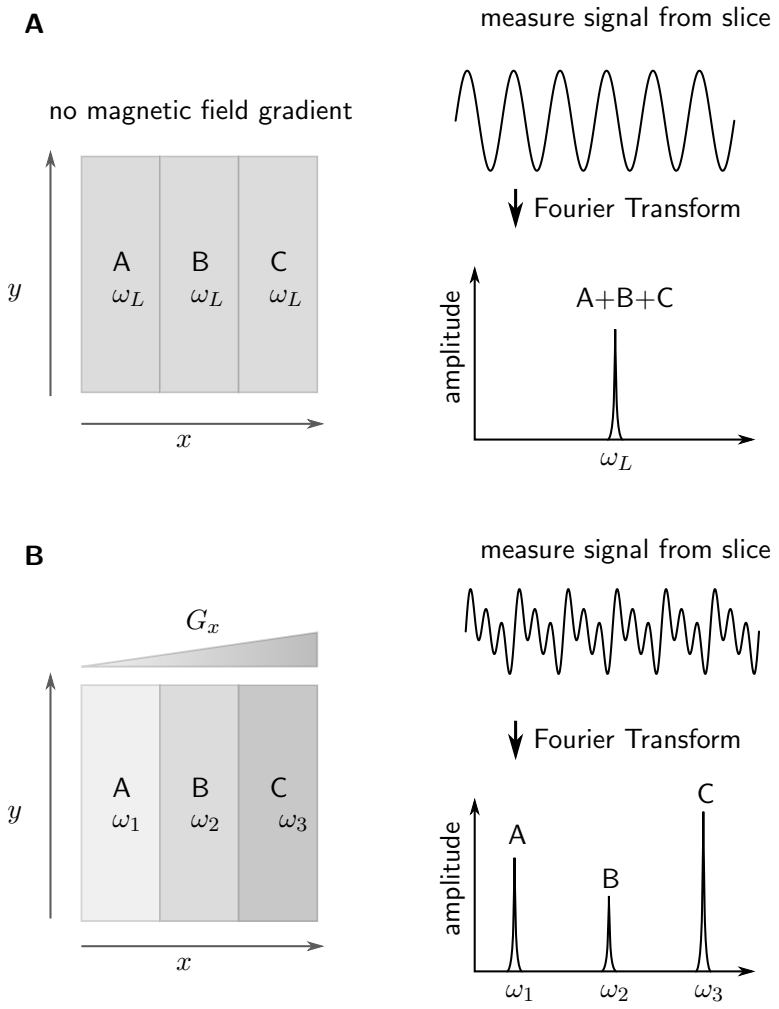


Figure 3.5: Frequency encoding of an excited slice. (A) Illustrates the frequencies across the slice with no magnetic field gradients. (B) illustrates the same slice with an applied magnetic field gradient along the x-axis, allowing the spin densities to be resolved. This is known as projection

can be acquired, allowing for projection reconstruction. This approach used in other imaging modalities such as computed tomography (CT).

3.2.3 Phase Encoding

Projection reconstruction was used by Paul Lauterbur to generate a 2D image from projections acquired at numerous orientations. An alternative method, first suggested by Sir Peter Mansfield, used the application of second magnetic field gradient in a perpendicular direction to the first, known as 'phase

encoding'.

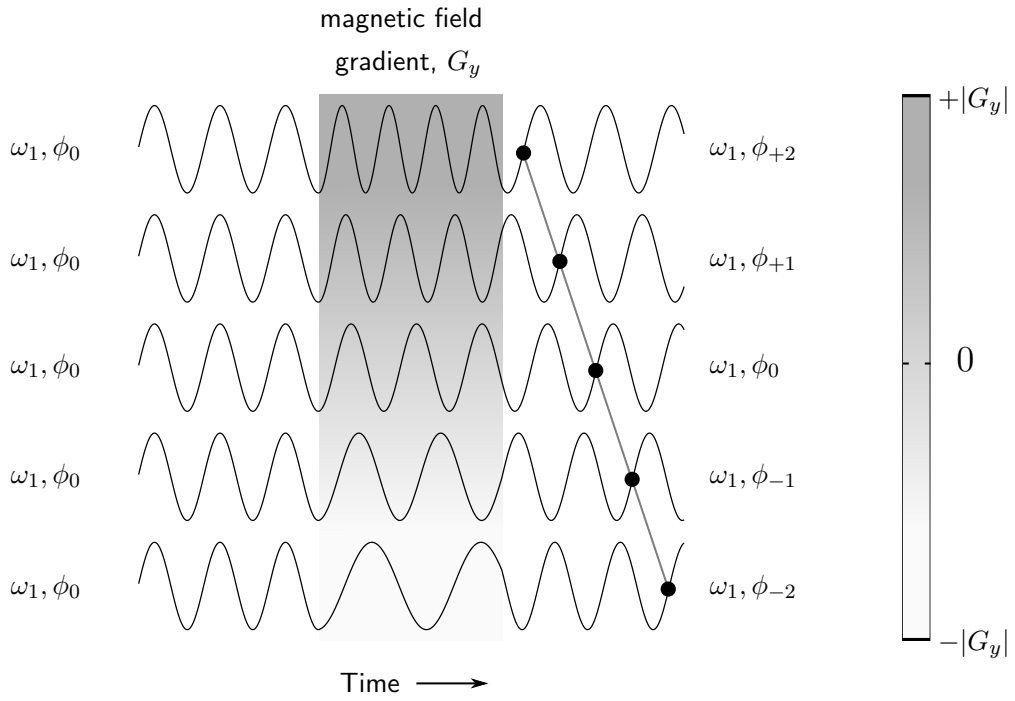


Figure 3.6: This figure illustrates the concept of phase encoding. A magnetic field gradient is applied in the y-direction for a small duration causing the signals to fall out of phase. The dots illustrate the phase difference between the signals.

By applying another magnetic field gradient in the y-direction for a brief time, the precessional frequency is temporarily increased before returning to the Larmor frequency. This causes a phase shift of the subsequent signal, where the size of the phase shift is dependent on the duration and magnitude of the gradient (Figure 3.6).

By successively changing the magnitude of G_y while keeping its duration constant, different phase shifts are applied to each signal. The rate at which the phase changes with each applied magnetic field gradient, identifies its position along the y-axis. When used in conjunction with the frequency encoding this allows for each location within the slice to be identified. A second Fourier transform can be used to separate signals which have rates of frequency shifts.

Phase and frequency encoding are applied such that the centre of the gradient causes no frequency or phase shifts in the sample. Therefore gradients are applied such that they range from a negative amplitude to an equal but opposite positive

amplitude.

3.3 k-Space

It is common to visualise the effect of frequency and phase encoding in 'k-space', which is the Fourier transform of the sample image. All MR images are acquired in k-space and are Fourier transformed to produced an image of the sample.

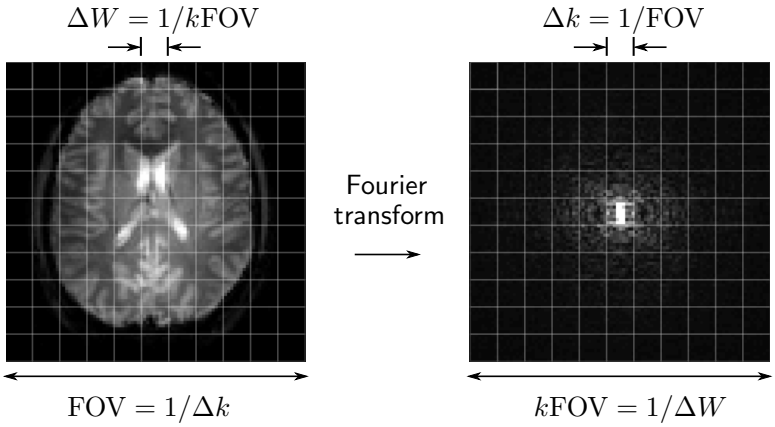


Figure 3.7: A brain image and its Fourier transform. The overlaying grid represents the pixels which the image is split into.

The discrete Fourier transform of an image with $n \times m$ pixels will produce a map of spatial frequencies with $n \times m$ pixels. However, one pixel in k-space does not correspond to one pixel in the image. Each pixel in k-space contains phase and frequency information of the whole image.

The k-space image, $S(k)$, can be found from the sample image, $s(r)$ using

$$S(k) = \int_{\infty}^{-\infty} s(r) e^{-i2\pi kr} dV \tag{3.7}$$

where k are the complex coordinates of k-space and r are the Cartesian coordinates of sample space.

Applying frequency and phase encoding can be thought of as sampling k-space. The amplitude and direction of the gradients in each direction determines which parts of k-space are being sampled (Figure 3.8).

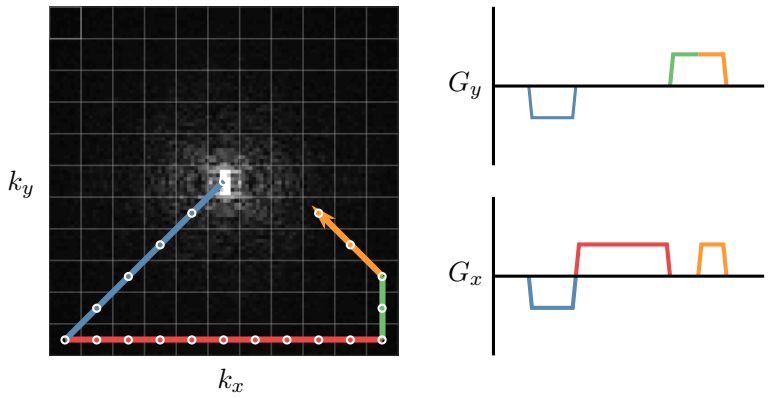


Figure 3.8: The amplitude and polarity of magnetic field gradients determines which parts of k-space are sampled. The white circles represent the points in k-space which have been sampled as the trajectory moves through them.

The points in k-space which are collected determines the spatial frequencies present in the final image. Lower spatial frequencies fall in the centre of k-space and high spatial frequencies fall towards the edges of k-space. Therefore if k-space is not sampled fully to the edges, the resulting image would be smoothed due to a lack of high spatial frequencies. Similarly if only the edges of k-space are sampled, only the boundaries between different proton densities can be visualised.

3.4 Imaging Techniques

The method by which k-space is sampled will determine the image contrast. For example, the resulting image may illustrate proton density, T_1 relaxation, T_2/T_2^* relaxation, or a combination. Choosing the correct imaging technique for a specific application to highlight features of interest is important in both research and clinical use. Different imaging techniques can also effect the image in other ways, such as distortions, resolution and FOV restrictions and their sensitivity to motion. This section presents common imaging techniques used to sample k-space, and discussions of their advantages, disadvantages and applications.

3.4.1 Spin Warp

Spin warp imaging is a 2D acquisition, meaning that signals are acquired from each slice individually. This technique requires multiple excitations in order to sample a single slice.

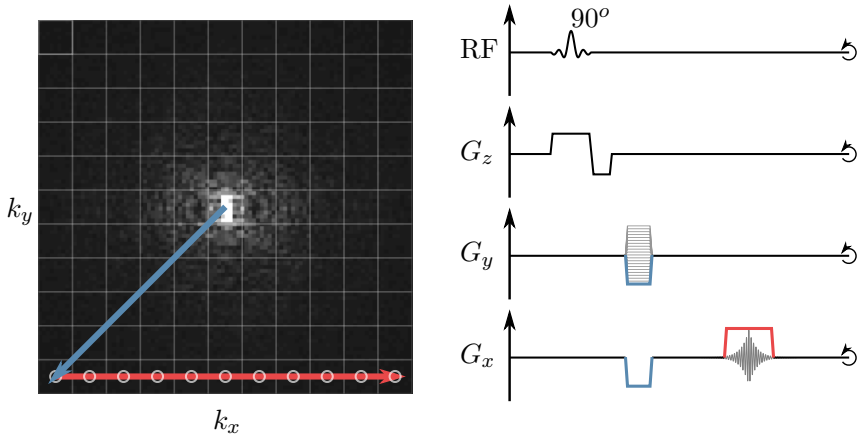


Figure 3.9: Illustration of the the k-space trajectory and associated pulse sequence diagram of the spin warp sequence. The circles represent which k-space voxels are sampled.

The pulse sequence for spin warp imaging is illustrated in Figure 3.9. An initial 90^0 pulse is applied to excite a slice, which is followed by short phase and frequency encoding gradients (Figure 3.9 - green line). These gradients are used to dephase the signal in both x and y directions simultaneously. These gradients will send the k-space trajectory to the edge of k_x, and to a height in k_y determined by the amplitude of the phase encoding gradient. Applying a second frequency encoding gradient will cause the initial frequency dephasing to be reversed, producing an echo (Figure 3.9 - pink line).

The echo acquired is representative of a single phase encoding. In order to acquire a 2D image, this sequence must be performed multiple times with different phase encoding amplitudes. This sequence was an early development in MR imaging. The acquisition time is slow as it requires many different repetitions to build up k-space for a complete image. It is necessary to wait for the magnetisation to fully recover before another line of k-space can be sampled. A larger flip angle will require a longer waiting period (TR) before the next line is sampled. An adaptation of the spin warp is the Fast Field Echo (FFE) sequence. This

sequence has a lower flip angle such that the relaxation time back to equilibrium is much shorter, allowing for a much shorter TR. The reduction of flip angle is accompanied by a reduction in SNR as the transverse signal is much smaller. A FFE sequence is used in Chapters 5, 6 and 7 to acquire high resolution structural images in a phase sensitive inversion recovery (PSIR) sequence.

3.4.2 Balanced Steady-State Free Precession

An adaptation of spin-warp is 'balanced steady-state free precession' (bSSFP). The term steady-state free precession describes a steady state which has non-zero transverse and longitudinal magnetisation components. The balanced term refers to the fact the total area under the gradient lobes over a repetition is zero.

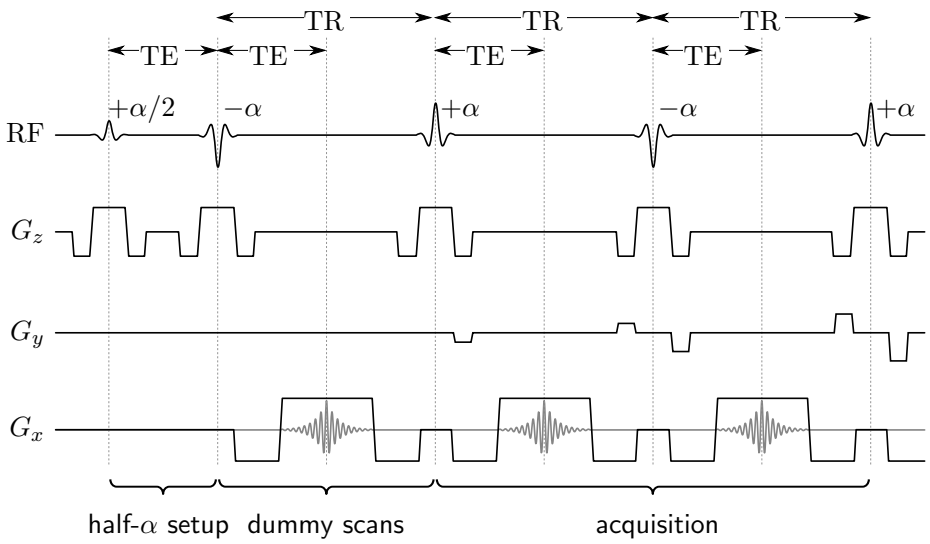


Figure 3.10: The pulse sequence for a balanced steady-state free precession acquisition. Illustrated here are the half-alpha setup scheme, a dummy scan and the acquisition.

The pulse sequence for a bSSFP acquisition is illustrated in Figure 3.10. The sequence begins with a half-alpha setup scheme, followed by a set of dummy scans allowing for a steady state to develop, and finishing with the signal acquisition.

The main features of the acquisition stage to note are the balanced gradient lobes, the echo time (TE) always being exactly half the repetition time (TR),

and the alternating direction of the RF pulses. The balanced nature of the sequence means that the net area of the gradient lobes over one repetition is zero $\left(\int_0^{TR} G_{x,y,z}dt = 0\right)$. By applying balanced gradients, the dephasing of spins after one repetition is due only to irreversible effects of T_2 and not due to gradients. This refocuses the transverse signal as much as possible, maximising the signal at the end of each repetition.

The echo time being exactly one half of the repetition time is a consequence of the balanced gradients. In order to fully refocus the magnetisation after the application of gradients, all gradients must be symmetrical about TE.

The alternating RF pulse scheme is especially useful for ultra-high field where B_1 inhomogeneities are common. When a non-alternating RF pulse scheme is used, the received signal is highly dependent upon the flip angle. The alternating RF pulse scheme is much less sensitive to imperfect RF excitations (Figure 3.11).

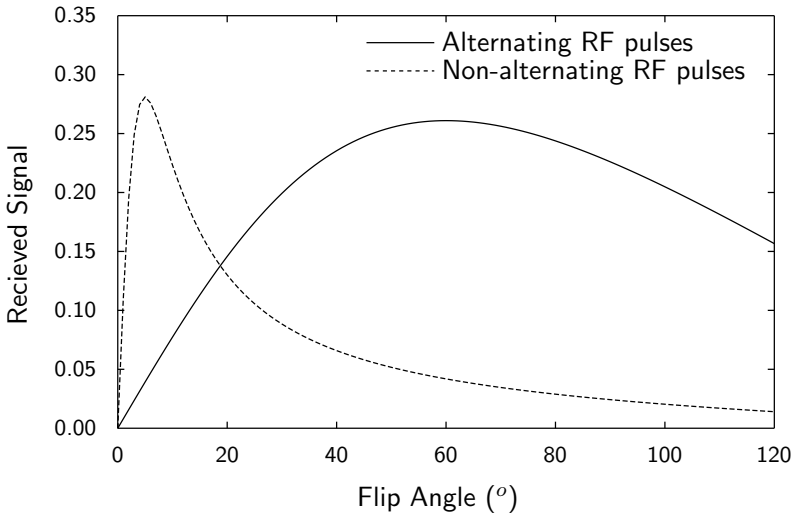


Figure 3.11: The dependency of the received signal at steady-state on the flip angle and the pulse scheme. Simulation parameters $T_1 = 600ms$, $T_2 = 100ms$, TE $= 10ms$ and TR $= 20ms$.

If the sequence uses a flip angle of α during the acquisition, the initial application of a half-α pulse allows the system to smoothly approach a steady state. The system would still reach a steady state in the absence of the half-α setup given enough time, however for rapid imaging it is desirable for the signal to become

stable as quickly as possible. The half-α preparation pulse immediately tips the magnetisation to the steady-state angle where it will remain for the remainder of the acquisition (Figure 3.12).

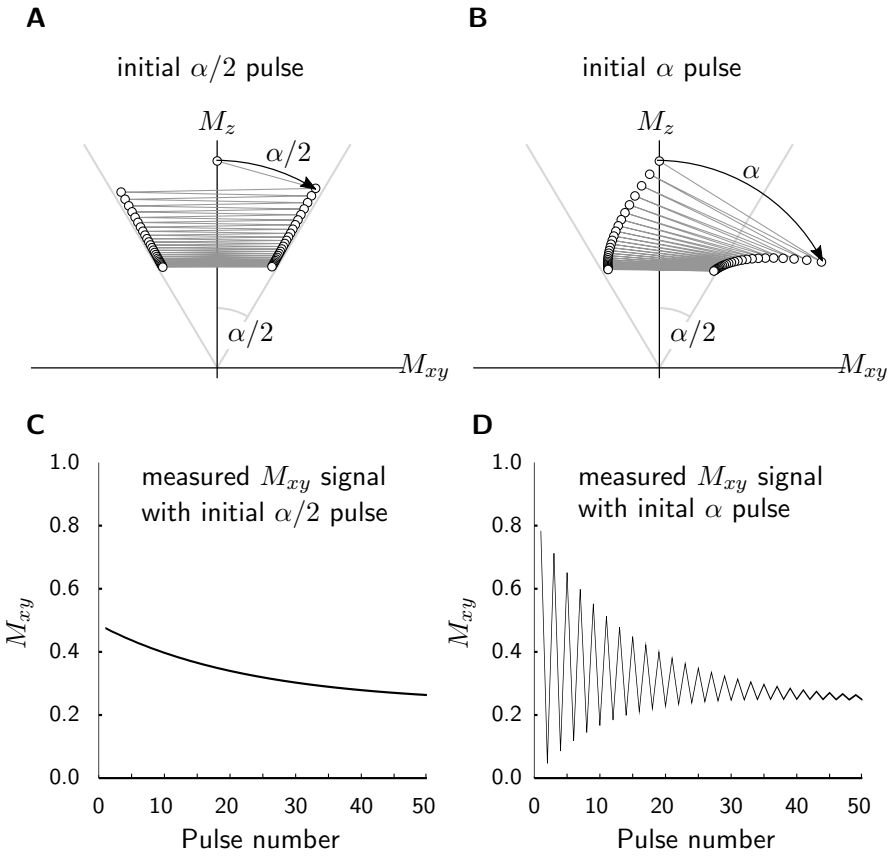


Figure 3.12: Illustrated here are the effects of the half-α setup scheme. (A) The evolution of the magnetisation with the half-α setup scheme. (B) The evolution of the magnetisation without the half-α setup scheme. (C) M_{xy} following the half-α setup. (D) M_{xy} following no half-α setup.

This sequence however, is susceptible to off-resonance effects. Periodic troughs in signal intensity occur, known as 'banding'. These bands are caused by B_0 inhomogeneities occurring due to boundaries in different susceptibilities, so it is important that shimming is applied to minimise off-resonance effects. The period of the signal troughs decreases as the TR increases, so in order to minimise banding effects the TR is kept as short as possible. A simulation of the banding effect is illustrated in Figure 3.13.

The bSSFP sequence is able to acquire distortion free images with a high signal

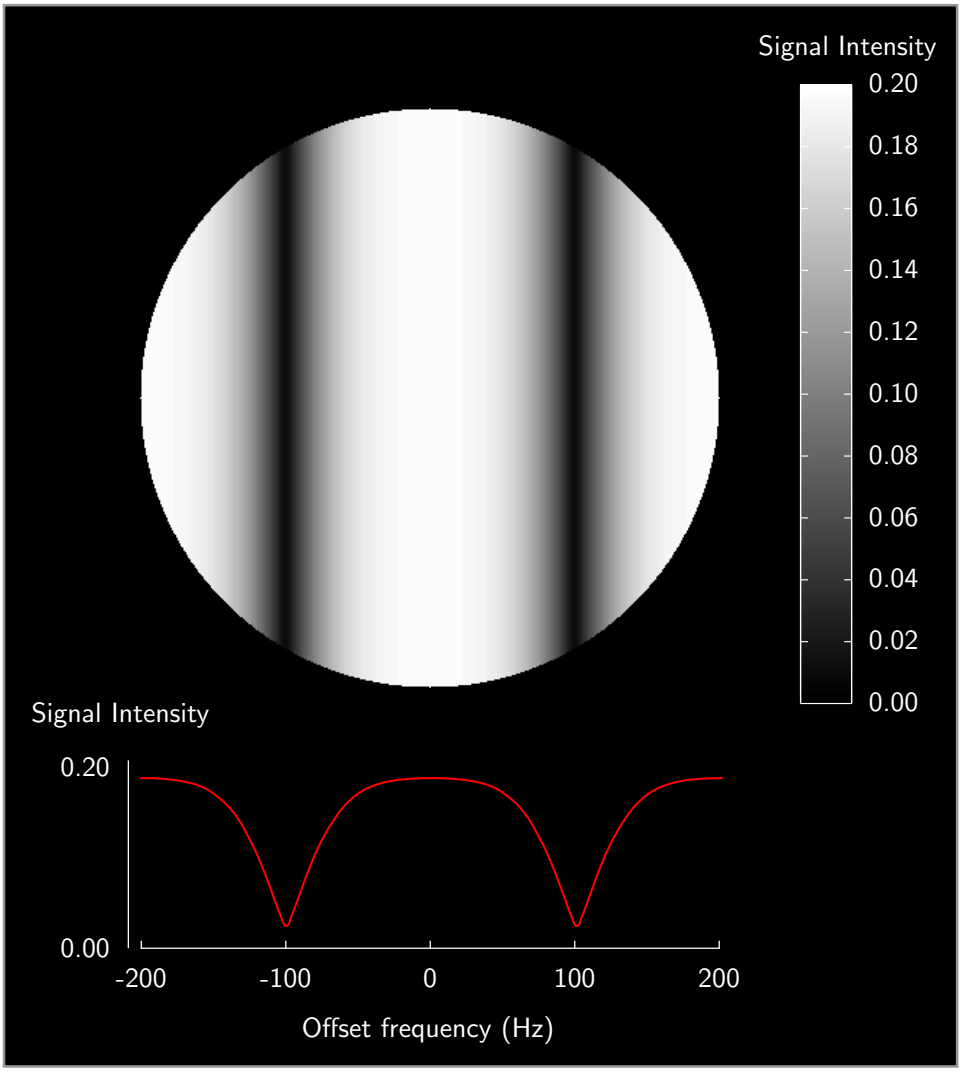


Figure 3.13: Simulation of banding artefacts caused by off-resonance effects of the bSSFP sequence, occurring periodically at 100Hz intervals. Simulation parameters $T_1 = 600$ ms, $T_2 = 100$ms, $TE/TR = 5$ /10 ms, flip angle $= 50^o$, M_0=1

to noise. The trade-off is that bSSFP requires a much greater time and deposits a large amount of RF power than EPI. Functional applications are therefore limited to a small field-of-view in the z-direction. The bSSFP readout is used in Chapter 7 to acquire high resolution, distortion free ASL data in a Multiple Sclerosis patient group.

3.4.3 2D Echo-planar imaging

Echo planar imaging (EPI) is an imaging technique where the entirety of k-space is acquired following a single excitation pulse. This has the benefit of having a very small acquisition time compared to the spin-warp technique. The EPI technique was first conceived by Sir Peter Mansfield in 1977 [3].

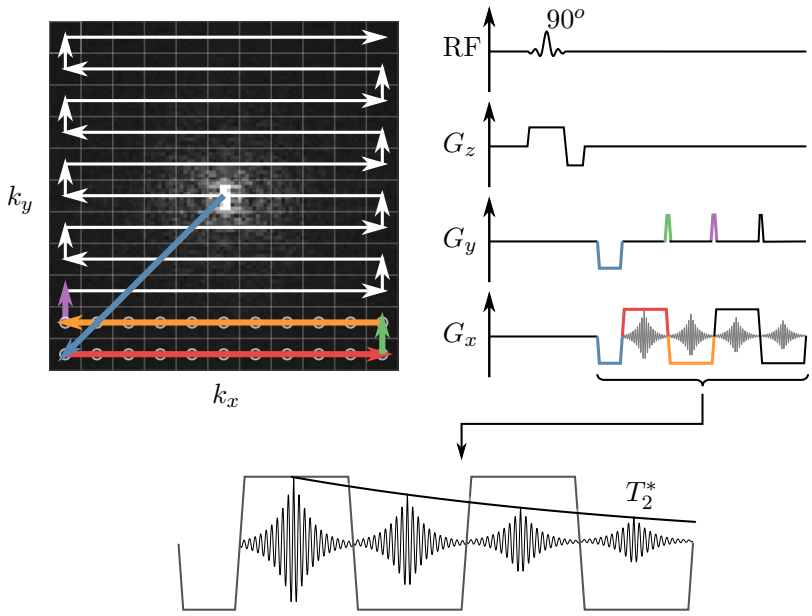


Figure 3.14: Illustration of k-space trajectory and associated pulse sequence diagram for a 2D-EPI sequence. The circles represent which k-space voxels are sampled. The recorded signal during the frequency encoding gradients decays at a rate defined bt T_2^*

2D gradient echo EPI technique begins with a 90^o slice excitation, then followed by short duration phase and frequency encoding gradients to dephase signals in both x and y directions which send the k-space trajectory to a corner of k-space (Figure 3.14 light blue line). A frequency encoding gradient of equal but opposite magnitude is applied to rephase the signal in the k_x direction and the signal is acquired (Figure 3.14 pink line). A small phase encoding 'blip' is applied which slightly adjusts the phase shifts of the signals, equivalent to stepping up a line in k-space (Figure 3.14 dark blue line). Another frequency encoding gradient is applied to sample a new line of k-space, but in the opposite direction (Figure 3.14 green line). By successively applying these small phase encoding blips and sweeping the frequency encoding gradients back and forth, the entirety of k-space

can be sampled from a single slice excitation in a short amount of time.

The signal is recorded during the alternating frequency encoding gradients, with the maximum amplitude of the echo occurring in the centre of the lobe. The amplitude decays at a rate defined by T_2^*.

Due to the very short duration and high T_2^* contrast of EPI, it is commonly used for functional experiments where temporal resolution is very important. However, when imaging a volume each slice is acquired at a slightly different time, causing temporal offsets across the volume. 2D-EPI is used in Chapters 5 and 6 to acquire arterial spin labelling and fMRI functional MRI data.

3.4.4 EVI and 3D Echo Planar Imaging

Echo Planar Imaging can be extended in order to acquire a 3D volume. One such way is the technique called echo volumar imaging (EVI). In this technique a volume is excited using an RF pulse and the phase and frequency encoding gradients are applied just as in EPI. However, before acquiring the plane of k-space, a phase encoding blip is applied in the z-direction. This is repeated with different k_z blips until the 3D k-space is sufficiently sampled, and the data is reconstructed using a 3D Fourier transform. This technique acquires an entire volume from one RF pulse, but it takes a time much longer than a typical T_2^*. As the signal decays with T_2^*, there is limited signal remaining by the end of the acquisition, causing a loss in signal to noise and a severe distortion. Further, EVI requires rapidly switching magnetic field gradients.

An improved method of using EPI to image a 3D volume is 3D-EPI (Figure 3.15). In this technique the entire volume of interest is excited by an RF pulse. A phase encoding gradient is then applied in the z-direction, followed by alternating frequency encoding gradients in the x-direction and phase encoding blips in the y-direction. Following this sequence, the same RF pulse is again applied to the volume but with a different phase encoding gradient in the z-direction. By stepping through varying phases in the z-direction, the volume can be spatially resolved in the z-direction using a 3D Fourier transform.

As the sequence applies repeated RF pulses, the magnetisation will eventually reach a steady state. In order to achieve the maximum signal, the flip angle

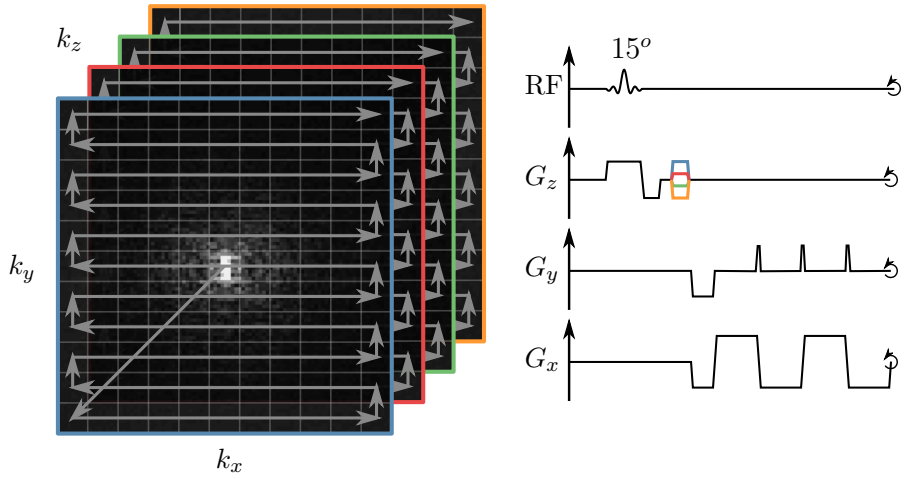


Figure 3.15: Illustration of the k-space trajectory and pulse sequence for a 3D-EPI acquisition. The outlines of each k-space plane correspond to a phase encoding gradient in the z-direction shown in the pulse sequence.

must be optimised to the repetition time and the T_1 relaxation. The amplitude of steady state signal can be found from

$$M_{ss} = \frac{M_0 \sin\theta \ (1 - \exp(-\mathrm{TR}/\mathrm{T}_1))}{1 - \cos\theta \exp(-TR/T_1)} \tag{3.8}$$

This equation is also true for the FFE sequence introduced in Section 3.4.1. The TR required for this steady-state signal is typically maximised at low flip angles (around 15^o), as larger flip angles would suppress successive planes of k-space. The low flip angle also reduces the amout of RF power deposited in the sample which is important when imaging *in-vivo*, especially at ultra-high field.

The benefit of 3D-EPI over the repeated single slice excitation of 2D-EPI is that the acquired signal originates from the whole volume rather than a single slice. This results in a much higher signal-to-noise, which increases with sample volume. 3D-EPI is also beneficial for functional imaging, as each slice has the same temporal weighting. However, this technique suffers from motion artefacts.

Due to the long echo trains and decaying signal, distortions are common in EPI based techniques, in particular at boundaries between different magnetic susceptibilities. It is often important in a clinical setting to acquire images

which reveal details regarding structure, which would require no distortions. The appropriate readout should therefore be chosen for the application.

3.5 Faster coverage of k-space

The duration of an acquisition is often a limiting factor in its application. Capturing dynamic processing in the brain often requires the fastest acquisition techniques and long acquisitions can be sensitive to effects of T_2^* decay and off-resonance effects. There are two common adaptations that can be made to acquisitions in order to decrease their acquisition duration, these are sensitivity encoding (SENSE) and Partial Fourier Imaging.

3.5.1 Partial Fourier

The symmetry of k-space is well understood, as illustrated in Figure 3.16, whereby the real components are symmetrical about axes and the imaginary components are anti-symmetric. This concept is known as 'phase-conjugate symmetry'. Therefore, theoretically, all of the information regarding the image can be stored within one half of k-space.

In practice, however, there are many factors which can ruin the phase-conjugate symmetry and affect the reconstruction. The addition of noise in the acquired section of k-space will cause a reduction in SNR by $\sqrt{2}$. This is because the same noise components are mirrored causing the effect of noise to double. In practice, the SNR is further decreased by such effects as B_0 inhomogeneities, patient motion and susceptibility effects as these ruin the phase-conjugate symmetry. It is therefore common to acquire slightly more than 50% of k-space to minimise SNR loss.

Figure 3.16 illustrates the case in which the partial Fourier technique is used in k_y, allowing for fewer phase-encoding steps. The partial Fourier method can also be applied in the k_x direction, allowing for a shorter echo time. However, most applications of partial Fourier imaging synthesise data in the k_y direction, as sampling has more effect on the acquisition time in the phase encoding direction than the frequency encoding.

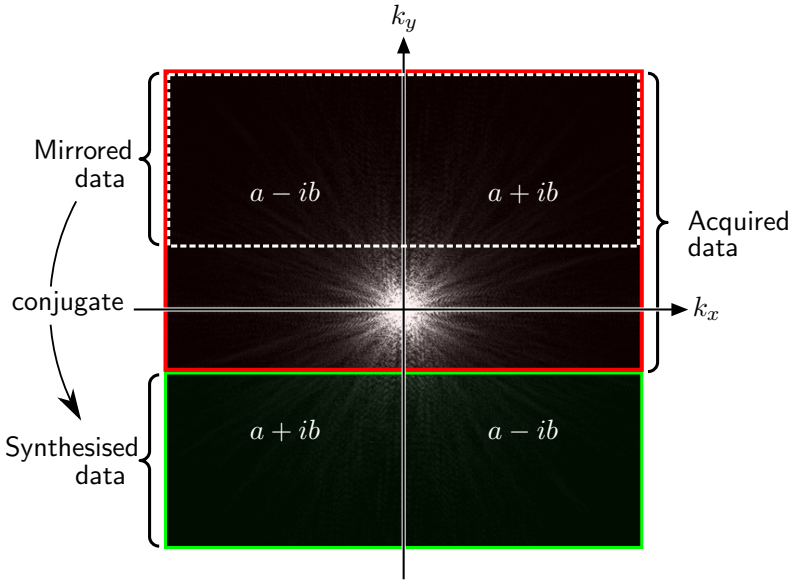


Figure 3.16: Partial Fourier imaging whereby slightly more than half of k-space is acquired in the phase encoding direction. The phase-conjugate symmetry about the centre allows for remaining data to be synthesised from acquired data.

3.5.2 SENSE

Sensitivity encoding (SENSE) is a technique which acquires images from undersampled k-space using numerous receive coils to decrease the duration of the acquisition. This concept was first described by *Pruessmann et al., (1999)* [44]. When k-space is undersampled, the duration of the scan is shorter. However, the image produced is aliased where signals are originating from different places and are incorrectly mapped to the same pixel. This is because the sampling is not dense enough to distinguish between two different frequencies, causing an overlap in signals (Nyquist Theorem). The shortening of the scan duration is described by a term known as the 'SENSE reduction factor', where a SENSE reduction factor of n means that the scan is n times quicker.

Images containing aliasing cannot be unfolded without additional information. The use of additional receive coils placed at different locations around the sample can provide this necessary information. Coils placed at different locations around the sample will possess their own unique sensitivity to the sample, such that

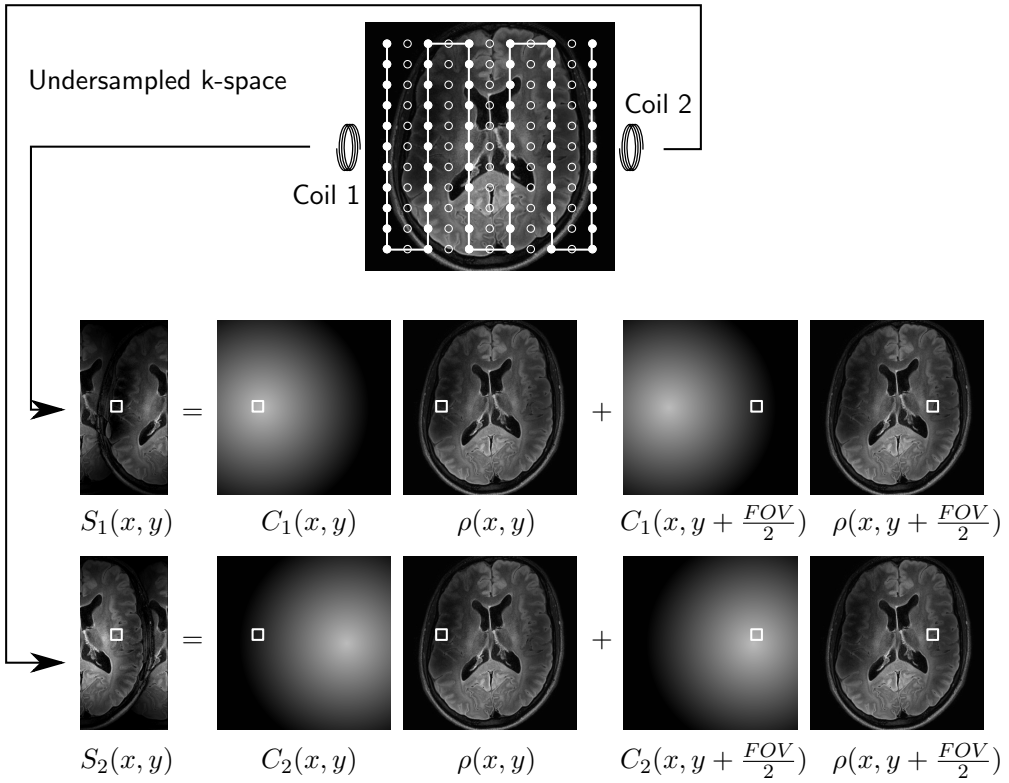


Figure 3.17: Sensitivity encoding using two coils and a SENSE reduction factor of 2.

signals originating from the same area will have different magnitudes if measured on different coils. If these coil sensitivities are known for several coils, a network of linear equations can be created to calculate the contributing signal (Figure 3.17).

In a scenario with n receive coils, an acquired image from undersamping k-space is given as S_n. Images acquired from each coil will have a spatial sensitivity which can be mapped, named C_n. The spin density of the sample, ρ, is the image which has been folded to produce S_n. Figure 3.17 highlights a pixel within S_n where aliasing has occurred and the the signal is made from the addition of two spatially separate signals. The summation of these signals can be written as

$$S_1(x,y) = C_1(x,y) \cdot \rho(x,y) + C_1\left(x, y + \frac{\text{FOV}}{2}\right) \cdot \rho\left(x, y + \frac{\text{FOV}}{2}\right)$$
$$S_2(x,y) = C_2(x,y) \cdot \rho(x,y) + C_2\left(x, y + \frac{\text{FOV}}{2}\right) \cdot \rho\left(x, y + \frac{\text{FOV}}{2}\right)$$

When dealing with a large number of aliased pixels, this is more simply written

as the matrix equation

$$\mathbf{S} = \mathbf{C}\rho \tag{3.9}$$

$\mathbf{C}$ is the matrix which describes the coil sensitivity, where the number of rows corresponds the the number of coils and the number of columns corresponds to the number of locations contained within a single pixel. The number of separable signals is bound by the number of coils, so to separate n overlapping pixels, n coils are needed. In order to determine ρ, the inverse of $\mathbf{C}$ must be found

$$\rho = \left(\mathbf{C}^H C\right)^{-1} \mathbf{C}^H \mathbf{S} \tag{3.10}$$

In practise, each coil may have different noise levels. In order to account for this, a noise matrix can be constructed, $\mathbf{\Psi}$, which can be inserted into Equation 3.10 to give

$$\rho = \left(\mathbf{C}^H \mathbf{\Psi}^{-1}\right)^{-1} \mathbf{C}^H \mathbf{\Psi}^{-1} \mathbf{S} \tag{3.11}$$

3.6 Hardware

The hardware required to perform the techniques descried in previous sections can be split into four main areas; the static magnetic field B_0, the gradient coils, shimming coils and the radiofrequency coils (Figure 3.18). All work presented in this thesis was performed on a 7T Philips Achieva system so hardware specifications discussed here are specific to this scanner.

3.6.1 Static magnetic field

The static magnetic field, orientated horizontally, is generated through the centre of the bore using a superconducting solenoid. The coils wound around the bore are cooled using liquid helium. The diameter of the bore is 55cm, however the usable field (i.e. where the field is most stable and uniform) is limited to a spherical volume at the centre of the magnet with a 25cm diameter. At the Sir Peter Mansfield Imaging Centre (SPMIC), the magnetic field outside the solenoid is reduced by lining the walls of the room with thick sheets of iron. Approximately 200 tonnes of iron is required to reduce the magnetic field from 7T to 5mT within a safe distance of the building.

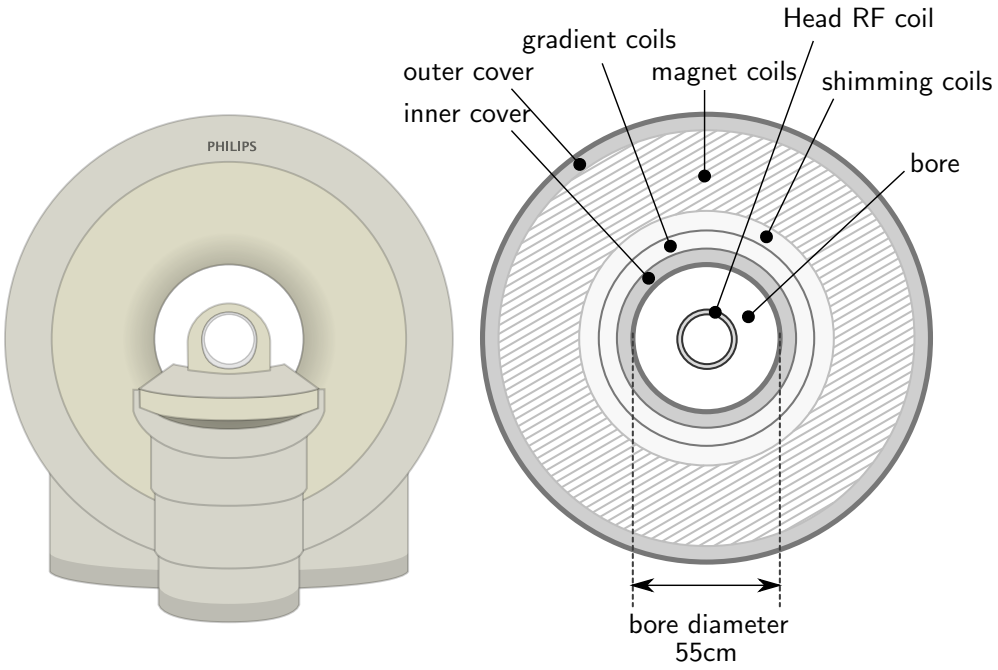


Figure 3.18: A schematic cross-section of a 7 T Philips Acheiva MR scanner.

3.6.2 Gradient Coils

The gradient coils are required to spatially encode the signals originating from the sample, as described in previous sections. The rapid gradient switching needed to produce an image requires quickly alternating high currents causing high temperatures, so they are therefore liquid-cooled. Gradient coils have different geometries based on which direction they need to be applied; gradients in the z-direction use a series of Maxwell coils, whereas the gradients in the x and y direction require 'fingerprint' windings. Three layers of gradient coils are therefore required to spatially encode a signal. The gradient coils at 7T can produce a maximum gradient of 40 mT/m, with a maximum rate of change (slew rate) of 200mT/m/s. Safety considerations also limit the maximum amplitude and slew rate, as rapidly changing gradients can induce a physiological effect known as peripheral nerve stimulation (PNS). Electrical currents are induced in human tissue when the rate of change of field breaches a certain threshold which can be uncomfortable or painful.

3.6.3 Shimming Coils

The principle behind MR imaging relies on adjusting the precessional frequencies away from the Larmor frequency using gradients to spatially encode signals. However, in practice the magnetic field is distorted by the presence of matter such that the magnetic field is not uniform. This causes the Larmor frequency to spatially vary in undesired ways, ruining the image quality. In order to counter these field effects, shimming gradients are used. The shimming required is dependent on the volunteers head size/shape and orientation so must be calculated and applied at the start of each scanning session. It is required that the calculations for shimming gradients must be fast as the volunteer must remain in the scanner until they found.

3.6.4 Radiofrequency Coils

Two sets of coils are needed to image samples; a transmit coil and a receive coil. The coils are layered such that the receive coil is closer to the sample than the transmit coil. The receive coil often has many channels in order to perform sensitivity encoding with large reduction factors. At lower field strengths the transmit coils are built into the lining of the scanner, however at 7T the transmit coil must be restricted to a smaller volume to provide sufficient power. Due to the higher field strength, the wavelength of the RF pulse (typically $\sim$10 cm) required to excite the spins (described by Equation 2.10) allows the RF power to be much more easily absorbed by biological matter.

The particular coil installed on the 7T is the Nova Medical 1TX/32RX, a single transmit - 32 channel receive coil. The receive coils sit inside the transmit coil, where the inner dimensions of the receive coils are 19x21x24cm.

3.6.5 Overview

The pulse sequence must first be pre-scripted using a console, defining the shape of the RF pulses, magnitude of gradients in each direction and their respective timings. Once a pulse sequence is created, the signals must be passed from the console to analogue based systems, which requires a digital to analogue converter (DAC).

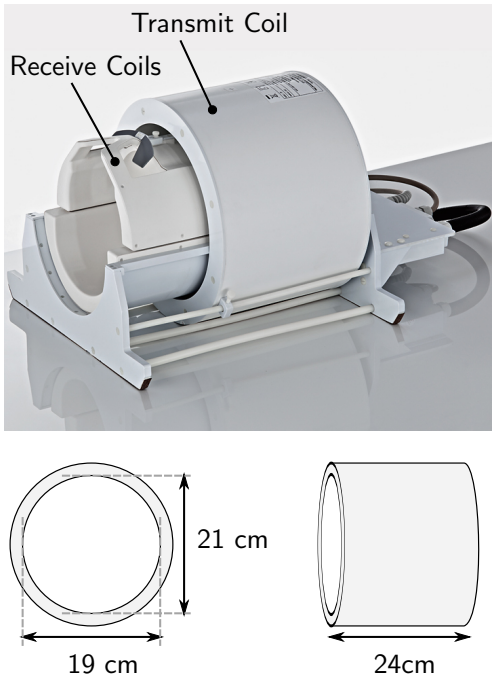


Figure 3.19: The Nova Medical 1TX/32RX Head coil installed in the 7T Philips Acheiva. The inner dimensions of the receive coil are 19x21x24cm.

The waveform of the gradients are therefore passed to a gradient amplifier so the necessary current can be generated to produce magnetic field gradients in the order of 10 mT/m.

The RF pulse when passed through the DAC only contains information regarding its shape and not its oscillatory frequency. In order for the RF pulse to oscillate at the Larmor frequency, it is mixed with a carrier frequency provided by a frequency synthesiser. The carrier frequency must match that of the Larmor frequency in order to achieve excitation. Once the RF pulse has been mixed, it is amplified such that it achieves amplitudes of tens of μT.

The RF transmit coil and RF receive coil are located within the same volume, however the transmitted RF field will induce a voltage many times the magnitude of precessing spins from the sample. In order to prevent damage to equipment, the receive coil is gated off during transmission.

The induced signal from the precessing spins is very small, and must therefore be amplified before being recorded using a preamplifier (pre-amp). A pre-amp is used in order to ensure that the recorded signals are many times greater than

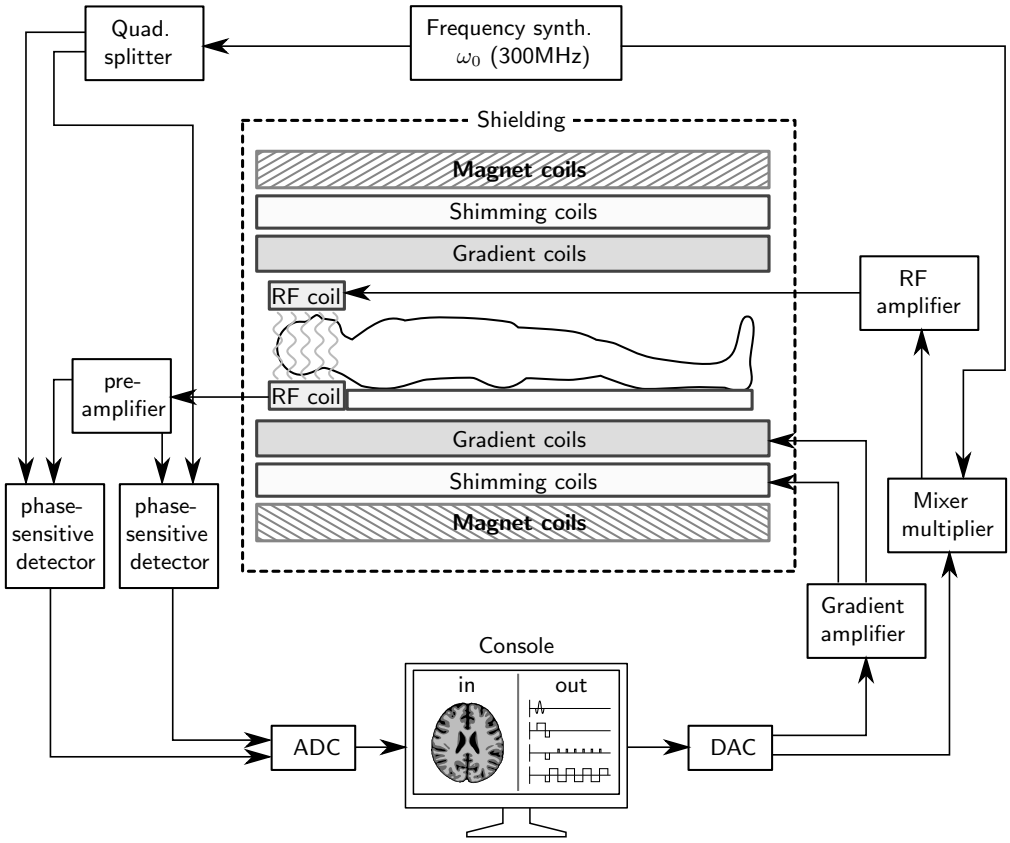


Figure 3.20: Illustrated overview of an MR imaging hardware, showing the interface between software and hardware.

noise that could be introduced by electronics. As described in Figure 2.7, the signal is recorded at two phases, 90^o offset using phase-sensitive detectors. By mixing the recorded signal with the Larmor frequency, the signal can be simplified allowing for better interpretation. As the phase-sensitive detectors record the signal at 90^o offset, this requires two mixing frequencies that are also 90^o offset. This is performed by running the mixing frequency through a quadrature splitter beforehand. Once final signals are processed, they are sent to an analogue to digital converter (ADC) and fed back into the console. The processing of signals to images is performed by the console.

3.7 Safety

MRI is a completely non-ionising imaging modality commonly used in clinical settings. Modalities such as x-ray photography and computed tomography (CT)

scans deposit energy via exposure to high frequency photons, which are known to have detrimental effects. Despite this advantage an MR scanner possesses, there are other safety concerns which are considered a trade-off to the lack of ionising radiation.

3.7.1 Static field

The static magnetic field produced through the bore of an MR scanner is extremely large and will exert strong forces on any ferrous metal. Therefore any magnetic materials must not enter the shielded area. It is therefore important to safety screen any human participants before they enter an MRI scanner. Contraindications to MRI include implants such as pacemakers, aneurysm clips, shrapnel and implants.

3.7.2 Gradients

The magnetic field gradients required to spatially encode signals vary rapidly with time, with the amplitude flipping on the order of kilohertz. Changing magnetic fields will induce a current as described by Faraday's Law. Sufficient enough, these currents will be induced within tissue and cause muscles to twitch, known as peripheral nerve stimulation (PNS). PNS can become very uncomfortable for volunteers, and therefore the US Food and Drug Administration have created guidelines on the maximum switching rate of the magnetic field gradients.

The rapidly switching current through the gradient coils will cause a Lorentz force to be felt by the coil, due to the presence of the large static field. Therefore, the gradient coils will vibrate at a frequency determined by the gradient switching rate, causing a loud acoustic noise. Human volunteers are therefore required to wear ear protection throughout the duration of the scan.

3.7.3 Radiofrequency Pulses

Radiofrequency pulses are necessary to excite nuclei in the sample, however the energy carried by the RF pulse is deposited in the sample. This manifests as heating of the sample which must be considered with human volunteers. The amount of energy deposited is calculated in terms of specific absorption rate

(SAR), which is the amount of power deposited to a kilogram of mass (W/kg). The US Food and Drug Administration have determined guidelines which represent limits of energy deposition and therefore tissue heating. Safety screening ensures that human volunteers with any condition which may affect their ability to regulate temperature in response to tissue heating are not eligible.

SAR typically increases as external magnetic field strength B_0 increases. This is because the wavelength of the RF pulses to excite spins becomes comparable to the dimensions of human volunteers, causing the RF power to be more readily deposited. Therefore SAR considerations are important at ultra-high field strength.

3.8 Summary

This chapter has explained the application of NMR to spatially extract information from a sample using encoding gradients and RF pulses. After spatial encoding, the signals can be sampled using many different sampling techniques such as spin-warp, bSSFP and EPI. It is possible to increase the speed of the acquisition by applying techniques such as SENSE and partial Fourier, however these come at the cost of signal-to-noise ratio. The hardware required to apply this theory and the safety concerns are addressed.

4 Functional Brain Imaging

In this Chapter, measures of brain function are described and the methods used to acquire these metrics are discussed. The methodology behind *Arterial Spin Labelling* (ASL) is emphasised, while *functional MRI* (fMRI) and contrast based perfusion mapping is introduced. The theory, acquisition, pre-processing, quantification and post-processing of ASL is discussed and a pipeline for processing ultra-high field data is described.

The hypothesis that brain activity is closely linked to blood flow was first suggested in 1880 by the physician Angelo Mosso. Upon treating a patient who had previously suffered a severe head injury exposing his temporal lobe, Mosso noticed that the ringing of church bells caused observable pulsations. This prompted a study by Mosso in 1890 to assess this phenomenon, which is described in an account by William James [45]. By laying volunteers down on a table delicately balanced on a pivot and exposing them to an sensory stimuli, the table would tip towards the head implying a redistribution of blood to the brain. However, this hypothesis was met with scepticism as it was believed that the rigid casing of the skull would not allow for an increase in blood volume. In the same year, Charles Roy and Charles Sherrington were able to indirectly monitor blood volume fluctuations in the heads of anaesthetised dogs using a novel device placed inside the skull [46]. Although these results suggested that cerebral blood volume can increase, the craniectomy suggested to many that the results were not representative of a natural environment. Technical limitations stunted this area of research until 1948 when *Kety and Schmidt et al., (1948)* [47] were able to acquire whole brain blood flow estimates in humans by the inhalation of nitrous oxide and measuring the concentration in the arterial and venous sides. Following on from this was work by Niels Lassen's group, where they developed an automagraphic technique of quantifying regional cerebral blood flow using a radioactive krypton injection [48] and a combination of scintillation detectors orientated around the head. This work was extended in 1965 by David Ingvar whereby subjects were asked to perform a memory test whilst regional cerebral blood flow measures were taken [49]. Significant increases in cerebral blood flow were found in the cortex during this activation, the first study to conclusively demonstrate this in humans. The invention of

positron emission tomography (PET) in 1974 allowed this research to develop, providing a new modality to acquire information on blood flow. In 1977, the first study using PET to measure regional cerebral haemodynamics was published by *Yamamoto et al., (1977)* [50]. This study administered a non-diffusible 68Ga-EDTA tracer for transit time and the diffusible tracer ^{77}Krypton to measure uptake. Yamamoto was able to create a cross-sectional map of the brain showing regional perfusion. The next major development came in 1991 when John Belliveau first showed that regional activity is strongly linked to blood flow using MR imaging [51]. This experiment acquired two cerebral blood flow maps from the volunteer using a gadolinium tracer; one during rest and the other during exposure to a visual stimulus. The differences between these blood flow maps revealed higher blood flow in the visual cortex during exposure to the visual stimulus than during rest. The need for such an observation to be made non-invasively with MR imaging was met only one year later by Seiji Ogawa's group where they used the different magnetic properties of oxygenated and deoxygenated blood to detect relative changes in regional blood flow [52]. By exposing a volunteer to blocks of a visual stimulus, they caused an increase in oxygen demand in the visual cortex which increased the concentration of oxygenated blood. Oxyhaemoglobin is diamagnetic and deoxyhaemoglobin is paramagnetic, which means that as the ratio of oxyhaemoglobin to deoxyhaemoglobin increases, an increase is signal is observed. They coined this method the Blood-Oxygen-Level Dependent (BOLD) effect. Despite acquisition methods evolving since this discovery, the underlying principle has become the most common way of observing regional brain activation using MR imaging. Despite not fully understanding the intricate coupling of blood flow and neuronal activity, BOLD measures have become hugely important in the diagnosis and treatment of neurodegenerative disease.

4.1 Functional Brain Measures

MR imaging is able to provide structural information on the brain which can be used in the diagnosis and treatment of disease, e.g. the location of tumours in cancer patients and severity of atrophy in neurodegenerative diseases. However, dynamic information of the brain can also be clinically important for a better

understanding of disease, e.g. detecting enhancing lesions in patients with Multiple Sclerosis. Explained here are important functional measures which can be acquired using MR imaging.

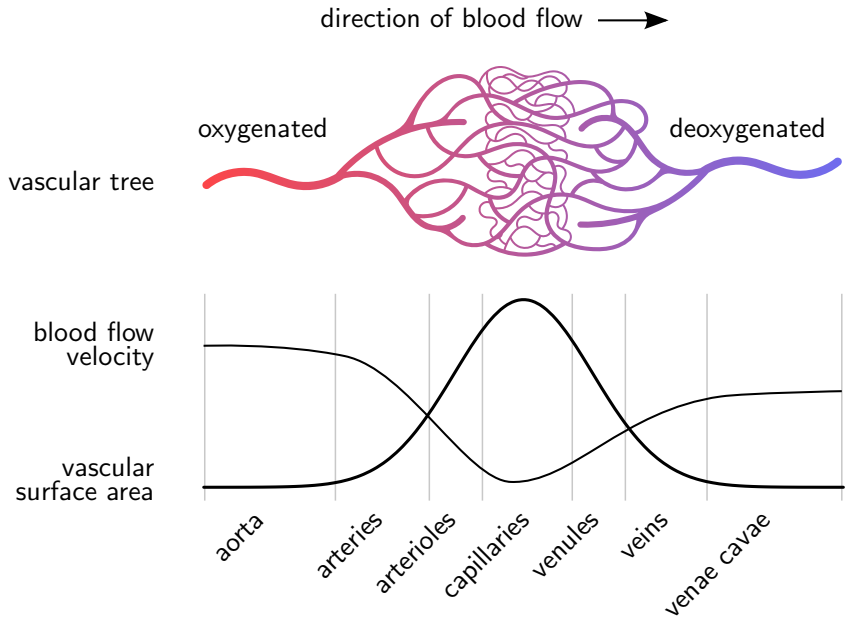


Figure 4.1: An illustration of the vascular network showing associated surface areas and blood flow velocities in the different sized vessels.

One important functional measure is *perfusion*. Perfusion is a fundamental physiological function whereby blood flows through networks of capillaries in tissue, which allows oxygen and nutrients to be exchanged between arterial blood and surrounding tissue. Tissues and organs contain large networks of capillaries, which when combined with their small diameter (5-10μm), produce a large surface area for oxygen and nutrient exchange. The velocity of the blood flowing through the vascular tree also drops significantly in smaller vessels to allow more time for exchange. These effects are illustrated in Figure 4.1. Perfusion is measured as the flow rate of blood (ml/min) normalised to tissue mass (typically per 100g), such that reported values are usually in units of ml/100g/min. In the brain, grey matter has a typical perfusion of 60 ml/100g/min, whereas white matter has perfusion of 20 ml/100g/min.

4.2 Arterial Spin Labelling

4.2.1 Introduction

The first attempt to measure perfusion using MR was performed by *Le Bihan et al.,* in 1986 [53] using established angiography techniques. However, it was recognised that perfusion manifests as the incoherent motion of water over distances much smaller than a typical voxel, whereas angiography relies on the motion of water over larger distances in order to tag the blood. Following this assertion, *Ackerman et al.,* published a paper in 1987 which demonstrated that perfusion could be measured using tracer kinetics, provided that the tracer was MR detectable. Early examples of such a tracer were deuterium oxide [54] and trifluoromethane [55], however gadolinium based contrast agents such as Gadovist^{TM} and Prohance^{TM} are now commonly used. Despite these being used to observe perfusion, the procedure is invasive. In 1992, *Detre et al.,* [56] demonstrated that blood water itself could be used as a tracer. By continuously saturating the magnetisation of blood flowing up through the arteries in the neck, a steady-state could be reached in the brain where the concentration of saturated spins is dependent on the regional perfusion. The technique was coined *Arterial Spin Labelling* (ASL). Since this early concept was developed, the technique has been continuously adapted and improved. This section describes the modern implementation of ASL.

ASL is a non-invasive technique, using endogenous blood water as a kinetic tracer to measure tissue perfusion. The basis of any ASL technique is the acquisition of two images; a 'label' and a 'control'. The label image is acquired following the inversion or saturation of inflowing blood spins, whereas the blood signal in the control image is not manipulated in any way. A short time period known as the the post-label delay (PLD), is allowed between labelling the inflowing blood and acquiring an image. This delay allows the blood to travel into the imaging plane, traverse the capillaries and exchange with the tissue water. By subtracting the label image from the control, a perfusion weighted (PW) image is obtained which provides information purely due to blood signal. Typically, the labelling of blood causes a 1-1.5% signal change from the control image at 7 Tesla, which falls within the noise level of most MR scanners. For this reason, many repeats

are required to increase the signal-to-noise ratio.

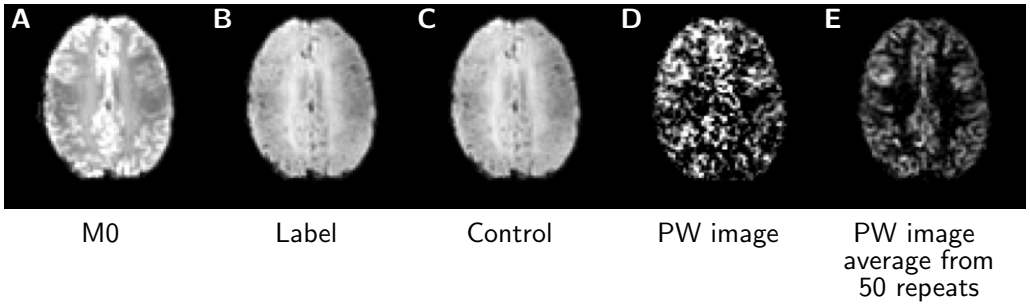


Figure 4.2: Typical images obtained form performing arterial spin labelling. (A) Equilibrium base image. (B) Label image containing labelled blood. (C) Control image with no labelled blood. (D) Perfusion weighted image from one set of label and control images. (E) Perfusion weighted images made from the average of 50 repeats.

The perfusion weighted image signal is affected by many parameters other than perfusion, such as the T_1 relaxation of both blood and tissue, the magnetic field strength and the method used to label the blood. All these parameters must be accounted for when interpreting a perfusion weighted image.

4.2.2 Labelling Schemes

Finding the difference between an image with labelled blood and one without is the basis of ASL. However, there are many different ways in which the blood can be labelled. There are three main categories of labelling schemes; Pulsed ASL (PASL), Continuous ASL (CASL) and Pseudo-Continuous ASL (PCASL). Labelling schemes must be carefully designed so that the only difference between the label and control is due to blood flow. Magnetisation Transfer (MT) effects must be accounted for, as failure to do so will introduce artefacts in perfusion weighted images that are not due to perfusion. This section outlines the theory behind each labelling scheme, with emphasis on PASL as this is the technique used in this thesis at ultra-high field.

4.2.2.1 Pulsed ASL

PASL is a labelling technique whereby the blood is spatially selected using a short duration RF pulse. A large slab of blood surrounding or next to the

imaging plane is labelled and the inflow of this into the imaging plane is observed. The location of the labelling slab and the pulse sequence used to label is what differentiates the PASL techniques. The three most common variations of PASL are flow-alternating inversion recovery (FAIR), signal targeting with alternating radiofrequency (STAR) and proximal inversion controlling for off-resonant effects (PICORE) (Figure 4.3).

The FAIR labelling schemes alternates the use of a spatially selective and non-selective inversion pulses centred on the imaging slab. The non-selective pulse is used to invert blood-water in the whole head (label), whereas the selective pulse inverts the blood-water in a much narrower region surrounding the imaging plane (control). As both label and control are exposed to the same RF pulse, the magnetisation transfer effects are identical. Labelling is typically performed using an adiabatic hyperbolic secant pulse which inverts the spins of the blood water by 180^o. This pulse is very insensitive to B_1 inhomogeneities and off-resonant effects, ensuring that the inversion profile is consistent at ultra-high field.

The STAR labelling scheme labels a slab of blood below the imaging plane using a single adiabatic inversion pulse of power of a 360^o. The associated control image has blood-water spin inverted in the same place, except with two 180^o pulses are applied back-to-back. This matches the magnetisation transfer effects between the label and control conditions as the same RF power is deposited.

The PICORE labelling technique uses the same labelling of blood as for the STAR scheme. The control image is exposed to an off-resonant global inversion pulse, such that it is exposed to the same RF power however the blood-water is not inverted.

4.2.2.2 Continuous ASL

CASL continuously excites blood flowing through a single plane using a long, low amplitude RF pulse. The common location for the blood to be labelled is in the neck where the blood velocity is largest to allow for more blood to be labelled. This induces a flow driven adiabatic inversion of the blood spins. The duration of the RF pulse is typically a few seconds in order to maximise the perfusion weighted signal. Ideally, the labelling of the neck is performed using a separate neck coil with transmit capabilities to remove MT effects however this is not

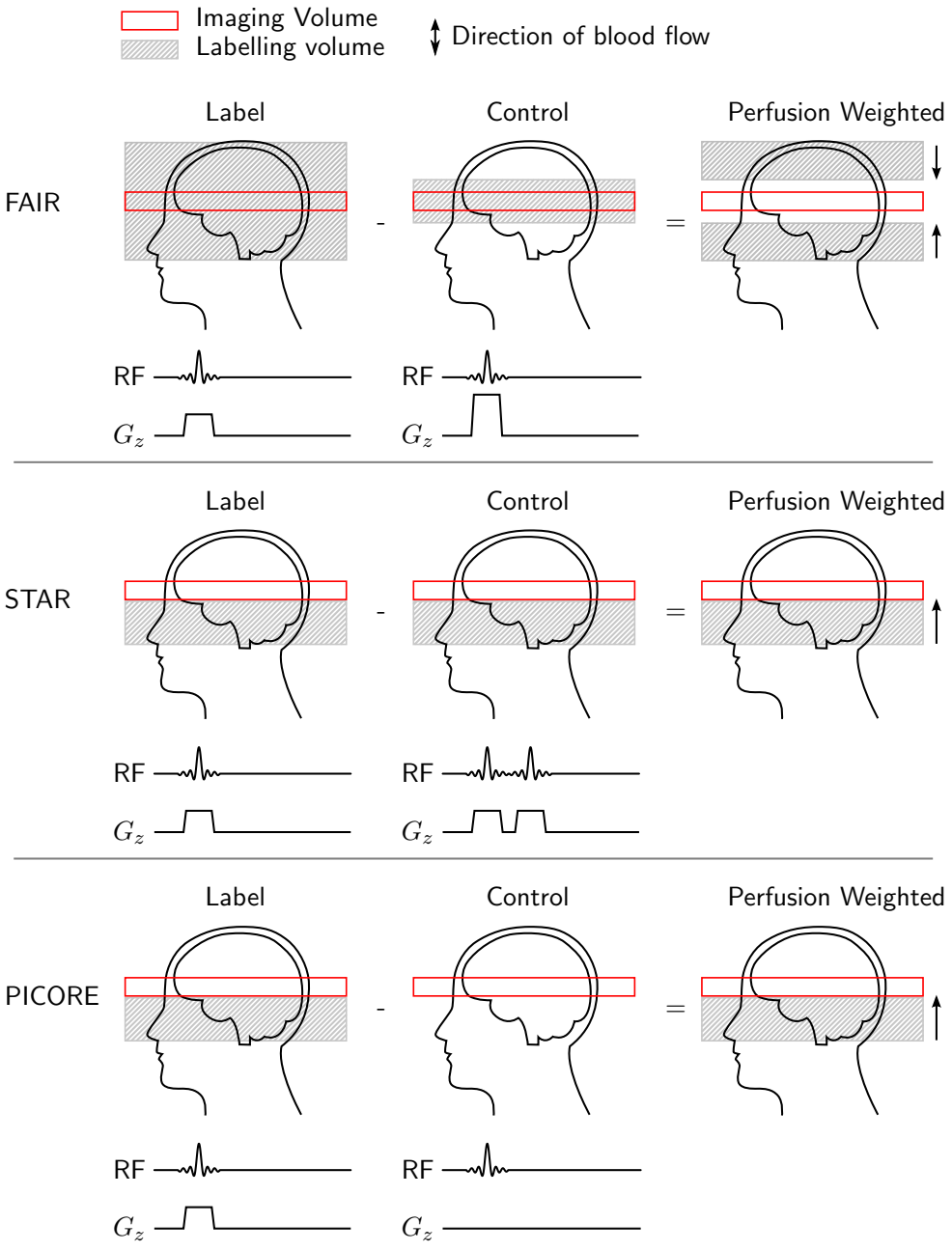


Figure 4.3: Illustrated here are three common PASL labelling schemes. The label and control conditions are explained in terms of the location of labelling volumes. From top to bottom; FAIR, STAR and PICORE.

common. The control condition for CASL does not require the application of any additional RF pulses as the magnetisation effects are already identical, assuming the neck coil is decoupled from the imaging coil. Figure 4.4 illustrates a typical CASL labelling scheme with associated pulse sequences.

Although CASL provides a high SNR, the long exposure to a constant RF pulse can cause SAR limits to be reached. This is especially a problem at ultra high field where the RF frequency is higher and more readily deposited. It is also important that blood flowing through the imaging plane is labelled uniformly requiring the need for good B_0 and B_1 homogeneity in the neck, this is also a challenge at ultra-high field.

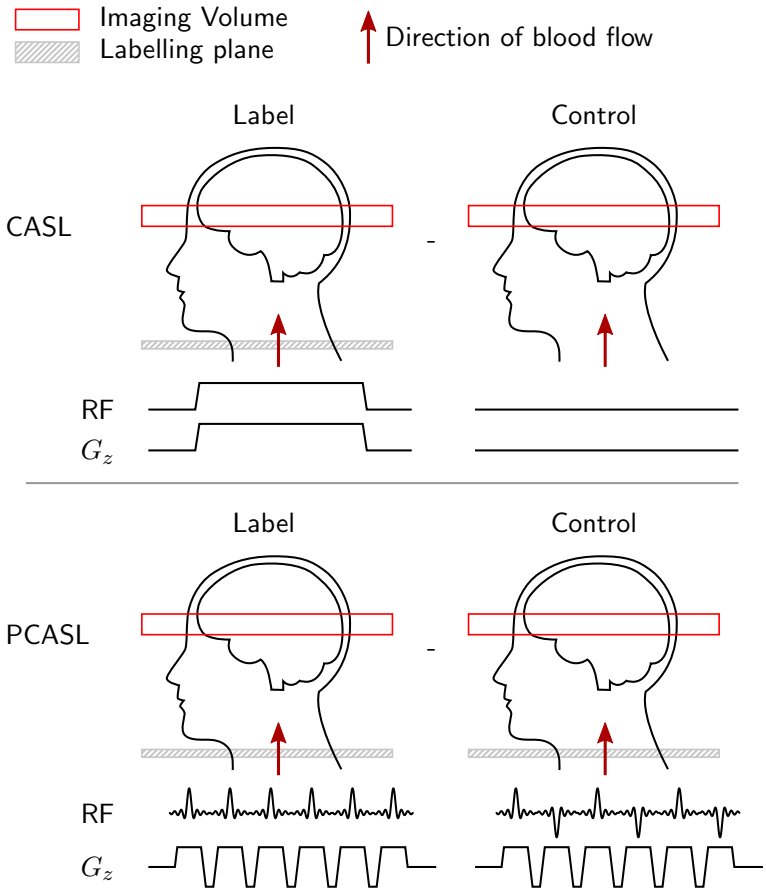


Figure 4.4: Illustration of Continuous and balanced Pseudo-Continuous ASL labelling schemes with associated RF pulses and z-gradients.

4.2.2.3 *Pseudo-continuous ASL*

PCASL is a technique which uses the basic principle of CASL. However steps are taken to reduce the SAR limitations imposed by CASL. PCASL uses a train of very short RF pulses to mimic continuous excitation using only a portion of the RF power. There are 2 types of PCASL which can be used; *balanced* and

unbalanced. Both schemes uses RF pulses with alternating polarity for the control condition but constant polarity for the label condition. The difference between the balanced and unbalanced schemes is due to the gradient waveforms. In the balanced scheme the net area under the gradients for both label and control conditions is equal to zero. In the unbalanced scheme, the gradients for the label condition have a non-zero net area but are zero for the control condition.

Despite a reduction in the RF power deposited compared to CASL, SAR limits are still quickly reached. Therefore CASL and PCASL are primarily suited for field strengths of 3T and lower. Other limitations include issues with B_0 and B_1 inhomogeneities in the neck at ultra-high field. The magnitude of these effects can be reduced using either a separate neck coil [57] or dielectric pads [58].

4.2.3 Acquisition

The label and control images are acquired after a given delay following the labelling, termed the post-label delay (PLD). Early ASL experiments chose a single post-label delay with many repeats and aimed to quantify perfusion from a single image [56]. However, perfusion is a dynamic process and numerous factors can affect the perfusion weighted image, all which cannot be obtained from one single image. There are two approaches used to observe this dynamic process; single-PLD and multi-PLD.

4.2.3.1 Single-PLD or Single-phase

One approach to capture the dynamic process of perfusion is to individually collect data at numerous post-label delays, known as single-PLD or single-phase. After applying the label, a PLD is waited before the acquisition is performed, and a TR waited until after the acquisition to allow a complete washout of labelled blood before the next repeat can be performed. This sequence is then repeated until a sufficient number of ASL repeats have been acquired for a good quality perfusion weighted image at the PLD. This whole process is then repeated with as many post-label delays as deemed necessary to observe dynamic in-flow of blood (Figure 4.5 i-iv).

The acquisitions used for ASL experiments must be rapid to provide a snapshot

of a dynamic process. For this reason, the most common acquisitions are EPI or GRASE (Gradient and Spin Echo) [59]. Generally, EPI is much quicker than GRASE, however GRASE does not suffer from distortions due to the periodic refocussing by the 180^o pulses. There are trade-offs for each acquisition type and the choice is primarily dependent on the study. However, the European Cooperation in Science and Technology (COST) Action have published recommended implementations of ASL in an attempt to normalise protocols used across research studies [60], which recommends the GRASE sequence.

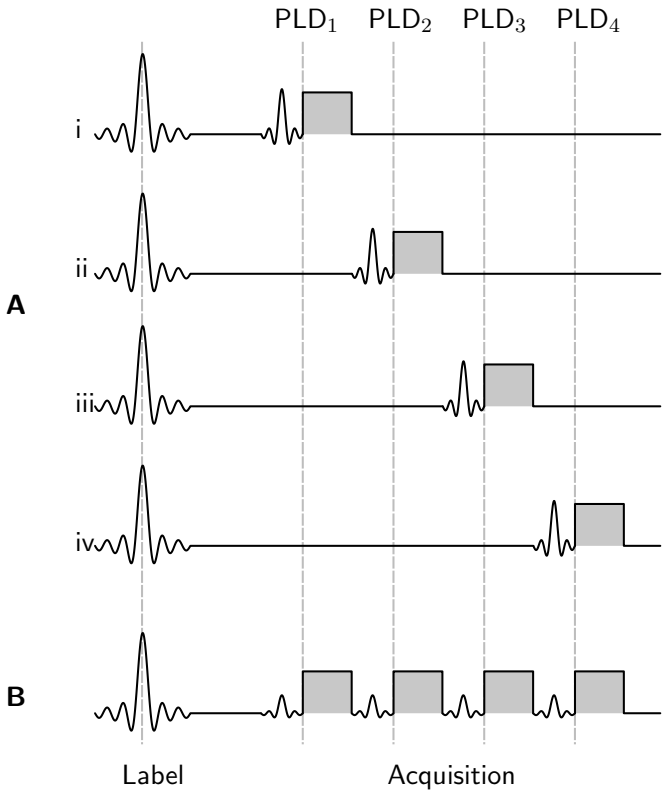


Figure 4.5: Schematic of the single-PLD and multi-PLD acquisitions collected in seperate runs. (A, i-iv) The single-PLD acquisition repeats the experiment multiple times using different PLDS. (B) The multi-PLD acquires multiple PLDs during a single experiment using the Look-Locker technique.

4.2.3.2 Multi-PLD or Multi-phase

There is large amount of unused time between the label and acquisition in the single-PLD method. *Gunther at al., (2001)* [61] proposed that this time can be utilised by collecting other PLDs. However, the blood label is dramatically affected by the acquisition meaning that many acquisitions cannot simply be run back to back. The technique developed by *Look and Locker (1970)* [62] can be adopted to bypass this problem, where a small flip angle RF pulse is applied immediately before each acquisition. Applying many back-to-back readouts with a 90^o flip would cause the longitudinal magnetisation to reach a steady-state with a very low magnitude, making the perfusion signal very hard to detect. By applying a small flip angle for each readout, the steady state longitudinal magnetisation is increased [63] (Figure 4.5 B).

The single-PLD and multi-PLD methods each have trade-offs. The single-PLD acquisition has a significantly longer duration than the multi-PLD if the same amount of PLDs are to be acquired, however it has a larger signal-to-noise as the blood label is not perturbed by multiple acquisitions. However, the SNR per unit time is increased when a multi-PLD acquisition is used. The small excitations required for the multi-PLD acquisition also has a complex effect on the blood label, therefore requiring more detailed modelling.

4.2.4 Improving SNR

As the perfusion weighted signal obtained from ASL is typically low compared to the tissue, typically of the order of 1-3%, efforts are made to increase the signal-to-noise ratio by minimising the sources of unwanted signal.

4.2.4.1 Pre- and Post Saturation pulses

In ASL, saturation pulses can be applied to the imaging volume immediately before (pre-sats) and immediately after (post-sats) the labelling. The benefit of saturation pulses is that they ensure that the tissue magnetisation is the same at the start of each label-control repeat which significantly simplifies the modelling process.

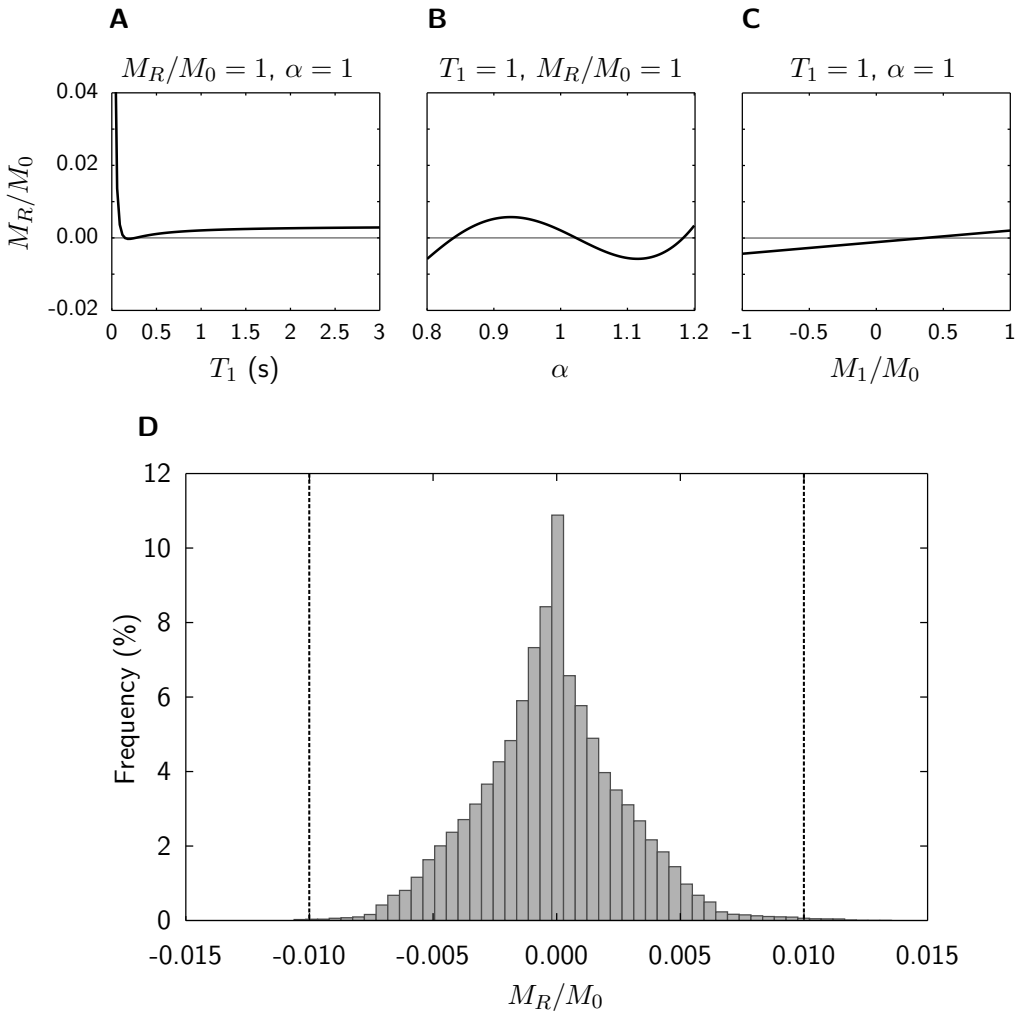


Figure 4.6: Simulations of the residual magnetisation after applying WET pre-saturation pulses on varying (A) T_1, (B) pulse efficiency and (C) M_1/M_0. (D) Histogram of 125,000 simulated residual magnetisations with unique combinations of T_1, M_1 and pulse efficiencies. The dashed lines indicate $\pm 1\%$ residual magnetisation.

The pre-saturation at 7 Tesla uses a *water suppression enhanced through T1 effects* (WET) scheme [64]. The WET pre-saturation at 7T consists of four pulses spaced 10 ms apart, with flip angles of $107^o, 87^o, 76^o$ and 154^o and dephasing gradients placed between them. This scheme is designed to suppress tissue within a range of T_1 values, B_1 values and initial magnetisation (M_1). This is particularly useful at ultra-high field where B_1 inhomogeneities are severe. A simulation of the WET pre-saturation pulses was performed using 50 T_1 values linearly spaced values between 0.5 and 5 s, 50 pulse efficiencies linearly spaced values between 0.5 and 1.5 and 50 M_1 values linearly spaced values between -1 and +1. The

residual magnetisation, M_R, after the WET pre-saturation pulses is plotted for varying T_1 (Figure 4.6.A), pulse efficiencies (α) (Figure 4.6.B) and M_1 (Figure 4.6.C).

The simulation of WET pre-saturation pulses at 7T (using 125,00 realistic and unique combinations of T_1, pulse efficiencies and M_1 parameters) shows that 99.78% of combinations saturates the magnetisations to less than 1% of its maximum (Figure 4.6D).

Following the ASL label, a post-saturation pulse can be used to suppress any residual in-plane signal after the saturation. The post-saturation typically uses one sinc RF pulse, as it can be assumed that the the remaining magnetisation is low. Further, a single pulse also ensures that SAR is kept to minimum.

4.2.4.2 Background suppression

ASL is a subtraction technique which requires the static signals from the label and control to cancel out and only the perfused blood signal to remain. However, the equilibrium tissue magnetisation is much larger than that of the change in signal due to tissue perfusion which means that any imperfect subtractions between label and control due physiological noise, which includes cardiac, respiratory contributions and head motion, will cause significant artefacts.

In order to minimise the effect of tissue subtraction leaving large residual signals not related to perfusion, *Ye et al., (2000)* [65] suggested that the tissue signal can be suppressed to a fraction of its equilibrium magnetisation with a series of specifically timed inversion pulses, termed background suppression (BS) pulses. The times of these BS pulses must be tailored to the tissue T_1 relaxation time such that at the time of the ASL readout, the tissue signal is suppressed to 5-10% of its equilibrium magnetisation. This avoids the need to sign correct the data prior to subtraction. In brain applications, the chosen tissue of interest is typically grey matter as its high perfusion makes it a region of interest (Figure 4.7.A).

Although background suppression generally increases the perfusion CNR and reduces the variance of ASL acquisitions [65, 66], it can be detrimental to the

perfusion signal if the background suppression pulses are not efficient. The blood label will be reduced by a factor of α^n where α is the inversion efficiency of the BS pulse and n is the number of background suppression pulses applied (Figure 4.7.B).

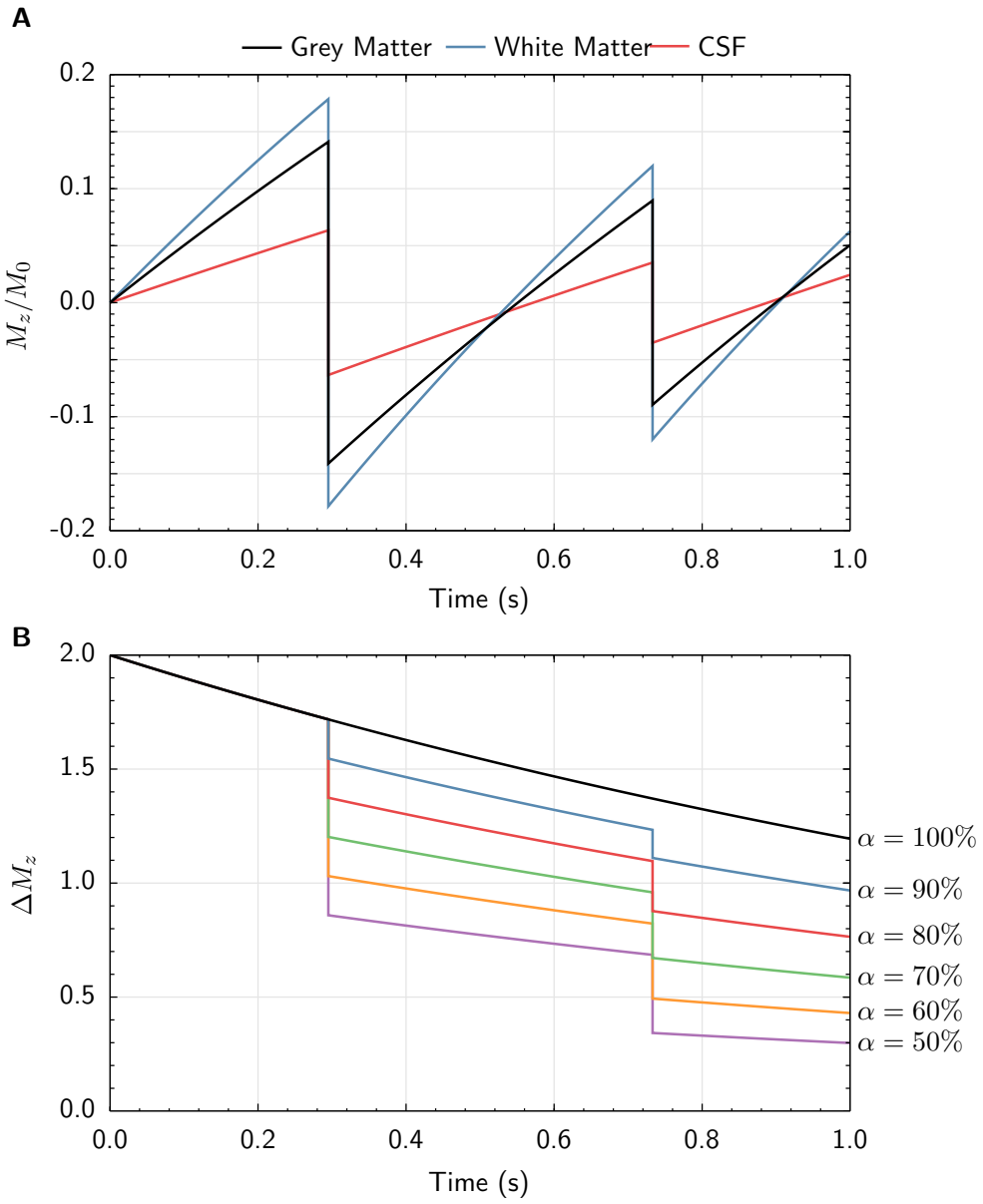


Figure 4.7: (A) Simulation of BS acting upon grey matter ($T_1 = 1.94s$), white matter ($T_1 = 1.5s$) and CSF ($T_1 = 4.5s$) at 7T, BS pulses are applied at 295 and 733ms after the label and pre-sat scheme. This causes causes the grey matter to reach 5% of its equilibrium value at a the time of the readout. (B) Simulation of the effect of changing the efficiency (α) of BS pulses on the blood label.

4.2.4.3 Vascular crushing

When performing ASL experiments, the desired outcome is typically a perfusion map containing spatial information about perfusion. However, the tissue perfusion signal can be contaminated by blood within the arterial components. In order to minimise this effect, a sufficiently long post-label delay can be used to ensure all of the blood label has moved from the arterial compartment into the tissue. However, early post-label delays are important to acquire as they contain information regarding arrival time.

Alternatively, the arterial component can be suppressed using a method known as *vascular crushing*. The basic concept of vascular crushing is to eliminate the magnetisation of blood-water travelling above a certain velocity, as the blood in the arterial compartment travels faster than perfusing blood in the tissue compartment. This can be achieved with the application of bipolar gradients before the acquisition. For stationary spins, bipolar gradients cause the spins to dephase before being rephased, whereas moving spins will not experience the gradient lobes equally and will dephase. The magnetisation of the spins after the bipolar gradients is dependent on the velocity of the spins, the amplitude and duration of the gradients, and is given by

$$M_z = M_0 \text{sinc}\left(2\gamma G\delta\Delta v\right) \tag{4.1}$$

where γ is the gyromagnetic ratio, G is the gradient amplitude, δ is the duration of the gradients, Δ is the time difference between the leading edge of each lobe and v is the velocity. This equation assumes laminar flow where the blood flow velocities are distributed uniformly between 0 and twice the average velocity. The encoding velocity (v_{enc}) is the velocity above which the signal is considered suppressed, given as $v_{\text{enc}} = \pi/2\gamma G\delta\Delta$. An appropriate v_{enc} is determined to be 5 cm/s [67], which eliminates moving signal from arteries and arterioles while the signal from tissue perfusion is retained (Figure 4.8). The addition of vascular crushing increases the echo time of the sequence as the bipolar gradients are applied following slice select excitations and prior to readout gradients.

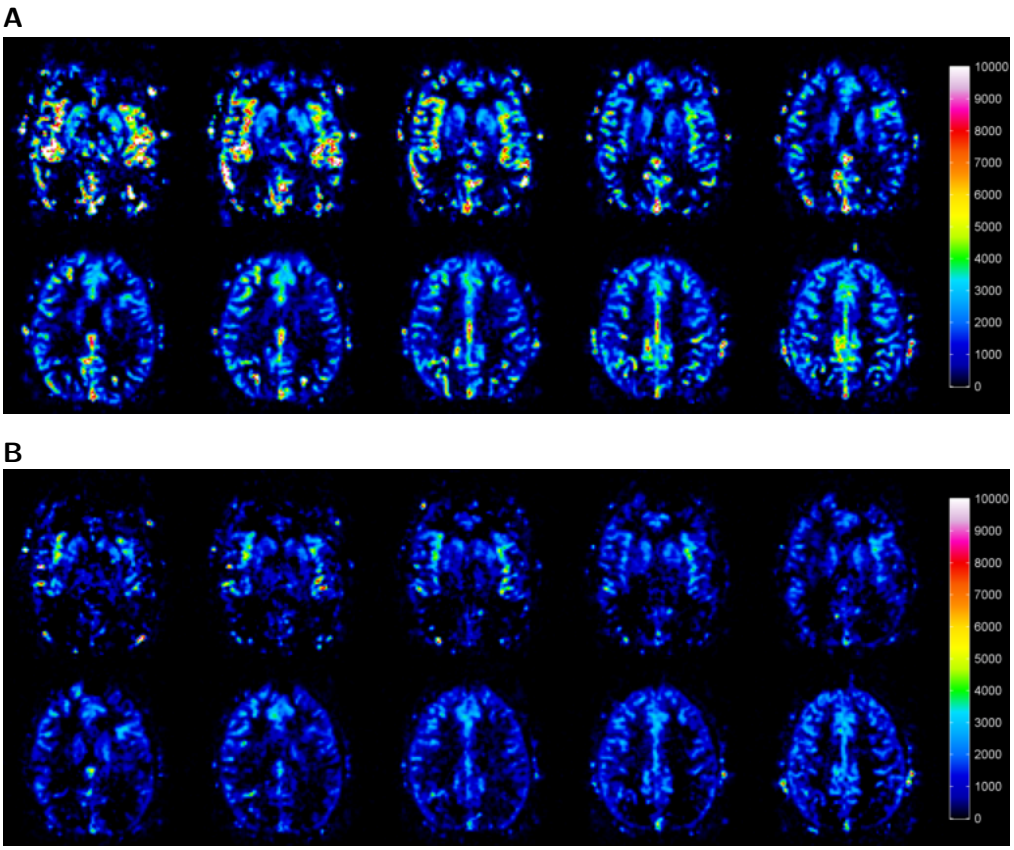


Figure 4.8: Perfusion weighted difference images acquired using a 2D-EPI readout, TE=22ms, PLD=0.9s, 10 contiguous slices, 2x2x3mm resolution with (A) no vascular crushing, (B) vascular crushing applied in x,y and z directions with velocity encoding of 5cm/s.

4.2.5 Quantification

In order to quantify perfusion, the evolving signal intensities from the perfusion weighted images with multiple PLDs must be modelled. The model must take into account such factors as labelling scheme, acquisition method and field strength. The models described here will be representative of the PASL FAIR labelling scheme as this is the scheme used at 7T within this thesis.

4.2.5.1 Calibration

The signal intensity observed from a perfusion weighted image cannot be quantified without additional information. To allow for quantification, the perfusion weighted image must first be normalised to the equilibrium

magnetisation of blood, $M_{0,B}$. Acquiring a map of blood magnetisation cannot be found by directly imaging the brain. However, a blood magnetisation map can be generated by acquiring a tissue magnetisation map and correcting for echo time, T_2^* and proton density ratios between blood and tissue [68]. The magnetisation of blood can be found using

$$M_B = R_i \; M_{0,i} \; \exp\left(\mathrm{TE}/T^*_{2,i} \; - \; \mathrm{TE}/T^*_{2,B}\right) \tag{4.2}$$

where R_i is the proton density ratio between tissue type i and blood, $M_{0,i}$ is the equilibrium magnetisation of tissue type i and $T^*_{2,i}$ is T_2^* of tissue type i, and $T^*_{2,B}$ is the T_2^* of blood.

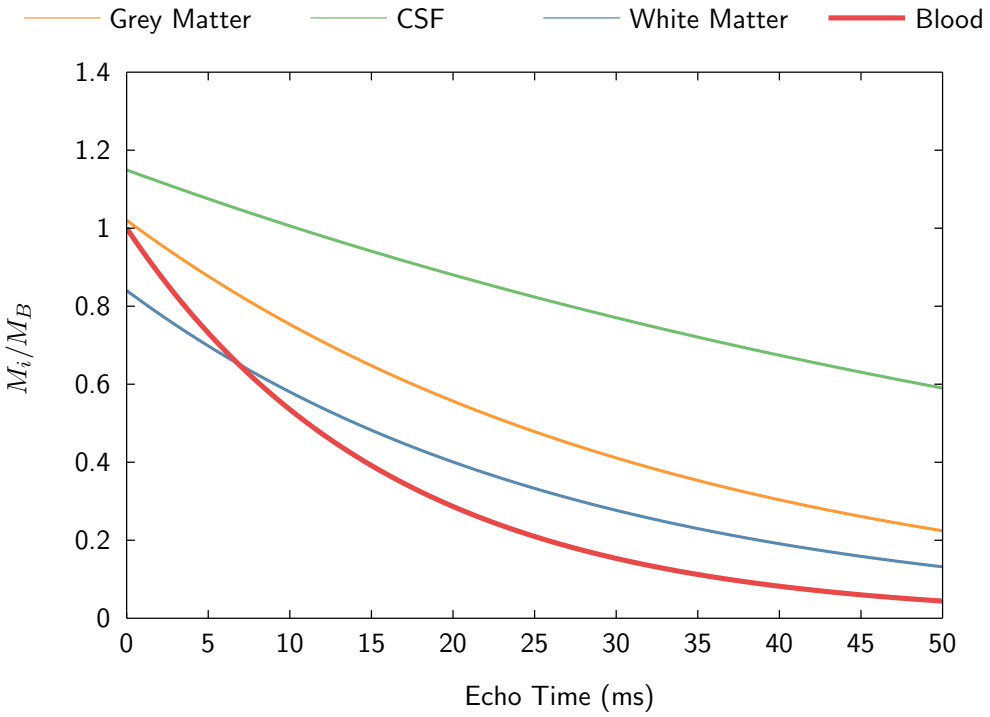


Figure 4.9: Magnetisation of grey matter, white matter, CSF and blood as a function of echo time. Simulation parameters T_2^* (GM, WM, CSF, blood) = 33, 27, 75, 16 ms, R (GM,WM,CSF) = 0.98, 1.19, 0.87.

Applying Equation 4.2 on a voxel wise basis to an M_0 map in conjunction with partial volume maps for each tissue type, a blood magnetisation map can be acquired. A map describing the blood magnetisation is preferable over a single value as B_1 inhomogeneities and coil sensitivities can spatially vary the blood magnetisation.

Division of the perfusion weighted image by the blood magnetisation will

normalise the signal, presenting the image in terms of percentage change from equilibrium. The percentage change can then be used in order to quantify perfusion.

4.2.5.2 Modelling the Single-PLD ASL data

In 1992, *Detre at al., 1992* [56] proposed to model the inflowing blood using the Bloch equations.

$$\frac{\mathrm{d}M_b}{\mathrm{d}t} = \frac{M_b^0 - M_b}{T_1} + fM_a - \frac{f}{\lambda}M_v \tag{4.3}$$

where M_b is the magnetisation of the blood, M_b^0 is the equilibrium magnetisation of blood, f is perfusion and λ is the blood-brain barrier coefficient. The first term in Equation 4.3 is recognisable as the relaxation of the longitudinal magnetisation of blood. The term $+fM_a$ is the arterial in-flow of blood into the imaging plane, whereas the term $-fM_v/\lambda$ is the venous out-flow of blood. The T_1 relaxation of the tissue was also expected to change during the label condition due to the in-flow blood with inverted spins. The apparent ($T_{1,\mathrm{app}}$) is a combination of the tissue T_1 and the in-flow of blood, given as

$$\frac{1}{T_{1,\mathrm{app}}} = \frac{1}{T_1} + \frac{f}{\lambda} \tag{4.4}$$

The longitudinal magnetisation of the label image will relax with the rate given by $T_{1,\mathrm{app}}$ whereas the longitudinal magnetisation of the control image will relax with the rate given by T_1. The difference between the two inversion recovery curves relaxing at different rates will model the magnetisation difference caused by perfusion. The inversion recovery equations for the label and control are given respectively as

$$M_{\mathrm{label}}(t) = M_0 \left(1 - 2\alpha e^{-t/T_{1,\mathrm{app}}}\right) \tag{4.5}$$

$$M_{\mathrm{control}}(t) = M_0 \left(1 - 2\alpha e^{-t/T_1}\right) \tag{4.6}$$

where α is the efficiency of the inversion. The difference between the label and

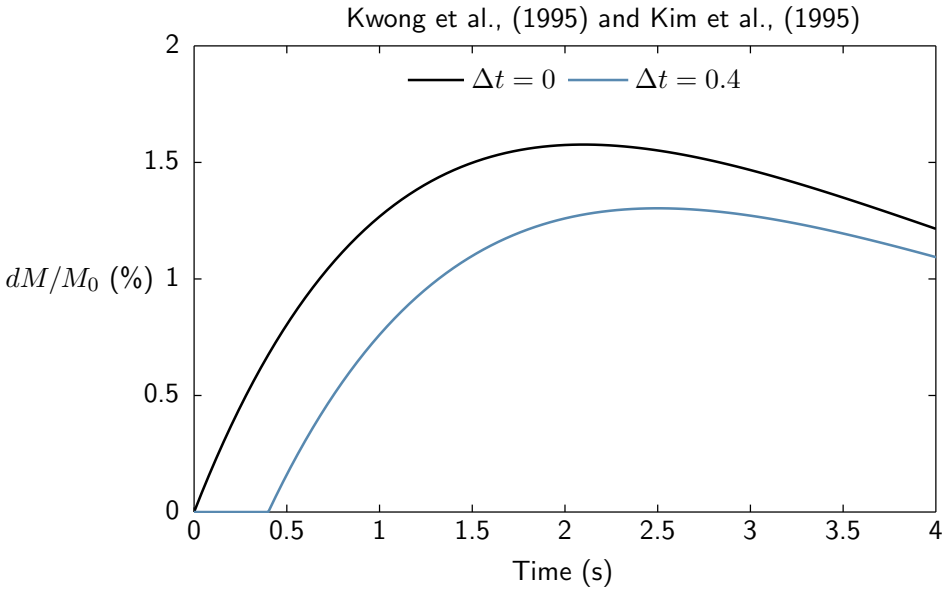


Figure 4.10: The change in magnetisation caused by inflowing blood modelled by *Detre et al., (1992)* as a function of post-label delay. Simulation parameters: f = 60ml/100g/min, λ = 0.98 ml/g, T_1 of tissue = 1.94.

control magnetisation is therefore

$$\begin{aligned}\Delta M(t) &= M_{\text{label}} - M_{\text{control}} \\ &= M_0 \left(1 - 2\alpha e^{-t/T_{1,\text{app}}}\right) - M_0 \left(1 - 2\alpha e^{-t/T_1}\right) \\ &= 2\, M_0\, \alpha \left(e^{-t/T_1} - e^{-t/T_{1,\text{app}}}\right) \\ &= 2\, M_0\, \alpha\, e^{-t/T_1} \left(1 - e^{-tf/\lambda}\right)\end{aligned} \tag{4.7}$$

Using the approximation $1 - e^{-a} \approx a$, Equation 4.7 can be approximated to

$$\Delta M(t) = 2\, M_0\, \alpha\, \frac{f}{\lambda}\, t\, e^{-t/T_1} \tag{4.8}$$

This model of the change in magnetisation due to the labelled blood was first proposed by *Kim et al., (1995)* [54] and *Kwong et al., (1995)* [69]. The time dependence of this magnetisation change is simulated in Figure 4.10.

This model assumes that blood immediately begins to flow into the imaging plane, whereas in practice the blood takes a finite time to reach the different parts of the imaging plane, known as the 'transit time' Δt. Equation 4.8 can be modified to accommodate the transit time

$$\Delta M(t) = 2\, M_0\, \alpha\, \frac{f}{\lambda}\, (t - \Delta t)\, e^{-t/T_1} \tag{4.9}$$

Secondly, this model assumes that the bolus is infinitely wide and labelled blood indefinitely flows into the imaging plane. Accounting for a finite bolus requires more intricate modelling, first described in *Buxton et al., (1998)* [70].

The delivery of labelled blood to a voxel in the imaging plane can be described using an arterial input function (AIF). The label bolus will take a time Δt in order to reach the voxel, where it will pass through for a duration of τ (Figure 4.11.A). The magnetisation caused by this label bolus will therefore only be present between Δt and $\Delta t + \tau$, which can be written as

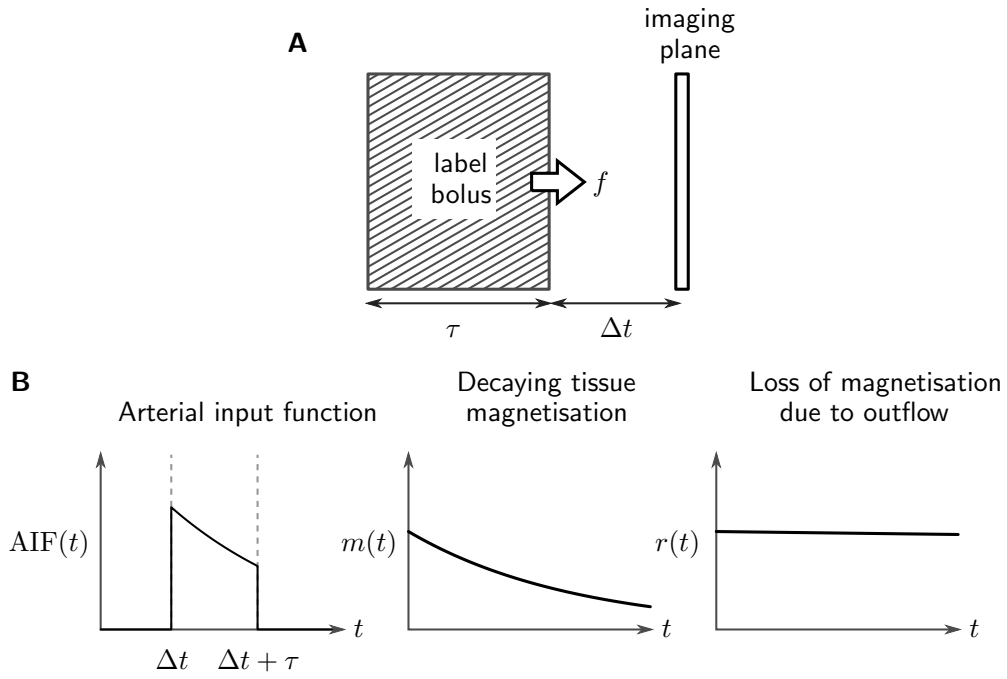


Figure 4.11: A. Schematic of the general kinetic model proposed by *Buxton et al., (1998)* [70]. B. The arterial input function, C. the decaying tissue magnetisation, D. loss of magnetisation due to outflow.

$$\mathrm{AIF}(t) = \begin{cases} 0 & t < \Delta t \\ 2\, M_a^0\, \alpha\, e^{-t/T_{1,b}} & \Delta t < t < \Delta t + \tau \\ 0 & t > \Delta t + \tau \end{cases} \tag{4.10}$$

where M_a^0 is the equilibrium magnetisation of arterial blood and $T_{1,b}$ is the longitudinal relaxation of the blood. The evolution of the AIF can be seen in Figure 4.11.B. The retention of the tracer in the voxel can be described by the

residue function. The residue function models the decay of tissue magnetisation $m(t)$ (Figure 4.11.C) and the loss of magnetisation due to venous outflow $r(t)$ (Figure 4.11.D). These are modelled as

$$m(t) = M_t^0 \, e^{-t/T_{1,t}} \tag{4.11}$$

$$r(t) = M_v^0 \, e^{-tf/\lambda} \tag{4.12}$$

where M_t^0 and M_v^0 is the equilibrium magnetisation of tissue and venous blood respectively and $T_{1,t}$ is the longitudinal relaxation of tissue. The residue function $R(t)$ is the product of $m(t)$ and $r(t)$. The model describing the difference in magnetisation can then be found from

$$\Delta M(t) = f(R(t) * \mathrm{AIF}(t)) \tag{4.13}$$

where the $*$ operator denotes a convolution. Solving this gives

$$\Delta M(t) = 2 \, M_a^0 \, \alpha \, \frac{f}{\lambda \left(\frac{1}{T_{1,\mathrm{app}}} - \frac{1}{T_{1,\mathrm{b}}} \right)} \, e^{-\frac{\Delta t}{T_{1,\mathrm{b}}}} \, \Gamma(t) \tag{4.14}$$

where

$$\Gamma(t) = \begin{cases} 0 & t < \Delta t \\ \left(e^{-\frac{(t-\Delta t)}{T_{1,\mathrm{b}}}} - e^{-\frac{(t-\Delta t)}{T_{1,\mathrm{app}}}} \right) & \Delta t < t < \Delta t + \tau \\ \left(e^{-\frac{\tau}{T_{1,\mathrm{b}}}} - e^{-\frac{\tau}{T_{1,\mathrm{app}}}} \right) e^{-\frac{(t-\Delta t-\tau)}{T_{1,\mathrm{app}}}} & t > \Delta t + \tau \end{cases} \tag{4.15}$$

This set of equations is known as the Buxton general kinetic model (Figure 4.12).

4.2.5.3 Modelling the Multi-PLD data

In the case where multiple readouts are used to acquire information about more than one post-label delay from a label, more intricate modelling can be performed.

The experiment described by *Günther et al., (2001)* [61] was the first to acquire and model a multi-PLD ASL experiment, which was named *inflow turbo-sampling EPI-FAIR* (ITS-FAIR). ITS-FAIR was shown to increase the SNR per unit time of the perfusion maps by a factor of 1.2 when compared to the single-PLD FAIR scheme. However, this model does not take into account the duration of the labelled blood arriving in the tissue, effect of the readout on

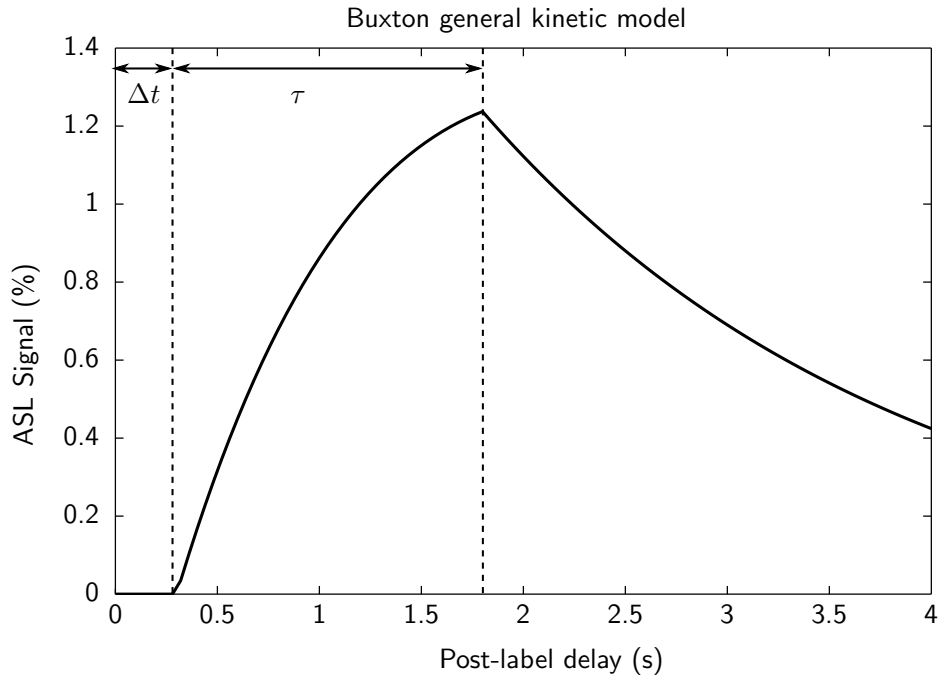


Figure 4.12: The Buxton general kinetic model (Equation 4.14). Simulation parameters: $f = 60$ ml/100g/min, $T_1 = 1.94$ s, $T_{1,b} = 2.1$ s, $\Delta t = 0.3$ s, $\tau = 1.5$ s

both arterial blood magnetisation and tissue magnetisation, and incomplete blood magnetisation recovery at short repetition times. These effects were accounted for in *Francis et al., (2008)* [63].

The model assumed by *Francis et al., (2008)* assumes three distinct compartments in which blood can reside. Compartment 1 (C_1) contains arterial blood located outside of the imaging volume, compartment 2 (C_2) contains arterial blood inside the imaging volume and compartment 3 (C_3) contains blood in the capillary bed in exchange with the tissue. In order to complete this model, four magnetisations caused by blood must be considered; that passing from C_1 to C_2 (M_{in}), that passing from C_2 to C_3 (M_{out}), that within C_2 (M_b) and that within C_3 (M_{tissue}) (Figure 4.13).

As a bolus of blood moves through the various compartments, the case will arise where some of the bolus will have entered the imaging volume and some will have not. In this case, only the bolus within the imaging volume will be subject to the effects of the RF pulses. This suggests the need to model the bolus in small time intervals so the bolus can be appropriately modelled. A suitable modelling

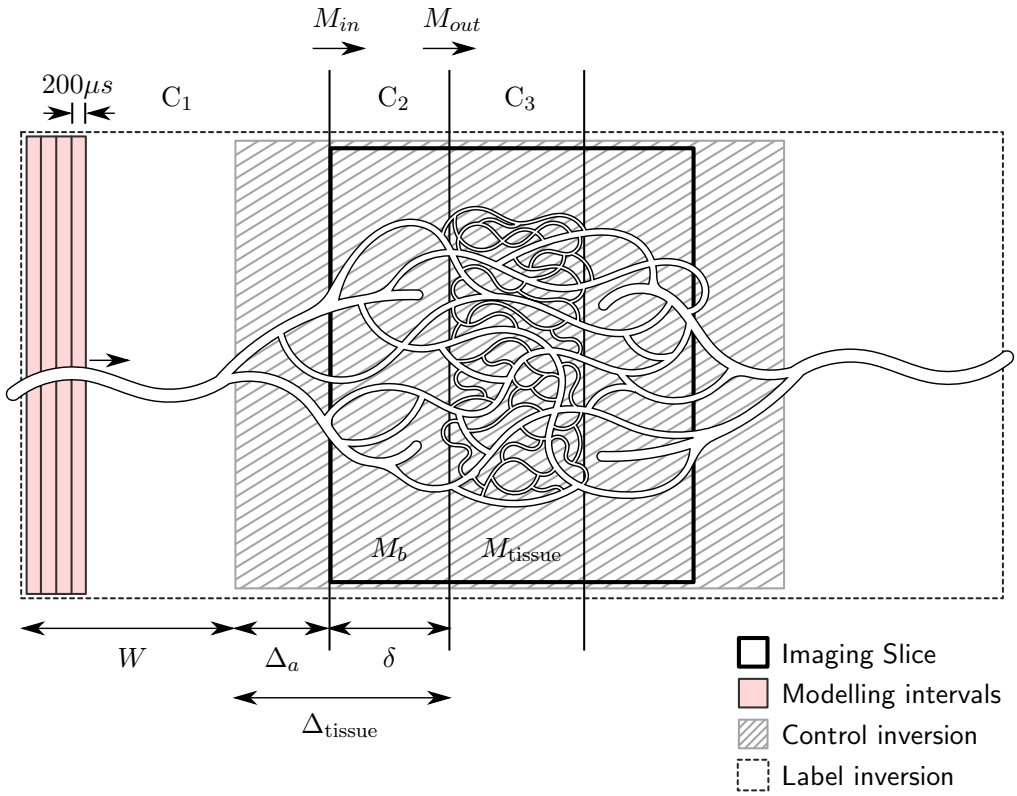


Figure 4.13: Illustration of the compartments considered when modelling the blood signal due to a Look-Locker readout.

interval time is considered to be 200 μs.

$\boldsymbol{M_{\text{in}}}$: The magnetisation of the arterial blood as it passes from C_1 to C_2 (M_{in}) is dependent on the time between the initial label inversion and the time the blood enters the second compartment (T). M_{in} is modelled for both label and control conditions ($M_{\text{in,L}}$ and $M_{\text{in,C}}$)

$$M_{\text{in,L}}(T) = M_{b,0}(1 - 2\mathrm{e}^{-T/T_{1,b}}) \qquad T < \Delta_a \tag{4.16}$$

$$M_{\text{in,C}}(T) = M_{b,0} \qquad T < W + \Delta_a \tag{4.17}$$

where $M_{0,b}$ is the equilibrium magnetisation of blood and $T_{1,b}$ is the longitudinal relaxation of blood. Δ_a is the time taken for the leading edge of the label to reach the imaging plane (arterial transit time) and W is additional time taken for the label to pass through C_1 compared to the control.

$\boldsymbol{M_{\text{out}}}$: The magnetisation of the arterial blood as it passes from C_2 to C_3 through impermeable arterioles can be written as

$$M_{\text{out}}(t) = Z(t)\mathrm{e}^{-t/T_{1,b}} + M_{0,b}(1 - \mathrm{e}^{-t/T_{1,b}}) \tag{4.18}$$

where $Z(t)$ is the magnetisation of blood exchanging out of C_2. This must be calculated for each modelling interval to take into account their different exposures to RF pulses from the Look-Locker readout. In order to model $Z(t)$, its initial state for both label and control conditions ($Z_{0,\mathrm{L}}$ and $Z_{0,\mathrm{C}}$ respectively) need to be determined for each interval.

$$Z_{0,\mathrm{L}}(t) = \begin{cases} -M_{b,0} & t \leq \delta + \Delta_a + W \\ +M_{b,0} & t > \delta + \Delta_a + W \end{cases} \tag{4.19}$$

$$Z_{0,\mathrm{C}}(t) = \begin{cases} -M_{b,0} & t \leq \delta + \Delta_a \\ +M_{b,0} & t > \delta + \Delta_a \end{cases} \tag{4.20}$$

where δ is the time taken for blood to traverse the arterioles and enter the capillary bed. These equations describe when the edge of inversions reach the imaging plane. With the initial conditions established, the relative timings of the RF pulses for each interval are found and applied within the time window δ.

$\boldsymbol{M_b}$: The magnetisation within C_2 can be found by modifying Equation 4.3 to

$$\frac{\mathrm{d}}{\mathrm{d}t}M_b(t) = \frac{M_{b,0} - M_b(t)}{T_{1,b}} + FM_{\mathrm{in}}(t) - FM_{\mathrm{out}}(t) \tag{4.21}$$

where F describes the arterial blood flow, and is assumed to be 180 ml/100g/min. Solving Equation 4.21 gives the general solution

$$M_b(t) = F\delta M_{b,0} + F\left(tM_{\mathrm{in}}(t) - tM_{\mathrm{out}}(t) + \delta m_b - \delta M_{b,0}\right)\mathrm{e}^{-t/T_{1,b}} \tag{4.22}$$

where m_b is the magnetisation of M_b from the previous interval.

$\boldsymbol{M_{\mathrm{tissue}}}$: the magnetisation within C_3 describing perfusing blood in the capillary bed, can be written as

$$\frac{\mathrm{d}}{\mathrm{d}t}M_{\mathrm{tissue}}(t) = \frac{M_{\mathrm{tissue},0} - M_{\mathrm{tissue}}(t)}{T_{1,\mathrm{tissue}}} + \frac{fM_{\mathrm{out}}(t)}{\lambda} - fM_{\mathrm{tissue}}(t) \tag{4.23}$$

where f is the perfusion in ml/100g/min, λ is the blood-brain barrier co-efficient (0.98 ml/100g for grey matter). Equation 4.23 can be solved (accounting for readout and labelling RF pulses) to give...

$$\begin{aligned} M_{\mathrm{tissue}}(t) =& M_{\mathrm{tissue},0}\left(1 - \mathrm{e}^{-t/T_{1,app}} + \beta\mathrm{e}^{-t/T_{1,b}} + \beta\mathrm{e}^{-t/T_{1,app}}\right) + \\ & M_{\mathrm{out}}(t)\left(\beta\mathrm{e}^{-t/T_{1,b}} + \beta\mathrm{e}^{-t/T_{1,app}}\right) + M_{\mathrm{tissue}}(0)\mathrm{e}^{-t/T_{1,app}} \end{aligned} \tag{4.24}$$

where

$$\beta = f\left(\frac{\lambda}{T_{1,b}} - \frac{\lambda}{T_{1,app}}\right)^{-1} \tag{4.25}$$

and

$$T_{1,app} = \left(\frac{1}{T_{1,\text{tissue}}} + \frac{f}{\lambda} \right)^{-1} \tag{4.26}$$

Having modelled M_b and M_{tissue} for both the label and control conditions, the ASL signal can be modelled by finding the difference between them and normalising to $M_{b,0}$ (Figure 4.14).

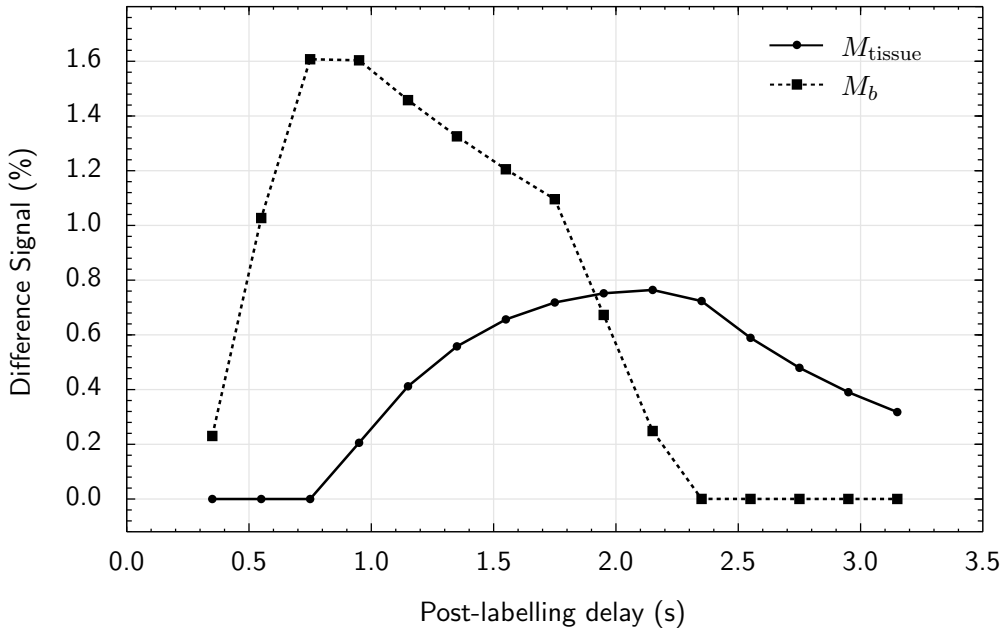


Figure 4.14: Simulated ASL signals from *Francis et al., (2008)* [63]. Simulation parameters: $\delta = 0.5$ s, $\Delta_a = 0.3$ s, $F = 180$ ml/100gm/min, $f = 60$ ml/100g/min, $W = 1.5$ s, $T_{1,b} = 2.1$ s, $T_{1,\text{tissue}} = 1.94$ s, 23 readouts, initial readout delay $= 0.35$ s, readout spacing $= 0.2$ s.

4.2.6 Pre-processing

Once ASL data has been acquired, a simplistic analysis would to compute the difference between the label and control to illustrate perfusion. However, it is common practice to "clean" the data before quantification is performed. This may include alternate subtraction methods, motion correction, rejection of poor quality control-label repeats, and partial volume correction as described below.

4.2.6.1 Subtraction methods

The difference between the label and control acquisitions ideally gives the magnetisation purely due to the perfusion signal. A typical ASL sequence collects the label and control images in an interleaved manner

$$[L_1, C_1, L_2, C_2, L_3, C_3, ..., L_n, C_n]$$

where L_i and C_i are the label and control acquisitions and the subscript i identifies the number of the repeat. A set of perfusion weighted images acquired from pairwise subtraction is then given by

$$[P_1, P_2, P_3, ..., P_n] = [C_1 - L_1, C_2 - L_2, C_3 - L_3, ..., C_n - L_n]$$

or alternatively

$$[P_1, P_2, P_3, ..., P_{n-1}] = [C_2 - L_1, C_3 - L_2, C_4 - L_3, ..., C_n - L_{n-1}]$$

where P_i is a perfusion weighted image. This method is the least computationally demanding out of the proposed methods, but any of the temporal variations between the time acquisition of the label and control are included in the perfusion weighted image.

A running subtraction is a method which includes all perfusion weighted images from a simple pairwise subtraction, but also includes the subtraction between other neighbouring pairs. This is based on the assumption that labels acquired either side of a control image are roughly equivalent as they are both acquired at similar time offsets to the control. The series of perfusion weighted images is therefore given by

$$[P_1, P_2, P_3, ..., P_{2n-1}] = [C_1 - L_1, C_2 - L_1, C_2 - L_2, ..., C_n - L_{n-1}, C_n - L_n]$$

This subtraction method doubles the temporal resolution of the pairwise subtraction method, however it has been shown to be susceptible to BOLD artefacts causing high frequency fluctuations across a time series.

Another subtraction method attempts to suppress noise variations by averaging the two labels surrounding the control image. The averaged label image is then subtracted from the control such that the series of perfusion weighted images is given as

$$[P_1, P_2, P_3, ..., P_{n-1}] = \left[C_1 - \frac{L_1 + L_2}{2}, C_2 - \frac{L_2 + L_3}{2}, ..., C_{n-1} - \frac{L_{n-1} + L_n}{2}\right]$$

This method is preferred when the acquisition contains some degree of BOLD weighting and a stimulus is applied as there will be a signal drift unrelated to perfusion. An ASL sequence typically has a TR of 8 seconds in order to acquire both label and control and allow for T_1 recovery, whereas BOLD acquisitions have much shorter TRs, typically 2 seconds.

4.2.6.2 Motion correction

As ASL is a subtraction technique, it requires minimal movement from the volunteer in order to acquire good quality data. If there is head motion between the label and control acquisitions, the same regions no longer subtract from each other. Typically head motion manifests as bright and dark edges where

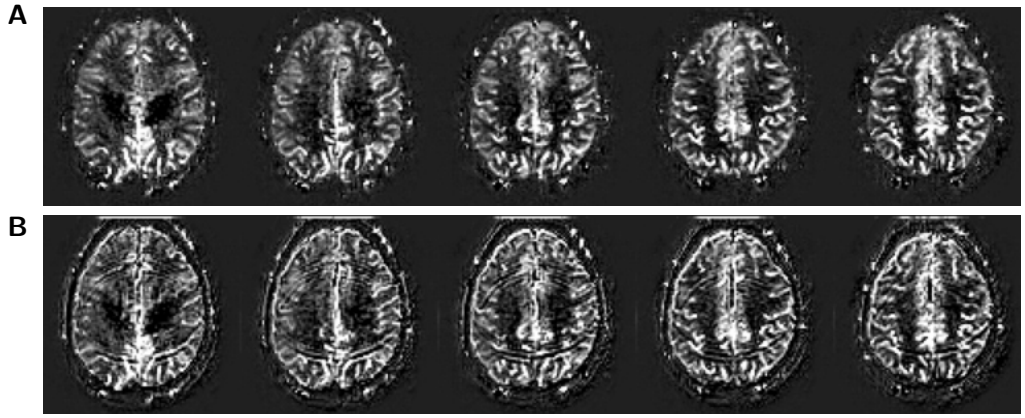


Figure 4.15: ASL perfusion weighted images with (A) little to no head movement, (B) severe head motion between label and control. Imperfect subtractions cause bright or dark edges and enhanced artefacts such as fat rings.

imperfect subtractions occur (Figure 4.15.B). In order to account for this motion, motion correction can be performed which attempts to realign all label-control repeats to a common image. A fast implementation of this was developed by *Jenkinson et al., (2002)* [71] and is used extensively throughout this thesis. Motion correction is especially useful when assessing patient groups whose condition causes involuntary muscle stimulation, such as Parkinson's or Huntington's disease.

4.2.6.3 Outlier detection

Since the ASL signal is low, a single outlying label-control pair can significantly affect sample mean and produce inaccurate perfusion signals. Outliers are commonly artefacts such as stimulated echoes in bSSFP readouts and subtraction errors due to movement. There are two approaches to dealing with these effects; discard entire label-control repeats from the dataset [72], or suppress outliers using a robust mean [73].

Outlying label-control repeats can be identified by firstly calculating the mean and standard deviations of the perfusion weighted images, denoted M_i and S_i respectively, where i represents the label-control repeat index between 1 and n. Secondly, the mean and standard deviation of M and S are found; M_μ and M_σ being the mean and standard deviation of M and S_μ and S_σ being the mean and standard deviation of S. The perfusion weighted image of label-controll repeat i is considered an outlier if

$$|M_i| = M_\mu > \gamma M_\sigma$$
$$S_i = S_\mu + \gamma S_\sigma$$

where γ is a tuning parameter, recommended to be set to 2.5 in the literature. This algorithm was able to significantly reduce the number of artefacts in perfusion weighted images. However, removing entire label-control repeats reduces the SNR of the experiment, and also may be removing information from regions which do not contain corruption.

An alternative way to remove outliers from the ASL dataset, suggested by *Maumet et al., (2014)* [73], is to find the robust mean for each voxel across all label-control repeats. This paper uses the Huber M-estimator in order suppress the effects of statistically abnormal values. M-estimators are functions which provide information on the similarity between two values, usually defined as $\rho(x_i - \theta)$ where x_i is a sample from a dataset and θ is a value to compare x_i to. For example, the square difference (used in many fitting algorithms to provide information on the quality of fit) is a simple M-estimator where $\rho(x_i - \theta) = (x_i - \theta)^2$. To determine the best fit, it is necessary to minimise the

sum of M-estimators with all sample values (x_i) and estimate a value of θ

$$\hat{\theta} = \underset{\theta}{\operatorname{argmin}} \left(\sum_{i=1}^{n} \rho(x_i - \theta) \right) \tag{4.27}$$

where $\hat{\theta}$ is the value of θ which minimises the function. However, when ρ is differentiable and ψ is its derivative, $\hat{\theta}$ can be found from

$$\sum_{i=1}^{n} \psi \left(x_i - \hat{\theta} \right) = 0 \tag{4.28}$$

The function used for the M-estimators determines the value of $\hat{\theta}$. For example, when using the sum of square differences where the M-estimator is defined as $\rho(x_i - \theta) = (x_i - \theta)^2$ and $\psi(x_i - \theta) = 2(x_i - \theta)$, the value of θ which minimises the sum is found to be the mean. As we know a standard mean operation is sensitive to outliers, a different M-estimator should be used to suppress their effects.

The Huber M-estimator is one of the most popular for dealing with datasets with outliers. This M-estimator can be 'tuned' to determine the influence of values lying outside a defined threshold. The derivative of the Huber M-estimator is given as...

$$\psi(x_i - \theta) = \gamma \left(\frac{x_i - \theta}{\hat{\sigma}} \right) \quad \text{where} \quad \gamma(x) = \begin{cases} -k, & x < -k \\ x, & -k < x < k \\ k, & x > k \end{cases} \tag{4.29}$$

where $\hat{\sigma}$ is the robust median absolute deviation (the median absolute deviation divided by 0.6745) and k is the tuning parameter where a value of 1.345 corresponds to a 95% confidence interval assuming the data is normally distributed. It is reported that this method produces more robust perfusion maps than that of the sample mean.

4.2.6.4 Partial Volume Effects

A perfusion map will often contain information arising from various tissue types. In the brain, for example, both grey matter and white matter may contribute to the perfusion detected within a single voxel. This effect becomes more severe in experiments with large voxels, particularly around grey matter and white matter boundaries. Commonly, only the mean perfusion from one tissue type is required, in which case the perfusion signal must be separated for each tissue type.

Various methods have been proposed in order separate the perfusion signal, but notable is the linear regression method described by *Asllani et al., (2008)* [74]. The algorithm supposes that the total perfusion signal is a weighted sum of fractional tissue volumes and and perfusion from each tissue type. Assuming no perfusion arises from CSF, the total perfusion f within voxel i can be written as

$$f_i = P_{\mathrm{GM},i} \cdot f_{\mathrm{GM},i} \; + \; P_{\mathrm{WM},i} \cdot f_{\mathrm{WM},i} \tag{4.30}$$

where $P_{\mathrm{GM},i}$ and $P_{\mathrm{WM},i}$ describes the fractional tissue volume of grey matter and white matter in voxel i, respectively and $P_{\mathrm{GM},i} + P_{\mathrm{WM},i} = 1$. A set of these equations can be formed by assessing a neighbourhood of n voxels around voxel i, which can be written in matrix form as

$$f_{\mathrm{total}} = P f_{\mathrm{tissue}} \tag{4.31}$$

$$\begin{bmatrix} f_1 \\ \dots \\ f_i \\ \dots \\ f_n \end{bmatrix} = \begin{bmatrix} P_{\mathrm{GM},1} & P_{\mathrm{WM},1} \\ \dots & \dots \\ P_{\mathrm{GM},i} & P_{\mathrm{WM},i} \\ \dots & \dots \\ P_{\mathrm{GM},n} & P_{\mathrm{WM},n} \end{bmatrix} \cdot \begin{bmatrix} f_{\mathrm{GM}} \\ f_{\mathrm{WM}} \end{bmatrix}$$

where P is $2 \times n$ matrix containing partial volumes of grey matter and white matter, and f_{tissue} is a 1×2 matrix which contains perfusion values for individual tissue types. The standard least-squares solution to Equation 4.31 can be found using the pseudo-inverse P, such that f_{tissue} is given by

$$f_{\mathrm{tissue}} = (P^T \cdot P)^{-1} \cdot P^T \cdot f_{\mathrm{total}} \tag{4.32}$$

4.2.7 Applications

Since its initial invention in early 1990s, ASL has continuously been developed to provide more accurate and robust perfusion information. Continued improvement has led to ASL being used to assess perfusion alterations with many different neurological conditions, such as stroke [75], dementia [76], epilepsy [77] and post traumatic stress disorder [78] at 1.5 and 3T. Its benefits over perfusion measurement methods such as PET (positron emission tomography) have led to ASL being introduced to clinical settings. ASL is now being used as a research tool to assess the treatment of cancerous tumours or

determine the region of the brain affected by a stroke. Increasing the magnetic field strength provides greater intrinsic SNR and prolonged T_1 of the blood label. But also introduces new challenges due to B_0 and B_1 inhomogeneities. Fewer research and clinical studies have been performed at this field strength due to these challenges.

Although ASL was initially developed for brain imaging, it has also been adapted for use in body imaging. ASL has been shown to be effective in assessing perfusion in both the liver and kidneys, for example providing insight into chronic kidney disease (CKD).

Despite the growing presence in the clinical settings, ASL currently only provides complimentary information to structural acquisitions and is not yet used as a sole tool for diagnosis. Due to the large number of variations in ASL techniques, a white-paper has been published regarding the recommended implementation of ASL at a clinical level [60].

4.3 Dynamic Susceptibility Contrast

4.3.1 Introduction

Prior to the development of arterial spin labelling, measurements of perfusion required the intravenous administration of tracers, known as *contrast enhanced techniques*. The basic concept is to introduce a tracer into the blood and track its movement. The dynamics of this tracer are assumed to reflect that of the blood, such that modelling the kinetics of the tracer provides information on blood flow.

This concept was first described by *Villringer et al., (1988)* [79], where their choice of tracer was a gadolinium based compound known as $\mathrm{Gd(DTPA)}^{2-}$. This tracer was used as it is paramagnetic with a high magnetic moment, which significantly decreases the detected MR signal on T_2^* weighted images in voxels where it is present. This is due to paramagnetic nature of the tracer which increases the local magnetic field, causing a local shortening of T_2^*. The amount of signal loss is dependent on the concentration of the contrast agent, such that a higher concentration of the contrast decreases the signal by a larger amount.

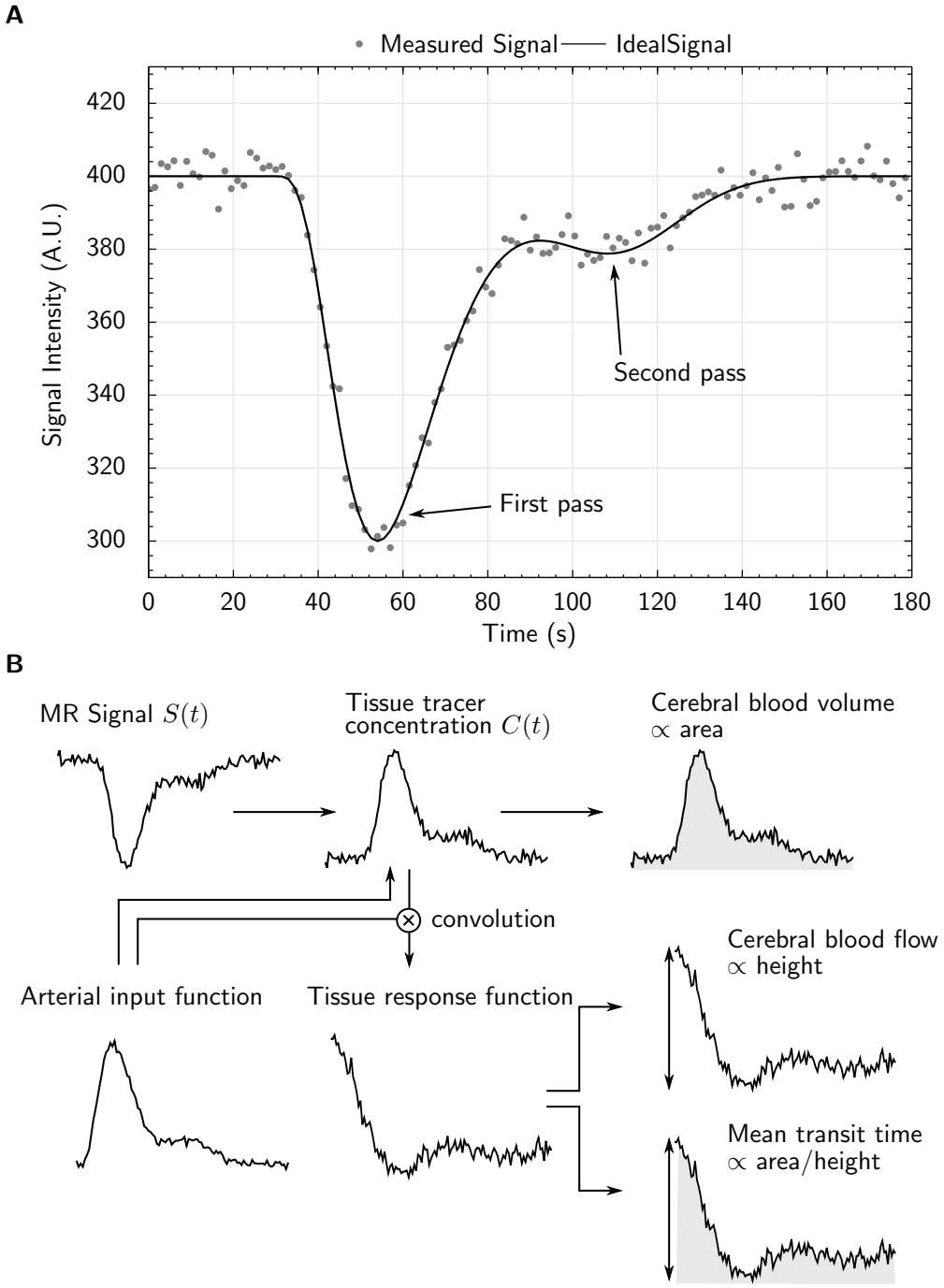


Figure 4.16: (A) Typical dynamic susceptibility contrast time-series consisting of an initial baseline and signal drops due to the first and second pass of the tracer bolus. The second pass is the recirculation of the tracer, however the first pass provides the crucial information. (B) The CBF, CBV and MTT can be estimated from the MR signal intensity and an arterial input function describing the delivery of tracer to the voxel.

4.3.2 Theory

Rapid measurement of the tracer's first pass through the circulatory system after administration is required in order to obtain haemodynamic measures such as cerebral blood flow, cerebral blood volume and mean transit time (Figure 4.16). Using a kinetic model derived from indicator dilution theory [80], these parameters can be estimated.

In order to estimate any haemodynamic parameters, the MR signal must first be converted to a tracer concentration map on a voxel-wise basis in a T_2^* weighted image. The concentration as a function of time, $C(t)$, is estimated as

$$C(t) \propto -\frac{k}{\mathrm{TE}} \ln\left(\frac{S(t)}{S_0}\right) \tag{4.33}$$

where $S(t)$ is the signal intensity as a function of time, S_0 is the baseline signal intensity, TE is the echo time of the sequence and k is a proportionality constant which accounts for tissue type, pulse sequence, field strength and tracer type.

In order to use the tissue concentration to estimate haemodynamic parameters, an *arterial input function* (AIF) which describes the delivery of blood (and hence) gadolinium to the ROI must be estimated. This can be identified by assessing the tracer concentration within a large vessel, such as the internal carotid or basilar artery when assessing cerebral haemodynamics.

The cerebral blood volume is proportional to the area under the tissue concentration curve and the AIF curve, such that

$$CBV = \frac{1 - H_{\mathrm{large}}}{\rho(1 - H_{\mathrm{small}})} \frac{\int_0^t C(t)\mathrm{d}t}{\int_0^t \mathrm{AIF}(t)\mathrm{d}t} \tag{4.34}$$

where H_{large} is the hematocrit in large vessels, H_{small} is the hematocrit in small vessels and ρ is the tissue density in g/cm^3. Estimating the cerebral blood flow requires the tissue response function, $R(t)$, which describes the fraction of tracer remaining in the tissue following the arrival of the bolus. The tissue response function is found from the deconvolution of the tissue tracer concentration and the arterial input function

$$R(t) = C(t) \otimes^{-1} \mathrm{AIF}(t) \tag{4.35}$$

With this, CBF can be determined using

$$CBF = \frac{1 - H_{\text{large}}}{\rho(1 - H_{\text{small}})} \frac{R_{\max}}{\int_0^t R(t)\mathrm{d}t} \frac{\int_0^t C(t)\mathrm{d}t}{\int_0^t \text{AIF}(t)\mathrm{d}t} \tag{4.36}$$

where $R_{\max}$ is the maximum value of the tissue residue function. The central volume theorem allows for the mean transit time to be found using both CBV and CBF, such that

$$MTT = \frac{CBV}{CBF} \tag{4.37}$$

Despite tracer theory being well established and understood, there are still many difficulties in absolutely quantifying these haemodynamic parameters. These difficulties mainly stem from the selection of the arterial input function. The arterial input function is determined from a single large vessel towards the base of the brain. However, it is then assumed that this AIF is consistent across the whole brain. This is not believed to be the case, so often CBF and CBV are reported in terms of $rCBF$ and $rCBV$, where the r means relative. The relative values do not included the AIF term, so are seen as semi-quantitative.

4.3.3 Applications

Contrast enhanced techniques are widely used in clinical settings due to their highly refined procedure, high sensitivity, robust measures and relatively inexpensive costs. The technique is also faster than arterial spin labelling.

DSC-MRI is used to assess a range of neurological conditions, such as stroke, multiple sclerosis and gliomas. It has been demonstrated that brain tissue at risk of stroke can be identified before the stroke has occurred, allowing treatment to be given. Gliomas can be identified with typical structural scans, but in order to assess the potential risk they pose, they must be graded. Grading cannot be determined from structural scans, but determining the cerebral blood flow of the glioma allows for this assessment to be made. In multiple sclerosis, scarring forms within the brain which initially begins with a period of inflammation, which is described as the lesion being active. Scarring can form due to numerous and unlinked conditions, however the presence of active lesions is useful to determine whether MS is the cause and aid with earlier diagnosis of MS.

However, recent publications have reported that gadolinium based tracers are not cleared, and gadolinium depositions have been found in neuronal tissue years after its administration [81, 82].

4.4 Magnetic Resonance Angiography

Magnetic Resonance Angiography (MRA) can be performed using magnetic resonance imaging. MRA can be performed either with or without exogenous contrast agents. In contrast-enhanced MRA, gadolinium is injected into the blood shortening its T_1 rendering the blood vessels bright. In non contrast-enhanced MRA, the contrast is obtained from the velocity of the blood and can be performed using two main techniques; time of flight MRA (TOF-MRA) or phase contrast angiography (PCA).

4.4.1 Time of Flight (TOF)

Time of flight angiography is based upon partially suppressing the static tissue signal and allowing the blood signal to retain its magnetisation. Tissue in an imaging volume is partially suppressed with a series of RF pulses such that the signal is forced into a steady-state. Fresh blood flowing into the imaging slab will not have been exposed to these RF pulses and as such the blood signal will not have been severely attenuated. The blood signal at the time of acquisition will ultimately depend on how many RF pulses the blood has been exposed to, which is affected by the velocity of the blood, the time in which the blood enters the imaging volume, and the location of blood within the volume.

Fast flowing blood will take a shorter amount of time to traverse the imaging volume and will therefore be exposed to fewer RF pulses, resulting in a high blood signal. Whereas slower blood will take a longer amount of time to traverse the imaging plane which means it will be exposed to more RF pulses causing a lower signal. The velocity of the blood is generally dependent on the size of the vessel, where larger vessels contain blood moving at higher velocities (Figure 4.17.A).

A smaller imaging slab will mean the window for blood to be exposed to RF pulses is reduced, meaning that the blood signal will be attenuated less than

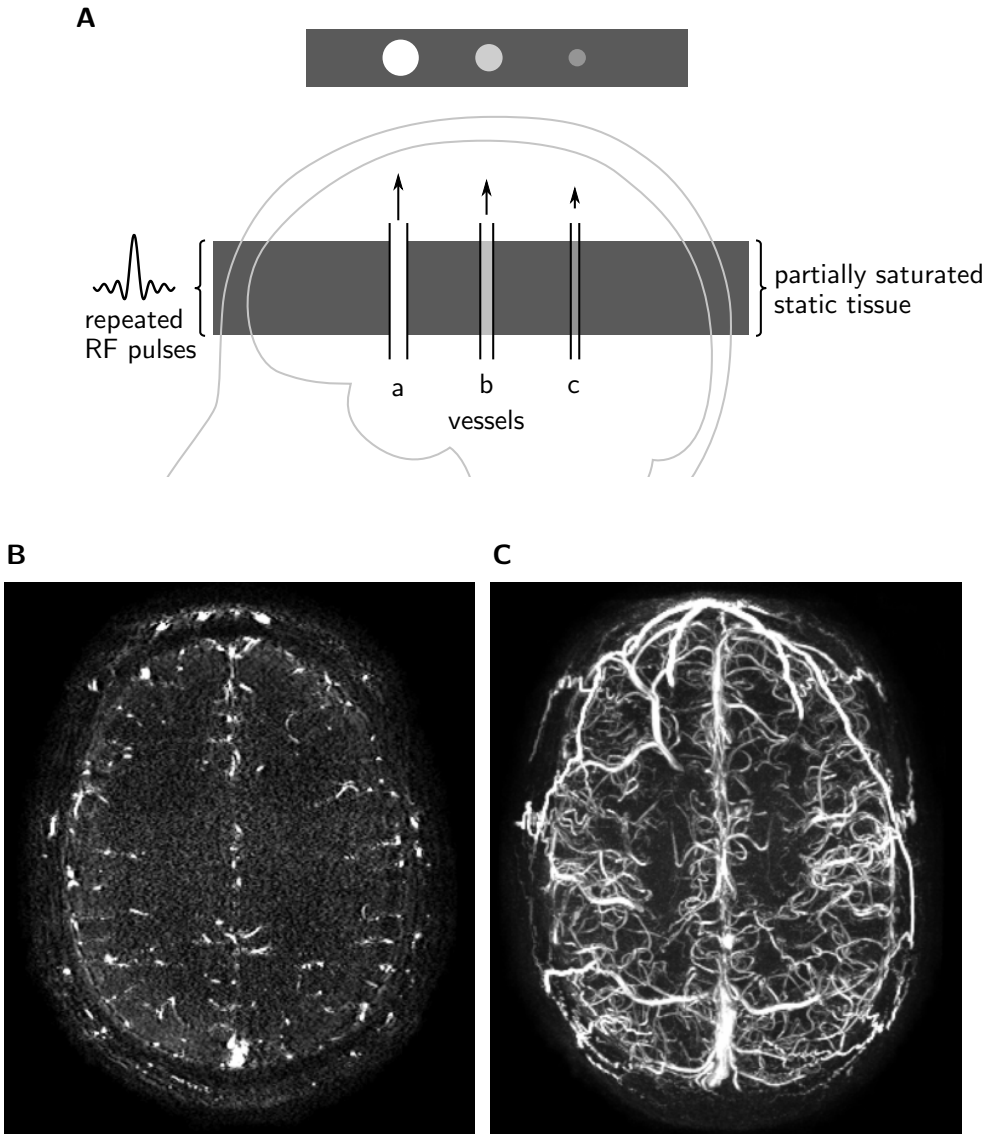


Figure 4.17: Time of flight angiography angiography - (A) The signal dependency of blood with velocity; faster moving blood results in a larger signal as it is exposed to less RF pulses. (B) Mid-slice from TOF acquisition demonstrating different contrasts between tissue and blood. (C) Maximum intensity projection through all slices in the foot-head direction.

if a larger volume was used. Therefore smaller imaging volumes provide better contrast between tissue and blood, limiting the maximum volume size. Small vessels residing in the middle of the imaging volume typically have poor contrast to the tissue as they have been exposed to most of the RF pulses used to partially saturate the tissue.

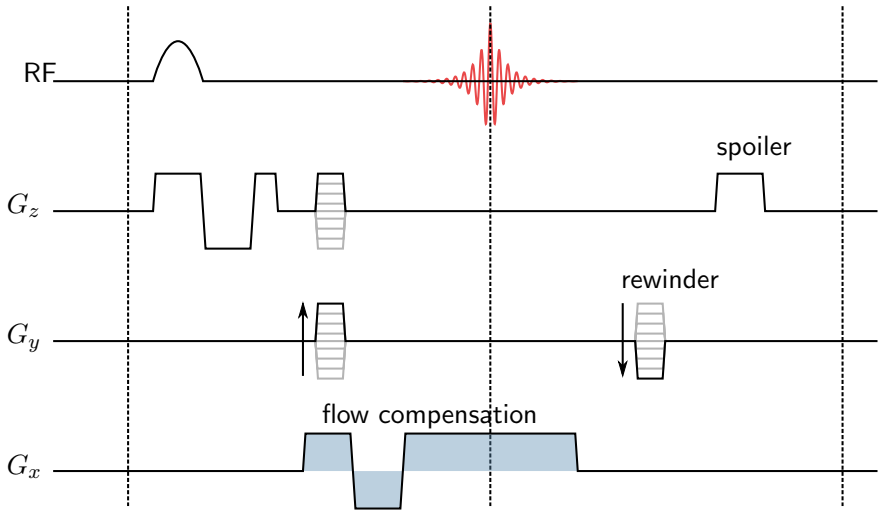


Figure 4.18: 3D time of flight pulse sequence diagram

4.4.2 Phase contrast angiography

Phase contrast angiography (PCA) is another MR technique used to observe flow effects from vessels. This technique is based upon manipulating the phase of tissue and blood differently in order to create a signal contrast. Bipolar gradients are used to achieve this; these are applied prior to the readout such that static spins experience the equal but opposite lobes equally and therefore acquire no phase difference. In contrast moving spins feel different gradient strengths as they change position, this results in imperfect rephasing and therefore a phase shift. This principle was introduced earlier in section 4.2.4.3 regarding vascular crushing. To simplify the phase shift into a quantifiable measure, the phase shift is found relative to a flow-compensated acquisition where phase shifts due to flow are suppressed.

The velocity of the moving spins can be calculated from the phase shift and the bipolar gradient properties. The total acquired phase shift is found by integrating the modelled precessional frequency of the spins

$$\phi = \int \omega \, \mathrm{d}t \tag{4.38}$$

With the application of a gradient (G_z) and accounting for blood moving at position x with velocity v, the phase of blood spins can be written as

$$\phi = \int \gamma \left(B_0 + G_z \left(x + vt \right) \right) \mathrm{d}t \tag{4.39}$$

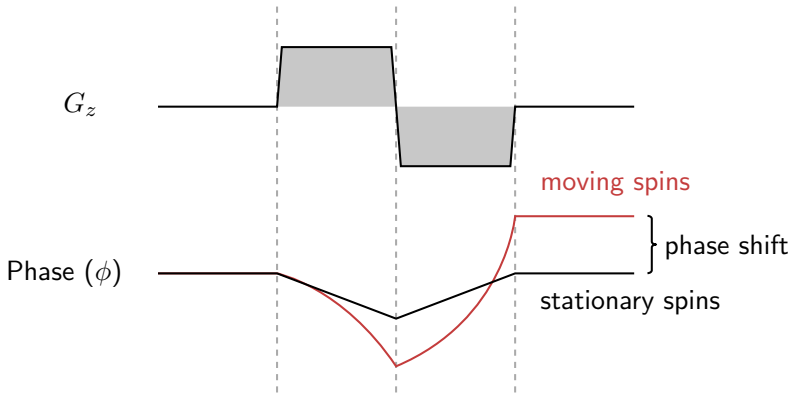


Figure 4.19: PCA phase shift.

When determining the phase shift $\delta\phi$ between static spins and moving spins, any time independent contributions can be ignored as the second gradient lobe will rephase these effects. Integrating between time 0 and the duration of the positive gradient lobe (T), the phase shift after the first gradient lobe can be determined to be

$$\begin{aligned}\delta\phi &= \gamma \int_0^T G_z v t \, \mathrm{d}t \\ &= \gamma \left[\frac{1}{2} G_z v t^2\right]_0^T = \frac{1}{2}\gamma G_z v T^2 \end{aligned} \tag{4.40}$$

If this is repeated with opposite polarity on the gradient, this will cause a phase shift of $-\frac{1}{2}\gamma G_z v T^2$. The total phase shift due to both lobes of bipolar gradients ($\Delta\phi$) is the difference between the phase shift caused by each lobe

$$\Delta\phi = \gamma G_z v T^2 \tag{4.41}$$

The phase-shift will be in units of radians, where data will wrap every 2π. In order to ensure there is no phase wrapping causing loss of data, a velocity encoding parameter must be specified. Velocity encoding (V_{enc}) is the velocity of blood which will cause a phase difference of π such that

$$\pi = \gamma \, G_z \, V_{enc} \, T^2 \tag{4.42}$$

which can be rearranged to give

$$V_{enc} = \frac{\pi}{\gamma G_z T^2} \tag{4.43}$$

It is important that this parameter be set to a higher velocity than the expected velocity within the vessel of interest, or phase wrapping will occur and

quantification will be incorrect. This modelling of the phase shift is correct if the bipolar gradients are applied in the same direction as the blood flow. This can be achieved by using a single slice acquisition, planned to intersect a vessel of interest, as seen in Figure 4.20. The phase shift is often measured at many

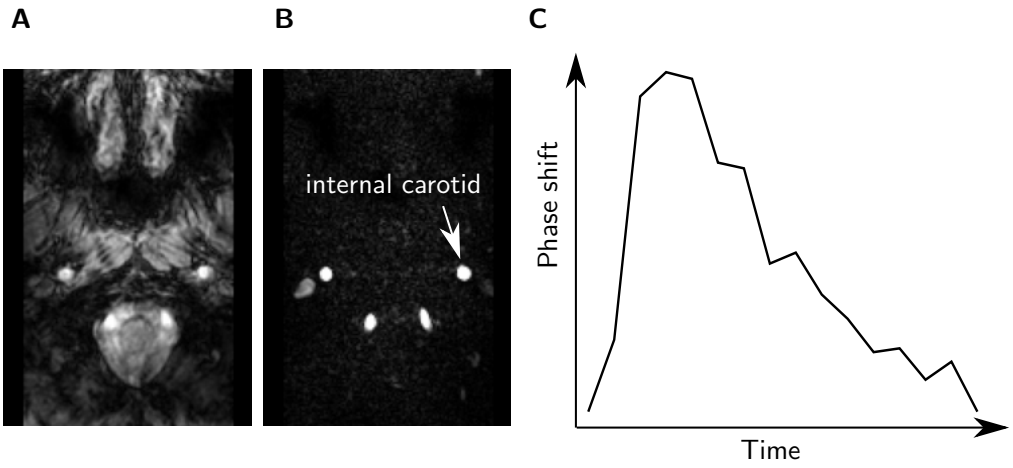


Figure 4.20: PCA data acquired from a single slice intersecting the internal carotid arteries. (A) The modulus image from a flow compensated acquisition. (B) The modulus image of difference between flow sensitive and flow compensated acquisitions. (C) The phase shift from within the internal carotid at 15 time points following a heart beat.

points through the cardiac cycle (Figure 4.20.C). This allows for the blood flow velocity to be found as a function of time, meaning that total volume of blood delivered per heartbeat can be found.

As well as being used to intersect particular vessels to quantify flow, it can also be used to map the network of vessels throughout the head. This can be achieved by using a 3D readout with flow compensation applied in all three dimensions.

4.4.3 Applications

The use of magnetic resonance angiography in clinical practice has been applied to identify abnormalities and help with diagnoses with many conditions. MRA can be applied to many parts of the body containing important vasculature, such as the brain, neck, heart and abdomen.

MRA has been used extensively to identify swelling of arterial walls (aneurysms)

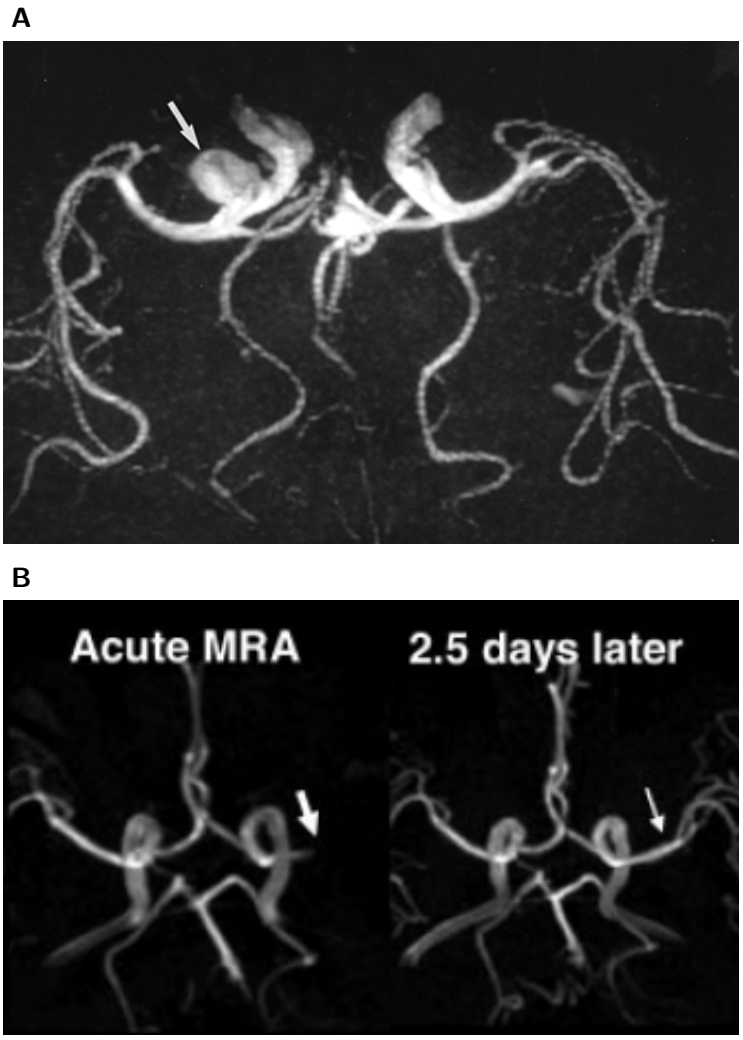


Figure 4.21: (A) Aneurysm of the right posterior communicating artery, taken from *Wardlaw et al., (2000)* [83]. (B) MRA acquisition of a patient with Atherosclerotic Middel Cerebral Artery Disease, showing an occlusion in the left MCA which resolved 2.5 days later, taken from *Kumral et al., (2005)* [84].

in the brain and chest (Figure 4.21.A). It can also be used to identify areas of occlusions which can limit blood flow to the brain causing a stroke (Figure 4.21.B).

Since MRA does not require an exogenous contrast agent, it has become an important tool in assessing vasculature in patient groups with contraindications to tracers, such as kidney disease.

4.5 Functional MRI

4.5.1 Theory

Pioneering work by *Ogawa et al,, (1990)* [8] demonstrated that there is a natural phenomenon which produces MR signal changes in response to brain activity. The human brain at rest is able to extract roughly 40% of oxygen from the blood in the capillary bed. When neurons in the brain are stimulated there is a regional increase in metabolic demand (∼5%), which is soon met with a significant increase in blood flow (∼25%). The amount of blood delivered to meet the increase in metabolic demand is much more than actually required, resulting in a drop in the fraction of oxygen required from the blood (∼15%) (Figure 4.22). The coupling between these haemodynamic properties was subsequently modelled by *Buxton and Frank, (1998)* [85].

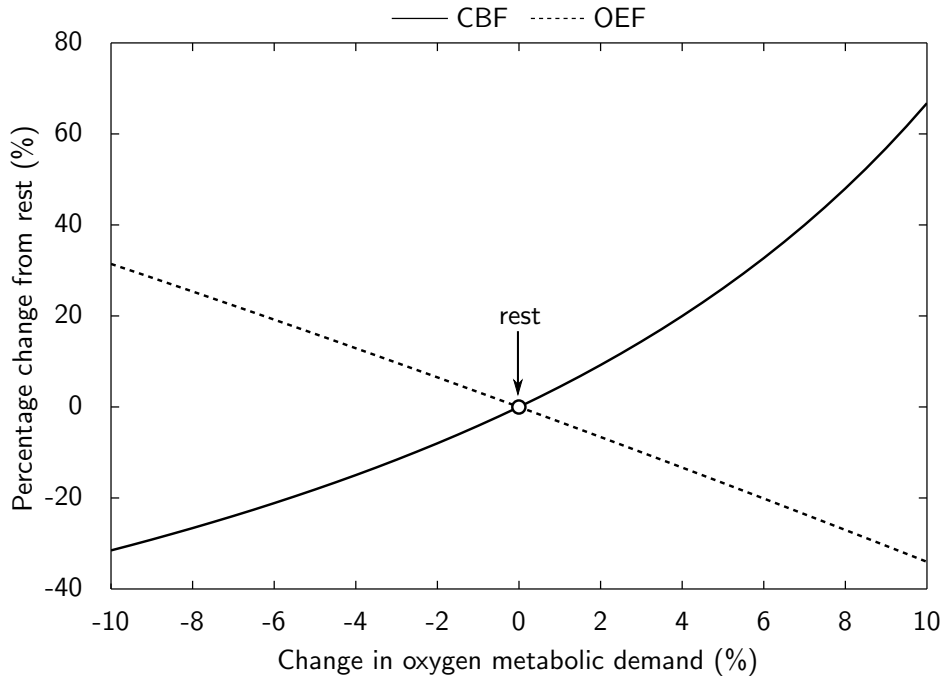


Figure 4.22: Change in cerebral blood flow and oxygen extraction fraction in response to a change in metabolic demand. The CBF increase is large compared the increase in metabolic demand, to compensate for this, the oxygen extraction fraction decreases.

The drop in oxygen extraction fraction and increase in blood flow, caused by an increase in metabolic demand, results in much more oxyhaemoglobin in the blood. Ogawa noticed that the magnetic susceptibilities of oxyhaemoglobin and

deoxyhaemoglobin were different, with oxyhaemoglobin having a similar susceptibility to tissue whereas deoxyhaemoglobin is paramagnetic.

Therefore at rest, when there is a high concentration of deoxyhaemoglobin in the blood, the paramagnetic nature of the de-oxygenated blood causes the MR signal to be attenuated. However after an increase in metabolic demand, the concentration of deoxyhaemoglobin drops causing the attenuation of the MR signal to be less severe. This can be summarised by saying areas of increased metabolic demand (and therefore activation) present as increase in MR signal in T_2^* weighted sequences. The change in MR signal due to varying levels of oxy- and deoxyhaemoglobin has become known as blood oxygenation level dependent (BOLD) signal.

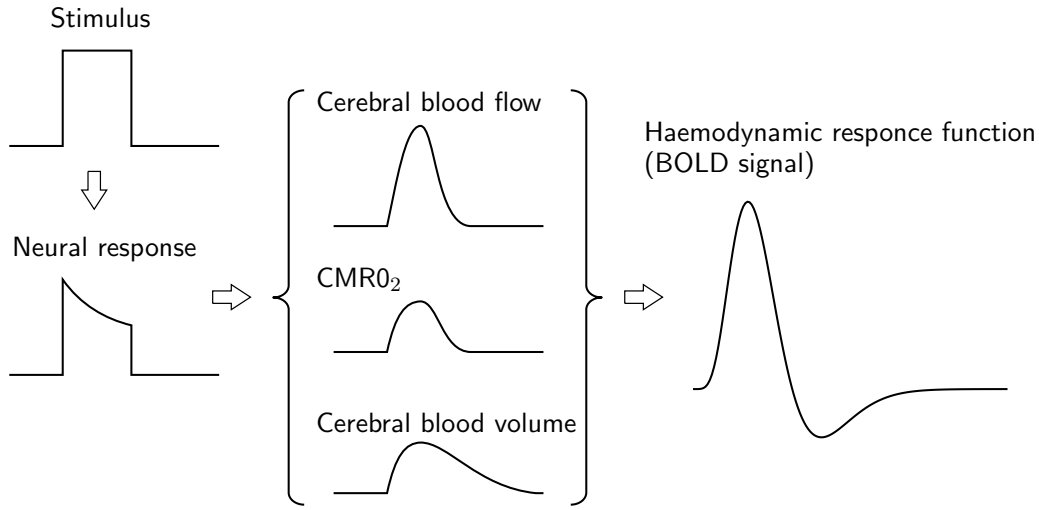


Figure 4.23: The sequence of physiological functions which lead to a change in BOLD signal. A stimulus causes a neurological response which then drives CBF, CMR0$_2$ and CBV in parallel. The combination of all these mechanisms manifests as the haemodynamic response function.

A change in BOLD signal is not observed immediately following neural activation. The change in BOLD signal due to an external stimulus is known as the haemodynamic response function (HRF). There is typically a 1 to 3 second delay between the application of a stimulus and any indication of a haemodynamic response, with the peak of the BOLD signal occuring at ∼5 to 8 seconds [86]. The BOLD signal will return to baseline around 20-30 seconds after a short stimulus has ended, and is followed by a post-stimulus undershoot

(Figure 4.23).

Modelling this haemodynamic response function is a complicated process, as there are many components which must be considered. Exposure to a stimulus causes a neurological response, which drives a change in physiological mechanisms such as CBF, CBV and $CMR0_2$. The CBF and $CMR0_2$ effects will also lead to a change in oxygen extraction fraction, as illustrated in Figure 4.22.

4.5.2 Applications

Functional MRI was first used to assess brain activity in response to a sensory stimulus, mainly in healthy volunteers. The underlying networks were discovered and the BOLD response to stimuli was soon modelled. This technique has since progressed to investigate functional abnormalities, for example in neurological conditions such as Alzheimer's, multiple sclerosis and epilepsy. fMRI experiments can be split into two categories; resting state (RS) and task-based. RS-fMRI is the acquisition of functional data when the brain is in an undirected state without any explicit stimulus, whereas task-based fMRI exposes the volunteer to stimuli (such as visual or motor). fMRI has more recently been used in the clinical patient setting. Resting state protocols have been used in pre-surgical mapping prior to neurosurgery to treat brain tumours and epilepsy.

4.5.3 Resting State Networks

The evolution of the BOLD signal is detected by acquiring a series of T_2^* weighted images with a TR of roughly 2 seconds. The BOLD signal originating from each voxel will contain temporal information regarding its apparent activity through its oxygen metabolism.

It can be seen that some voxels across the brain present with similar BOLD fluctuations over the course of the scan. When subjects are not performing a task, the similarity and synchronisation of BOLD signals from different areas of the brain can be interpreted as being functionally connected. These functionally connected networks can be identified by determining the correlation between the BOLD signal originating from each voxel with a reference signal from a seed region. The correlation coefficient between the two signals is mapped for each

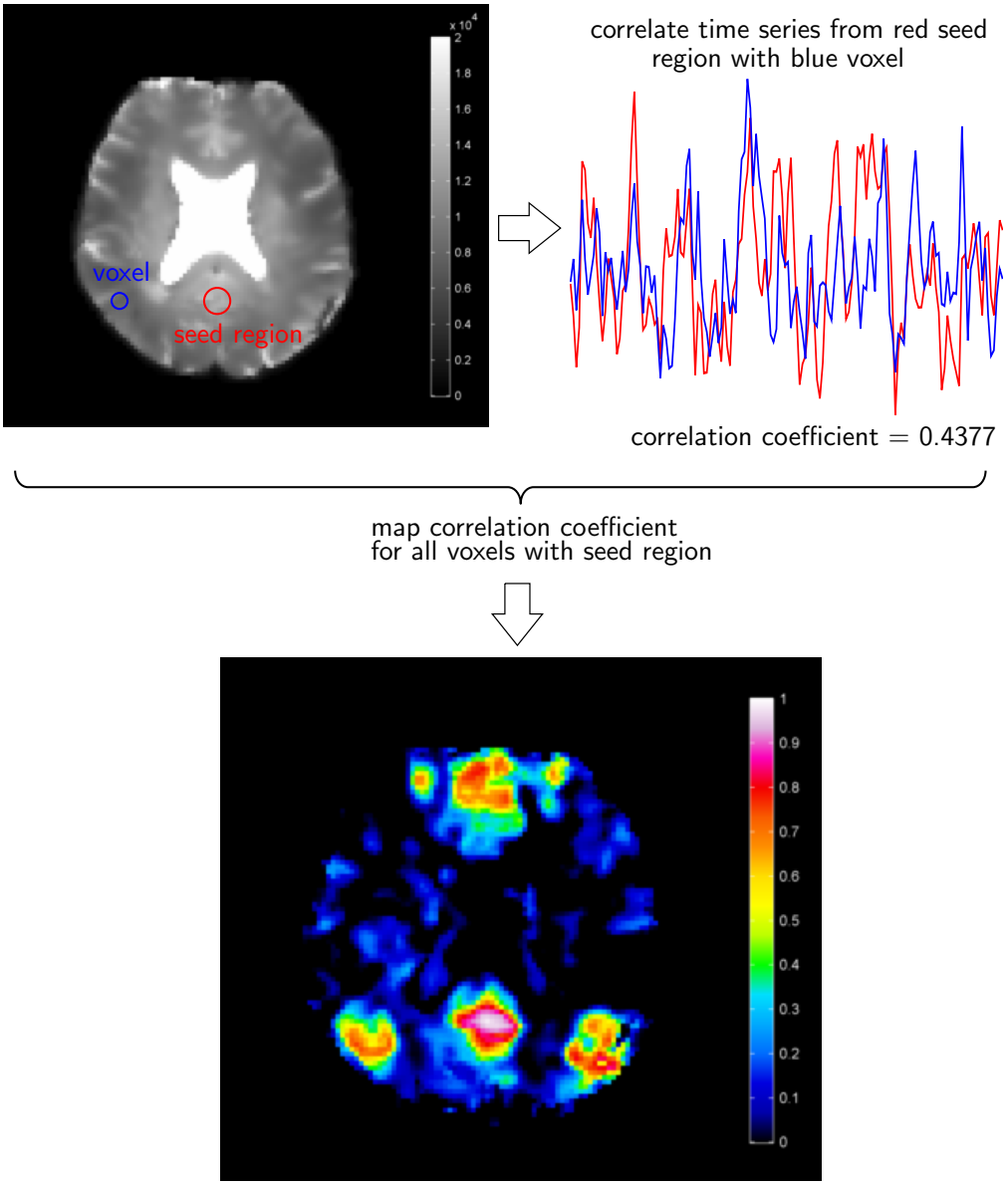


Figure 4.24: A reference BOLD signal is acquired from the posterior cingulate cortex and correlated with the bold signal from all other voxels. The network identified from this seed region is the default mode network, containing the posterior cingulate cortex, medial prefrontal cortex and both left and right inferior parietal lobes.

voxel, which can reveal regions that are synchronised (Figure 4.24). Areas demonstrating similar BOLD signals are known as networks, and each network is associated with a particular activity. A study by *Smith et al., (2009)* [87] isolated 20 independent functional networks common among subjects at rest, including the default mode network (DMN), visual and motor networks. For

example, visual stimuli cause neural activation within the visual cortex located to the rear of the brain.

In this correlation analysis, a seed region is often placed in an area known to be part of a network in order to isolate that particular network. However, there are more advanced methods to automatically isolate BOLD signals characteristic of a network. Independent component analysis (ICA) is such a technique. This method attempts to spatially and temporally separate signals with are independent from each other, where each separated signal is associated with a hypothesised network. This is discussed further in Section 5.4.3.

4.6 Summary

This chapter has explained various functional brain imaging concepts with emphasis on Arterial Spin Labelling. The concept of Arterial Spin Labelling was discussed and the methods used to pre-process and quantify acquired data were also explained. Contrast enhanced perfusion methods were introduced, with an explanation of how the inflow of a contrast agent can be modelled and quantified in terms of perfusion. Both time-of-flight and phase contrast approaches to Magnetic Resonance Angiography were explained. Finally, the concept of functional MRI was introduced, with explanations of how networks make themselves apparent from an fMRI time series and methods of identifying their specific activity.

The techniques discussed here are used in the subsequent experiments chapters to assess cerebral haemodynamics of Alzheimer's Disease, Huntington's Disease and Multiple Sclerosis.

5 Alzheimer's Disease

5.1 Outline

In this Chapter, the pathology of Alzheimer's Disease (AD) and the role of magnetic resonance imaging in diagnosing AD is introduced. The literature regarding MRI studies in AD is summarised, focusing on the use of structural measures, perfusion measures using arterial spin labelling data and fMRI data to assess network activity as potential biomarkers. The study rationale is described, followed by the MR acquisitions and processing pipelines used to obtain physiological measures. The measures are compared between patients with AD and age-matched healthy controls (HC) and the group differences compared to the literature.

This work was presented as an electronic poster at the 23th Annual Meeting of the International Society for Magnetic Resonance in Medicine (2015).

5.2 Introduction

Alzheimer's Disease (AD) is the most common form of Dementia, accounting for up to 50-60% of cases [9]. The risk of developing AD increases exponentially with age and it is estimated that it will affect 1 in 14 people over 65 years and 1 in 6 over 85 years.

AD presents with both psychological and physical symptoms. In the very early stages of AD no symptoms may be seen. As disease duration increases, symptoms begin to appear which progressively become more severe over time. Typically, early symptoms to appear are short term memory loss followed by some loss of language and motor skills. These will eventually progress to long term memory loss and disorientation. Motor skills continue to decline until the patient becomes bedridden which increases the likelihood of infection.

Currently, there is no cure for Alzheimer's Disease or any means by which to halt its progression. The medications prescribed to AD patients are given to reduce the effects or suppress the symptoms.

5.2.1 Pathology

There are thought to be two main indicators of Alzheimer's; amyloid-β plaques and neurofibillary tangles. Amyloid-β plaques (AβP) are clumps of amyloid-β peptides which have formed between neurons. The fatty membranes of neurons contain proteins known as amyloid precursor proteins (APP) which are responsible for neuron growth and repair. APP is repeatedly broken down and recycled by secretase, a family of enzymes which splits APP into smaller components. APP is most commonly split with γ and α secretase which yields two soluble peptides (P3 and APPsα), a process known as the *nonamyloidgenic pathway*. However, APP can also be split with β and γ secretase which produces one soluble peptide (APPsβ) and one insoluble peptide amyloid-β, a process known as the *amyloidgenic pathway* (Figure 5.1). In AD, the amyloidgenic pathway occurs more frequently than in those without the disease, causing excess amyloid-β to accumulate and bind between neurons. The amyloid-β plaques disrupt the electrical signals being passed between neurons, and with recent studies suggesting they are directly responsible for cell death due to their toxicity to adjacent neurons.

Neurofibrillary tangles (NFT) are another indicator of AD. Within neurons, micro-tubules act as pathways for organelles to be transported. The structure of micro-tubules is supported with a protein named *tau* which keeps the micro-tubules straight and parallel to each other. The tau proteins are usually removed from the micro-tubules at a slow rate driven by the presence of the kinase enzyme. However, in AD the rate of the removal of the tau protein from micro-tubules is accelerated which has two primary consequences. Firstly, the micro-tubules collapse meaning organelle transport is disrupted within the neuron. Secondly, the free tau proteins clump together between the micro-tubules which are known as neurofibrillary tangles.

Although the AβP and NFT are well recognised indicators of AD, their contributions to disease progression are poorly understood. It is not yet known whether they are causes of the common symptoms or whether they are a peripheral effect. However, a recent study suggested an amyloid cascade hypothesis which suggests that the effects of the AβP will incite the formation process of NFT.

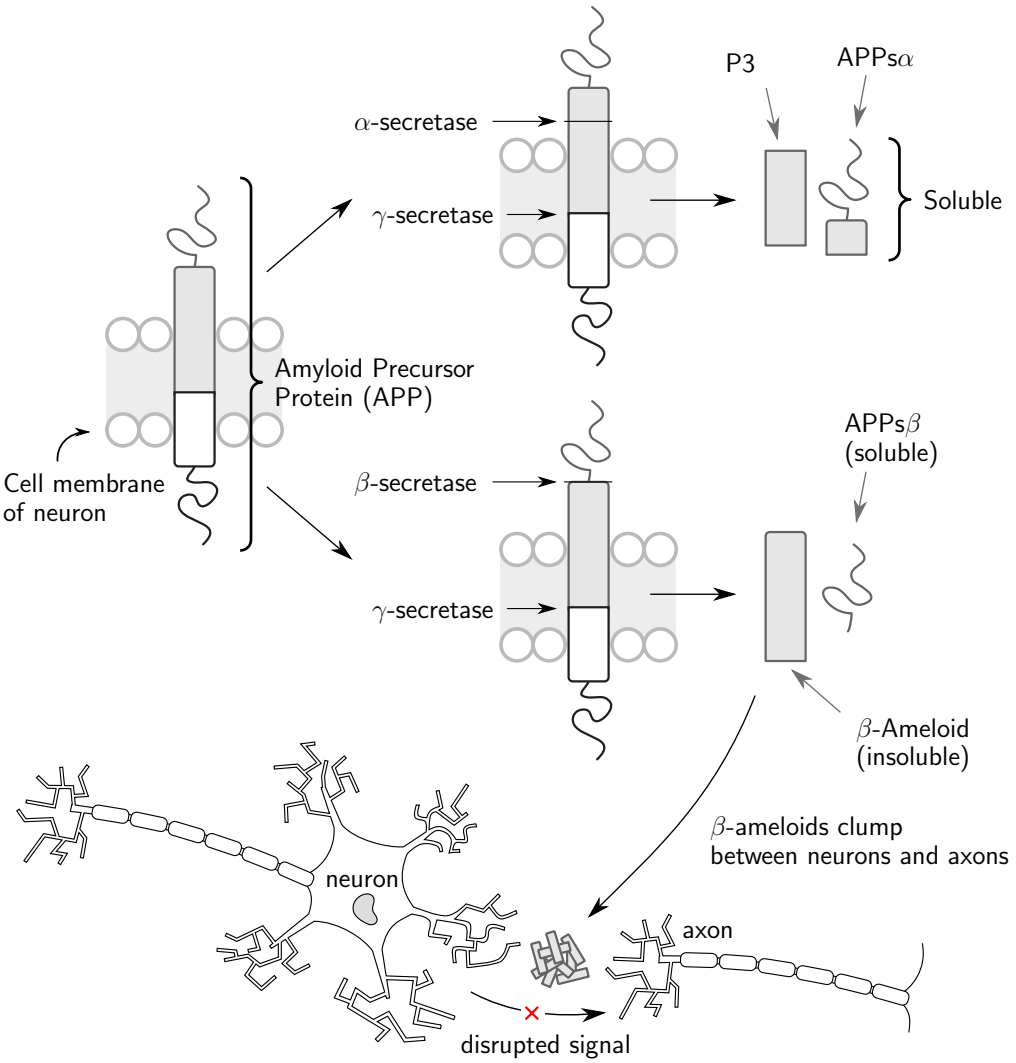


Figure 5.1: Illustration of the pathways which cause the build up of amyloid-β plaques in Alzheimer's Disease.

5.2.2 Use MRI in Alzheimer's Disease

Acquiring an accurate diagnosis of Alzheimer's Disease is important to ensure the patient receives the correct treatment. Previous diagnostic criteria to identify AD has included family history, a series of neurological tests and longitudinal cognitive assessments. Despite the relatively successful criteria, it is now becoming more important to have measures with increased sensitivity and specificity, allowing for early detection and ruling out diseases with similar symptoms. This early detection would allow for mild cognitive impairment (MCI) to be identified.

Mild cognitive impairment is a condition where the cognitive abilities, such as

memory or language skills, are noticeably reduced compared to the expected ability of a healthy person of the same age. Those suffering from MCI have a much greater chance of developing AD, to the extent that MCI is considered an intermediate stage between initial symptoms and diagnosis of AD [88]. Early detection of MCI or AD is an important issue, allowing individuals to make legal and financial decisions while still capable, and giving them an opportunity to find the necessary care.

Below is a summary of literature which uses MR as a method to differentiate between patients with AD, MCI and healthy volunteers. MR methods summarised are those using high resolution structural scans, perfusion studies which have used ASL and resting state functional MRI studies to assess abnormalities in the default mode network (DMN).

5.2.3 Overview of structural changes in Alzheimer's Disease

Structural changes associated with the progression of AD are well reported. Typical progression of AD causes atrophy of the cortical grey matter, atrophy of the hippocampus [89], and enlargement of the ventricles [90]. The hippocampus is the first brain region to be affected, succeeded by cortical grey matter atrophy and ventricular enlargement [91, 92]. The progression of structural changes, measured using MRI, have strongly correlated a decline in brain volume with a decline in a number of cognitive scores in AD patients [93–105]. The strength of correlations and extent of literature producing such similar findings suggests structural MR imaging can be used as a valid biomarker of disease progression.

The reproducibility and sensitivity of structural MRI in assessing AD is now so convincing that its implementation into the traditional Alzheimer's Association (previously known as NINCDS-ADRDA) diagnostic criteria (designed in 1984) was highly recommended by *Dubois et al.,* in 2007 [106]. In particular, the assessment of hippocampal atrophy by visual inspection from a high resolution T_1 weighted MRI has a sensitivity and specificity of 80-85% when distinguishing between AD patients and healthy volunteers [107–111]. Hippocampal volume is found to decrease by 10-15% in subjects with MCI [112] and 15-30% in mild dementia [113] when compared to healthy volunteers. Although the sensitivity

and specificity are high, these measures alone are not sufficient to be used for diagnostic purposes. In 2011, the Alzheimer's Association incorporated the use of structural MRI in the diagnostic criteria as a supportive feature, along with beta-amyloid accumulation and tau protein.

5.2.4 Overview of ASL perfusion studies in Alzheimer's Disease

The application of ASL to investigate perfusion related biomarkers in AD is well studied [10–24]. A common finding among these studies is a hypoperfusion in AD patients compared to healthy controls (HC) in various cortical regions [10–12, 15, 17], as well as the grey matter as a whole [13]. When patients with MCI were considered, they also presented a decrease in grey matter compared to HCs [12, 15, 18, 19, 21]. The literature is divided between those who observe no difference between MCI and AD [12, 19, 21], and those who identify reduced perfusion in AD compared to MCI [15, 18]. However results are particularly consistent in the literature for the posterior cingulate cortex (PCC), with a reduction in perfusion occurring in all forms of AD (full AD, MCI, high-risk elderly) compared to HC. These has important implications for functional MRI studies, as the PCC is a major node in the default mode network (DMN). Although the majority of studies report hypoperfusion in the cortex, some studies have detected localised hyperperfusion in areas of the middle temporal cortex, including the hippocampus, amygdala and basal ganglia [14–16]. These areas are known to have severe atrophy in fully developed AD [114], implying that structural changes may be accompanied by haemodynamic alternations.

Despite the extensive literature surrounding perfusion abnormalities in AD measured using ASL, there are very few studies which have assessed transit time changes in AD [115, 116]. It is well known that perfusion quantification is sensitive to transit time variations [117] which occur with vascular disease and age. However, the majority of perfusion studies have assumed a fixed transit time for both AD and HC populations allowing the use of a simple MR protocol. It is acknowledged in most of these studies however, that assuming a fixed transit time for both AD and HC is not optimal and should be carefully considered.

5.2.5 Overview of DMN studies in Alzheimer's Disease

Although the only current MR biomarker for AD is high-resolution T_1 weighted structural imaging to assess hippocampal volume loss, functional connectivity in resting state fMRI is emerging as a promising method for early diagnosis [118–120]. In particular, the DMN functional connectivity is of interest as it is a structure largely affected by atrophy.

The literature surrounding functional connectivity (initially described in Section 4.5) within the DMN in AD has suggested a decrease in connectivity within its components (posterior cingulate cortex, medial prefrontal cortex and L/R inferior parietal lobes, which can be seen in Figure 4.24) [25–31]. This has been demonstrated using correlation analysis with the PCC as a seed [26, 27], independent component analysis [28, 29] and regional coherence [30, 31]. There are also numerous reported cases of decreased hippocampal connectivity with the DMN in cases of AD [25, 26, 28]. The functional connectivity between DMN regions has also been shown to decrease with disease severity in a small number of studies [121–123].

Despite the majority of studies indicating a loss of connectivity associated with AD, there are studies where functional connectivity between DMN regions has been shown to be elevated in AD patients compared to HC [30, 122]. One possible explanation for the observed increase in functional connectivity is the compensatory-recruitment hypothesis. This is a process, originally proposed by *Grady et al., (2003)* [124], whereby the brain calls upon additional regions in order to recover from a functional defect in a particular area, helping to improve cognition associated with affected areas.

In summary, there is overwhelming evidence for DMN connectivity in AD patients to be reduced compared to HC of similar ages. However, *Hafkemeijer et al., (2012)* [125] notes that despite the reduced connectivity in AD patients, the majority of studies have not used grey matter volume or other atrophy measures as a confound in their analysis, and is not yet understood how grey matter differences alter connectivity scores.

5.3 Aims and Objectives

There is extensive literature describing cerebral structural changes, perfusion deficits and functional connectivity disturbances in AD, with the majority of the literature in agreement. However, studies using ASL and fMRI in AD have all been performed at MR field strengths of 3T or lower. With these techniques now being implemented at ultra-high field it may provide the methods with a higher degree of sensitivity necessary to detect more subtle changes. In this study, we utilised ultra-high field 7T MR to acquire high resolution structural data, perfusion estimates using arterial spin labelling and functional connectivity measures using fMRI. These measures were assessed for group differences to determine changes associated with AD.

5.4 Methods

5.4.1 Participants

15 AD patients (age 67 ± 6 years, 10 males and 5 females) and 12 healthy age matched controls (age 64 ± 8, 4 males and 8 females) were recruited to this study. All volunteers were asked to complete an MMSE (mini-mental state examination), and a 30-point questionnaire designed to assess cognitive impairment [126], which is used extensively in studies concerning AD (Table 5.1).

All volunteers were recruited following the ethical guidelines approved by the Leicester Research Ethic Committee and the Leicestershire Partnership NHS Trust. All patients were recruited from the academic department of Psychiatry for the Elderly, Leicester General Hospital.

5.4.2 MR Acqusition

All volunteers were scanned on a 7T Philips Achieva scanner with a Nova Medical 1TX/32RX head coil.

Healthy Controls				Alzheimer's Disease				
ID	Age	Gender	MMSE	ID	Age	Gender	MMSE	Duration
HC01	74	M	28	AD01	65	M	16	5
HC02	65	F	28	AD02	66	M	12	7
HC03	68	F	30	AD03*	84	F	25	2
HC04	63	F	30	AD04	77	F	27	1
HC05	66	F	30	AD05†	54	F	26	12
HC06	61	F	29	AD06	59	M	27	2
HC07	71	F	30	AD07	65	M	29	1
HC08	71	M	30	AD08	61	M	29	3
HC09	54	F	30	AD09	67	M	15	4
HC10	68	M	30	AD10	62	F	17	6
HC11	77	F	30	AD11	62	F	23	2
HC12	60	M	30	AD12‡	66	M	-	4
				AD13‡	64	M	-	1
				AD14	56	M	29	2
				AD15	57	M	24	1

Table 5.1: Summary of participants for the study, showing their age (years), gender, mini-mental state examination and disease duration (years) for the AD patients. *Patient was discarded due to poor quality of age matching. †Patient was discarded as an outlier to the group due to extremely long disease duration and young age. ‡No MMSE available.

5.4.2.1 Structural Data Acquisition

Structural data was acquired using a PSIR (phase sensitive inversion recovery) scheme with a turbo field echo (TFE) readout as described by *Mougin et al., (2016)* [127] (resolution = 0.6×0.6×0.6 mm, FOV (AP,RL,FH) = 200×181×120 mm, SENSE factor (AP,RL,FH) = 2, 1, 2, 200 contiguous slices, AP readout direction, radial phase encoding in RL and FH directions, flip angle = 8^o, TE/TR = 6/13 ms, acquisition time 11.92 minutes). A complete list of imaging parameters can be found in Table 5.3.

The initial inversion is performed using a tailored adiabatic inversion pulse in

order to reduce effects from B_1 inhomogeneities [128]. The PSIR sequence involves two TFE readouts at time TI_1 and TI_2 after the inversion. TI_1 is timed such that grey matter and white matter have equal but opposite longitudinal magnetisation. This results in voxels with equal amounts of grey matter and white matter to be nulled, resulting in a clear boundary between the two tissue types ($TI_1 = 780ms$). TI_2 must be as short as possible to allow fast acquisition, but must allow sufficient recovery past the null point ($TI_2 = 2380ms$). The phase and modulus data are saved.

The PSIR acquisition was designed to have a large enough coverage to image the whole head, specifically covering the entire cortex extending to at least the amygdala region, a deep lying structure within the temporal lobe. However due to variability of brain sizes, the cerebellum was not completely acquired for all volunteers.

5.4.2.2 Arterial Spin Labelling Data Acquisition

ASL data were collected using a FAIR labelling scheme using a 2D EPI readout (FOV(AP,RL,FH) = 192×21×42 mm, selective/non-selective thickness = 62/300mm, TE = 24 ms, flip angle = 90^o, TR = 3 s, SENSE factor 2 in AP direction, WET pre- and post-saturation pulses, background suppressed (BS), contiguous slices, ASL data were collected at post-label delays of 400, 700, 1000, 1300, 1700 and 2000 ms).

The early post-label delays (400, 700, 1000 and 1300 ms) were acquired at reduced slice resolution (3×3×6 mm, 7 slices) compared to the later post-label delays of 1700 and 2000ms (3×3×3 mm, 14 slices). The number of ASL averages was also lower for the early post-label delays at 10 label/control pairs compared to the later post-label delays which had 50 label/control pairs. The early post-label delays contain information regarding the arrival time of the label, which is rapidly and adequately sampled using lower spatial resolution and fewer label-control repeats [129]. In order to quantify perfusion,a specific M_0 for both early and later PLDs was acquired. Table 5.2 summarises the parameters which differ for each post-label delay, while Table 5.3 provides an extensive list of all scan parameters.

Post-label Delay (ms)	Resolution (mm)	Slices	BGS times (ms)	Averages
400	3×3×6	7	N/A	10
700	3×3×6	7	100, 350	10
1000	3×3×6	7	300, 650	10
1300	3×3×6	7	400, 900	10
1700	3×3×3	14	400, 1150	50
2000	3×3×3	14	500, 1350	50

Table 5.2: Table of ASL parameters for each post-label delay.

The placement of the ASL imaging volume was set to cover the cortex above the AC-PC (anterior commissure - posterior commissure) line. The shim box was positioned to cover the imaging volume extending towards the neck in order to achieve a homogenous B_0 good inversion of the labelled blood. The temporal slice gap of the 2D-EPI slices was 65ms and this was accounted for in the perfusion fit. Note that the blood label will have decayed if a long post-label delay and a large number of slices is used.

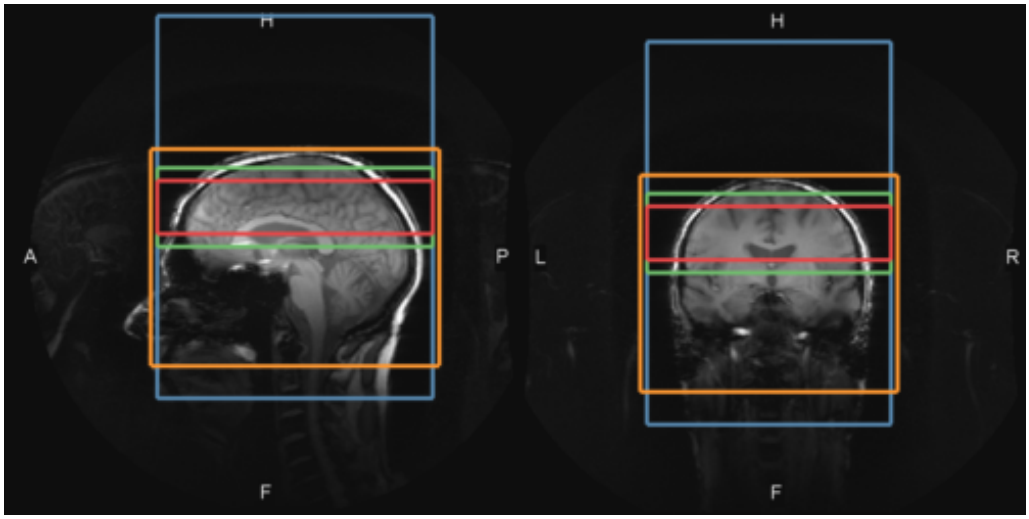


Figure 5.2: The geometry used for the ASL acquisition. The red box is the imaging volume, the green box is the selective label, the blue box is the non-selective label and the orange box is the shim box.

An inversion recovery sequence is performed in order to quantify T_1, using 10 inversion times (100, 200, 300, 500, 1000, 1300, 1700, 2000, 2500 and 3000ms). The readout used is identical to that of the late PLD ASL data.

Parameter	ASL (Early PLD)	ASL (Late PLD)	fMRI	PSIR
Scan Duration (mm:ss)	01:06	05:26	05:12	12:55
FOV (RL, AP, FH) (mm)	192 × 216 × 42	192 × 216 × 42	212 × 212 × 73	200 × 181 × 120
REC Matrix	80 × 80 × 7	80 × 80 × 7	112 × 122 × 36	336 × 336 × 200
REC Resolution (mm)	2.67 × 2.70 × 6.00	2.67 × 2.70 × 3.00	1.89 × 1.89 × 2.00	0.60 × 0.59 × 0.60
TE / TR (ms)	24 / 3000	24 / 3200	25 / 2000	6 / 13
WFS (pix)	24.002	24.002	26.999	8.795
BW (Hz)	42.4	42.2	37.5	115.2
SENSE (RL, AP, FH)	1, 2, 1	1, 2, 1	1, 3, 1	2, 1, 2
Fold-over direction	AP	AP	AP	RL
Fat-shift direction	P	P	A	P
Scan Mode	2D	2D	2D	3D
Imaging Mode	EPI	EPI	EPI	TFE
Shot Mode	Single-shot	Single-shot	Single-shot	Multi-shot
Flip angle (deg)	90	90	75	8
Temporal Slice Gap (ms)	65	65	55	N/A
Slice Ordering	Ascending	Ascending	Ascending	N/A
Lines per shot	39	39	37	109
Averages	10	50	150	1

Table 5.3: An extended list of parameters for ASL (both early and late PLDs), fMRI and PSIR data.

5.4.2.3 *Functional MRI Data Acquisition*

Resting state fMRI data was collected using a 2D-EPI readout (resolution = 1.89×1.89×2 mm, FOV(RL,AP,FH) = 212×212×73 mm, TE = 25 ms, TR = 2 s, 36 contiguous slices, SENSE factor 3 in AP direction, equidistant temporal slice spacing, 150 repeats, flip angle = 75^o, 5 dummy repeats). Complete imaging parameters can be found in Table 5.3. The fMRI image volume was positioned primarily to cover the areas of the default mode network (posterior cingulate cortex, medial prefrontal cortex and left/right inferior parietal lobes).

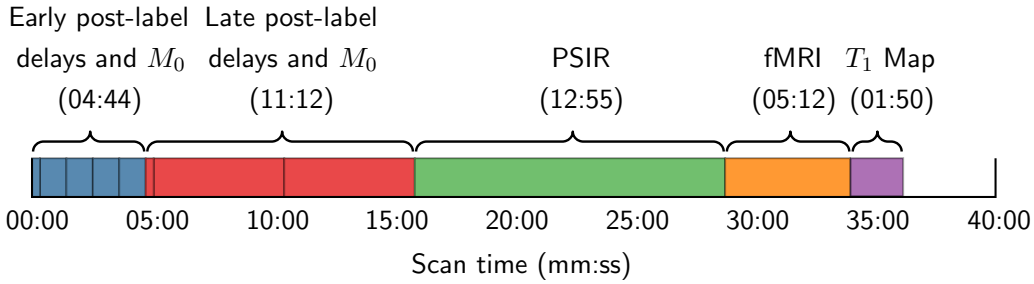


Figure 5.3: The duration of each acquisition relative to the total session duration.

5.4.3 Data processing

5.4.3.1 *Structural*

The acquired PSIR data must be reconstructed before useful measures can be extracted. The processing pipeline to reconstruct the PSIR data is described in *Mougin et al., (2016)* [127] and summarised in Figure 5.4. The phase difference between the two acquired phase images was found and used to correct the sign of the first acquired modulus image. However at 7T, a significant amount of B_1 inhomogeneity can be observed in this image. This is corrected by summing both acquired magnitude images and smoothing with a large Gaussian kernel to estimate the bias field. Dividing through by the estimated bias field creates an image with flat contrast for each tissue type allowing for more robust segmentation.

Brain extraction was performed using FSL BET on the Modulus (2) acquisition

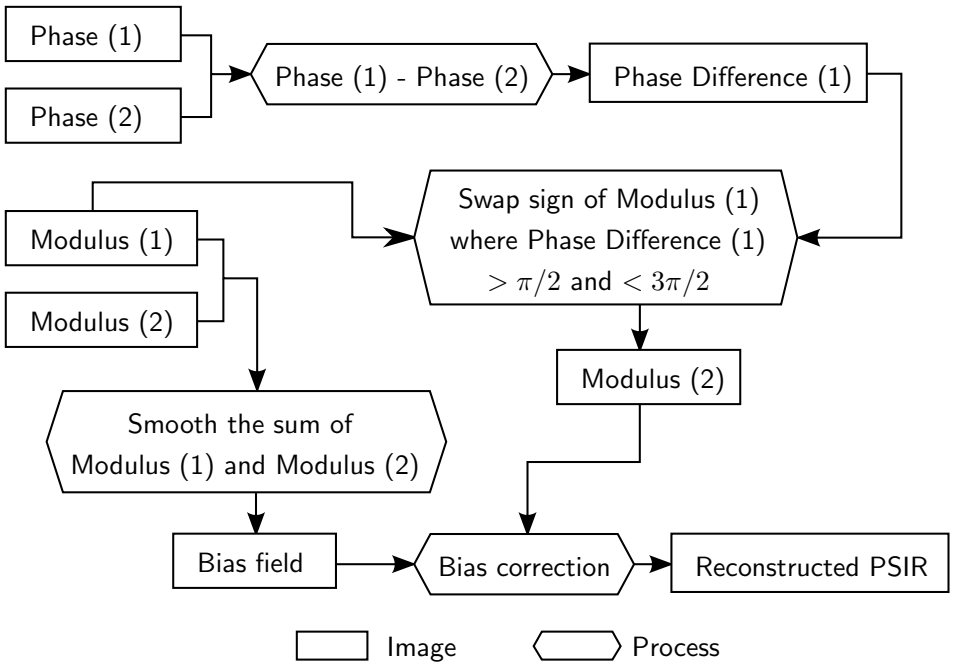


Figure 5.4: The processing pipeline used to reconstruct the PSIR anatomical scan.

and the brain mask was applied to the reconstructed image. Segmentation of tissue types (grey matter, white matter and cerebral spinal fluid) and spatial normalisation was performed using SPM8. These images were then used to estimate both grey matter volume and cortical thickness measures. To avoid biased brain volume estimates influenced by the proportion of cerebellum contained within the FOV, the cerebellum was ignored in the volume calculation. This was performed by computing a mask of the cerebellum for each volunteer by first co-registering the reconstructed PSIR data to MNI space using FNIRT [130]. The inverse warp was then found and applied to a mask of the cerebellum, cortex and ventricles in MNI space using nearest neighbour interpolation, to obtain a mask of these structures in native space. The Computational Anatomy Toolbox 12 (CAT12) in SPM12 was then used to estimate grey matter volume, white matter volume, CSF volume, total intracranial volume (TIV) and cortical thickness (CT). VBM (voxel-based morphometry) analysis was performed using SPM12, using TIV and cortical thickness as a covariate.

5.4.3.2 Arterial Spin Labelling Data Analysis

ASL data was processed using a standardised processing pipeline developed for this dataset (Figure 5.5). As the total duration of the ASL sequences was around 16 minutes (Figure 5.3), it was expected that there would be movement between the acquisitions of each post-label delay. Label 1 of the non-selective condition for each PLD was averaged over all repeats. These were then all co-registered to the PLD which occurred at the centre of the entire ASL acquisition (1700ms). The transformation matrices describing this co-registration were then applied in conjunction with the motion correction parameters such that only one transform was applied to the labels. Each application of an affine transformation causes the image to blur due to interpolation effects, so minimising the number of transforms applied is important. Motion correction was performed using the FSL MCFLIRT algorithm, whereby both label 1 and label 2 are concatenated in the fourth dimension and the central repeat of label 1 is used as the reference. Despite the slightly different contrast of label 1 and label 2 due to blood inflow, this method was found to out perform motion correcting each label individually. The transformation matrices to motion correct each repeat were decomposed to determine the amount of translation and rotation which was applied. If the translation required to motion correct a volume exceeded one voxel (3mm), the repeat was discarded. The image was split back into label 1 and label 2 formats before brain extraction was performed using FSL BET. A perfusion weighted image (PWI) was then created by computing the difference between label 1 and label 2 using simple pairwise subtraction. Using the method described by *Tan et al., (2009)* [72], each repeat of the PWI was assessed to determine if it was an outlier. The PWI was then averaged over all repeats to create a final perfusion weighted image for each PLD. The PWIs from the early PLDs were resampled to match the matrix size of the later PLDs, performed using cubic interpolation. All PWIs were then concatenated in the fourth dimension.

In order to calibrate the ASL timeseries, the M_0 of blood ($M_{0,b}$) was determined from the acquired $M_{0,t}$. This is performed using Equation 4.2 using partial volume maps for each tissue type acquired from segmenting the T_1 map using FSL FAST.

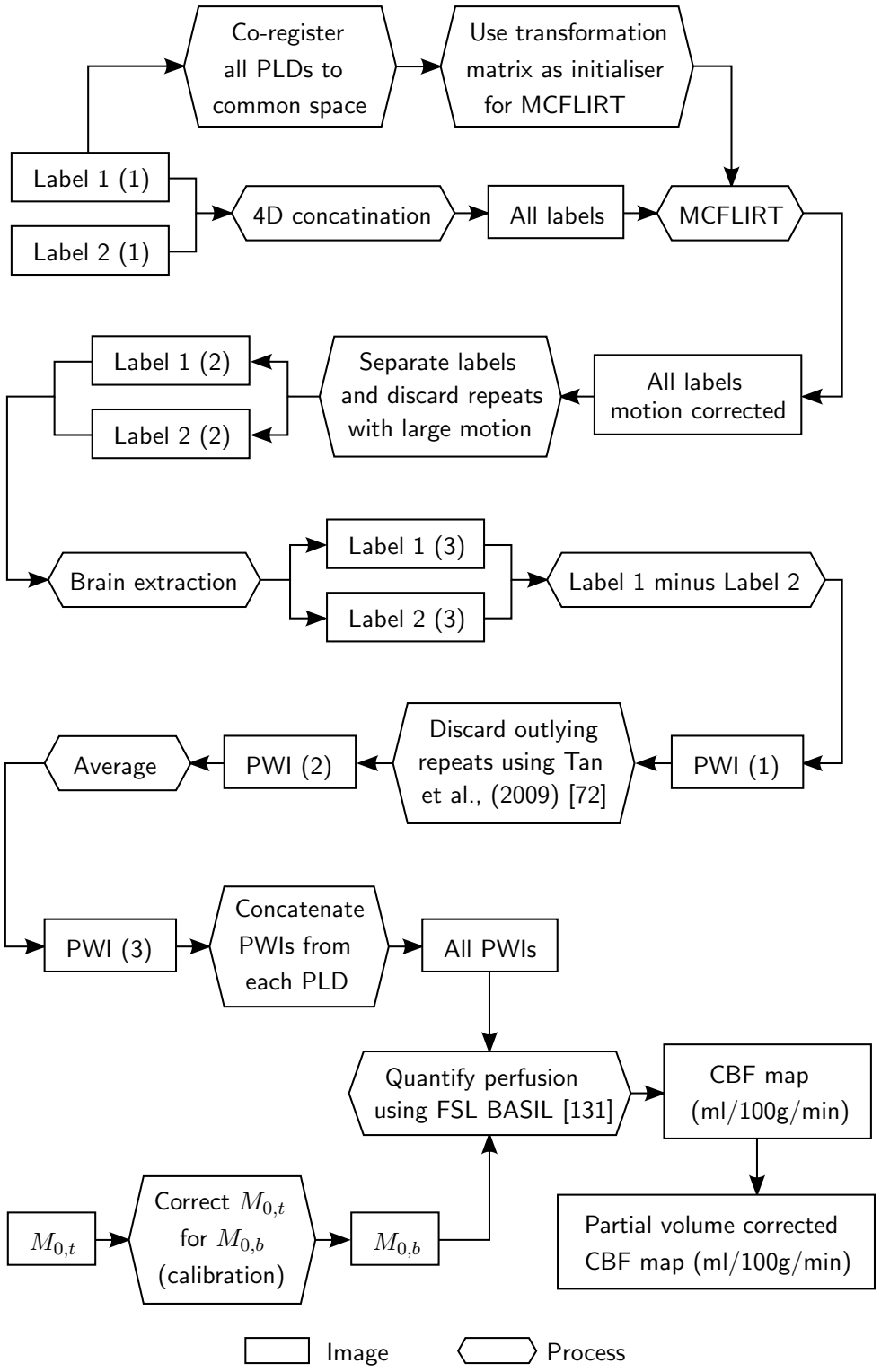


Figure 5.5: Processing pipeline used to create perfusion maps from ASL data.

Perfusion quantification was performed using FSL BASIL [131]. As the early PLDs were resampled in the slice direction, the temporal slice gap was different for

each PLD which required a custom version of BASIL to be edited and recompiled. As BASIL uses a Bayesian inference approach, the temporal slice spacing had a negligible effect between both versions of BASIL. The inversion pulse used during the IR acquisition was also used to apply the blood label, therefore the median inversion efficiency in grey matter was used as the label efficiency for the perfusion fit. The perfusion maps were also partial volume corrected using the regression algorithm described in Section 4.2.6.4 [74], using a spherical kernel with radius of 2 mm.

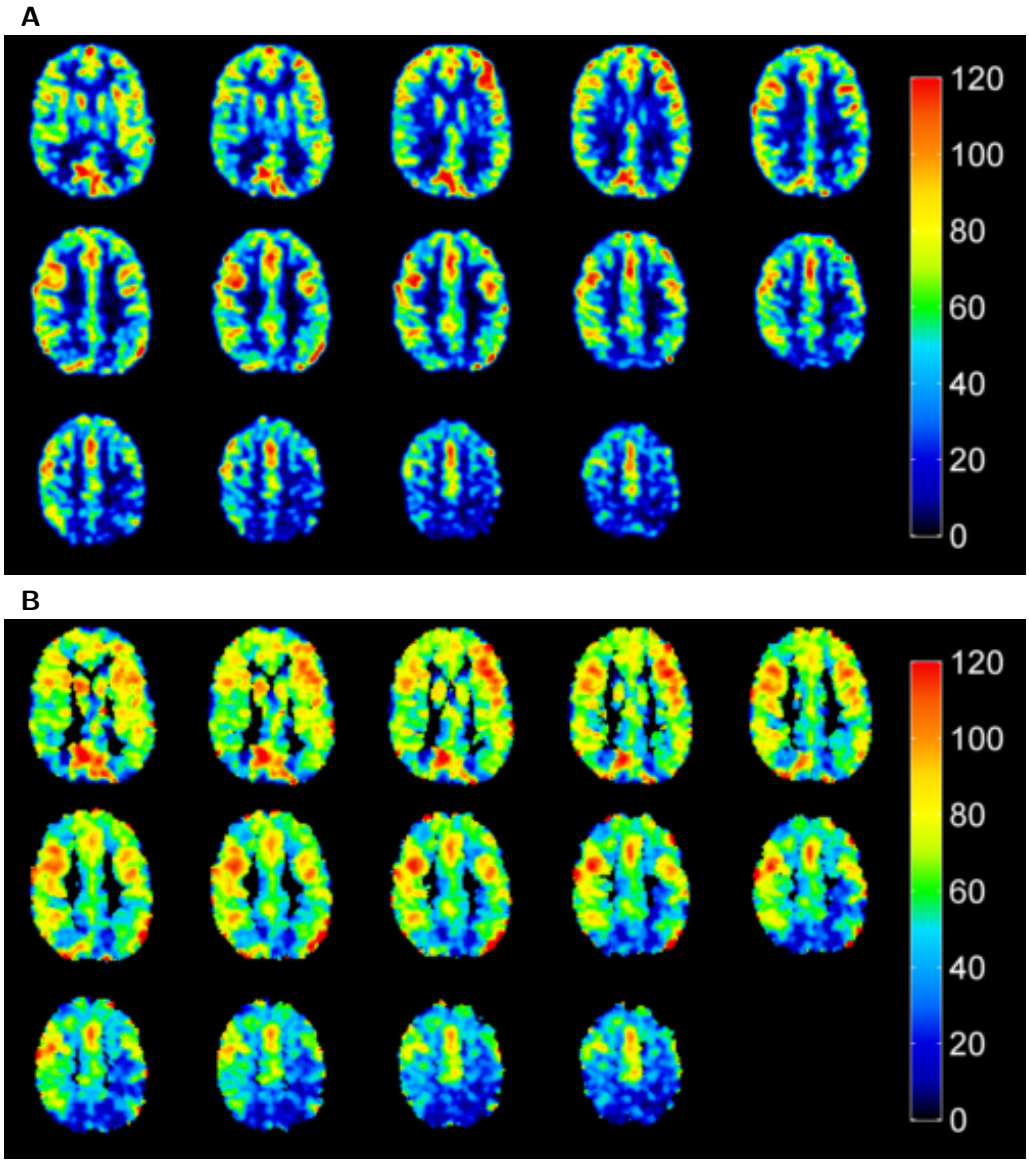


Figure 5.6: Perfusion map (in ml/100g/min) obtained from a young, healthy volunteer (A) without partial volume correction, (B) with partial volume correction.

The ASL protocol was developed on a young healthy volunteer to ensure validity of the pipeline, comparing the final perfusion estimates to accepted values in the literature.

5.4.3.3 Inversion Recovery

The inversion recovery (IR) data was fitted for M_0, α and T_1 on a voxel-wise basis using the equation

$$IR(t) = M_0 \left(1 - 2\alpha e^{-t/T_1}\right) \tag{5.1}$$

where M_0 is the equilibrium magnetisation, α is the inversion efficiency of the label and T_1 is the longitudinal relaxation. In order to reduce the occurrence of a poor fit, the acquired IR curves for each voxel were compared to a look-up-table (LUT) of simulated recoveries. The parameters giving the smallest sum of square differences were used as the initial search parameters. This improved the quality of the fit as T_1 values in the brain range from 1.13 seconds in the white matter [132] to 4.63 seconds in the CSF [133]. The T_1 map was then segmented into grey matter, white matter and CSF using FSL FAST [134].

5.4.3.4 Functional MRI

Functional MRI data was preprocessed using FSL FEAT and network connectivity was assessed using a seed correlation analysis (Figure 5.7). Motion correction was performed using FSL MCFLIRT [71], using a normalised correlation cost function, a rigid body transform and the temporal mean as a reference. As the readout used was a 2D-EPI sequence, each slice was acquired at a slightly different time, where the temporal slice gap is denoted as dt. Slice timing correction (performed using the FSL `slicetimer`) was performed to shift the time series of every voxel using a Hanning-windowed sinc function to estimate the BOLD signal as if the entire volume was collected at the same point in time. As the slices were acquired in an ascending order, all slices are shifted to match the acquisition time of the central slice. Brain extraction was then performed using FSL BET on the first volume, where a slight dilation was applied to the brain mask before being applied to every volume. Spatial smoothing was then performed using FSL SUSAN [135], an edge preserving

smoothing function using non-linear filtering. A high pass filter cutoff of 100 seconds was then applied to remove low frequency components.

Independent component analysis (ICA) was performed using FSL MELODIC [136] to differentiate spatial components. The fMRI time series was separated into 30 components; this was a compromise which avoids splitting a single network into too many components and also avoids combining multiple networks into a single component. The time-courses were also variance normalised such that estimation is less influenced by the mean signal and more influenced by the temporal dynamics. Often, components identified are not representative of functional connectivity, but instead noise components driven by head, respiratory and cardiac motion. The noisy components were identified by manual inspection and removed from the time series using `fsl_regfilt`, known as cleaning.

The fMRI time series was co-registered to MNI space by co-registering to the PSIR structural scan and the PSIR scan to MNI space. These transformation matrices were concatenated and applied to the fMRI.

In order to assess the connectivity within the default mode network (DMN) a seed based correlation analysis was used. The time course of every voxel was correlated with a template signal from the posterior cingulate cortex (PCC). The template signal was obtained by averaging all signals within a spherical volume placed in the PCC (MNI co-ordinates 44, 36, 50 / 2, -54, 28 mm) with a radius of 4 mm. In order to ensure there was no bias intrinsic within each group data set, the visual network was used as a control region. The template signal for the visual network was obtained by averaging all signals within a spherical volume (MNI co-ordinates 45, 25, 41 / 0, -76, 10 mm) with a radius of 4 mm.

The fMRI data was also assessed using FSL dual regression [137]. Dual regression is a method used to assess group differences in networks extracted using ICA. Each fMRI dataset was pre-processed as illustrated in Figure 5.7 up until co-registering to MNI space. All the fMRI datasets (both AD patients and HC) were then used in a multi-session temporal ICA, extracting 30 independent components. The term 'dual regression' refers to the two steps of regression which are performed following the extraction of these networks from concatenating all fMRI data; spatial regression and temporal regression. Spatial

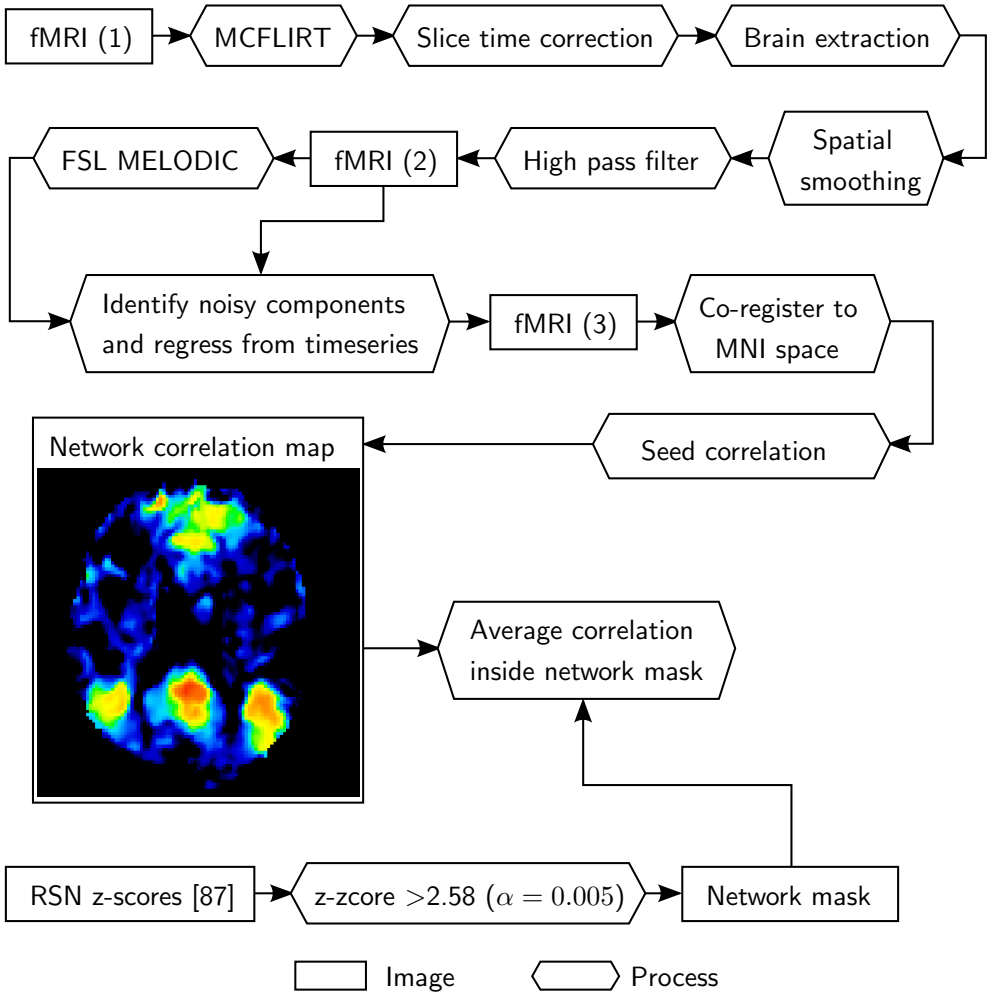


Figure 5.7: The processing pipeline to assess connectivity within networks. All preprocessing steps prior to seed correlation were performed using FSL FEAT.

regression attempts to find a time series which corresponds to each component found using the group ICA for each subject, and the temporal regression attempts to find voxels in each separate fMRI dataset which correspond to the regressed time series. Group differences between the AD patients and HC group were then assessed using the FSL randomise permutation tool [138], a tool used to threshold statistical maps when the null distribution is unknown.

5.5 Results

5.5.1 Volunteers

One scan was unusable due to poor data quality from head motion, and not all volunteers had complete datasets. In order to maximise the number of data sets used in statistical testing, all available scans were fed into an algorithm and age matched to within ±5 years. A two-sample equal variance t-test on ages was performed on age matched volunteers with available scans in order to assess the quality of age matching. The age matching showed no significant difference for the structural data (p=0.42), ASL data (p=0.33), or fMRI data (p=0.50) and the MMSE scores (p=0.47)

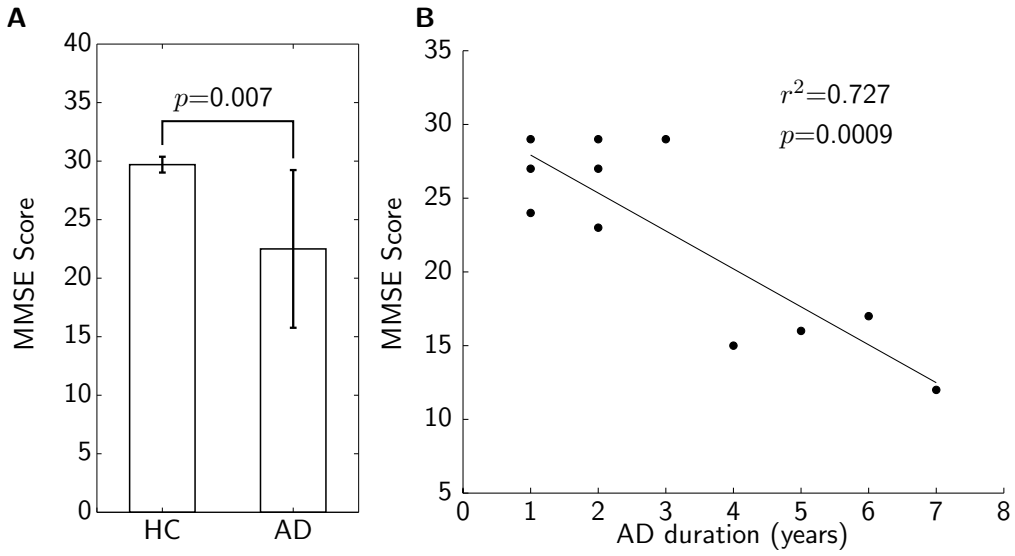


Figure 5.8: (A) A significant reduction in MMSE score was found for the AD group sompared to the HC group (p=0.007). (B) A significant negative correlation between AD duration and MMSE score was found in the AD group.

5.5.2 Clinical Scores

The MMSE scores were assessed for group differences between the HC and AD groups using a paired two-sample t-test, matching for age. A significant decrease in MMSE score was found for the AD patients compared to the HC (p=0.007) (Figure 5.8A). The MMSE scores were found to significantly reduce with increasing disease duration (r^2=0.727, p=0.0009) (Figure 5.8B).

5.5.3 Perfusion as assessed by Arterial Spin Labelling

The perfusion within the grey matter was assessed for each volunteer using the partial volume corrected perfusion maps. Voxels containing grey matter perfusion were isolated using the grey matter partial volume map obtained from T_1 segmentation, and selecting voxels containing $>$ 50% grey matter. The distribution of grey matter perfusion and transit time were all found to be normal using a one-sample Kolmogorov-Smirnov test. All perfusion and transit time maps were transformed into MNI space using the structural image as an intermediate and group maps were created (Figure 5.10 - 5.11).

The average grey matter perfusion was found to be 46±13 ml/100g/min in the HC group, and 32±7 ml/100g/min in the AD group. A significant reduction in grey matter perfusion was found in the AD group compared to the HC group (p=0.0178 using a paired t-test matching for age) (Figure 5.9A). The average grey matter transit time was found to be 1.06±0.14 seconds in the HC group, and 1.29±0.2 seconds in the AD group. The transit time increase in the AD group compared to the HC group was found to be significant (p=0.0063 using a paired t-test matching for age) (Figure 5.9B). A paired two-tailed t-test was performed on a voxel-by-voxel basis on the smoothed perfusion maps in order to obtain a map of areas where perfusion is significantly different between the AD and HD groups (Figure 5.13). A significant negative correlation is observed between the perfusion and the transit time values, indicating larger perfusion is accompanied by shorter transit times (r^2=0.533, $p = 0.0097$).

The perfusion for each volunteer was also assessed in a number of cortical regions. A modified version of the Oxford-Harvard cortical atlas was used whereby divided structures (such as anterior and posterior divisions of the Superior Temporal Gyrus) were combined. This reduced the number of cortical regions from 48 to 37. Cortical regions were not included when <80% of volunteers were able to contribute towards the average, leaving 26 viable cortical regions. Of the 26 cortical regions assessed, there was a significant reduction in perfusion in 13 regions of the AD group compared to the HC group (using a paried two-tailed t-test matching for age).

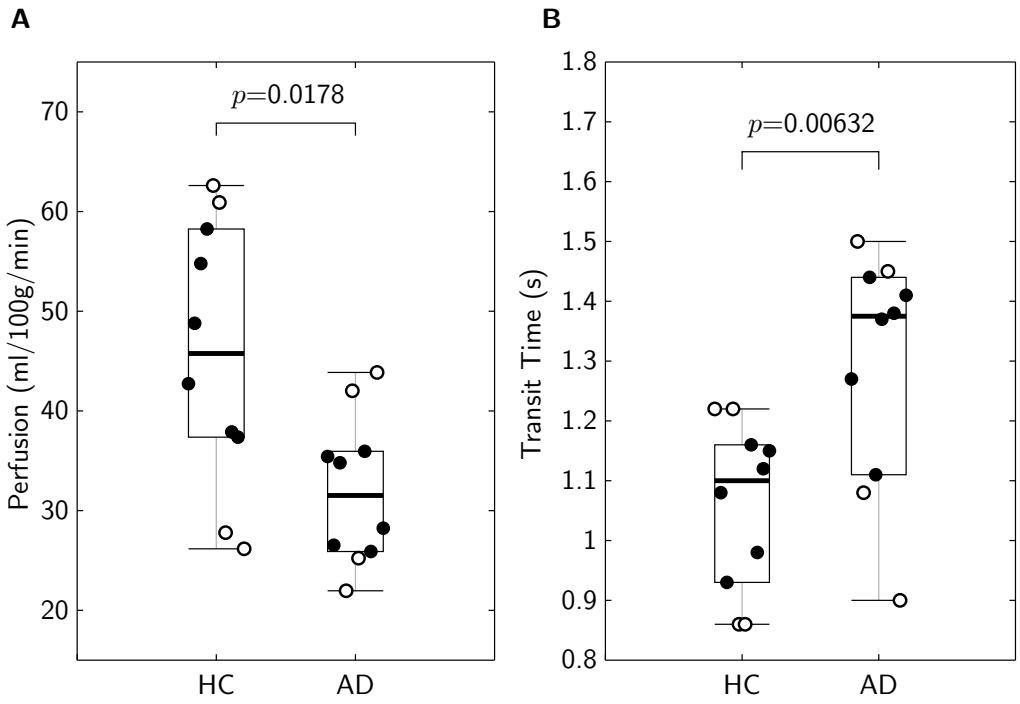


Figure 5.9: Box plot of (A) grey matter perfusion and (B) grey matter transit times in healthy controls and Alzheimer's Disease patients, with each volunteer's measurement. Black circles represent data within the interquartile range and white circles represent data outside the interquartile range.

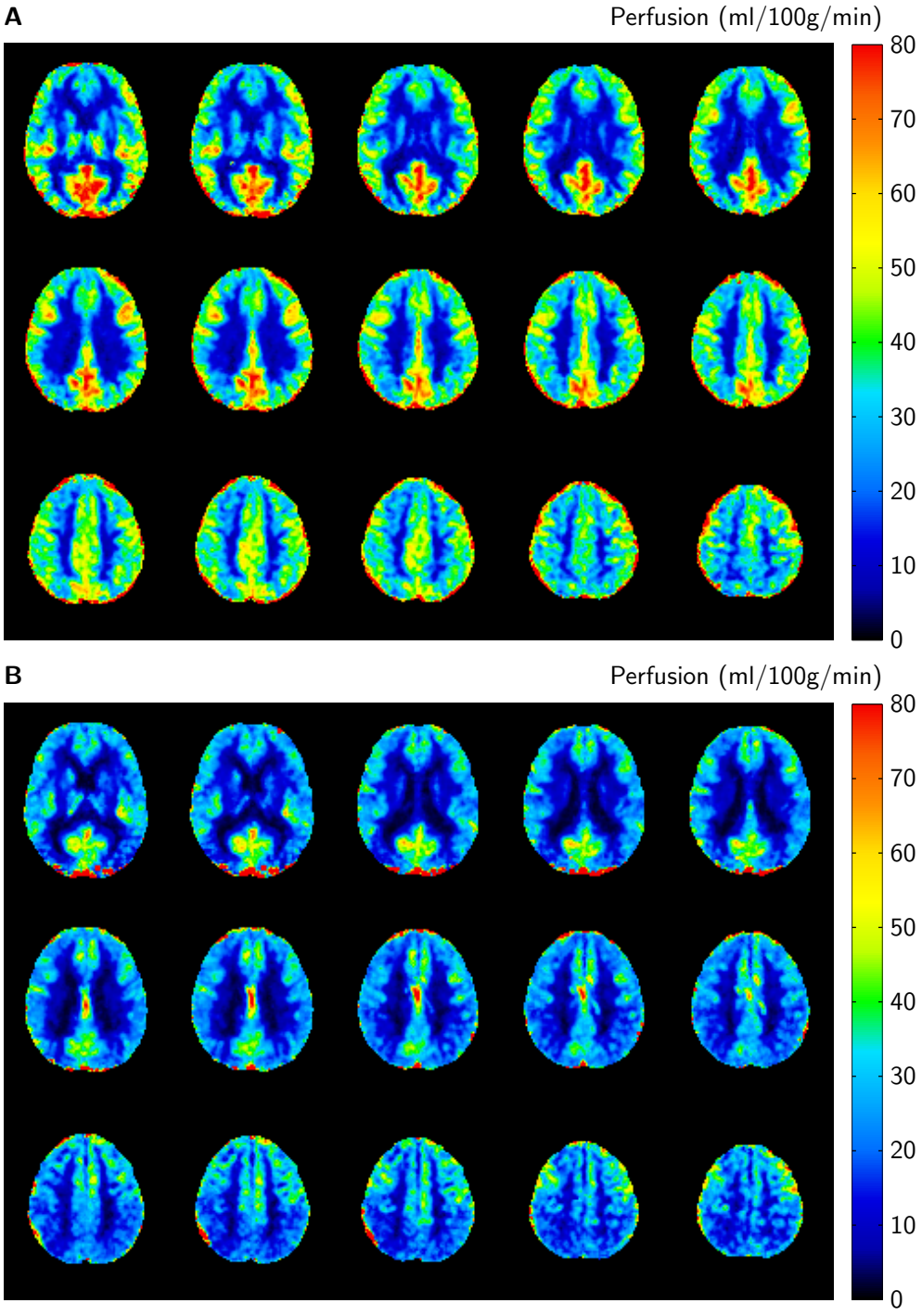


Figure 5.10: Group maps in MNI space of grey matter perfusion in (A) healthy controls and (B) Alzheimer's Disease patients

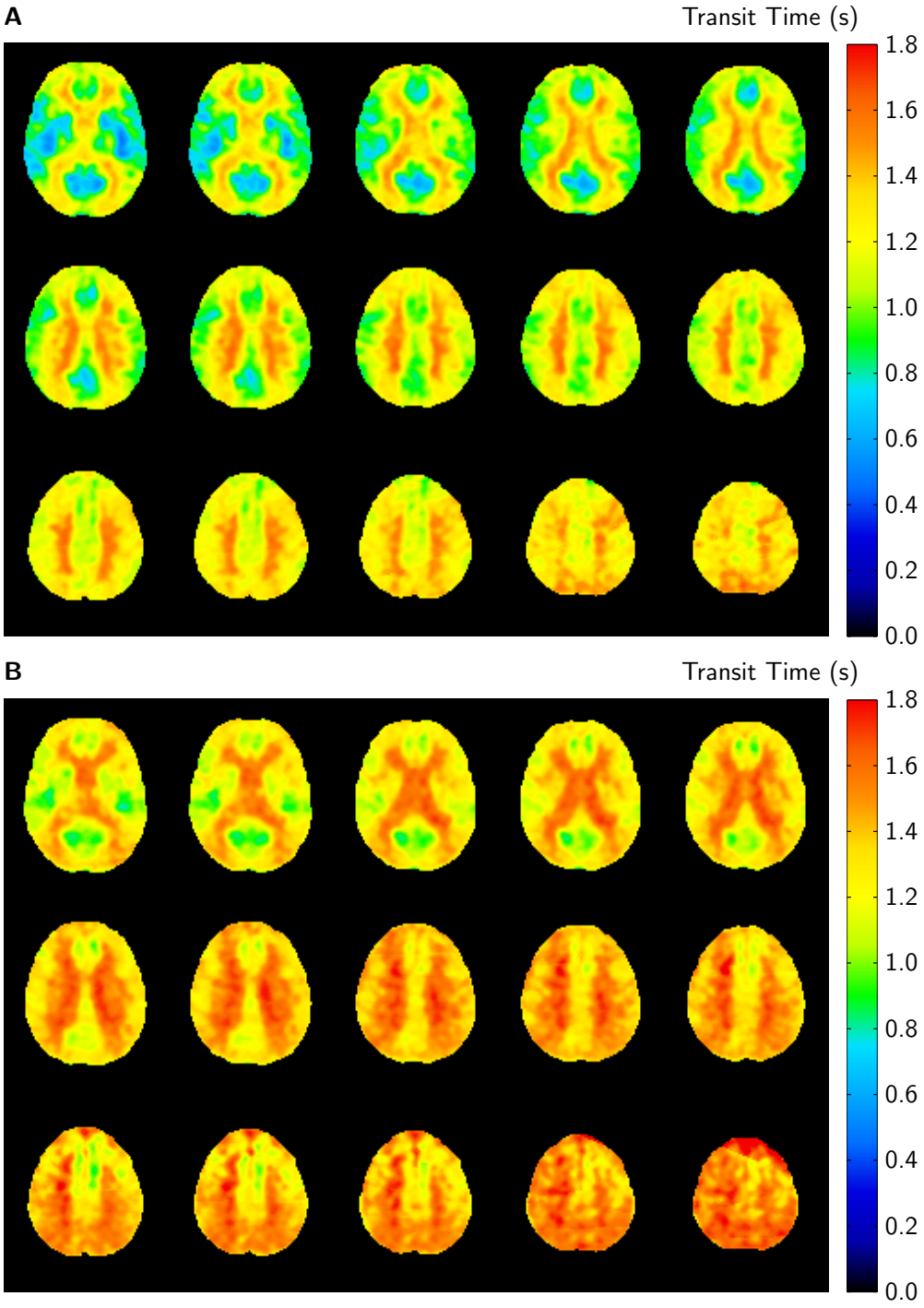


Figure 5.11: Group maps in MNI space of transit time for (A) healthy controls and (B) Alzheimer's Disease patients

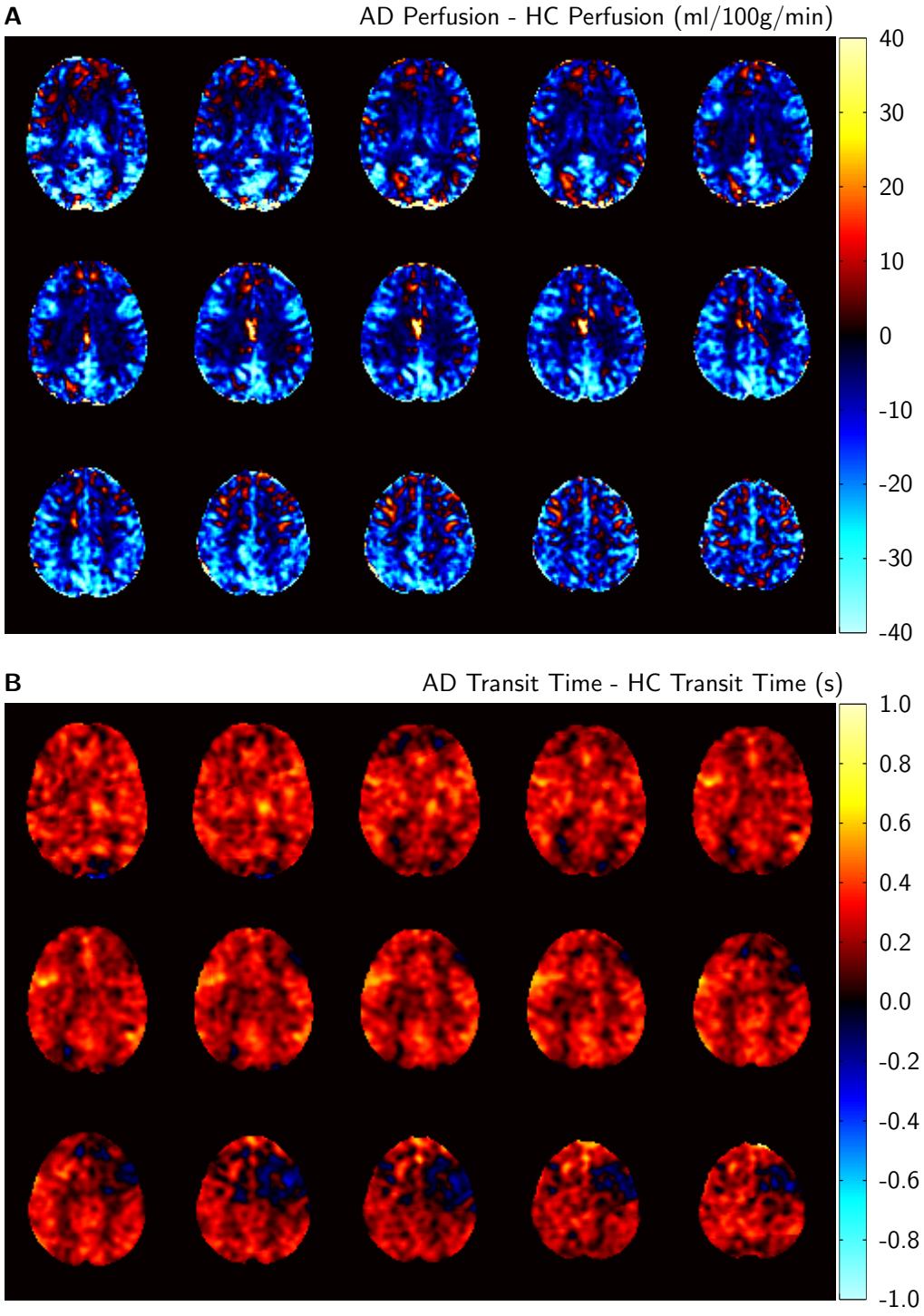


Figure 5.12: Group maps in MNI space of difference in (A) perfusion and (B) transit time between AD patients and the HC group.

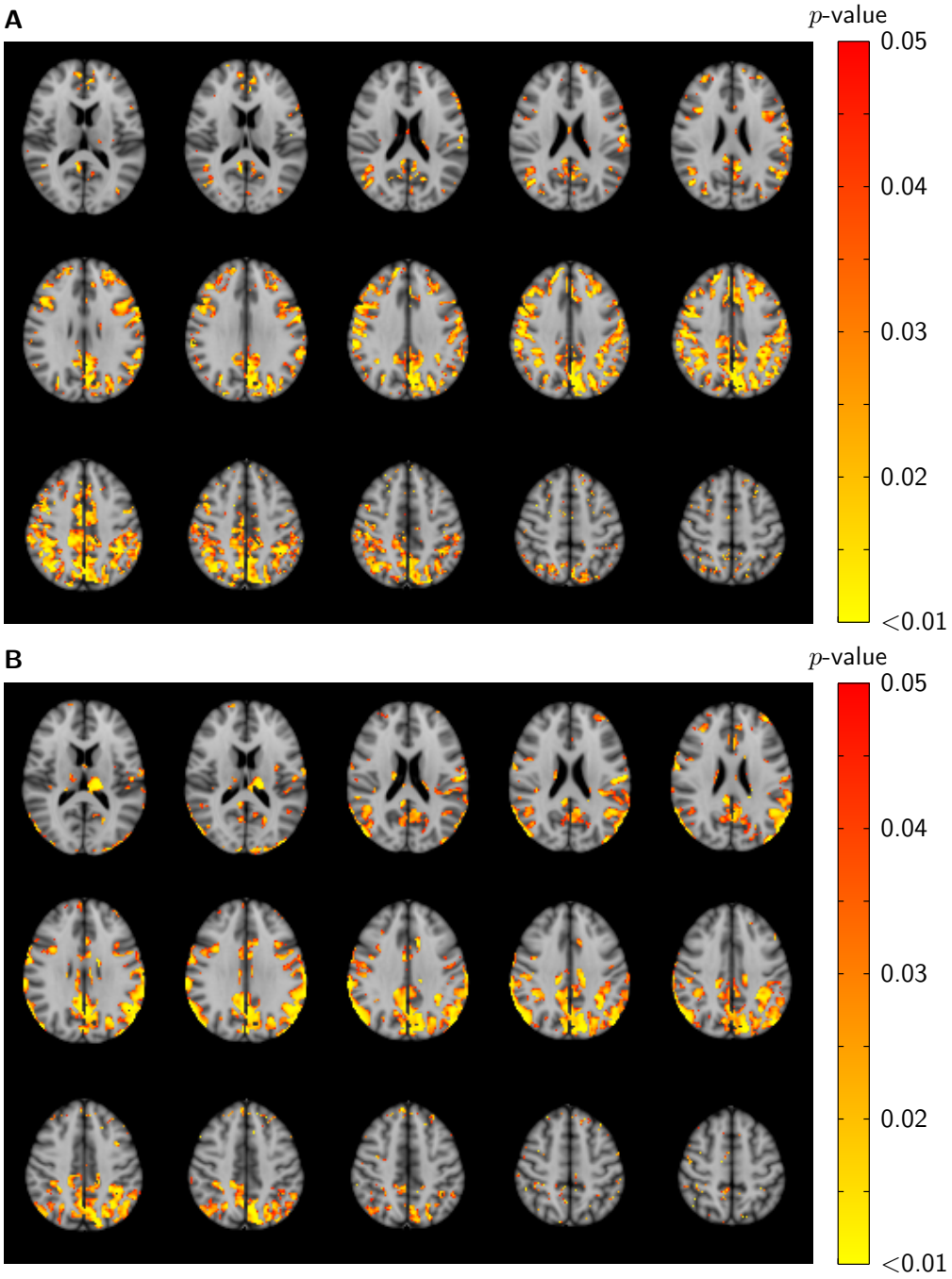


Figure 5.13: Voxel-by-voxel two-tailed t-test showing areas of significant group differences in (A) perfusion (reduction) and (B) transit time (increase) between the AD group and HC group.

5.5.4 Structural

The relative total grey matter volume (total grey matter volume / total intracranial volume) was assessed between the HC and AD groups. It was found that the AD group had a significantly reduced relative GM volume compared to

Cortical Region	HC Perfusion (ml/100g/min)	AD Perfusion (ml/100g/min)	Percentage difference	p value
Frontal Pole	37±13	25±9	-30.69	0.046
Insula Cortex	39±11	28±11	-28.42	0.047
Inf. Frontal Gyrus	48±16	32±12	-32.31	0.023
Precentral Gyrus	45±14	27±12	-40.16	0.005
Postcentral Gyrus	40±13	24±9	-39.19	0.006
Sup. Parietal Lobe	33±16	13±8	-61.55	0.003
Supramarginal Gyrus	38±11	22±11	-40.99	0.005
Angular Gyrus	41±13	22±12	-45.67	0.003
Lat. Occipital Lobe	35±12	18±10	-48.37	0.002
Juxtapositional Lobe	42±16	23±15	-44.61	0.014
Cingulate Gyrus	44±15	23±9	-29.06	0.032
Precuneus	52±17	34±15	-34.01	0.019
Occipetal Lobe	42±12	28±11	-32.96	0.009

Table 5.4: A summary of cortical regions displaying significantly reduced perfusion in Alzheimer's Disease patients compared to healthy controls.

HC group (p=0.0318, paired two-tailed t-test).

The cortical thickness in the AD group (2.3±0.2 mm) was reduced compared to the HC group (2.4±0.1 mm) but did not reach significance (p=0.193, paired two-tailed t-test), however after normalising the data for TIV, a significant reduction was observed in the AD group (1.8±0.2 mm/L) compared to the HC group (2.0±0.1) (p=0.0174, paired two-tailed t-test) (Figure 5.14A). The normalised cortical thickness also showed a significant negative correlation with disease duration in the AD group (p=0.008, r^2=0.445) (Figure 5.14B).

In order to spatially assess this observed grey matter loss in the AD group, voxel-based-morphometry was performed using TIV as a covariate (Figure 5.15). Significant atrophy was found in the occipital, temporal and parietal lobes (p <0.05) in the AD group compared to the HC group.

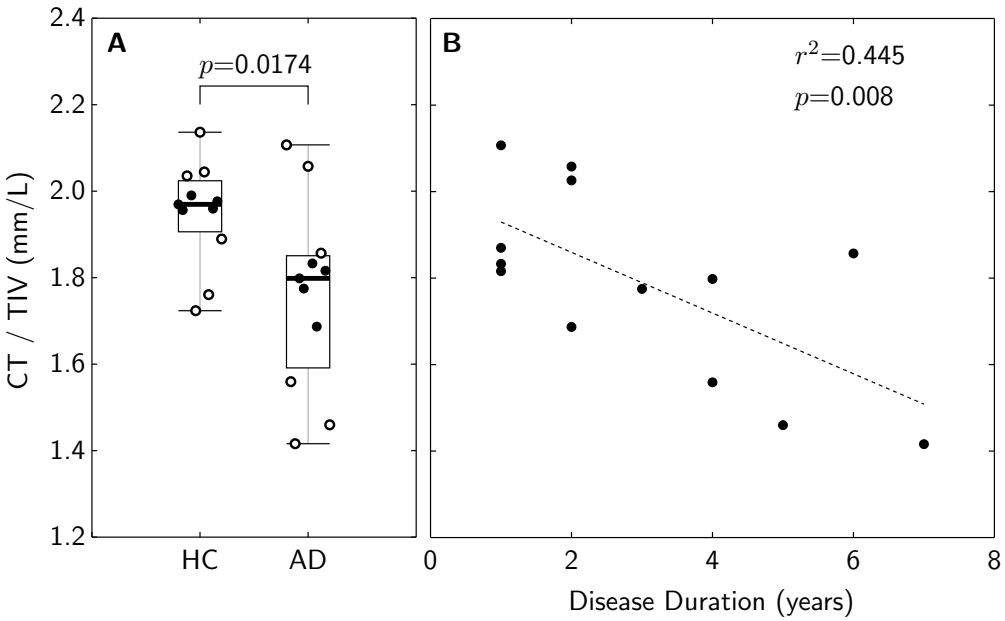


Figure 5.14: (A) Cortical thickness normalised to total intracranial volume is found to be significantly reduced in the AD group compared to the AD group. (B) Normalised cortical thickness is found to have a significant negative correlation with disease duration in the AD group.

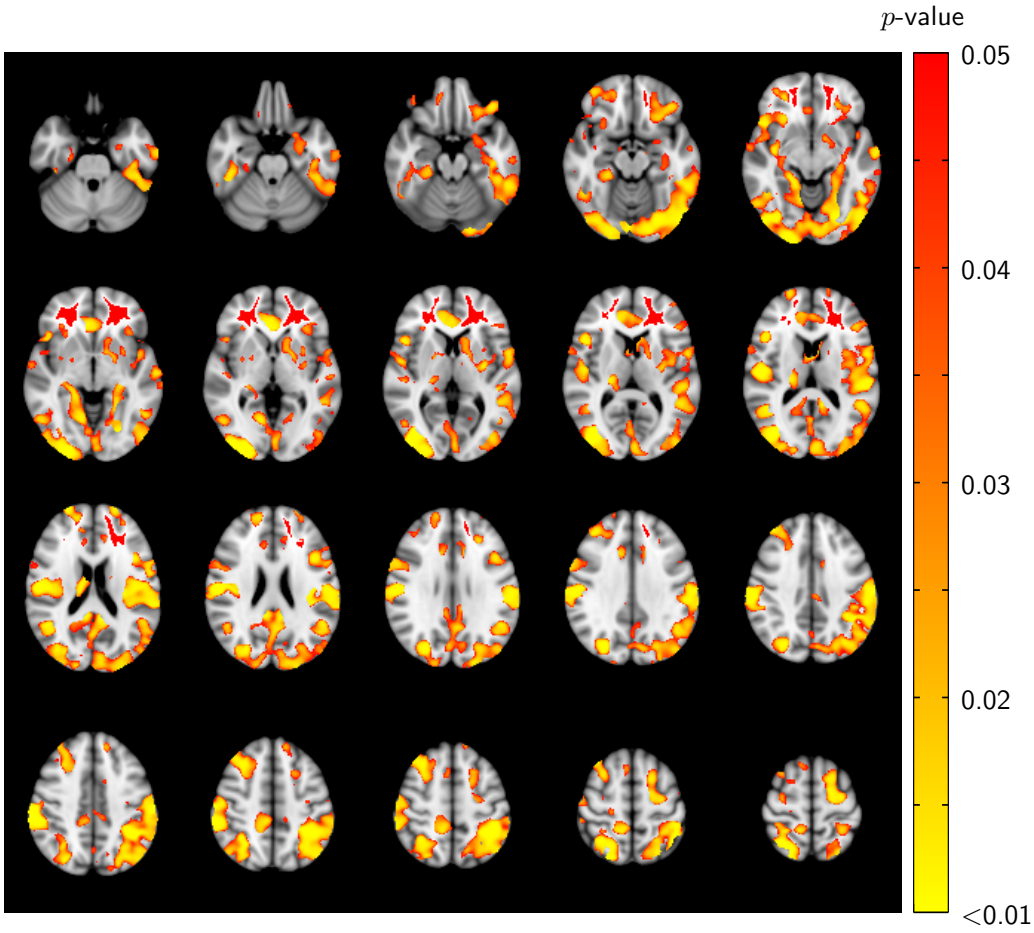


Figure 5.15: Results of voxel-base-morphometry to assess grey matter loss associated with Alzhiemer's Disease. p-values calculated using a two-sample t-test using TIV as a covariate, with group contrast defined as HC > AD. Significant clusters were found in the occipital, temporal and parietal lobes.

5.5.5 Clinical scores and Structural Correlation

A significant positive correlation is found between normalised cortical thickness and MMSE score in the AD patient group ($r^2 = 0.483$, p=0.018) (Figure 5.16) (Figure 5.16A). A significant positive correlation is also found between relative grey matter volume and MMSE score in the AD patient group ($r^2 = 0.590$, p=0.0058) (Figure 5.16B).

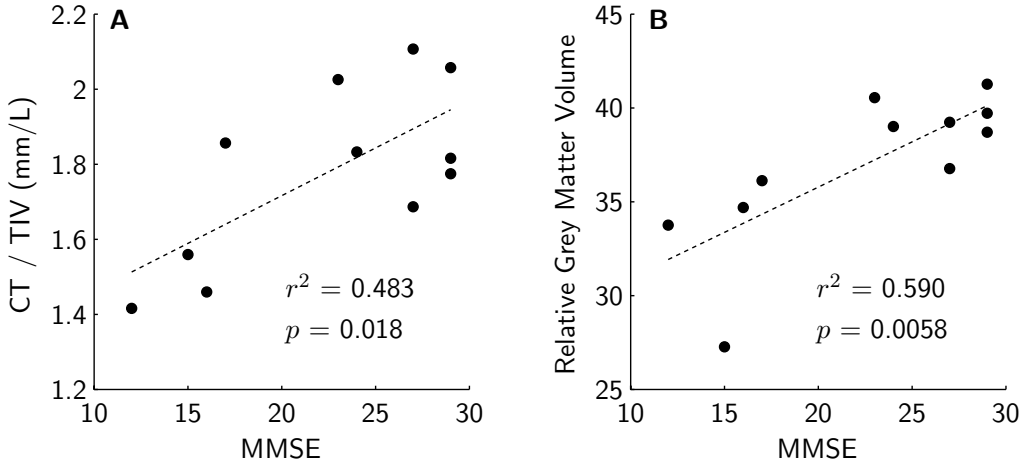


Figure 5.16: The correlation between MMSE score and (A) normalised cortical thickness and (B) relative grey matter volume. A significant positive correlation is found between MMSE and normalised cortical thickness (r^2 = 0.483, p=0.018), and MMSE and relative grey matter volume (r^2 = 0.590, p=0.0058)

5.5.6 fMRI Network Analysis

A trend was observed for a reduction in network connectivity (correlation) in the AD group compared to the HC in all regions of the DMN (Figure 5.17). However, significance was only observed in the mPFC (p=0.025), the PCC (p=0.277), LIPL (p=0.066) and RIPL (p=0.477) did not reach significance when using a paired two-tailed t-test. The correlation within the visual cortex (used as the control network) was not significantly different between the groups (p=0.814).

5.5.7 Perfusion and Structural Correlation

A significant correlation was found between the normalised cortical thickness and average grey matter perfusion in the AD group, whereby a reduction in normalised cortical thickness was accompanied by a reduction in grey matter perfusion (r^2 = 0.568, p=0.0341) (Figure 5.18B). However, the HC group did not demonstrate any correlation between normalised cortical thickness and average grey matter perfusion after partial volume correction (r^2 = 0.105, p=0.760) (Figure 5.18A).

A strong correlation was also found between the relative grey matter volume and

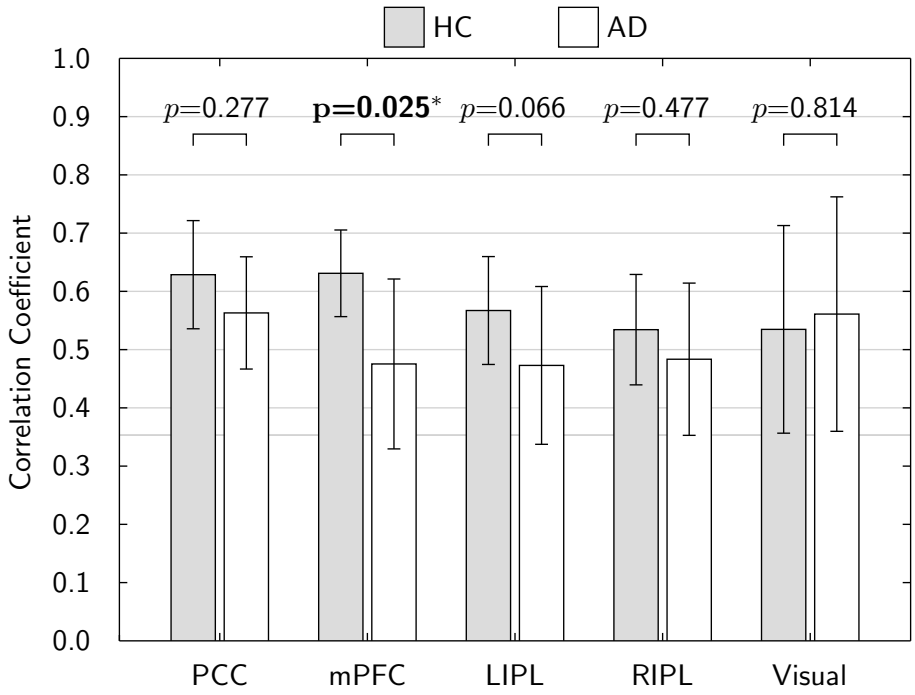


Figure 5.17: The average correlation coefficient (with error bars indicating standard deviation) within each region of the DMN and the visual network. A trend indicating a reduction in the correlation coefficient of all areas of the DMN in the AD group compared to HC, but significance was only observed in the mPFC. No difference was seen in the visual network between groups.

average grey matter perfusion in both HC group (r^2=0.556, p=0.076) and the AD group (r^2=0.485, p=0.092). However, on combining the AD and HC subjects, a statistical significant positive correlation was found (r^2=0.600, p=0.0019) (Figure 5.19).

5.5.8 Perfusion and fMRI correlation

When each region of the DMN (PCC, MPFC, RIPL and LIPL) is considered individually, the average grey matter perfusion does not correlate with correlation coefficient. There was an indication that when the whole DMN was considered, the average correlation coefficient positively correlated with grey matter perfusion and negatively correlated with transit time, however neither trend reached significance (Figure 5.20).

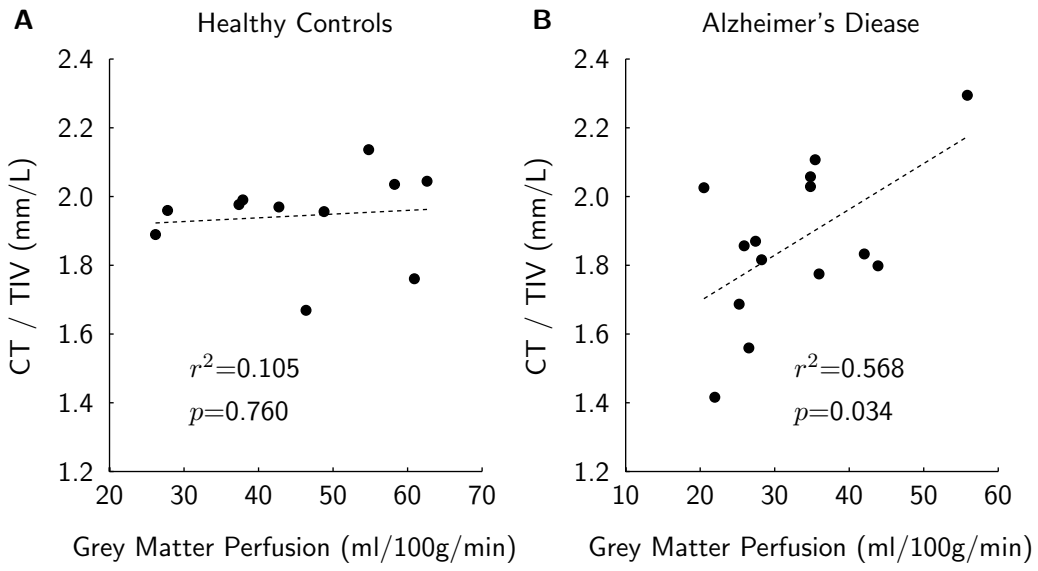


Figure 5.18: Correlation between normalised cortical thickness and average grey matter perfusion in (A) healthy controls and (B) Alzheimer's Disease patients. A significant positive correlation is found in the AD cohort meaning the cortical thickness increases with perfusion (p=0.034).

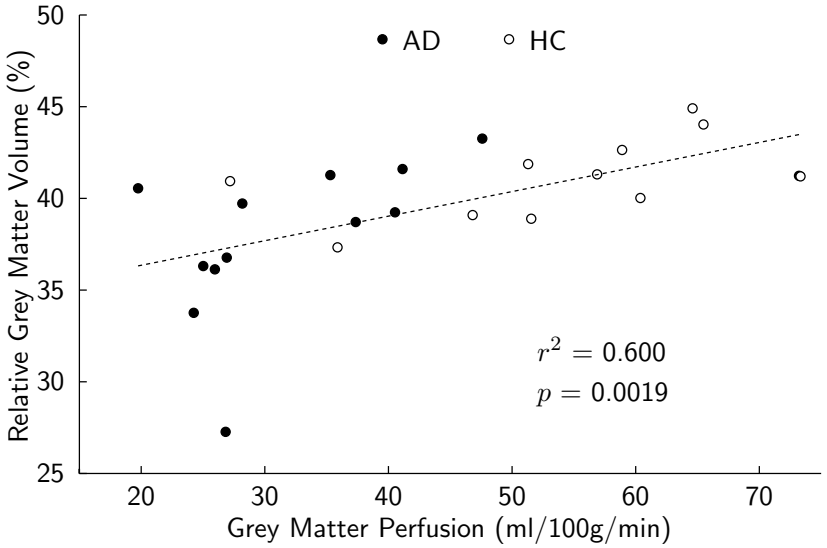


Figure 5.19: A significant positive correlation between relative grey matter volume and grey matter perfusion was found when the AD and HC group were combined (r^2=0.600, p=0.0019).

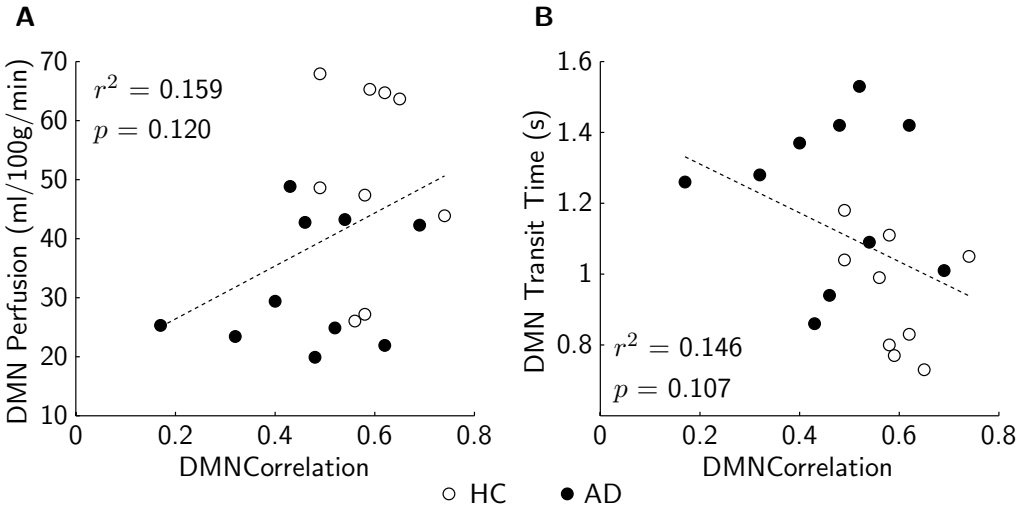


Figure 5.20: Correlation of functional connectivity within the DMN with (A) grey matter perfusion, (B) grey matter transit time.

5.6 Discussion

5.6.1 Clinical Scores

A significant reduction in MMSE scores was found in the AD group (22.5 ± 6.4) compared to the HC group (29.6 ± 0.8). As the average AD duration was 3.0 ± 2.0 years, a reduction in MMSE score was expected in the AD group. A significant negative correlation was found between MMSE and disease duration, with the MMSE score decreasing on average by 2.6 per year. Although a significant linear decline was found in this work, the decline of MMSE is thought to be non-linear [139], with the initial drop in MMSE occurring years before a clinical diagnosis (Figure 5.21). In this study, there was not sufficient subject numbers.

5.6.2 Arterial Spin Labelling

A significant reduction in grey matter perfusion was found in the AD group compared to the HC group. This agrees with much of the literature on perfusion differences measured using ASL [10–13, 15, 17]. One feature to notice is the wide spread of grey matter perfusion in the HC group compared to the AD group. There is an intrinsic degree of variability of grey matter perfusion within a healthy population, however in the case of AD there are continuous physiological effects reducing perfusion and narrowing the spread.

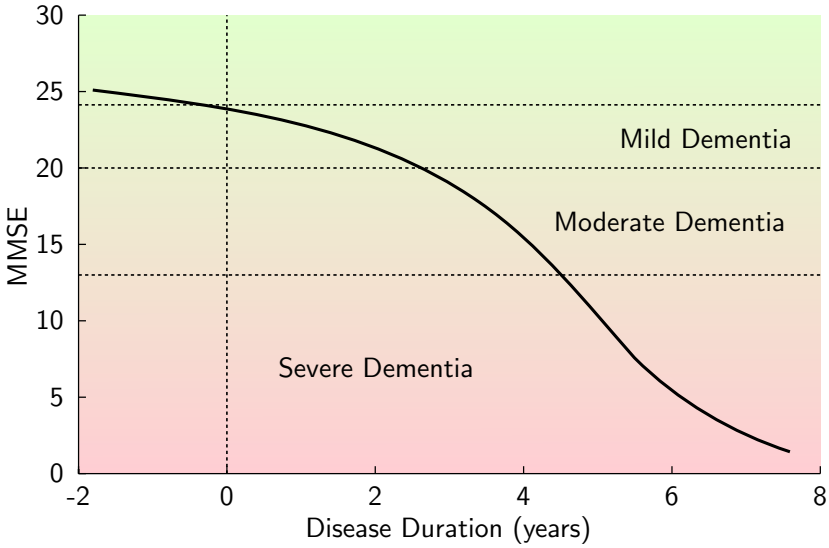


Figure 5.21: MMSE decline of patients with Alzheimer's disease as described by *Ashford et al., (1995)* [139].

When comparing transit time between the two groups, it was found that the AD group had a significantly longer transit time compared to the HC group. Previous publications have only assessed arterial transit time [115] when using ASL, making this the first study to assess tissue transit time using arterial spin labelling in AD. The significant increase in transit time in the AD group supports the findings of the reduction in perfusion into the AD group. The spread of the transit times in the AD group is noticeably larger than that of the HC group, with an inverse relationship between perfusion and transit time. This suggests that the physiological effect which reduces the spread of perfusion increases the spread of transit times.

This coupled nature of perfusion and transit time demonstrated here reinforces the importance of using multiple post-label delays during ASL acquisitions, as assuming a fixed transit time (as seen in previous literature) can artificially bias the perfusion between groups with significantly altered transit times. In the case of AD where transit times are prolonged, using a shorter transit time typical of healthy controls when fitting for perfusion will artificially cause a perfusion deficit.

On dividing the brain into 26 viable cortical regions to assess grey matter perfusion changes, 13 regions showed a significant reduction in perfusion in the AD group. The remaining 13 regions also demonstrated a reduction, however

this reduction was not statistically significant. This does, however, indicate that grey matter perfusion is globally reduced and not isolated to specific cortical regions, as described by *Asllani et al., (2009)* [13]. The precuneus demonstrated a significant reduction in the AD group compared to the HC group, which appears in the literature as the most common and robust area to detect perfusion deficits. The voxel-by-voxel paired two-tailed t-test on the perfusion and transit time maps also highlights the PCC as an area of significant difference. This further reinforces the use of absolute perfusion in the PCC as a biomarker to AD, as described by *Sierra-Marcos et al., (2017)* [140].

5.6.3 Structural Measures

A significant reduction in relative grey matter (total grey matter volume normalised to total intracranial volume) was found in the AD group compared to the HC group across the whole head. This is expected due to the acknowledged atrophy which occurs with AD, eroding the cortical grey matter, hippocampus and ventricular enlargement.

On comparing the cortical thickness between the groups, no significant differences were found. The cortical thickness was normalised to total intracranial volume to remove the effect of head size, assuming that a larger brain will have a larger cortical thickness. Once this normalisation was performed, a significant reduction was observed in cortical thickness in the AD group compared to the HC group. This effect is expected due to the atrophy which occurs with disease progression. However, the spread of normalised cortical thicknesses is much larger in the AD group compared to the HC group. This can be explained when the normalised cortical thickness is assessed with disease duration. A significant correlation between disease duration and normalised cortical thickness was found, suggesting that the cortex shrinks progressively with disease duration, as described in the literature.

Voxel based morphometry (VBM) was also performed on grey matter structures. There were significant changes in grey matter structures in the AD group compared to the HC group, notably within the occipital, temporal and parietal lobes. However, the effect of atrophy seems to be less severe in the frontal lobe. *Pini et al., (2016)* [141] describes the topological trajectory of

atrophy in AD, beginning with the hippocampus and extending into the cortex, where between 10-20% volume was lost in the medial temporal and posterior cingulate regions. Only later does the atrophy extend to the frontal areas as AD progresses. As the average disease duration in this study was 3.0 ± 2.4 years, the atrophy may not have extended to the frontal lobe in this time, explaining why the atrophy appears less severe.

5.6.4 fMRI

When the voxel-wise correlation between the PCC template signal and the DMN regions (PCC, mPFC, LIPL and RIPL) was considered, a reduction in correlation was seen in the AD group compared the HC group in all areas of the DMN. However, only the mPFC demonstrated a significant reduction. This reduction can be interpreted as a disruption of the connectivity between the DMN regions, in agreement with the majority of the literature.

The fMRI data was also assessed using FSL dual regression [136,137] to spatially and temporally regress networks found using a group ICA approach, and assess group differences using permutation methods. The permutation test revealed no areas of significant change between the AD group and the HC in any of the 30 extracted networks. Although dual regression has been used to assess group differences in networks successfully in [19], the sample size was significantly larger (39 AD patients and 43 healthy controls), compared to the number of available datasets in this study (12 AD patients and 10 HCs).

The small number of subjects in both groups is problematic when dealing with functional MRI data. In task based experiments, *Thirion et al., (2007)* [142] reports that 20-25 subjects are required to achieve reliable results. The number of subjects needed to achieve reliable results in resting state fMRI data has not yet been addressed, but it is likely more subjects are needed than in task based experiments. In addition to the number of subjects, the length of the acquisition is also a consideration. Reliability of fMRI has been shown to increase with acquisition duration [143], where 12 minutes is reported as an optimum time for intra-session reliability. The combined effects of a small sample size and relatively short fMRI sequence suggests the results should be considered with caution.

It is recommended that physiological noise such as cardiac and respiratory motion

are regressed out, as they can be the source of variance within the BOLD signal [144, 145]. In this data set, these physiological parameters were not recorded and could not be regressed from the BOLD signal. Changes in heart rate and respiratory rate are observed at low frequencies (typically <0.1 Hz), which have been shown to correspond to the BOLD signal within grey matter and tissue near large vessels [146, 147]. This may have affected the results of the dual regression and the connectivity analysis, so care must be taken when interpreting the results as they may not be only representative of functional activity.

5.7 Conclusion

This work in this chapter has studied haemodynamic, functional and structural changes in Alzheimer's Disease compared to healthy age-matched volunteers. It was demonstrated that perfusion alterations occur in the grey matter in Alzheimer's Disease, as assessed using arterial spin labelling at 7T. Also a significant loss of grey matter was detected in AD, which manifests as cortical thinning. A trend indicating a reduction in functional connectivity with the DMN was found, but it was not significant.

6 Huntington's Disease

6.1 Outline

In this Chapter, the pathology of Huntington's Disease (HD) is described and relevant studies using MRI to investigate HD are summarised. The rationale for assessing vascular and perfusion changes in HD is described, followed by the MR acquisition and processing pipelines used to obtain physiological parameters. Measures are compared between patients with HD and healthy controls (HC), and the group differences are compared to literature.

The work presented in this Chapter was presented as an electronic poster at the 24th Annual Meeting of the International Society for Magnetic Resonance in Medicine (2017), where it was awarded a Summa Cum Laude award. A component of the results from this analysis is published in *Drouin-Ouellet et al., (2015)* [148].

6.2 Introduction

Huntington's Disease (HD) is an autosomal-dominant neurodegenerative disease affecting approximately 5 in every 100,000 people [149], and is prominent in the Caucasian population. The age of onset is generally between 35-44 years [150], with a duration of 17-30 years.

HD presents with both psychological and physical symptoms. The early cognitive symptoms of HD are apathy, anxiety, irritability, and difficulty planning, while physical symptoms present as subtle changes in eye motion and small involuntary movements. During the intermediate stages, chorea (quick involuntary muscle movement in the hands and feet) becomes more prominent, and voluntary movement becomes increasingly difficult. Dysarthria (slow and slurred speech) also develops along with dysphagia (difficulty swallowing), these symptoms usually lead to the patient retiring. The distinctive cognitive traits at this stage are stubbornness and outbursts of aggression. In the later stages of the disease, patients often lose their ability to walk and speak. Symptoms progressively worsen until the patient is no longer able to care for themselves,

particularly problematic is the dysphagia which poses a severe risk of choking.

There is currently no medication to stop, reverse or slow the effects of HD. However, medication can be given to manage the symptoms. Antipsychotics are most commonly used to suppress the chorea, and antidepressants to help improve mood swings. Speech therapy is also commonly used to help counter the dysarthria and enable patients to communicate on a day-to-day basis. There is also recent evidence supporting the role of regular exercise in improving physical health [151].

6.2.1 Pathology

Huntington's Disease is a rare autosomal dominant neurodegenerative disease, whereby a repeated base sequence of DNA causes the over-formation of an abnormal protein. The affected gene is Huntingtin (HTT), which resides in chromosome 4. This gene contains a triple of CAG (cytosine, adenine, guanine), which typically repeats itself 10-35 times in healthy people. However in HD this triplet repeats itself 36 or more times. The CAG repeat codes for the amino acid Glutamine, which means that people with HD will have a huntingtin protein containing 36 or more glutamines in a row. For this reason, HD is often also known as a polyglutamine disorder. The reason why the abnormal huntingtin protein causes the observable symptoms in HD is not fully understood. However, it is observed that the huntingtin protein accumulates in the putamen and caudate nucleus, two grey matter structures within the basal ganglia. Neuronal cell death is subsequently observed in these structures, possibly caused by excitotoxicity leading to high intracellular calcium (Ca^{2+}).

The large amount of CAG repeats does not only lead to the formation of the abnormal huntingtin protein, but also causes issues with DNA replication. The particular effect which occurs during huntingtin protein replication is known as 'repeat expansion'. During the replication of many repeating triplets (such as CAG), the DNA polymerase may unintentionally copy an additional triplet. The more triplet repeats there are, the more often repeat expansion occurs.

There is a 50% chance that the affected gene will be passed on to a child. As

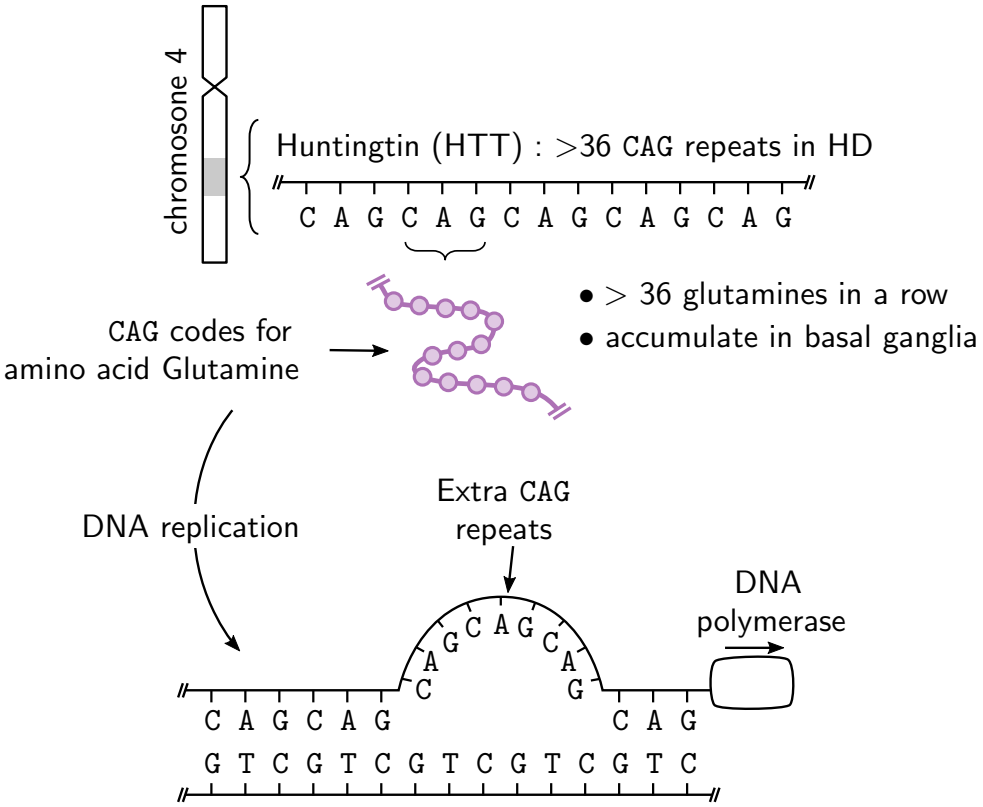


Figure 6.1: Illustration of the effected Huntingtin gene and the effect of repeat expansion during DNA replication.

cell replication begins as early as the zygote, there is a lot of time for additional CAGs to be added through repeat expansion as it develops into a foetus. This means that children may have even more CAG repeats than that of their parents. A larger number of CAG repeats leads the symptoms of HD to present earlier, so successive generations who have inherited the affected gene are diagnosed earlier. This is known as 'anticipation'.

6.2.2 Overview of structural changes in Huntington's Disease

The structural changes which occur due to Huntington's Disease are well studied, with the most consistent change being atrophy of the striatum; a deep grey matter structure consisting of the caudate nucleus and putamen [152–162]. The volume loss of the putamen is severe, with ∼50% reduction in moderate HD cases [160, 161]. The volumetric loss of the caudate is less severe with a volumetric reduction of ∼28% in moderate HD. As progressive atrophy of the striatum occurs, there

is also enlargement of the lateral ventricles. The total volume loss is strongly correlated with clinical measures such as age of onset, disease duration, number of CAG repeats and MMSE score [153, 155–159, 162]. Along with atrophy of the striatum, cortical thinning has also been observed in HD [102, 153, 155–157, 163]. Volumetric loss of the cortex is progressive, with HD initially beginning with loss in posterior regions and propagating towards the anterior regions of the brain [163, 164].

6.2.3 Overview of perfusion studies in Huntington's Disease

The literature regarding cerebral perfusion in HD is sparse [33–37, 165], with only three studies utilising SPECT [33–35], two utilising ASL [36, 37] and one utilising Inflow-based vascular-space-occupancy (iVASO) MRI [165]. The majority of the literature reports a reduction in perfusion in HD patients compared to healthy controls, and this appears to be a global affect.

Ichise et al., (1993) [33] assessed the basal ganglia (BG) perfusion using Technetium-99m-HMPAO SPECT imaging in healthy controls (n=22), subjects at risk of HD (n=20) and early symptomatic HD patients (n=4). Brain perfusion measures of the BG were reported semi-quantitatively, with perfusion being expressed as the ratio between BG and the frontal cortex (FC), cerebral cortical hemispheres (HE) and cerebellum (CE). The ratios were all found to be significantly decreased in the early symptomatic HD group compared to the HC and at risk group, however no significant difference was observed between the HC and at risk group.

Sax et al., (1996) [34] assessed perfusion of the prefrontal cortex, motor cortex, sensory cortices and basal ganglia between healthy controls (n=9) and HD patients (n=29) using Technetium-99m-HMPAO SPECT. Perfusion was reported as a ratio of signal intensity between the ROI and the ipsilateral cerebellar region with greatest tracer uptake. A significant reduction in perfusion was found in all ROIs in the HD group compared the the HC group, where the extent of the perfusion reduction correlated strongly with disease duration and severity of atrophy.

Harris et al., (1999) [35] assessed perfusion within the basal ganglia using Technetium-99m-HMPAO SPECT in HD gene-positive (n=20) and

gene-negative (n=24) patients. Perfusion measures are reported in semi-quantitative units as a ratio of mean brain perfusion. A reduction in perfusion was found in the caudate and putamen of the HD gene-positive group compared to the HD gene-negative group, however only the putamen perfusion difference was significant. No differences were found in the globus pallidus and thalamus.

Wolf et al., (2011) [36] assessed cerebral perfusion using continuous arterial spin labelling (CASL) in a pre-HD group (n=18) and healthy controls (n=18). The mean CBF was very similar between the two groups, however there were significant reductions in perfusion in the pre-HD group in the medial prefrontal cortex, the left dorsolateral prefrontal cortex, and the left superior frontal gyrus.

Chen et al., (2012) [37] assessed cerebral perfusion using pulse arterial spin labelling (PASL) in an early stage HD group (n=17) and gender/age matched healthy controls (n=41). Perfusion in cortical and subcortical ROIs was reduced in the early HD group compared to the healthy controls, this perfusion reduction was not attributed to the severity of atrophy.

Hua et al., (2014) [165] assessed arterial cerebral blood volume (aCBV) using Inflow-based vascular-space-occupancy (iVASO) MRI in prodromal HD patients (n=7) and healthy age matched controls (n=9). It was found that aCBV was increased in the cortex of the HD patients compared to healthy controls.

6.2.4 Overview of vascular changes in Hutnington's Disease

The literature surrounding vascular changes in HD is in its early stages, with only three papers having investigated vascular abnormalities that occur in HD [38–40].

Franciosi et al., (2012) [38] assessed age-dependent neurovascular abnormalities in YAC128 HD mice (n=8) and control mice. The vessels were dyed using collagen IV immunostaining to distinguish vessels from the background tissue. The study reported an increase in vessel density and decrease in vessel diameter in the AC128 mouse model of HD compared to the controls. These vessel abnormalities also correlated with disease duration.

Cisbani et al., (2013) [39] assessed vessel density in post-mortem HD brains and a control brain with no history of neurological disease. Blood vessels were dyed with von Willibrand factor (vWF) for capillaries and α-smooth muscle actin (α-SMA) for larger blood vessels. The HD brains had an decreased number of larger blood vessels compared to the control brain.

Lin et al., (2013) [40] assessed vessel volume fraction in mouse models using 3D microscopic magnetic resonance angiography (3D-μMRA), and vessel size and density in mice models and post-mortem human brains using collagen IV immunostaining. The 3D-μMRA analysis showed an increase in vessel volume fraction and blood volume in the HD mice compared to the control mice. The immunostaining of the mouse brain showed an increase in vessel density compared to the control mouse brain, and a decrease in vessel size in the human HD brain compared to controls.

6.3 Aims and Objectives

A review of current literature regarding the vascular changes in HD [38–40] has demonstrated an increase in vessel density and reduced vessel diameter in HD patients compared to controls. These changes have only been observed in mice models and post-mortem human brains, and have not been observed *in-vivo*. The aim of this study is to investigate vascular abnormalities in the human brain *in-vivo* using phase contrast angiography (PCA) at 7T.

Studies [33–37] have generally reported a decrease in perfusion and an increase in blood volume in HD compared to a HC group. However, these measures cannot be correlated with vascular abnormalities as current methods can only be assessed using post-mortem data. It is unknown if narrowing of blood vessels has an effect on cerebral perfusion. To assess this, arterial spin labelling data will be collected and will be assessed for perfusion and arterial cerebral blood volume, and correlated with vascular data.

6.4 Methods

6.4.1 Participants

9 HD patients (age 56 ± 14 years, 7 males and 2 females) and 9 healthy age matched controls (age 48 ± 14, 7 males and 2 females) were recruited to this study (refer to Table 6.1). All patients were recruited from the HD clinic at the John van Geest Centre for Brain Repair in Cambridge, following ethics approved by the East of England Research Ethics Committee. The healthy controls had no previous history of neurovascular disease.

Healthy Controls			Huntington's Disease			
ID	Age	Gender	ID	Age	Gender	Disease Duration
HC01†	46.0	M	HD01†	44.2	F	Unknown
HC02	54.0	F	HD02	65.2	M	7
HC03	27.6	M	HD03†	26.9	M	6
HC04	24.1	F	HD04†	67.2	M	13
HC05†	46.9	M	HD05†	63.3	M	22
HC06	64.5	M	HD06	50.7	M	11
HC07	60.6	M	HD07	50.7	M	14
HC08	52.6	M	HD08	76.7	M	10
HC09†	63.4	M	HD09	59.7	F	25

Table 6.1: Overview of age and gender of healthy controls and Huntington's Disease (HD) patients assessed in this study. Disease duration is also reported for the HD patients. † ASL data was discarded due to excessive head motion.

6.4.2 MR Acquisition

All volunteers were scanned on a 7T Philips Achieva scanner with a Nova Medical 1TX/32RX head coil.

6.4.2.1 Structural Data Acquisition

Structural data was acquired using a PSIR (phase sensitive inversion recovery) scheme with a turbo field echo (TFE) readout as described by *Mougin et al., (2016)* [127] (resolution = 0.8×0.8×0.8 mm, FOV (AP,RL,FH) = 200×178×120 mm, SENSE factor (AP,RL,FH) = 2, 1, 2, 150 contiguous slices, AP readout direction, radial phase encoding in RL and FH directions, flip angle = 8^o, TE/TR = 4.7/10 ms, acquisition time 7 minutes 5 seconds). The inversion is performed using a tailored adiabatic inversion pulse [128] to minimise effects of B_1 inhomogeneities. Two TFE readouts are performed following the inversion pulse at TI_1 = 780ms and TI_2 = 2380 ms. TI_1 is chosen to acquire data when the grey matter and white matter signals are equal but opposite, causing any voxels containing equal amounts of grey matter and white matter to produce no signal. This produces a distinct boundary between grey matter and white matter. The coverage of the PSIR was of the entire cortex, but did not generally extend low enough to acquire the entire cerebellum (Figure 6.2).

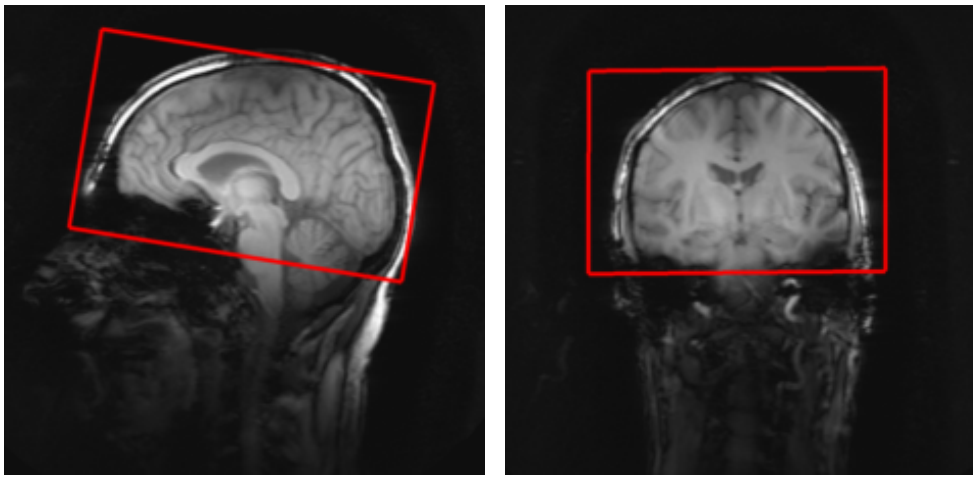


Figure 6.2: The imaging volume of the PSIR acquisition overlaid onto a volunteer's survey scan.

6.4.2.2 Arterial Spin Labelling Data Acquisition

Two ASL acquisition schemes were used in this study; a single-PLD approach to assess perfusion (CBF) and a multi-PLD approach to assess arterial cerebral blood volume (aCBV). ASL data to assess perfusion were collected using a FAIR

Post-label Delay (ms)	Resolution (mm)	Slices	BGS times (ms)	Averages
300	2.7×2.7×3	10	N/A	10
600	2.7×2.7×3	10	100, 350	10
900	2.7×2.7×3	10	300, 650	10
1200	2.7×2.7×3	10	400, 900	10
1500	2.7×2.7×3	10	400, 1070	50
1700	2.7×2.7×3	10	400, 1150	50
2000	2.7×2.7×3	10	400, 1150	50

Table 6.2: Table of ASL parameters for each post-label delay.

labelling scheme with a 2D EPI readout (FOV(AP,RL,FH) = 216×192×30 mm, selective/non-selective thickness = 50/300mm, TE = 24 ms, flip angle = 90^o, TR = 3 s, SENSE factor 2 in AP direction, WET pre- and post-saturation pulses, background suppressed (BS), contiguous slices. ASL data were collected at post-label delays of 300, 600, 900, 1200, 1500, 1700 and 2000 ms). The number of ASL averages was lower for the early post-label delays (300, 600, 900 and 1200 ms) at 10 label/control pairs compared to the later post-label delays (1500, 1700 and 2000 ms) which had 50 label/control pairs. An overview of these parameters can be found in Table 6.2. The placement of the ASL imaging volume was centred on the striatum as illustrated in Figure 6.3.A. The shim box was positioned to cover the imaging volume extending towards the neck in order to achieve a homogenous B_0 field and thus good inversion of the labelled blood. The temporal slice gap of the ten 2D-EPI slices was 65 ms and this was accounted for in the perfusion fit. Note that a significant amount of decay of the blood label will have occurred if a long post-label delay and a large number of slices is used.

ASL data to assess aCBV were collected using a FAIR labelling scheme using a 2D-EPI readout (FOV(AP,RL,FH) = 216×192×3 mm, selective/non-selective thickness = 29/300mm, TE = 24 ms, flip angle = 90^o, TR = 3 s, SENSE factor 2 in AP direction, WET pre- and post-saturation pulses. ASL data were collected using a multi-PLD or Look-Locker (LL) readout scheme with 21 image readouts at an interval of 100ms with an initial delay of 150ms). In order to assess arterial cerebral blood volume, many early post label delays must be acquired as discussed in Section 4.2.5.3. The short PLD intervals of 100ms used in the aCBV acquisition

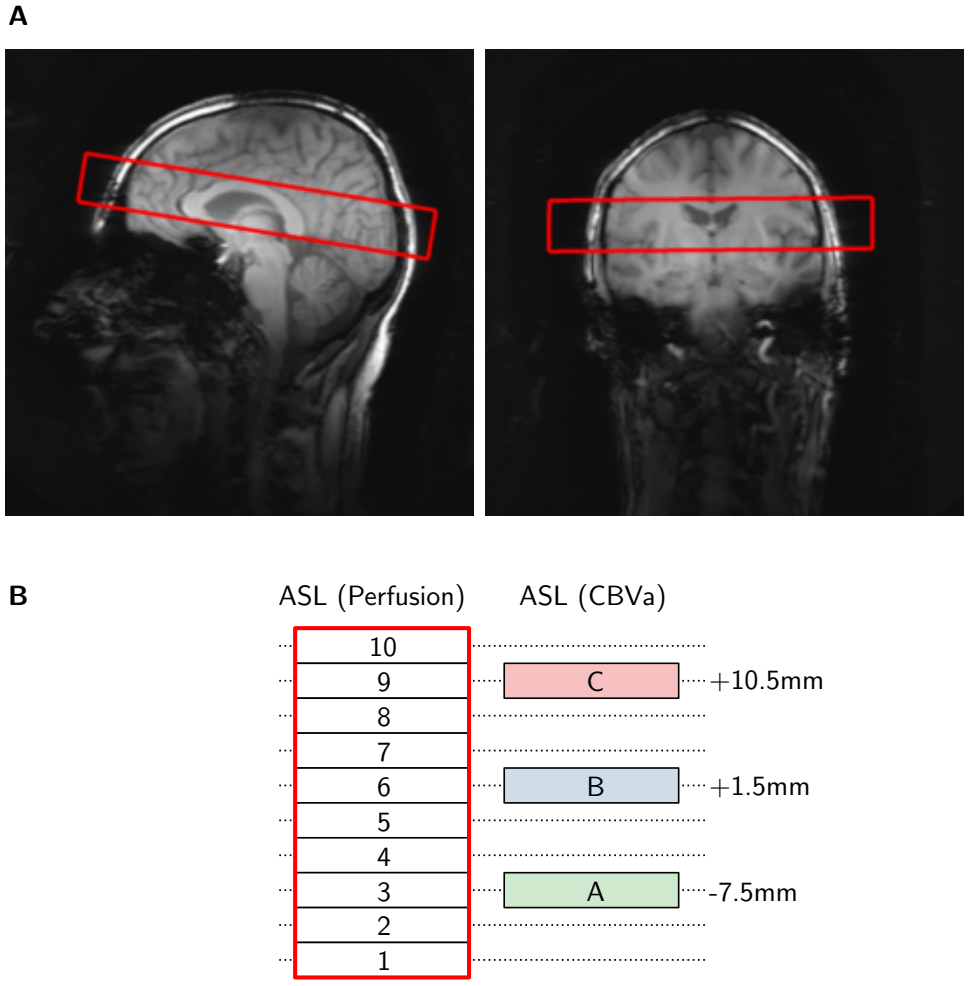


Figure 6.3: A. Sagittal and coronal views of the perfusion ASL imaging volume overlaid on an anatomical image. The imaging volume is centred on the striatum. B. The slice alignment between the perfusion ASL acquisition and the aCBV ASL acquisition, labelled as A, B and C.

limits the scheme to a single slice acquisition, as the time required to acquire a single slice is 65ms. In order to obtain representative coverage, the aCBV acquisition was repeated three times at different FH positions to align with given slices in the perfusion ASL acquisition (-7.5, +1.5 and +10.5 mm from the centre of the perfusion ASL imaging volume). The slice alignment of the CBF and aCBV acquisitions is illustrated in Figure 6.3B.

An associated inversion recovery is also acquired using an identical readout scheme. Following the initial inversion, readouts are acquired at 100, 200, 300, 500, 1000, 1300, 1700, 2000, 2500 and 3000 ms. This will be used during the

CBF and aCBV quantification.

6.4.2.3 Phase Contrast Angiography Data Acquisition

PCA data were collected using a 3D gradient echo readout (resolution = 0.6×0.6×0.6 mm, FOV(AP,RL,FH) = 230×170×60 mm, SENSE factor(AP,RL,FH) = 1, 1.4, 1, 100 contiguous slices, TE/TR = 11/19 ms, flip angle = 7^o, partial Fourier fraction = 0.625, velocity encoding(AP,RL,FH) = 5, 5, 5 cm/s). The imaging volume was centred around the striatum (Figure 6.4). The images obtained from the PCA scheme are a base image and a vessel image, seen in Figure 6.5. The vessel image is the difference between two modulus images with flow compensation on and off, such that the only difference is due to moving spins.

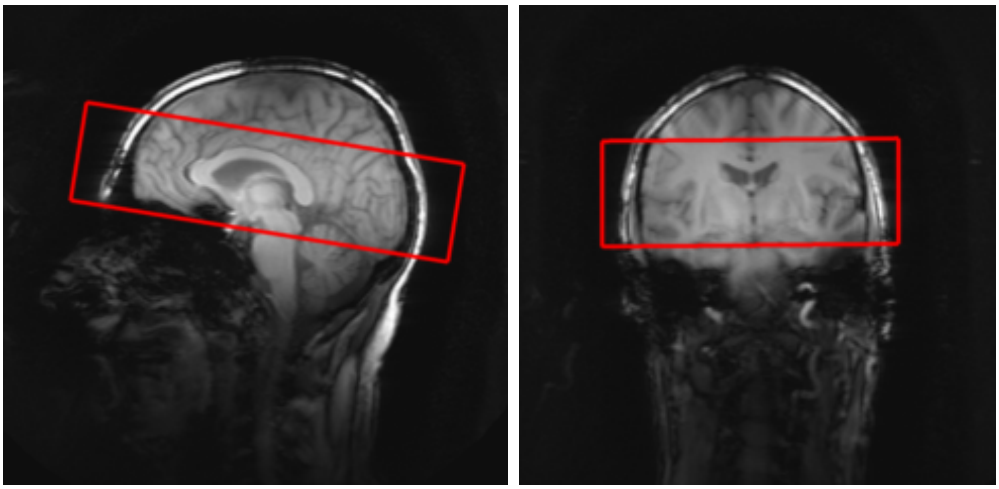


Figure 6.4: Sagittal and coronal view of the phase contrast angiography imaging volume overlaid on an anatomical image.

6.4.3 Data Processing

6.4.3.1 Structural Data

Structural data was processed according to the pipeline described in Chapter 5, Figure 5.4 as detailed in Section 5.4.3.1. To recap, the phase difference between the two acquired phase images was found and used to correct the sign of the first acquired modulus image. The bias field was estimated by summing the two

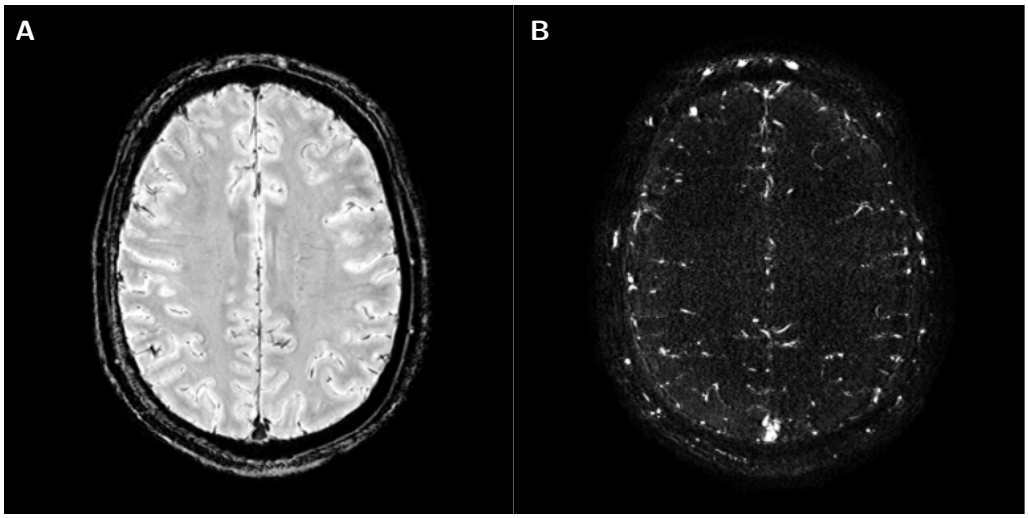


Figure 6.5: Images obtained from the phase contrast angiography; (A) base image, (B) vessel image.

modulus images and smoothing using a large Gaussian kernel, which was then used to normalise the acquired signals.

Brain extraction was performed on the second modulus image using FSL BET, and then applied to the reconstructed PSIR image. Before further processing, the cerebellum was removed from the reconstructed image, as varying amounts of coverage of the cerebellum are acquired from each volunteer, influenced by subject head size. This was performed by computing a mask of the cerebellum for each volunteer by first co-registering the reconstructed PSIR to MNI space using FNIRT. The inverse warp transform was then found and applied to a mask of the cerebellum, cortex and ventricles in MNI space using nearest neighbour interpolation to obtain a mask of these structures on native space. Masks of the caudate and putamen were created using manual segmentation in PSIR space using MIPAV (Medical Imaging Processing Analysis and Visualisation, CIT, NIH, Bethesda).

The Computational Anatomy Toolbox 12 (CAT12) was then used to spatially normalise the reconstructed PSIR images and segment them into grey matter, white matter and CSF. The absolute and relative volumes of these tissue types were estimated, along with total intracranial volume and mean cortical thickness. VBM (voxel base morphometry) was performed on the grey matter using SPM12, with cortical thickness and total intracranial volume used as covariates.

6.4.3.2 Arterial Spin Labelling Data

The ASL pre-processing used for both single-PLD and multi-PLD followed the same pipeline as described in Figure 6.6. Label 1 of the non-selective condition for each PLD was averaged over all repeats. These were then all co-registered to the PLD which occurred at the centre of the entire ASL acquisition (1700ms). The transformation matrices describing this co-registration were then applied in conjunction with the motion correction parameters such that only one transform was applied to the labels. Each application of an affine transformation causes the image to blur due to interpolation effects, so minimising the number of transforms applied is important. Motion correction was performed using the FSL MCFLIRT algorithm, whereby both label 1 and label 2 are concatenated in the fourth dimension and the central repeat of label 1 is used as the reference. Despite the slightly different contrast of label 1 and label 2 due to the blood label, this method was found to out perform motion correcting each label individually. The transformation matrices needed to motion correct each repeat were decomposed to determine the amount of translation and rotation which was applied. If the translation required to motion correct a volume exceeded one voxel (3mm), the repeat was discarded. The image was split back into label 1 and label 2 formats before brain extraction was performed using FSL BET. A perfusion weighted image (PWI) was then created by computing the difference between label 1 and label 2 using simple pairwise subtraction. Using the method described by *Tan et al., (2009)* [72], each repeat of the PWI was assessed to determine if it was an outlier. The PWI was then averaged over all repeats to create a final perfusion weighted image for each PLD. All PLDs are concatenated in the fourth dimension and calibrated for $M_{0,b}$.

The multi-PLD data were fitted to the model described by *Francis et al., (2008)* [63] to compute the cerebral arterial blood volume. The single-PLD data was quantified for perfusion using FSL BASIL [131]. Following the perfusion quantification, partial volume correction was performed using the method described by *Asllani et al., (2008)* [74]. Partial volume maps for grey matter, white matter and CSF were obtained from segmenting the fitted T_1 map (described in Section 6.4.3.3). The partial volume maps were used in order to

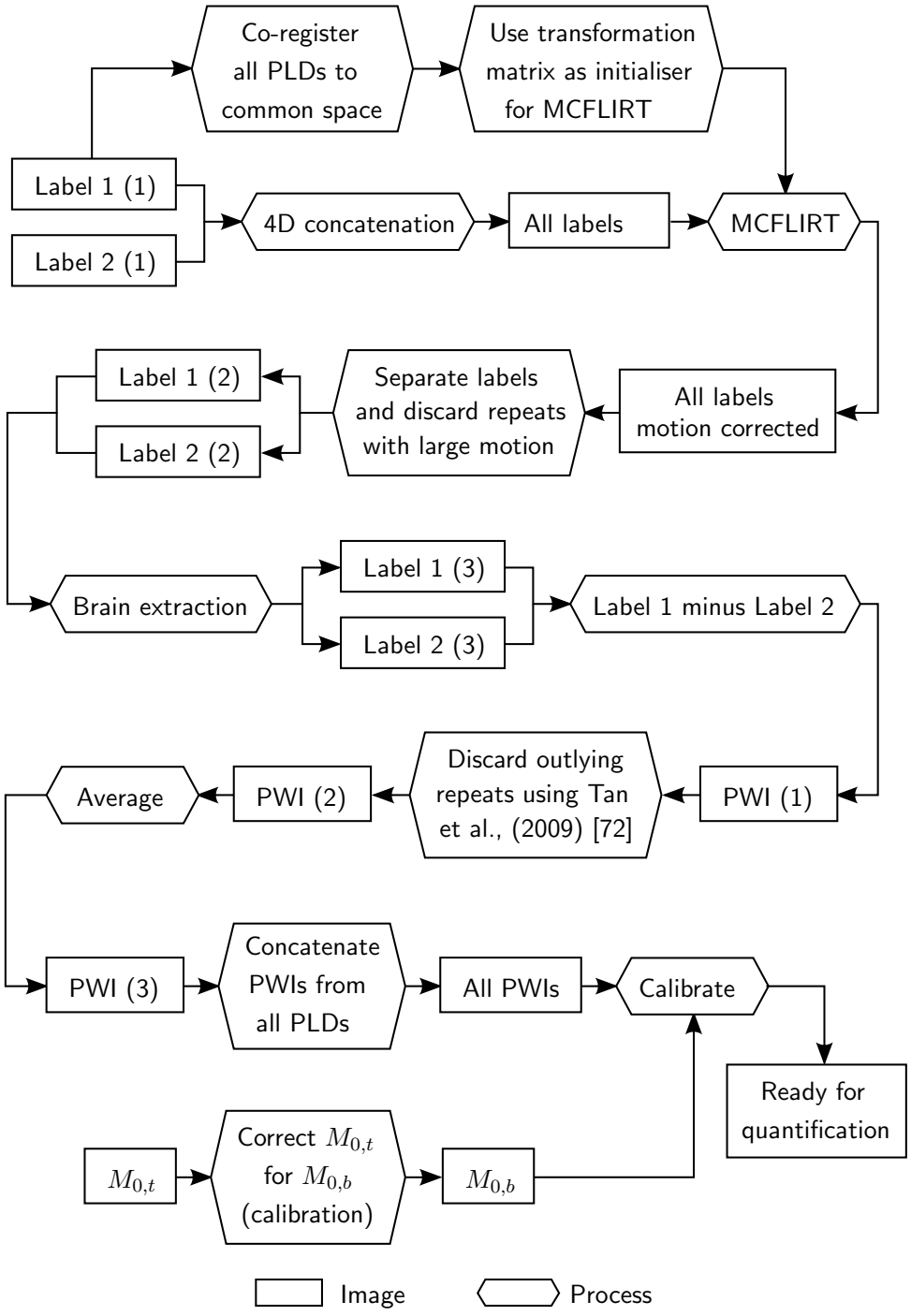


Figure 6.6: ASL preprocessing pipeline used to prepare the single-PLD and multi-PLD data for quantification.

spatially and linearly regress the contribution of each tissue type to perfusion. A spherical neighbourhood with a radius of 3 voxels was used to partial volume correct each voxel. Perfusion, transit time and aCBV were assessed in the grey matter, caudate and putamen.

6.4.3.3 Inversion Recovery Data

The inversion recovery (IR) data was fit for M_0, α and T_1 on a voxel-wise basis using

$$IR(t) = M_0 \left(1 - 2\alpha e^{-t/T_1}\right) \tag{6.1}$$

where M_0 is the equilibrium magnetisation, α is the inversion efficiency of the label and T_1 is the longitudinal relaxation. In order to reduce the occurrence of a poor fit, the acquired IR curves for each voxel were compared to a look-up-table (LUT) of simulated recoveries. The simulated inversion recoveries were calculated for each slice taking into account the temporal slice gap (65 ms). The parameters giving the smallest sum of square differences were used as the initial search parameters. This improved the quality of the fit as T_1 values in the brain range from 1.13 seconds in the white matter [132] to 4.63 seconds in CSF [133]. The T_1 map was then segmented into grey matter, white matter and CSF using FSL FAST [134].

6.4.3.4 Phase contrast angiography

In order to calculate a distribution of vessel radii from the PCA data, the raw vessel data (Figure 6.7 - PCA (1)) was first bias corrected using SPM8. The B_1 inhomogeneities are severe at ultra-high field, so correcting for this is important to allow for more accurate vessel segmentation at a later point in the processing pipeline. The bias corrected image (Figure 6.7 - PCA (2)) was interpolated up to 0.2 mm isotropic spatial resolution with trilinear interpolation using ImageJ. This produces a more continuous distribution of vessel radii at the end of the pipeline. Brain extraction is then performed on the modulus image and applied to the PCA vessel image (3) to remove large vessels from the surface of the skull. In order to assess vessel properties, the image had to be converted to a binary map where ones represent a vessel volume and zeros represent the background tissue. A spatially adaptive threshold was applied to segment the vessels, as vessel intensities vary across the image despite the bias correction. The spatially adaptive threshold assesses the intensity of every voxel and its neighbouring voxels (within a 3×3×3 neighbourhood). If the central voxel is greater than the mean of the neighbourhood, it is classed as a vessel and

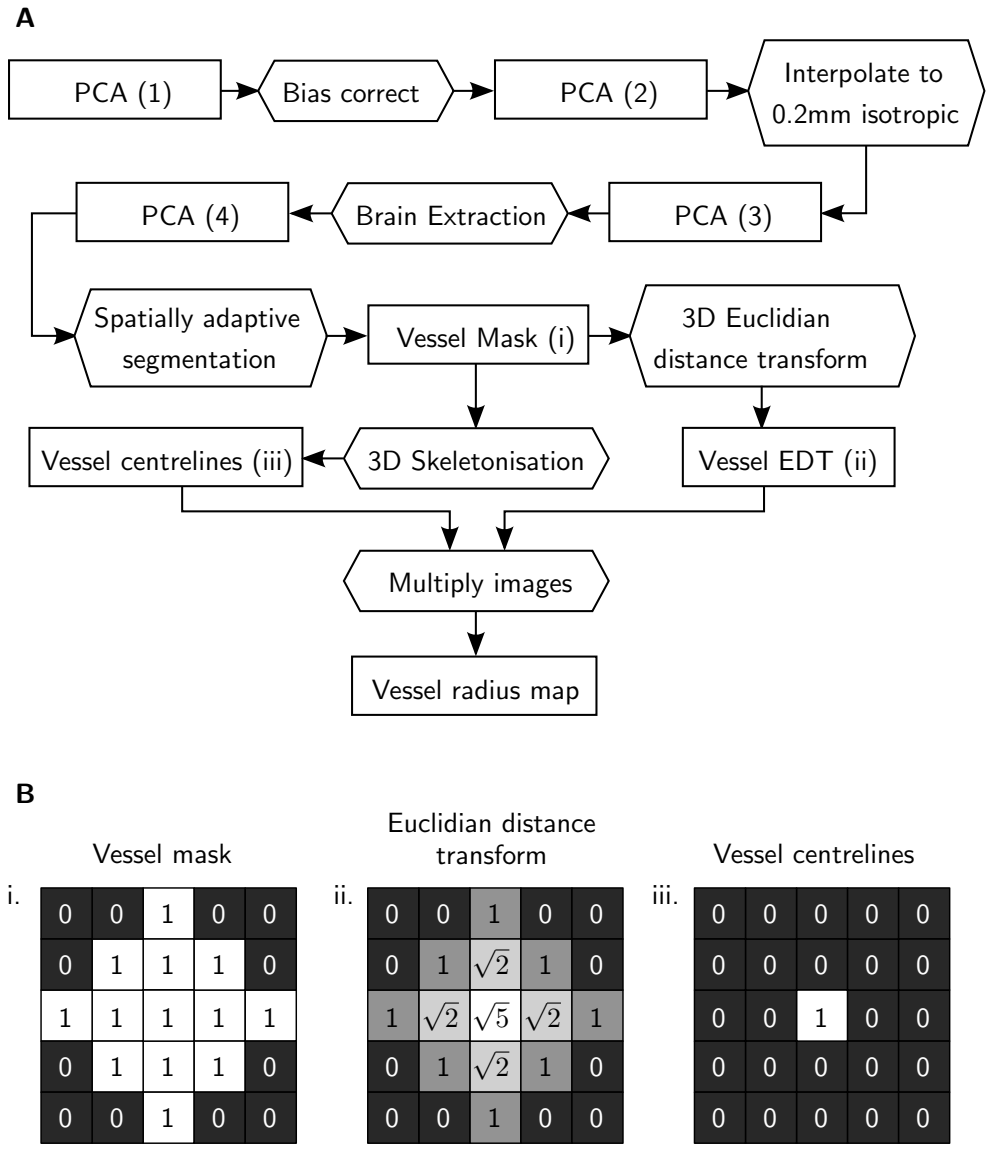


Figure 6.7: (A) The processing pipeline used to assess vessel radii from PCA volumes. (B) i. A 2D illustration of a binary vessel, ii. the effect of the Euclidean distance transform on the vessel mask, iii. the effect of the skeletonsiation of the vessel mask.

labelled with a 1. Once a vessel mask is obtained, two processes were performed; a 3D Euclidean distance transformation (3D-EDT) and a 3D skeletonisation. The 3D-EDT calculates the distance between every voxel labelled with a one, and the closest voxel labelled with a zero (Figure 6.7.B.ii). The 3D-EDT is then multiplied by the voxel size to convert the distance from voxels to millimetres. The 3D skeletonistation iteratively narrows the vessel mask such that every vessel becomes one voxel thick, representing the

centrelines. By multiplying the 3D-EDT with the 3D skeletonisation, all remaining nonzero values are representative of the radii of the vessels. The modulus image is coregistered to MNI space, and the transformation is applied to the vessel radius map using nearest neighbour interpolation. In order to fairly assess the vessel radii between all subjects, a common mask is formed from all overlapping voxels when the modulus image has been transformed into MNI space. The vessel radii are counted and binned into 0.15-0.45mm, 0.45-0.75 mm, 0.75-1.05 mm and 1.35-1.65 mm, and the counts are divided by the total number of voxels to determine their relative frequency.

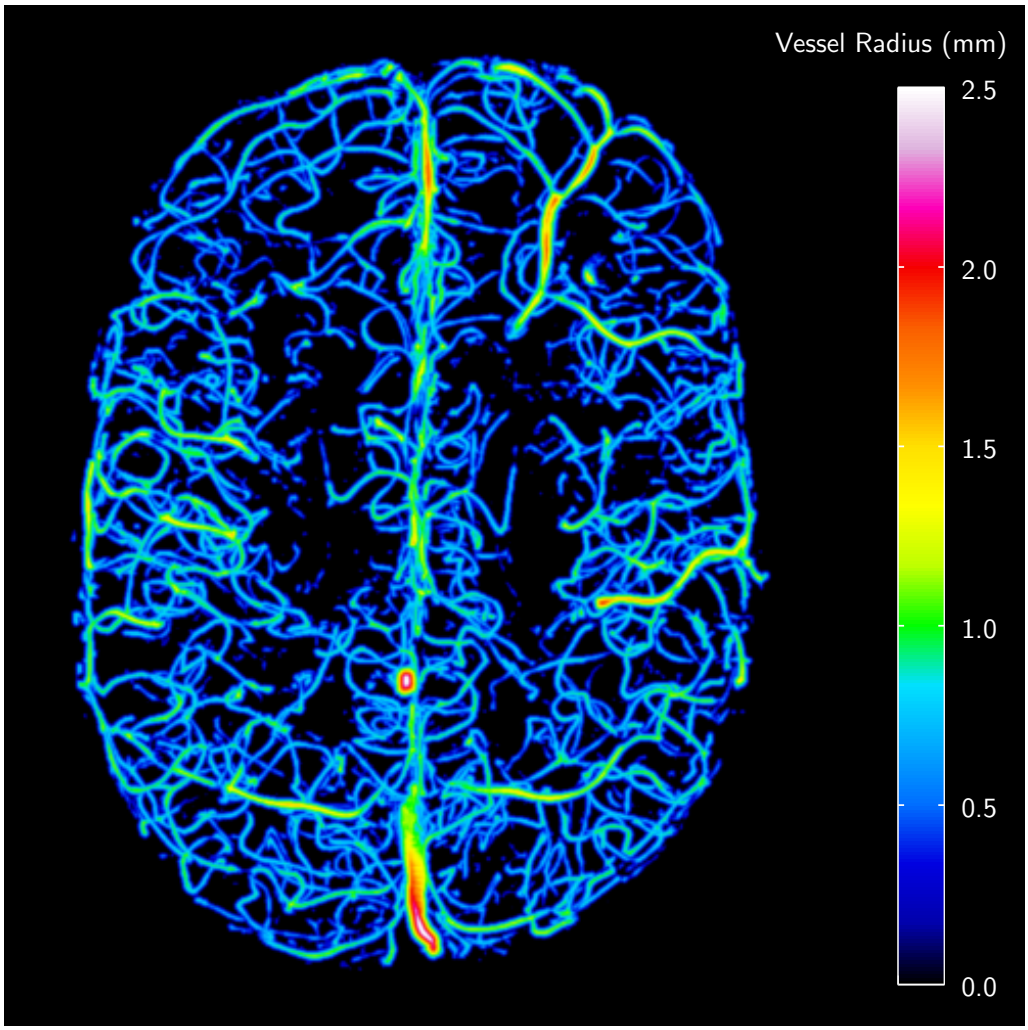


Figure 6.8: The vessel mask following a 3D Euclidean Distance Transform and converted to millimetres, as described in Figure 6.7.A.

As well as assessing vessel radii distributions, the vessel density can also be assessed by counting the number of vessel voxels in the vessel mask and dividing by the volume of the brain. The vessel density was found in 46 cortical regions

as defined by the Harvard-Oxford cortical atlas, however only cortical regions where at least 50% of their volume is covered by the common mask are considered.

6.5 Results

6.5.1 Volunteers

All HD patients were age-matched with healthy controls to within ±6 years. A two-sample unequal variance paired t-test was performed on age to assess the quality of age matching. The age-matching showed no significant difference between the HD and healthy control groups (p=0.81).

6.5.2 Structural

The cortical thickness was significantly reduced in the HD group (2.34±0.17 mm) compared to the HC group (2.53±0.05) ($p = 0.011$). However, when the cortical thickness was normalised to total intracranial volume, there was no significant difference between the two groups ($p = 0.12$).

The absolute and relative grey matter, white matter and CSF volume was assessed between the HD and HC groups (Figure 6.9). It was found that the absolute grey and white matter volume was significantly lower in the HD group compared to the HC group (p=0.012 and p=0.004 respectively), whereas the absolute CSF volume was increased in the HD group compared to HC group (p=0.001). When the relative volumes were assessed (absolute volume normalised to intracranial volume), it was found that the relative grey and white matter volume was significantly lower in the HD group compared to the HC group (p=0.002 and p=0.0008 respectively), whereas the absolute CSF volume was found to be increased in the HD group compared to HC group (p=0.0009).

In order to spatially assess the observed grey matter volumes loss, voxel-based morphometry was performed using TIV and cortical thickness as a covariate. Significant grey matter loss was observed in the striatum (caudate nucleus and putamen), the cuneus and lingual gyrus.

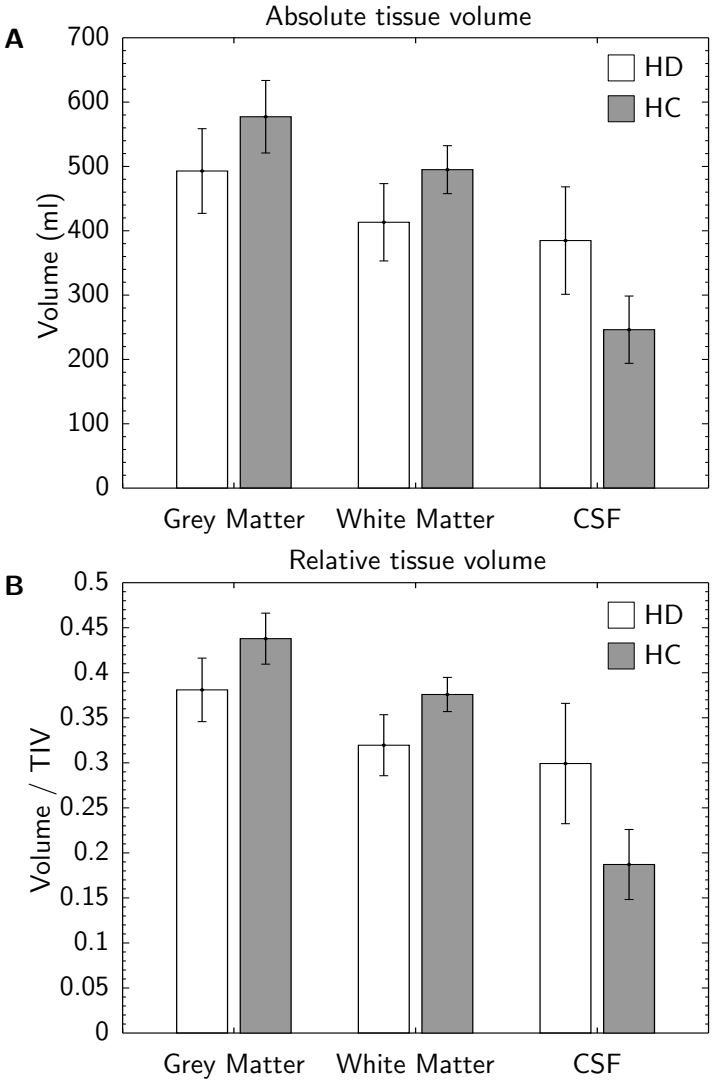


Figure 6.9: (A) Absolute and (B) relative grey matter, white matter and CSF volumes for HD and HC groups. The error bars represent the standard deviation.

It was found that relative grey matter volume negatively correlated with age in both the HC and the HD group ($p = 0.004$ and $p = 0.025$ respectively). In contrast, relative CSF volume positively correlated with age in both the HC and the HD group ($p = 0.0009$ and $p = 0.006$ respectively).

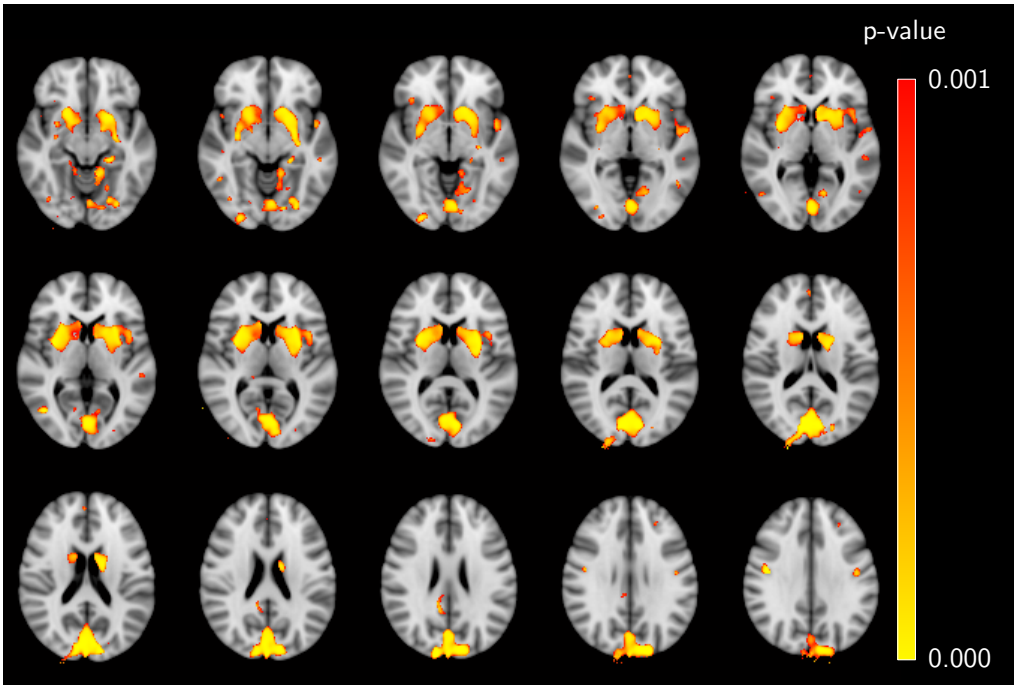


Figure 6.10: Results from voxel-base morphometry performed between HD and HC. The clusters represent a loss of grey matter in the HD group compared to the HC group where $p < 0.001$. The striatum and occipital lobe show significant atrophy in the HD group.

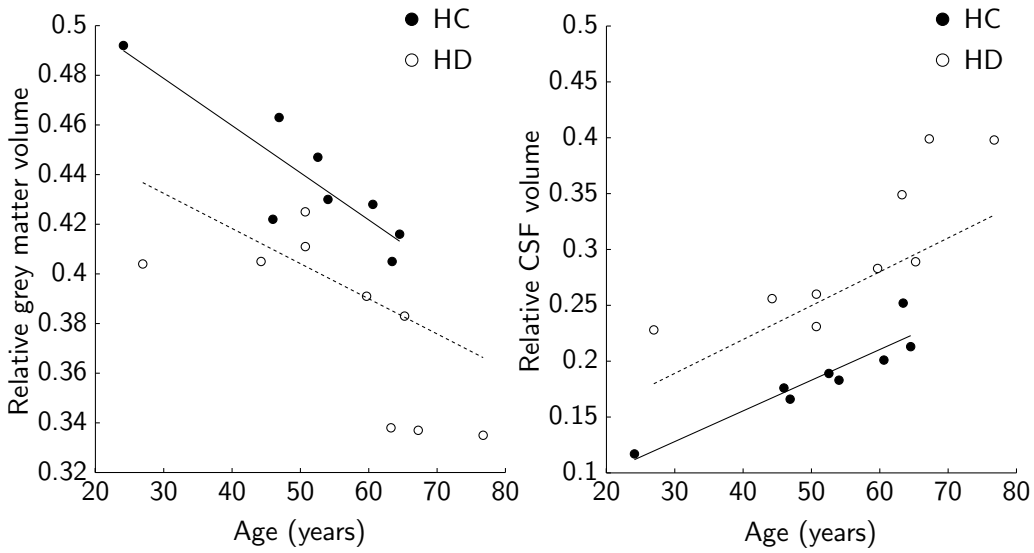


Figure 6.11: The relative (A) grey matter and (B) CSF volume for HD and HC groups as a function of age.

6.5.3 Arterial Spin Labelling

The perfusion within the grey matter, caudate and putamen was assessed within each volunteer using the partial volume corrected perfusion maps. Voxels containing grey matter perfusion were isolated using the grey matter partial volume map from the T_1 segmentation at a threshold of 0.5. The distribution of grey matter perfusion and transit time were all found to be normal using a one-sample Kolmogorov-Smirnov test. All perfusion and transit time maps were transformed into MNI space using the structural image as an intermediate and group maps were created (Figure 6.12 - 6.13). The average grey matter

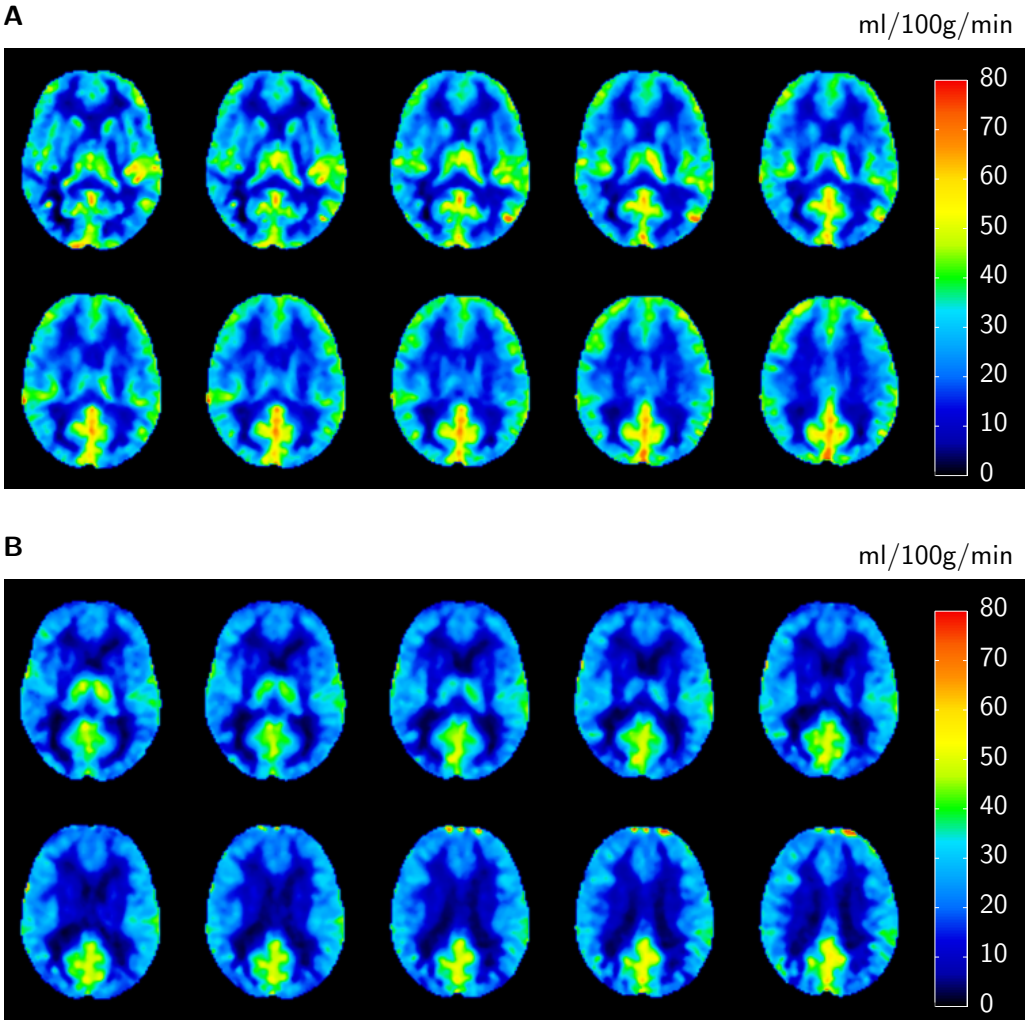


Figure 6.12: Group perfusion maps in MNI space from (A) healthy controls and (B) HD patients.

perfusion was found to be 41.7±6.3 ml/100g/min in the HC group, and 31.1±6.7 ml/100g/min in the HD group. A significant reduction in grey matter

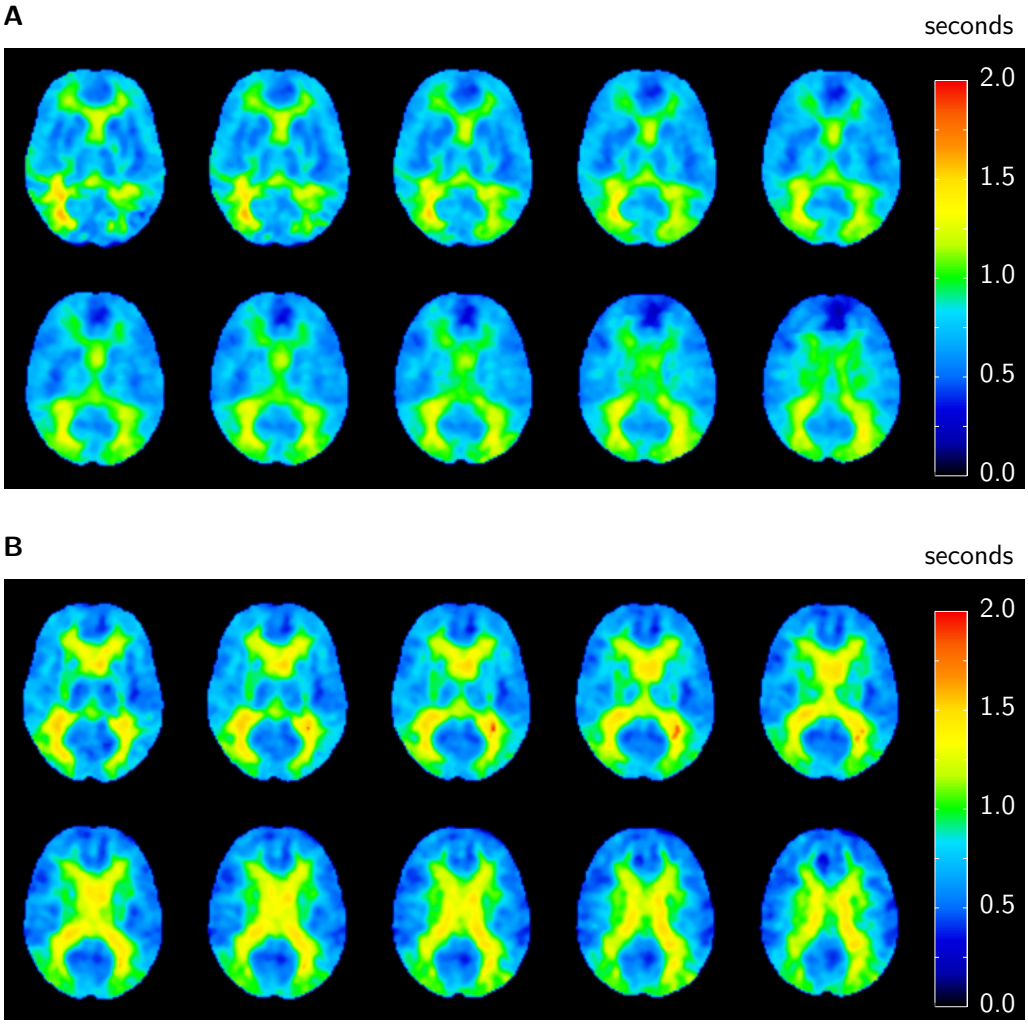


Figure 6.13: Group transit time maps in MNI space from (A) healthy controls and (B) HD patients.

perfusion was found in the HD group compared to the HC group (p=0.027 using a two-tailed unequal variance t-test) (Figure 6.14.A). The average white matter perfusion was found to be 16.2±2.9 ml/100g/min in the HC group, and 16.8±4.5 ml/100g/min in the HD group. No significant difference in white matter perfusion was found between the HD and HC group (p=0.79 using a two-tailed unequal variance t-test) (Figure 6.14.B). The average caudate perfusion was found to be 27.3±1.0 ml/100g/min in the HC group, and 13.6±5.9 ml/100g/min in the HD group. A significant reduction was found in caudate perfusion in the HD group compared to the HC group (p=0.005 using a two-tailed unequal variance t-test) (Figure 6.14.C). The average putamen perfusion was found to be 25.3±2.0 ml/100g/min in the HC group, and 18.2±5.6 ml/100g/min in the HD group. A significant reduction was found in

putamen perfusion in the HD group compared to the HC group (p=0.044 using a two-tailed unequal variance t-test) (Figure 6.14.D). The average grey matter

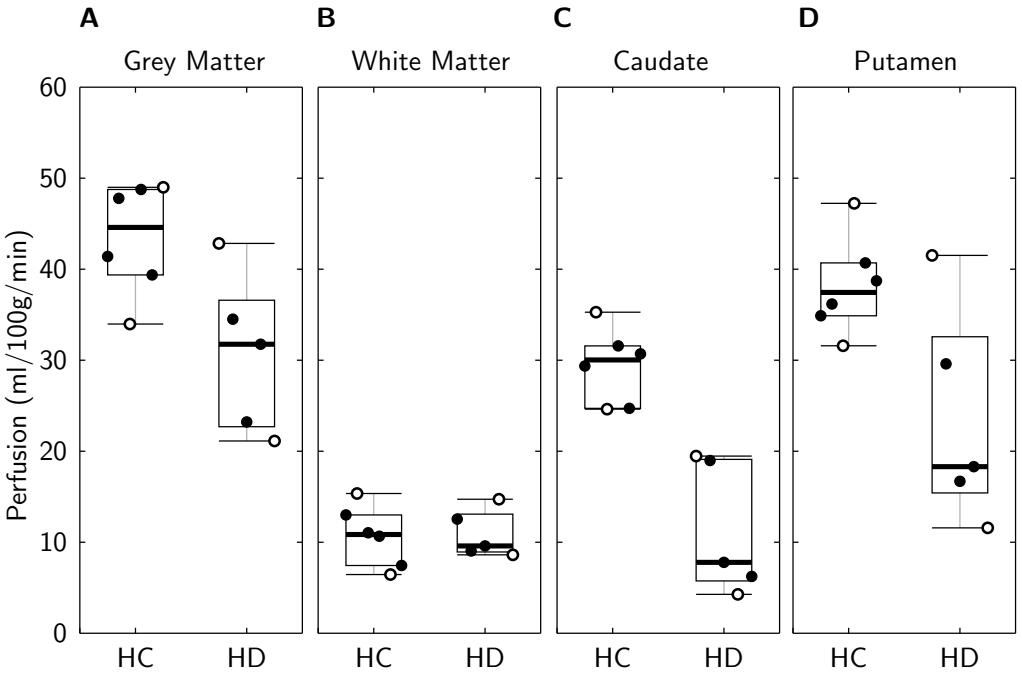


Figure 6.14: Perfusion for the healthy controls and HD patients in the (A) grey matter, (B) white matter, (C) caudate and (D) putamen. Filled circles indicate measures inside the interquartile range, and empty circles indicate measures outside the interquartile range.

transit time was found to be 0.64±0.14 seconds in the HC group, and 0.64±0.09 seconds in the HD group. No significant difference in grey matter transit time was found between the HD and HC group (p=0.98 using a two-tailed unequal variance t-test) (Figure 6.15.A). The average white matter transit time was found to be 0.88±0.24 seconds in the HC group, and 0.91±0.14 seconds in the HD group. No significant difference in white matter transit time was found between the HD and HC group (p=0.92 using a two-tailed unequal variance t-test) (Figure 6.15.B). The average caudate transit time was found to be 0.71±0.20 seconds in the HC group, and 1.01±0.17 seconds in the HD group, with a significant increase in the caudate transit time in the HD group compared to the HC group (p=0.024 using a two-tailed unequal variance t-test) (Figure 6.15.C). The average putamen transit time was found to be 0.58±0.10 seconds in the HC group, and 0.83±0.10 seconds in the HD group. A significant increase in the putamen transit time was found in the HD group compared to

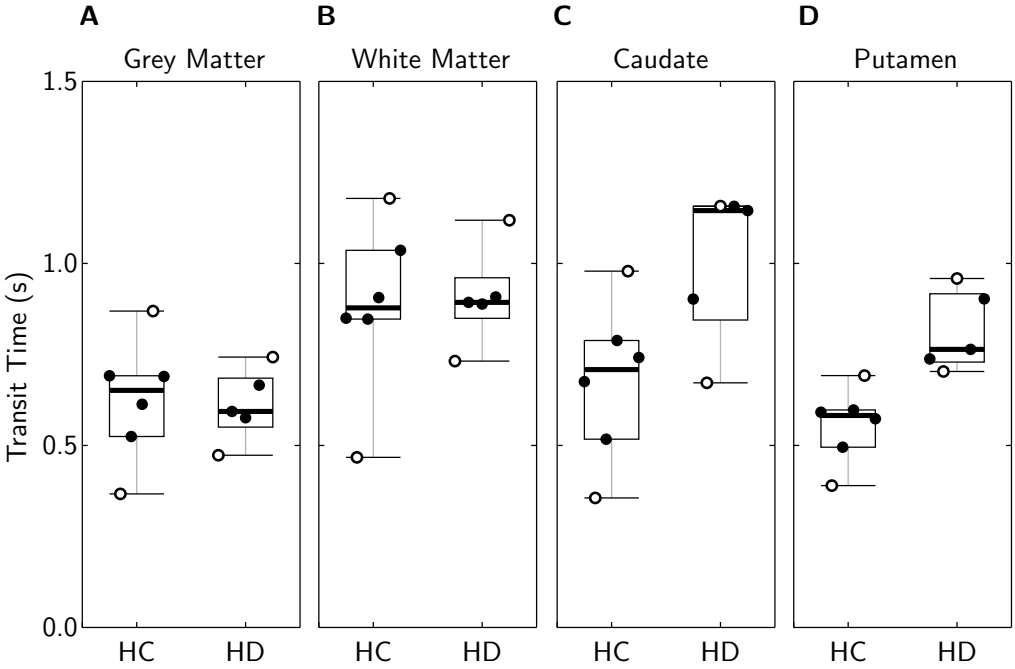


Figure 6.15: Transit time for the healthy controls and HD patients in the (A) grey matter, (B) white matter, (C) caudate and (D) putamen. Filled circles indicate measures inside the interquartile range, and empty circles indicate measures outside the interquartile range.

the HC group (p=0.003 using a two-tailed unequal variance t-test) (Figure 6.15.D). The average grey matter arterial cerebral blood volume was found to be 1.42±0.22 ml/100g in the HC group, and 1.90±0.55 ml/100g in the HD group. A significant increase was found in the grey matter arterial blood volume in the HD group compared to the HC group (p=0.039 using a two-tailed unequal variance t-test) (Figure 6.16.A). The average caudate arterial cerebral blood volume was found to be 0.60±0.18 ml/100g in the HC group, and 0.70±0.19 ml/100g in the HD group. No significant difference in the caudate arterial blood volume was found between the HD group and the HC group (p=0.306 using a two-tailed unequal variance t-test) (Figure 6.16.B). The average putamen arterial cerebral blood volume was found to be 0.70±0.30 ml/100g in the HC group, and 0.96±0.40 ml/100g in the HD group. No significant difference was found in the putamen arterial blood volume was found between the HD group and the HC group (p=0.103 using a two-tailed unequal variance t-test) (Figure 6.16.C).

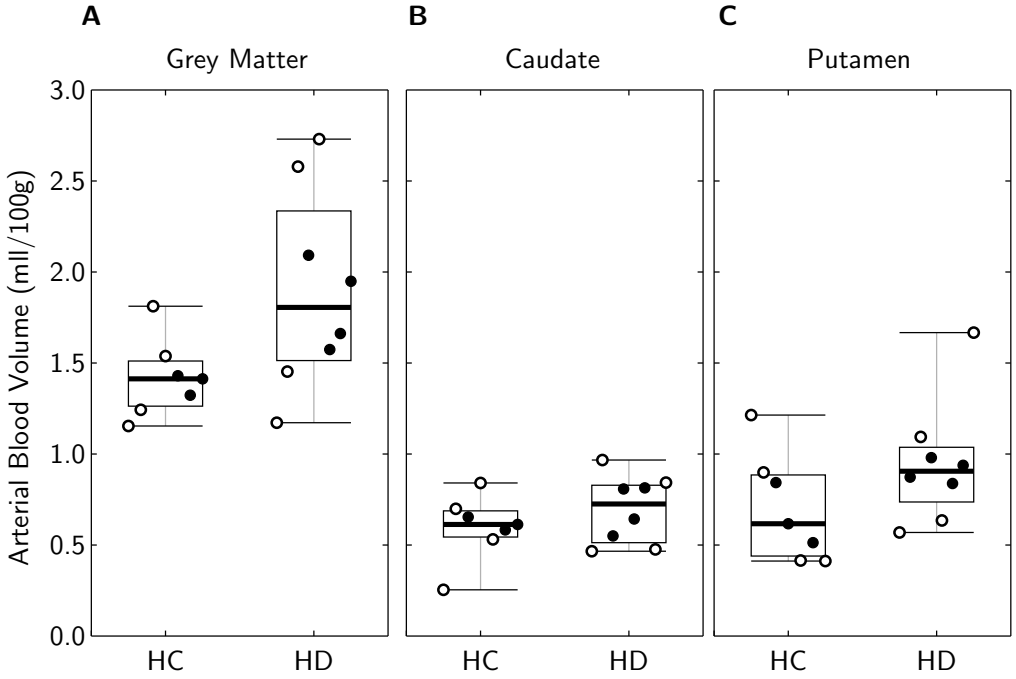


Figure 6.16: Arterial cerebral blood volume for the healthy controls and HD patients in the (A) grey matter, (B) caudate and (C) putamen. Filled circles indicate measures inside the interquartile range, and empty circles indicate measures outside the interquartile range.

6.5.4 Phase contrast angiography

There was a trend for an increased fraction of vessels with small radii (0.15-0.45 mm) in the HD group compared to HCs, and a decreased fraction of vessels with medium radii (0.45-0.75mm and 0.75-1.05mm) in the HD group. Larger radii vessels (>1.05 mm) occurred at the same frequency in both groups (Figure 6.17.A). The difference between the vessel radii frequency for each bin can be seen in Figure 6.17.B. From the 46 cortical regions defined in the Harvard-Oxford atlas, 39 had at least 50% of its volume contained within the PCA data. From these 39 regions, 35 regions showed a significant reduction in volume of 17.2±3.6% (p¡0.001 after correcting for multiple comparisons using the Bonferroni).

In order to assess the validity of this pipeline explained in Section 6.4.3.4, vessels with known radii were simulated with varying amounts of noise, and the pipeline was applied. Vessel were simulated with radii from 0.2 to 4.0 voxels in 0.2 steps, taking into account partial volume effects on the edge (Figure

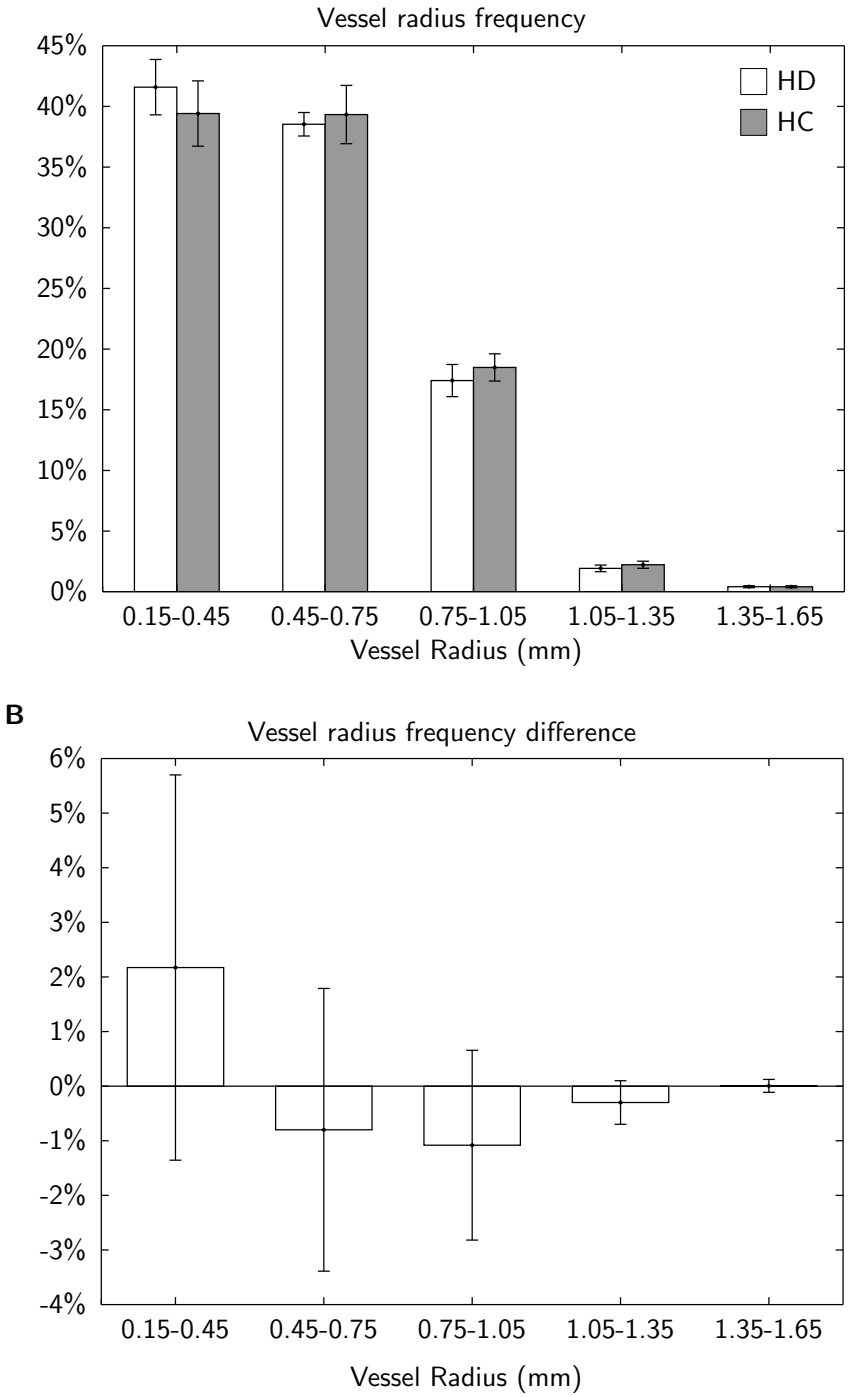


Figure 6.17: (A) The vessel radius frequency distributions in the HD and HC groups. (B) The difference in frequency between the HD group and the HC group.

6.19.A). The vessels were interpolated to 3 times resolution (Figure 6.19.B), followed by an adaptive spatial threshold technque Figure 6.19.C. Finally the Eucledian distance transform was applied (Figure 6.19.D).

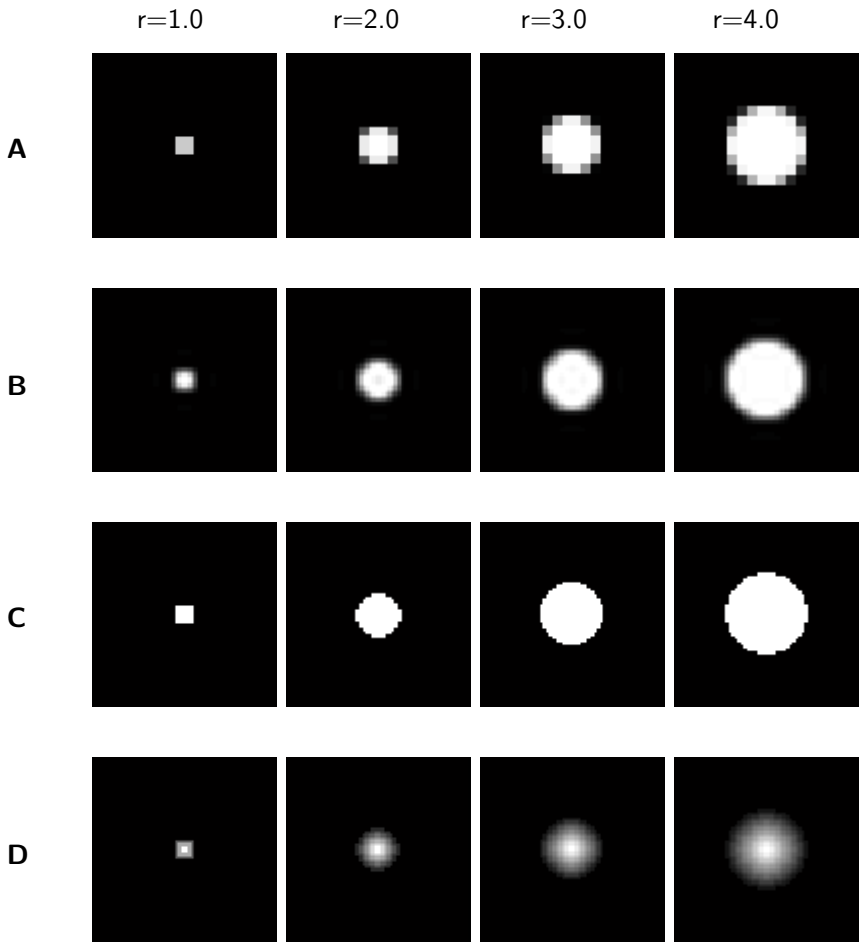


Figure 6.18: Effect of pipeline on simulated vessels. (A) Simulated vessel with radii of 1, 2, 3 and 4 with partial volume effects on the edges. (B) Interpolated to 3 times resolution. (C) Spatially adaptive threshold to binarise vessels. (D) Eucledian distance transform.

The radii were estimated in the presence of Gaussian noise with differing variance (Figure 6.19). In the absence of noise (Figure 6.19.A), the algorithm is capable of detecting estimating vessels with a radii of 0.6 voxels and above, however it fails to detect any vessels below this. As the variance of noise increases the estimation of vessel radii begins to underestimate the true value, which is more significant at larger radii. However, even with added noise vessels with radii of 0.6 voxels or above can still be detected, implying that vessels greater or equal to 0.36mm can be identified in this PCA dataset.

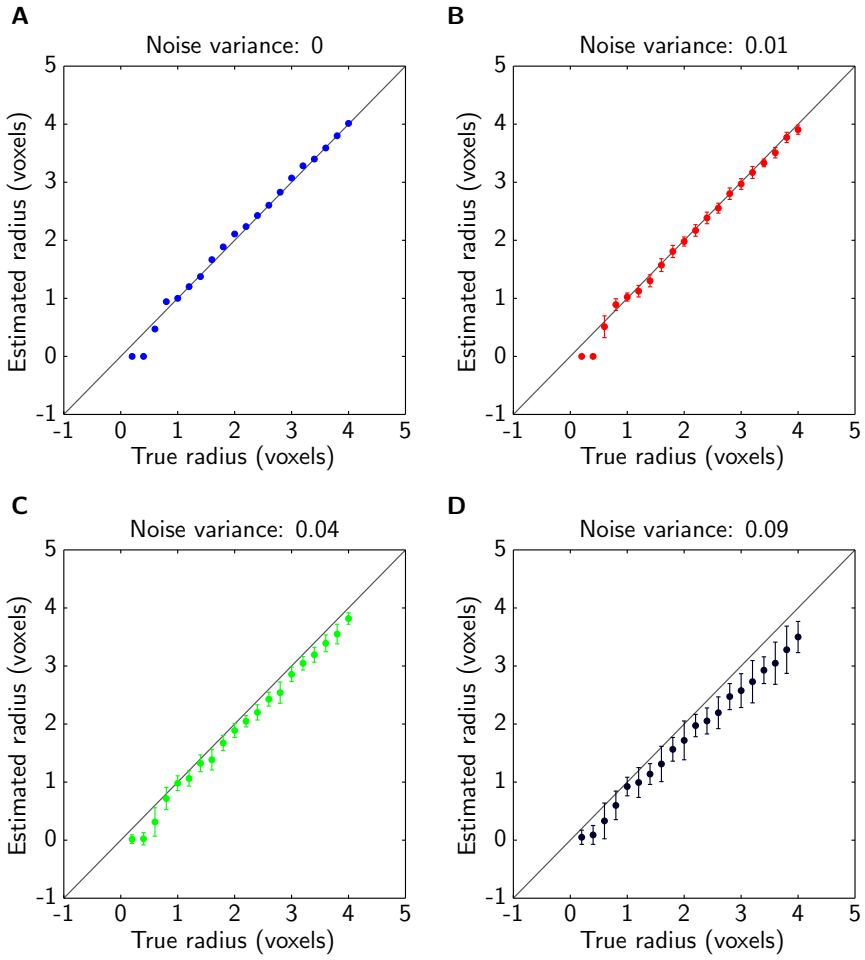


Figure 6.19: The estimated radii as a function of ground-truth radii with different noise levels (A-D).

6.6 Discussion

The structural analysis showed significant cortical thinning in the HD group compared to the HC group (p=0.011), however this did not retain significance when the cortical thickness was normalised to total intracranial volume (p=0.12). This total intracranial volume was not significantly different between the HD and HC groups (p=0.55), but this normalisation can introduce additional noise to the measurements. In order to fully understand the extent of cortical thinning, a larger sample size is needed to minimise the noise from the TIV and cortical thickness measures. Another possible source of error is the quality of cerebellum extraction from the structural images. A large imaging volume could be used to acquire the full cerebellum, however this would require a significant amount

of additional scan time which can be problematic in HD patients who can move significantly during the scan.

A significant absolute and relative loss of grey matter was observed in the HD group compared to the HC group (p=0.012 and p=0.002 respectively), along with a significant absolute and relative loss of white matter in the HD group compared to the HC group (p=0.004 and p=0.0008 respectively). In contrast, a significant increase in absolute and relative CSF was observed in the HD group compared to the HC group (p=0.001 and p=0.008 respectively). These measures indicate that a significant loss of brain tissue occurs in Huntington's Disease, with CSF replacing the lost tissue. This effect is well understood in the literature as a symptom of HD. The loss of brain tissue can also be assessed spatially on a voxel-by-voxel basis using voxel-based morphometry. Significant grey matter loss was observed in the striatum (caudate nucleus and putamen) and the lingual gyrus / occipital lobe. Atrophy is well reported in these regions, and has been shown to be linked to cognitive abilities [166].

When the relative grey matter volume was assessed as a function of age, both the HD and HC group demonstrated a decline in relative grey matter volume with increased age. In contrast, both the HD and HC group demonstrated an increase in relative CSF volume with increased age. This suggests that atrophy of brain tissue also occurs in healthy controls, however this is either accelerated or systematically offset due to Huntington's Disease.

The arterial spin labelling data revealed a significant perfusion reduction in grey matter in the HD group compared to the HC group (p=0.03). This result agrees with previous literature which also reported decreased cortical perfusion in HD [33–37]. The caudate nucleus and putamen were also assessed for perfusion changes between the groups, and it was found that both showed a significant perfusion reduction in the HD group compared to the HC group (p=0.002 and p=0.042 respectively). This also agrees with results reported in the literature [37, 160]. No perfusion differences were found between the groups when white matter perfusion was assessed. The transit time differences were also assessed between the HD and HC groups, grey matter and white matter showed no significant difference. The caudate and putamen however both demonstrated significantly increased tissue transit times in the HD group

compared to the HC group (p=0.024 and p=0.003 respectively). These results demonstrate that HD has a negative impact on the brain's ability to regulate blood flow. When the arterial cerebral blood volume was compared between the HD and HC groups, a significant increase in aCBV was found in grey matter in the HD group (p=0.039). However, no significant difference in aCBV was found between the groups in the caudate nucleus or putamen (p=0.306 and p=0.103 respectively). The increase in aCBV found in the grey matter agrees with the study from *Hua et al., (2014)* [165], where an increase is aCBV was found using the iVASO technique.

The involuntary muscle stimulation which occurs with HD could have had a large effect on the quality of the ASL data. Motion has a very detrimental effect on the perfusion weighted image, which could mean that the motion caused by muscle twitching has artificially lowered the apparent perfusion. Many steps were taken to reduce the effect of motion including motion correction, discarding repeats demonstrating significant motion and discarding repeats where motion correction did not perform sufficiently. Three datasets in the HD group were removed entirely as a usable perfusion signal could not be salvaged. This reduced the sample size significantly, and therefore a large spread was observed in the perfusion and transit time measures. A summary of the motion parameters obtained from motion correction are shown in Figure 6.20. It can be seen that translation and rotation parameters (Figure 6.20 A-B) estimated from motion correction are more severe for the HD patients than the healthy controls. The root mean squared deviation can be found from the estimated rotation and translation parameters, which is a summary statistic related to the geometrical distance between all voxel pairs before and after transformation (Figure 6.20 C). It can be seen that overall, voxels are transformed over a greater distance in order to motion correct in HD patients.

The aCBV acquisition has a larger SNR than that of the CBF acquisition due to the high blood flow and fresh blood signal within arterioles, however the coverage of this acqusition was limited. As each slice takes 65ms to acquire, only one slice can be obtained each 100ms. More slices could be acquired either using a simultaneous multi-slice (SMS) or multiband (MB) acquisition, or using a 3D-EPI readout scheme. This could similarly be applied to the readout used to acquire perfusion information, in particular the 3D-EPI readout such that the temporal

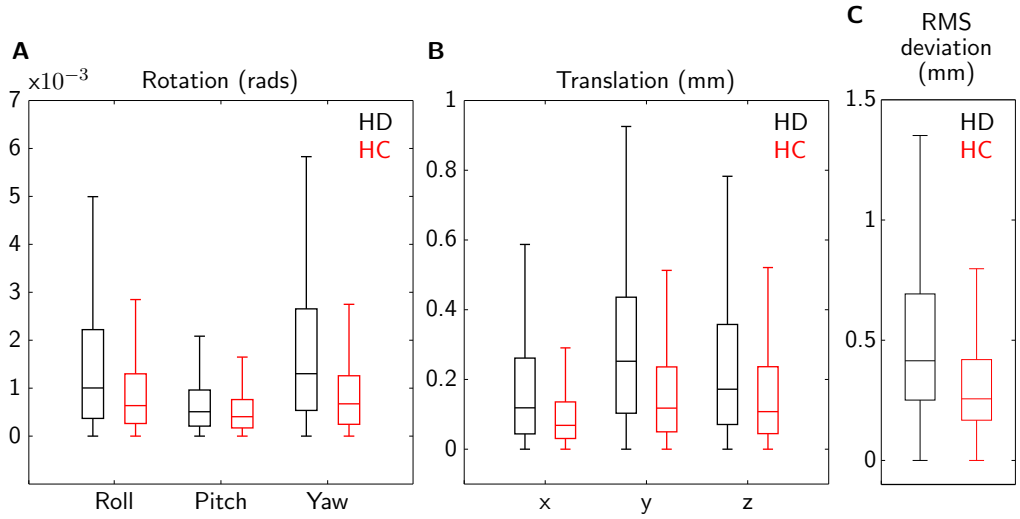


Figure 6.20: Transformation parameters obtained from performing motion correction on the patients with HD and healthy controls (HC). (A) The rotation parameters and (B) the translation parameters. (C) The root-mean squared displacement

slice spacing can be neglected from the analysis.

The phase-contrast angiography (PCA) data demonstrated a trend towards an increased frequency of narrow vessels (0.15-0.35mm) in the HD group compared to the HC group, however subsequent larger vessels in HD group become less frequent. This result was also reported in the *Cisbani et al., (2013)* [39] and *Franciosi et al., (2012)* [38]. However, when the vessel density was assessed, the HD group showed significantly reduced vessel density compared to the healthy volunteers. This does not agree with the results reported in the literature, as *Franciosi et al., (2012)* [38] and *Lin et al., (2013)* [40] both report an increase in vessel density in HD mice compared to control mice. This discrepancy could be due to numerous factors. Firstly, the motion due to chorea in HD patients could be causing the blurring and loss of the signal originating from the vessel, which may then not be detectable by the spatial thresholding. Secondly, the PCA data had a velocity encoding of ± 5 cm/s, meaning any vessels containing blood flow outside of this range are poorly encoded. The increase in vessel density may be originating from the vessels outside of this range in the reports from *Franciosi et al., (2012)* [38] and *Lin et al., (2013)* [40]. A possible solution to this issue is to adopt a time-of-flight (TOF) approach rather than use a PCA, allowing for the arterial side of the vasculature to be optimally detected. At 7 Tesla,

TOF has demonstrated positive results understanding vascular abnormalities in small vessel disease [167]. Finally, the resolution may be insufficient to detect the smallest vessels which cause the increase in vessel density. A larger sample size and a higher resolution PCA acquisition could help to better understand the vascular changes.

The vessel simulations demonstrate that vessels with a radii of 0.36mm or above (or 0.6 voxels) can be detected and adequately estimated. However, vessels below this cannot be identified. At large radii, the quality of estimation reduces with increased noise. This could be improved using a spatially adaptive thresholding technique that uses the SNR as an additional parameter.

6.7 Conclusion

The work in this chapter has studied haemodynamic, vascular and structural changes in Huntington's Disease compared to healthy age-matched controls. It was demonstrated that perfusion alterations occur in the grey matter in Huntington's Disease, as assessed using arterial spin labelling at 7T. Also a significant loss of grey matter was detected in HD, which manifests as cortical thinning and atrophy of the striatum. A trend indicating an increased fraction of smaller vessels in the HD group was found, but this was not significant.

7 Assessment of cortical lesion perfusion in MS using high resolution ASL at 7T

7.1 Outline

In this chapter, the pathology of Multiple Sclerosis (MS) is introduced followed by an overview of studies which have assessed the properties and effects of cortical lesions (CL) in MS. The study rationale is described, with a description of the patient group, the MR acquisitions used and data processing steps implemented to investigate perfusion of CLs in MS. The results of perfusion assessment inside and outside CLs are summarised, followed by a discussion of the possible mechanisms for the observed results.

This work was presented as an electronic poster at the 24th Annual Meeting of the International Society for Magnetic Resonance in Medicine (2016).

7.2 Introduction

Multiple Sclerosis (MS) is a chronic and progressive autoimmune disease whereby the myelin which surrounds the axons of neurons is attacked and destroyed by the immune system. Latest figures from the MS Society estimate that there are currently 107,800 people in the UK with MS with 5,110 newly diagnosed cases of MS each year [168], around 75% of patients are aged between 40-69 years (Figure 7.1).

7.2.1 Pathology

Neurons in the brain are made up of a cell body, the axon (surrounded my myelin), and the axon terminal (Figure 7.2A). The myelin sheath surrounding axons is developed and maintained by oligodenrocytes connecting pathways.

The blood-brain barrier prevents unwanted molecules from the blood reaching the neurons in the brain. However, constituents of the autoimmune system (such as T-cells) are able to tunnel through this barrier to protect the brain. In the case

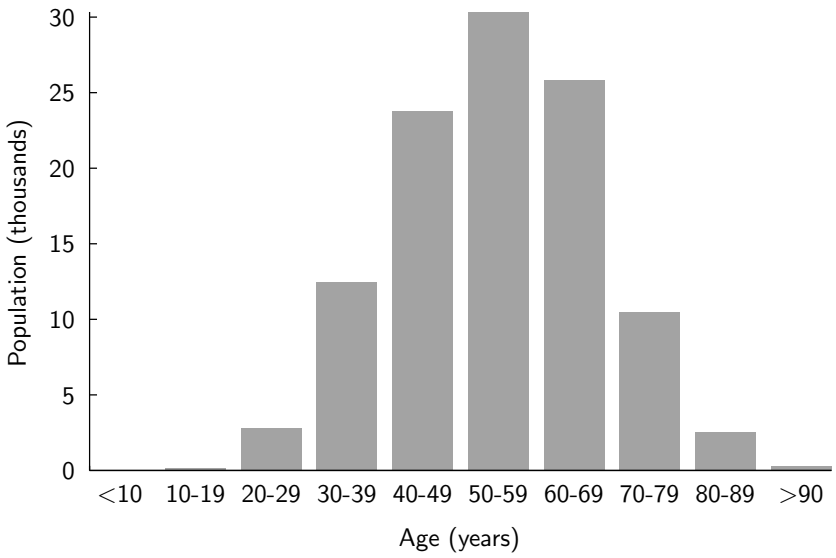


Figure 7.1: MS population in the UK as a function of age.

of MS, the T-cells are inappropriately triggered by myelin in the brain causing cytokines to signal an immune response (Figure 7.2A).

The release of cytokines causes three main processes; firstly it causes a large influx of autoimmune cells to arrive at the site of the cytokines. Secondly, it causes the BBB to express more receptors to T-cells, allowing more T-cells to enter the brain. Thirdly, these dilate the BBB, allowing larger members of the autoimmune system (B-cells and macrophages) to enter the brain. The B-cells recognise the myelin sheath incorrectly as a threat and label them with antibodies, the macrophages then use the antibodies to attack the oligodenrocytes (Figure 7.2B). The macrophage engulfs the oligodenrocytes, causing the myelin sheath to be destroyed, leaving an exposed axon. The destroyed myelin sheaths leave a scarring, recognised as 'plaques' or 'lesions'.

The exact cause of MS is unknown, however both genetic and environmental factors are thought to play a role. Genetic factors include being female (roughly 75% of the MS population are female) and having genes which encode a specific type of immune molecule known as HRA-DL2, an antigen which identifies and binds to foreign bodies. Environmental factors include infections and vitamin D deficiency, a newly introduced hypothesis for explaining the geographical distribution of MS with the occurrence of MS being much lower close to the equator [169].

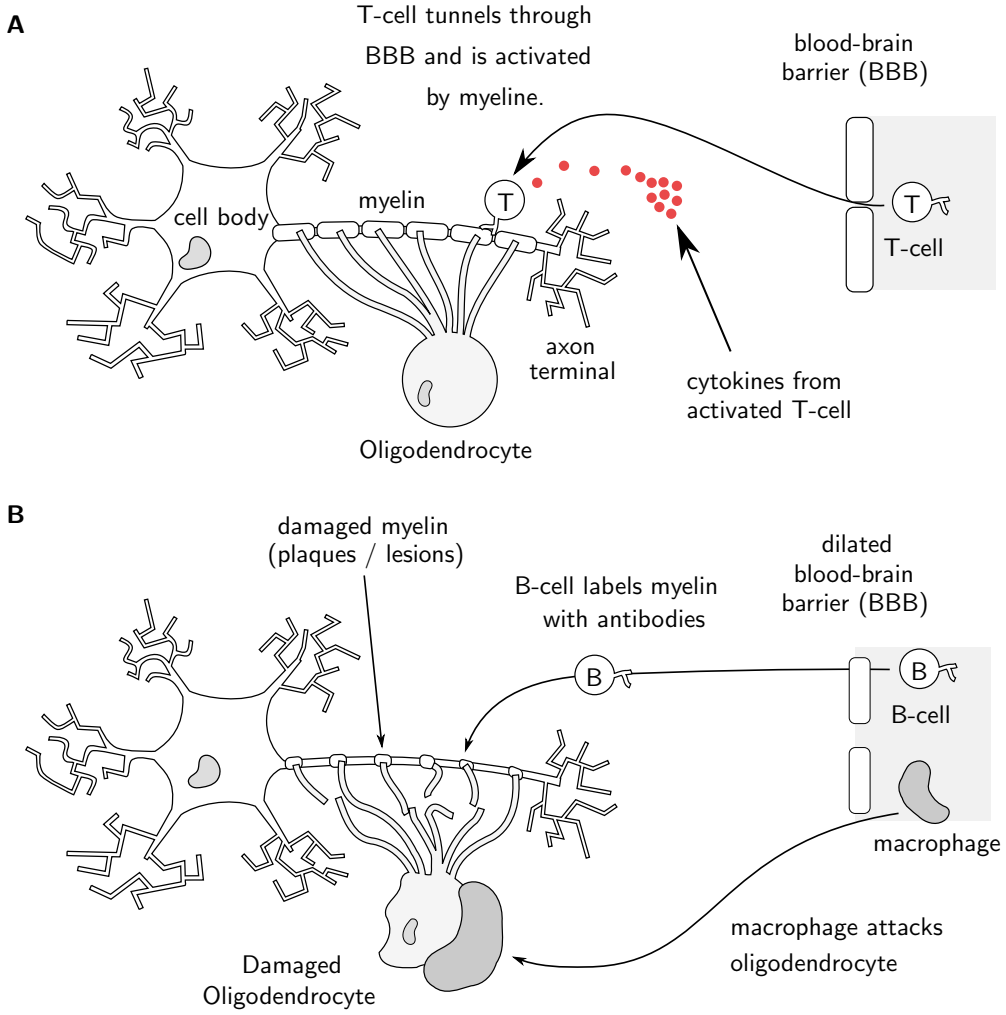


Figure 7.2: (A) T-cells tunnel through the BBB and are activated by the myelin, which causes cytokines to be released. (B) The release of cytokines has three effects: 1. They cause a large influx of autoimmune cells, 2. they cause the BBB to express more T-cell receptors, 3. they dilate the BBB allowing B-cells and macrophages into the tissue.

7.2.2 Types of MS

MS can manifest in three different forms; Relapsing Remitting (RR-MS), Secondary Progressive (SP-MS) and Primary Progressive (PP-MS). RR-MS is the most common form of MS with 85% occurrence, whereby the patient has a series of autoimmune attacks elevating the severity of the symptoms for a brief period in time. After each attack has subsided the patient is left with increased residual disability, but remains stable between each attack (Figure 7.3A).

SP-MS begins in the same manner as RR-MS with intermittent attacks which increase residual disability, however a point is reached where attacks no longer occur but disability consistently increases (Figure 7.3B). Most people with RR-MS transition to SP-MS at some point during their disease. PP-MS is an uncommon form of MS occuring in only 15% of cases, where there are no autoimmune attacks, but symptoms become increasingly worse, increasing disability (Figure 7.3C).

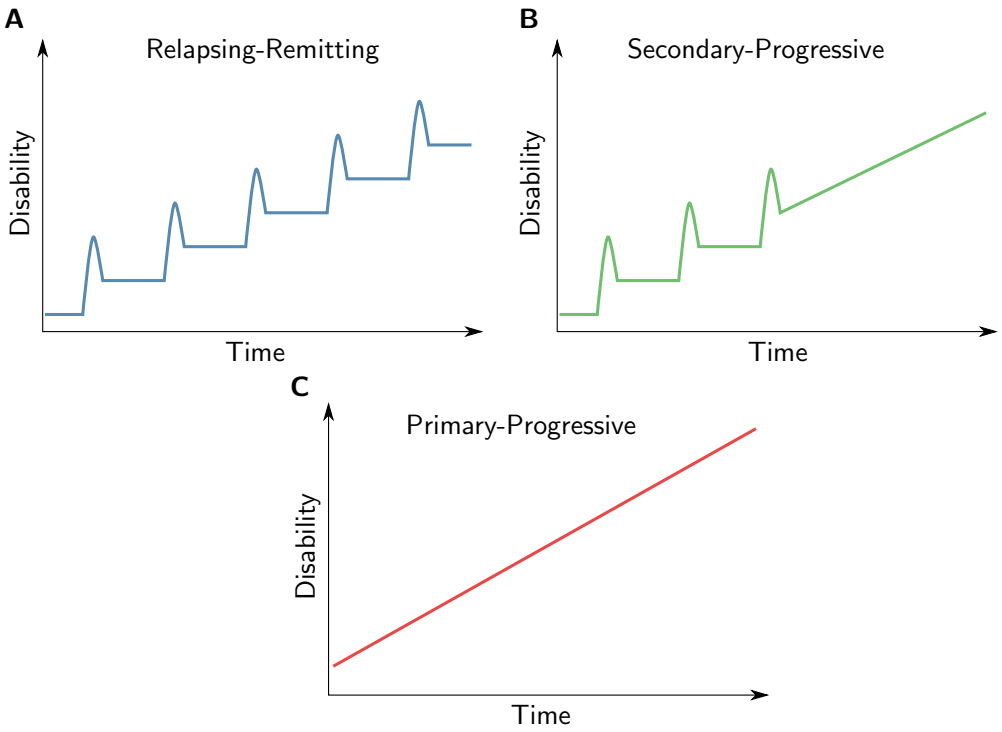


Figure 7.3: Types of MS and the associated resultant change in disability over time. (A) Relapsing Remitting; a series of attacks but the patient remains stable between them, (B) Secondary Progressive; at some point during RR-MS, the attacks will stop and symptoms become progressively worse, (C) Primary Progressive; the patient experiences no attacks during their disease but symptoms continuously worsen.

7.2.3 Symptoms

It is not trivial to predict the effect MS will have on each patient as symptoms vary and can affect any part of the body. However, the location of the lesion is thought to provide a good marker as to the severity and types of symptoms.

However, generally symptoms include fatigue, numbness or tingling of arms or legs, mobility problems, vision problems and depression or anxiety. During a relapse, the severity of symptoms are elevated until the relapse subsides.

7.2.4 Treatment

Currently there is no cure for MS, but there are treatments which have been shown to be effective in increasing the quality of life if RR-MS. These treatments aim to increase the time between each relapse and decrease the severity of relapses. Treatments such as steroids (anti-inflammatory drugs), interferons (synthesised proteins which can prevent inflammation) and disease modifying drugs can all be used to achieve this. Treatments for the progressive types of MS are less effective, and medication instead aims to manage symptoms rather than treat the cause.

7.2.5 Overview of Cortical Lesions in MS

Lesion formation is MS is more common in some locations, and the location can be used in the diagnosis of MS. In MS, lesions commonly appear in the periventricular, juxtacortical and infratentorial space and they also tend to form symmetrically (Figure 7.4). The line of periventricular lesions running parallel to the midline of the brain (often through the corpus callosum also) are known as 'Dawson's Fingers', which are a specific marker for MS. Despite the wide spread of lesions across the brain, they are rarely visible in the basal ganglia, which can distinguish MS from a vascular disease. Lesions can also appear in the cortical grey matter, however the occurrence of this is roughly in only 25% of MS patients, such that they are not a reliable feature upon which to form a diagnosis of MS [170].

Common imaging modalities are not very sensitive to detecting the appearance of cortical lesions, which could explain their apparent sparse occurrence. Due to this reason, less is known about cortical lesions than white matter lesions. Developments in magnetic resonance (MR) imaging techniques, such as fluid-attenuated inversion recovery (FLAIR) [171], phase sensitive inversion recovery (PSIR) [127, 172] and double inversion recovery (DIR) [173, 174] have increased the sensitivity to cortical lesions. The sensitivity to detecting cortical

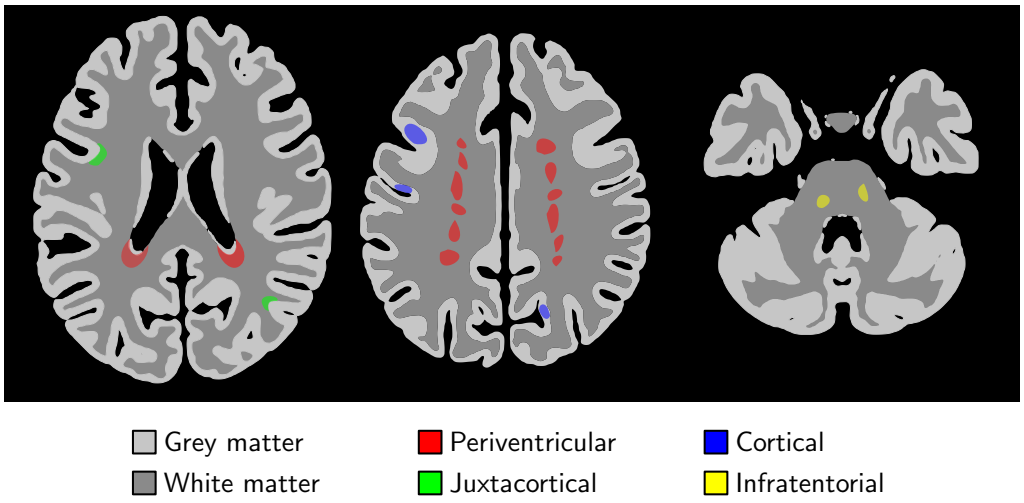


Figure 7.4: Common locations of lesions which occur in MS.

lesions has been shown to increase further with the use of higher magnetic field strength [175]. An increased magnetic field strength allows for higher resolution structural acquisitions, allowing smaller lesions to be detected and boundaries to be better localised [176]. However, it is still expected that the actual cortical lesion load is much greater than we can detect [177]. The ability to detect cortical lesions *in-vivo* has led to numerous studies investigating the role they play in pathophysiology, with studies attributing cortical lesions to cognitive impairment [178, 179], epilepsy [180, 181] and depression [182].

The formation of lesions through the breakdown of the blood-brain barrier and associated micro-vascular abnormalities has prompted many studies to investigate cerebral perfusion [183–197]. The haemodynamics of both white matter lesions [198] and cortical lesions [42, 43] have been assessed in previous studies using dynamic susceptibility contrast MRI (DSC-MRI). Chronic white matter lesions were demonstrated to have reduced cerebral blood volume (CBV) compared to normal appearing white matter (NAWM) by roughly 20%, while acute lesions were demonstrated to have increased CBV by roughly 15% [186]. Two studies have compared the perfusion of cortical lesions with the surrounding cortex [42, 43], reporting a decrease in perfusion by 46% and CBV by 41%, however mean transit time (MTT) was unaffected. There are also reported changes in perfusion prior to lesion formation suggestive of inflammation [184], this has been suggested to indicate that the blood flow of lesions is a very dynamic process dependent on the stage of the lesion. Proximal perfusion around cortical lesions has not

been assessed, but it has been shown that proximal tissue around white matter lesions is damaged [199]. However, assessing such changes longitudinally using DSC-MRI is not recommended given the safety concerns surrounding gadolinium based contrast agents [81, 82, 200, 201].

Work by *Kanda et al., (2014)* [200] acquired T_1 weighted structural scans of 381 volunteers with a history of contrast enhanced scans. A strong positive correlation was seen between signal intensity on T_1 weighted images and number of contrast enhanced scans in the dendate nucleus and globus pallidus. A similar study by *Radbruch et al., (2015)* [201] found hyperintensities on T_1 images in the dendate nucleus and globus pallidus in subjects with a history of contrast enhanced scans compared to subjects which have no history of contrast enhanced scans. *Kanda et al., (2015)* [82] extended this work by performing inductively coupled plasma mass spectrometry on post-mortem brain tissue to assess gadolinium concentration. Five subjects with a history of contrast enhanced scans and five subjects with no history of contrast enhanced scans were assessed for gadolinium concentration in the dendate nucleus, global pallidus, cerebellar white matter, the frontal lobe cortex, and frontal lobe white matter. The gadolinium concentration was higher within tissue from all brain regions from the five subjects with a history of contrast enhanced scans. Work by *McDonald et al., (2015)* [81] utilised both T_1 weighted images and inductively coupled plasma mass spectrometry in groups with and without a history of contrast enhanced scans. They reported significant gadolinium content in neuronal tissue in the group with a history of contrast enhanced scans, and a negligible amount in the group with no history of contrast. For this reason, regular doses of gadolinium are cautioned against until the clinical significance of the accumulation is established.

As arterial spin labelling can assess perfusion without the use of an exogenous contrast agent, the risks surrounding contrast agents can be avoided. This would allow for perfusion to be assessed repeatedly in longitudinal studies. There is, however, a trade off as contrast enhanced scans are considered the gold standard for measuring perfusion.

Authors	Resolution (mm)	ASL Scheme	Field Strength (T)
Rashid et al., (2004) [193]	3.75×3.75×6.00	PASL	1.5
Amann et al., (2012) [194]	4.60×4.60×4.00	PASL	1.5
Ota et al., (2013) [196]	3.75×3.75×7.00	pCASL	3
Steen et al., (2013) [197]	3.00×3.00×7.00	pCASL	3
Debernard et al., (2013) [195]	3.75×3.75×5.00	pCASL	3

Table 7.1: Summary of ASL acquisitions in MS perfusion studies.

7.3 Aims and Objectives

Here we propose to use high spatial resolution Arterial Spin Labelling (ASL) at ultra-high field (7 Tesla) to assess if this technique possesses sufficient sensitivity to detect perfusion abnormalities in cortical lesions. The use of ASL has previously been applied to study perfusion abnormalities in MS [193–197], with the focus on white matter and deep grey matter. However, the spatial resolution at which this data was acquired (see Table 7.1) would make it unsuitable to assess cortical lesions, as their average diameter is measured to be around 1.67mm [202]. Here we apply a balanced steady state free precession readout (b-SSFP, TrueFISP, FIESTA) in conjunction with flow alternating inversion recovery (FAIR) ASL labelling scheme to acquire high spatial resolution single slice ASL data.

The recommended readout schemes for cerebral arterial spin labelling are EPI based, with the ASL white paper [60] recommending the 3D-GRASE sequence. This implementation strikes a balance between coverage, image quality and availability. The use of non-EPI based ASL readouts are less common are are primarily utilised for body imaging at 1.5 and 3T. The use of non-EPI ASL readouts, particularly fast low angle shot (FLASH), at ultra-high field are reported but not yet used for clinical purposes [203–205]. Studies collecting ASL data at 7T have generally used a gradient echo EPI readout [206] which suffers from a limited field-of-view (FOV) at high spatial resolution. In order to acquire a larger FOV at high spatial resolution without high SENSE factors and partial Fourier methods (as described in Section 3.5), a significant increase in

echo time is needed. An increase echo time in EPI sequences causes significant signal loss due to T_2^* decay which in turn leads to anatomical distortions and poor SNR. In order to acquire rapid high spatial resolution with an adequate FOV and SNR, alternative acquisitions such as bSSFP and FLASH can be used. These sequences benefit from very small echo and repetition times which produces are greater SNR than EPI sequences. The bSSFP and FLASH sequences also acquire data during a steady state achieved via repeated RF pulses, which means that no distortions occur due to signal loss. This is particularly important for this study, as the lesion masks are created from a high resolution distortion free structural image which must be translated into ASL space. bSSFP possess a higher SNR than the FLASH acquisition due to the balanced gradients rephasing the spins between each RF pulse, whereas the FLASH sequence destroys the transverse magnetisation.

Here we use a high spatial resolution bSSFP sequence to assess perfusion within cortical lesions and compare this to local surrounding grey matter in a cross sectional study. To assess the spatial distribution of changes in perfusion, the perfusion profile is assessed as a function of the distance from the centre of the cortical lesion.

7.4 Methods

7.4.1 Participants

This cross-sectional study was performed with the approval of the Nottingham Research Ethics Committee (REC). Twelve patients with MS were recruited for this study, four MS patients with Primary Progressive, one MS patient with Secondary Progressive and seven Relapsing Remitting MS patients. The patient group comprised of eight males (mean age 47 years, range 33-62 years) and four females (mean age 55 years, range 51-64 years), with a group mean age of 50 years and range 33-64 years. Patients were recruited to the study based on previous clinical MRI scans, on which cortical lesions were identified above the temporal lobe. Access to prior clinical scans followed the ethical guidelines to which consent was given. Patients were asked to complete a modified fatigue impact scale (MFIS) questionnaire, fatigue severity score (FSS) questionnaire and an expanded disability status scale (EDSS) questionnaire prior to the scan.

The MFIS questionnaire consists of 21 questions relating to how often physical, cognitive and psychosocial issues occur. The questionnaire is scored between 0 and 84, with a higher score indicating more severe symptoms. The FSS questionnaire is comprised of seven questions addressing the severity of fatigue within the previous week. The questionnaire is scored out 63, with a higher score indicating more severe fatigue. The EDSS examination quantifies the extent of disability within MS. The score is determined with a physical examination by a neurologist and is scored between 0 and 10 in 0.5 increments. A larger EDSS indicates more severe disability. Table 7.2 outlines the patient demographics, providing details of age, gender, MS type and their questionnaire scores.

Study ID	Age	Gender	MS Type	MFIS	FSS	EDSS
MS01	53	M	SP	59	57	6
MS02	52	F	RR	0	29	2
MS03	51	F	RR	62	52	6
MS04	35	M	RR	59	53	4
MS05†	43	M	RR	80	59	6
MS06	54	F	RR	49	55	5
MS07	44	M	RR	84	54	6
MS08	49	M	RR	0	44	2.5
MS09	46	M	PP	45	56	6
MS10†	43	M	PP	60	59	7
MS11	64	F	PP	25	15	3.5
MS12	62	M	PP	27	39	3.5

Table 7.2: Demographics of the MS patient group used in this study. †Data from these volunteers had to be discarded due to excessive head motion.

7.4.2 MR Acquisition

All volunteers were scanned on a 7T Philips Achieva system with a Nova Medical single channel transmit (Tx) coil and 32 channel receive (Rx) coil.

7.4.2.1 Structural

Structural data was acquired using a PSIR (phase sensitive inversion recovery) scheme with a turbo field echo (TFE) readout as described by *Mougin et al., (2016)* [127] (resolution = 0.6×0.6×0.6 mm, FOV (AP,RL,FH) = 200×181×120 mm, SENSE factor (AP,RL,FH) = 2, 1, 2, 200 contiguous slices, AP readout direction, radial phase encoding in RL and FH directions, flip angle = 8^o, TE/TR = 6/13 ms, acquisition time 11.92 minutes).

The initial inversion was achieved using a tailored adiabatic inversion pulse in order to reduce effects from B_1 inhomogeneities [128]. The PSIR sequence involves two TFE readouts at time TI_1 and TI_2 after the inversion. TI_1 is timed such that grey matter and white matter have equal but opposite longitudinal magnetisation. This results in voxels with equal amounts of grey matter and white matter to be nulled, resulting in a clear boundary between the two tissue types ($TI_1 = 780ms$). TI_2 must be as short as possible to allow fast acquisition, but must allow sufficient recovery past the null point ($TI_2 = 2380ms$). The phase and modulus data are saved.

The PSIR acquisition was designed to have a large enough coverage to image the whole head, specifically covering the entire cortex. However, due to variability of brain sizes, the cerebellum was not completely acquired for all volunteers.

The PSIR sequence used has increased sensitivity to cortical lesions compared to a traditional PSIR sequence. Two important modifications were made to achieve this; firstly, a 3D-TFE readout was used compared to the traditional fast spin echo (FSE). The 3D-TFE is able to provide a high resolution scan of the entire cortex in a reasonable amount of time, necessary for identifying small cortical lesions and avoiding partial volume effects. The scan duration for the 3D-TFE is significantly shorter than the FSE, with a scan duration of 12:54 compared to 1:59:20 with and FOV of 192×192×120 mm at a resolution of 0.6×0.6×0.6 mm. The 3D-TFE also reduced SAR and the effect of B_1 inhomogeneities compared to a FSE. Secondly, phase and modulus data is acquired at two inversion times (TI_1 and TI_2) as opposed to one. TI_1 collects data where grey and white matter have equal and opposite signals, and TI_2 collects data where all tissue types have recovered above the null. The phase difference between TI_1 and TI_2 can be used to restore

signal polarity as described by *Gowland et al., (1991)* [207], which provides more accurate reconstruction compared to traditional phase correction methods [208, 209]. The modulus image acquired at TI_2 is also dominated by receive and transmit coil inhomogeneities, which can therefore be used to correct for signal bias. This produces increased SNR between grey and white matter compared to the MP2RAGE bias correction approach often used [210]. In addition, a useful feature of the modulus data from TI_1 is the distinct boundary between grey matter and white matter, which can be used to determine if lesions are cortical or juxtacortical.

7.4.2.2 Arterial Spin Labelling

Arterial spin labelling (ASL) data were acquired using a balanced SSFP (bSSFP) readout scheme (FOV = 192×192×3mm, spatial resolution = 1.2×1.2×3mm, single-shot acquisition. Single slice, TE/TR = 1.9/3.8ms) to achieve high spatial resolution with minimal distortions, essential for accurate co-registration of small cortical lesions to the PSIR scan. An axial imaging slice was positioned to transect one or more cortical lesions identified from the PSIR image by an experienced clinician. Single post-label delay (PLD) ASL data were collected at PLDs of 1400 and 1800ms to determined tissue perfusion (50 label-control pairs were acquired at each PLD using a flip angle of 50^o). In addition, a multi-PLD ASL dataset was acquired using a Look-Locker readout at 8 PLDs (200, 550, 900, 1250, 1600, 1960, 2300, 2650ms; 40 label-control pairs with a flip angle of 35^o) to locate the intravascular signal. An M_0 map was acquired for both single and multi-phase acquisitions for quantitative perfusion estimation.

7.4.3 Data processing

7.4.3.1 Structural Data

The processing pipeline to reconstruct the PSIR data is described in *Mougin et al., (2016)* [127] and summarised in Figure 7.5. The phase difference between the two acquired phase images was found and used to correct the sign of the first acquired modulus image. However at 7T, a significant amount of B_1 inhomogeneity can be observed in this image. This is corrected by summing

both acquired magnitude images and smoothing with a large Gaussian kernel to estimate the bias field. Dividing through by the estimated bias field creates an image with flat contrast for each tissue type allowing for more robust segmentation. Brain extraction was performed using FSL BET on the Modulus (2) acquisition and the brain mask was applied to the reconstructed image. Segmentation of tissue types (grey matter, white matter and cerebral spinal fluid) and spatial normalisation was performed using SPM8.

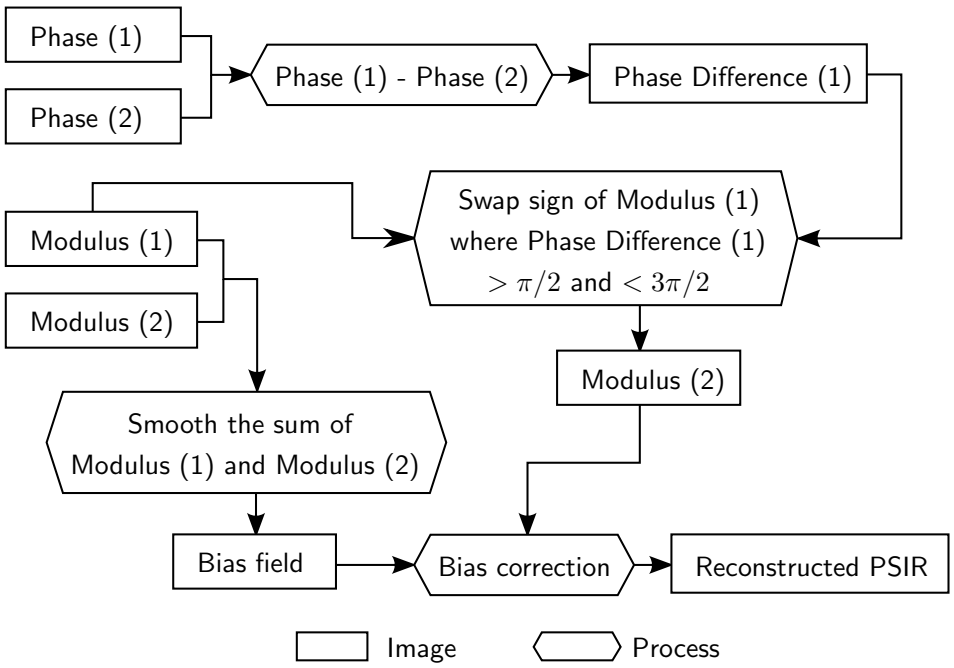


Figure 7.5: The processing pipeline used to reconstruct the PSIR anatomical scan.

7.4.3.2 T_1 Map

A T_1 map was acquired by fitting to a saturation recovery to the label of the multi-PLD ASL data on a voxel-by-voxel basis. Fitting to a saturation recovery yields the apparent T_1 (T_1^*) which must be converted into an actual T_1 using

$$T_1 = \left(\frac{1}{T_1^*} - \frac{\ln \cos\theta}{\tau} \right)^{-1} \tag{7.1}$$

where θ is the flip angle (35^o) and τ is the interval between each readout in the multi-PLD scheme (350ms). Measuring the venous blood T_1 ($T_{1,vb}$) required an inversion recovery curve to be fit in the signal in the sagittal sinus. This

was converted to the T_1 of arterial blood ($T_{1,ab}$) using the relationship described by *Blockley et al., (2008)* [211], where the $T_{1,ab}$ is roughly 4.5% greater than $T_{1,vb}$ (Figure 7.6). The fast flow of the sagittal sinus and the small FOV means that blood visible in the imaging plane at the time of acquisition has not been exposed to either the presaturation pulses or has been continually suppressed by the multiple readout pulses in the multi-PLD scheme. Therefore the blood in the sagittal sinus is only affected by the global inversion pulse used for labelling.

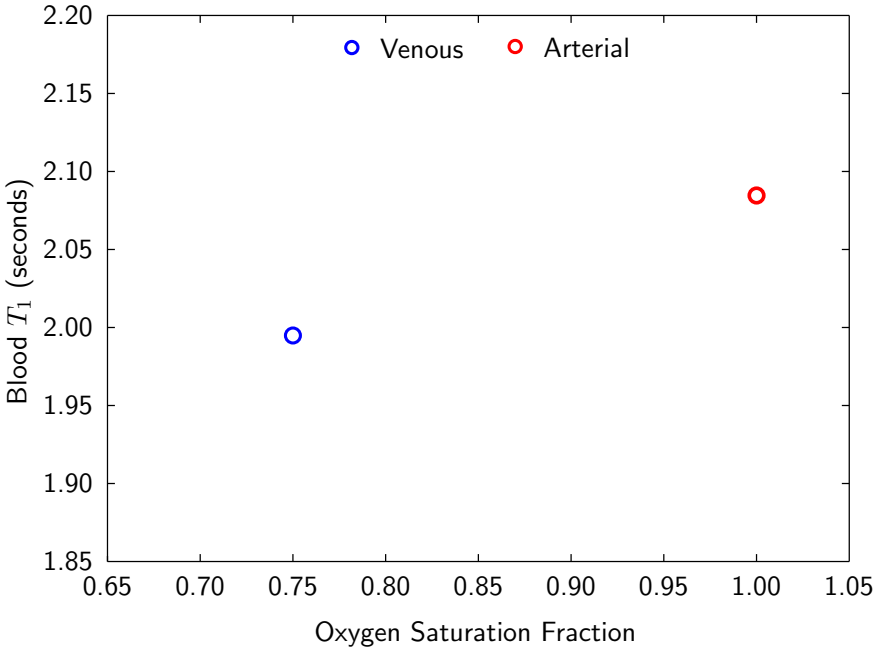


Figure 7.6: Blood T_1 dependence on oxygen saturation at 7T, as reported by *Blockley et al., (2008)* [211].

7.4.3.3 Arterial Spin Labelling

The ASL pre-processing pipeline used for both single-PLD and multi-PLD followed the same pipeline as described in Figure 7.7. Label 1 of the non-selective condition for each PLD was averaged over all repeats. These were then all co-registered to the first PLD (1400ms). The transformation matrices describing this co-registration were then applied in conjunction with the motion correction parameters such that only one transform was applied to the labels. Each application of an affine transformation causes the image to blur due to interpolation effects, so minimising the number of transforms applied is important. Motion correction was performed using the FSL MCFLIRT

algorithm, whereby both label 1 and label 2 are concatenated in the fourth dimension and the central repeat of label 1 is used as the reference. Despite the slightly different contrast of label 1 and label 2 due to the blood label, this method was found to out perform motion correcting each label individually. The transformation matrices to motion correct each repeat were decomposed to determine the amount of translation and rotation which was applied. If the translation required to motion correct a volume exceeded one voxel (3mm), the repeat was discarded. The image was split back into label 1 and label 2 formats before brain extraction was performed using FSL BET. A perfusion weighted image (PWI) was then created by computing the difference between label 1 and label 2 using simple pairwise subtraction. Using the method described by *Tan et al., (2009)* [72], each repeat of the PWI was assessed to determine if it was an outlier. The PWI was then averaged over all repeats to create a final perfusion weighted image for each PLD. All PLDs are concatenated in the fourth dimension and calibrated for $M_{0,b}$.

The multi-PLD data were fit to the model described by *Francis et al., (2008)* [63] to compute a transit time map. Although this method also fits for perfusion, the SNR is significantly lower than the single-PLD ASL data. Thus in this study, using the transit time map, the T_1 map, the calculated value for arterial blood T_1, the single-PLD data is fit to the model described by *Buxton et al., (1998)* [70]. In order to best optimise this fit, the starting parameters are chosen by comparing the ASL signal on a voxel-by-voxel basis to a look-up table of simulated ASL signals. The parameters producing the best estimate (assessed using the sum of square differences) is used to begin a Nelder-Mead simplex direct search implemented by MATLAB.

7.4.3.4 Lesion Identification

In order to accurately locate each cortical lesion in ASL space, the PSIR data was co-registered to the ASL data. In the absence of patient movement, the exact PSIR slices which contribute to the ASL data are known. However, the high resolution of both ASL and PSIR acquisition cause the sub-millimetre translations and rotations of the patient's head to have a large effect which must be accounted for. The robustness of automated 2D to 3D co-registration is not sufficient for

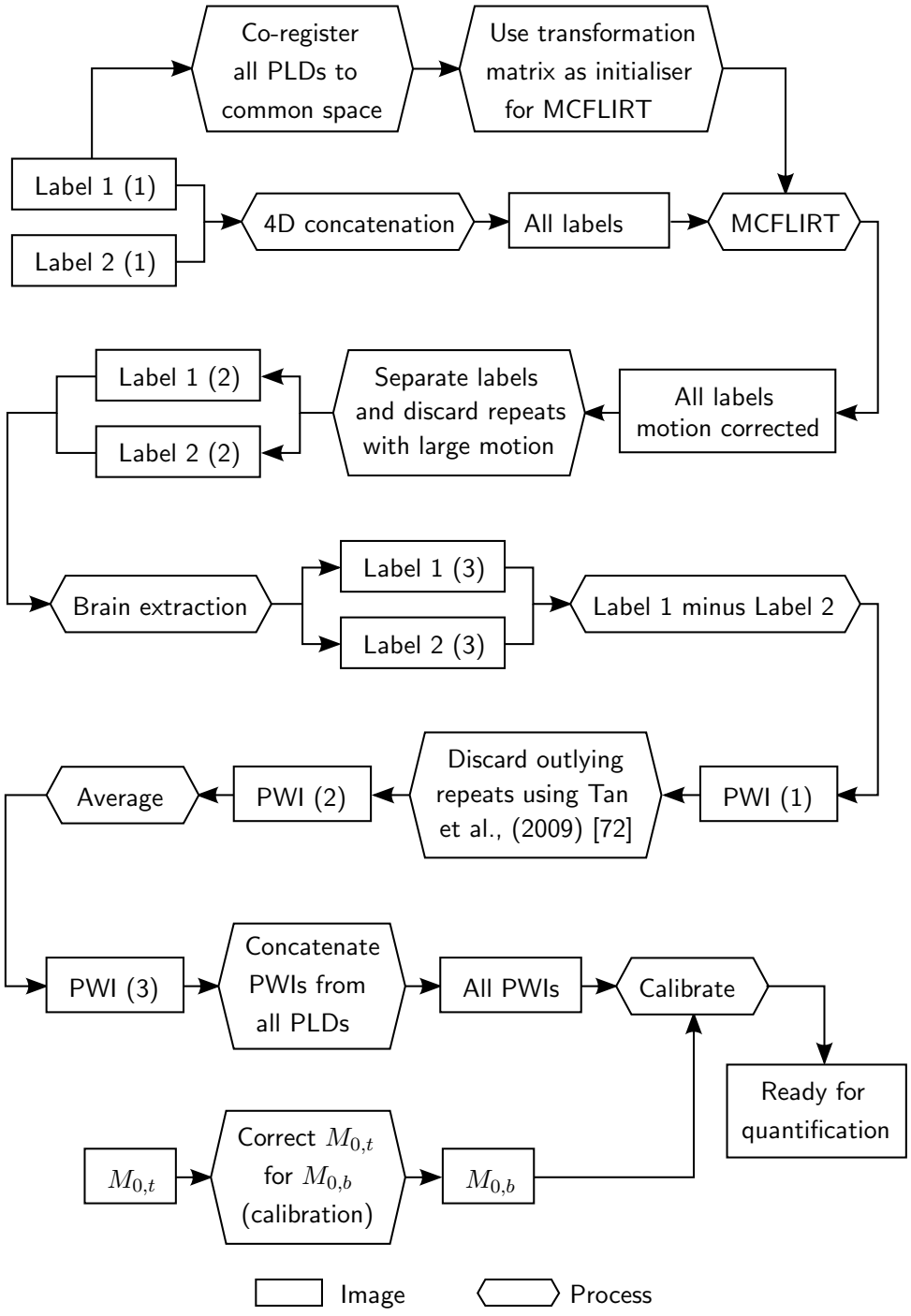


Figure 7.7: ASL preprocessing pipeline used to prepare the single-PLD and multi-PLD data for quantification.

the accuracy required to match the two scans. This was addressed by visually inspecting the co-registration of a range of slices surrounding the expected PSIR slices, and methodically applying rotations when needed.

Masks were drawn around the cortical lesions using the modulus image, which

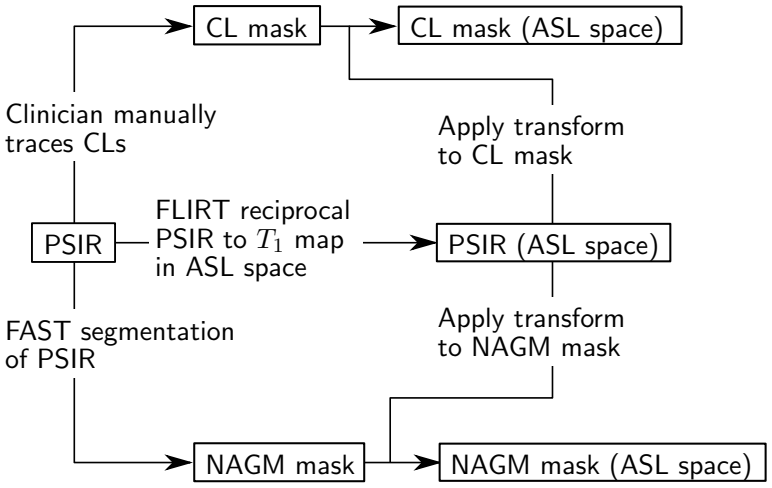


Figure 7.8: Pipeline used to obtain masks of cortical lesions and normal appearing grey matter in ASL space from PSIR space.

provides a more suited contrast to cortical lesions compared to the reconstructed PSIR, using MIPAV (Medical Imaging Processing Analysis and Visualisation, CIT, NIH, Bethesda). These were then transformed into ASL space using the transformation matrix obtained from the PSIR to ASL co-registration. The segmented grey matter mask obtained from Section 7.4.3.1 is also transformed using the same transform to obtain a grey matter mask in ASL space.

7.4.3.5 Lesion Eligibility

To ensure a sufficient sample size of voxels representative of the lesion, any lesion with a volume less than three ASL voxels (12.96 mm^3) was discarded. As vascular crushing could not be applied to this particular ASL bSSFP acquisition, there was arterial vascular contamination present in the data which meant that fitted perfusion values may contain a vascular contribution and not be representative of tissue, despite longer PLDs being used for the single PLD data acquisition. A vascular map was therefore created by fitting a double Gaussian to the grey matter perfusion distribution; any voxels containing a perfusion value five times greater than the tissue perfusion peak were considered vasculature. If the lesion fell inside this vascular map, then there was considered arterial contamination inside the lesion and it was discarded from subsequent analysis.

7.4.3.6 *Lesion Perfusion comparison*

The perfusion values inside the cortical lesion mask were averaged to determine the grey matter perfusion in each lesion. In order to compare this to the local normal appearing grey matter (LNAGM), the cortical lesion mask was dilated with a radius of 12mm and confined to the grey matter mask. The mean perfusion inside this NAGM mask, removing the lesion, is considered to be the LNAGM perfusion. The average perfusion value across all available grey matter is also considered (Figure 7.9B). The mean grey matter perfusion in 4 zones surrounding the cortical lesion in steps of 6mm (6, 12, 18, 24mm) (Figure 7.9C) was also assessed.

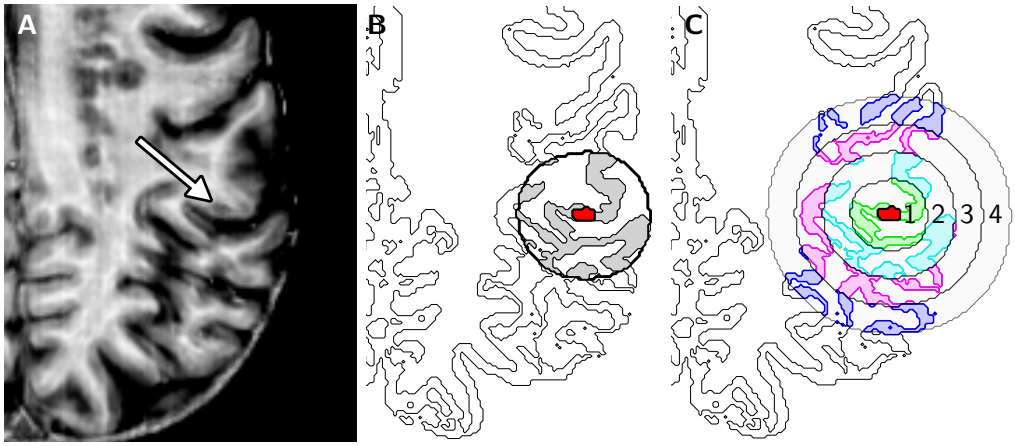


Figure 7.9: (A) A reconstructed PSIR image with a cortical lesion indicated with the arrow. (B) Outline of grey matter (white fill), LNAGM (grey fill) and cortical lesion (red fill). (C) Outlines of the four zones at 6 mm steps of increasing radius from the centre of the cortical lesion.

7.5 Results

7.5.1 Cortical Lesion Identification

In total, 40 cortical lesions from the ASL slice were identified from the ten patients scanned (data from two subjects was discarded due to excessive head motion). After applying the eligibility criteria, 26 of the 40 cortical lesions remained for analysis (67.5%); 13 were discarded as 5 contained vascular contamination (10%),

Study ID	Number of CLs	CL Volumes (mm^3)
MS01	4	27.86†, 21.60†, 8.42†*, 16.63
MS02	5	13.18†, 15.12, 47.09, 14.04
MS03	1	17.50
MS04	3	44.50, 17.50, 19.44
MS06	3	17.71, 30.02, 26.35
MS07	6	29.38, 8.64*, 17.93, 15.55, 6.48*, 21.17
MS08	4	22.03, 14.90, 25.49, 16.42
MS09	5	15.98, 15.34, 7.13*, 19.44, 15.98†
MS11	7	12.96, 7.56*, 8.86*, 8.86*, 8.42*, 14.26, 25.49
MS12	2	12.53*, 18.36

Table 7.3: Summary of cortical lesions and their volumes identified from PSIR image acquisitions. Lesions (*) with a volume of <12.96 mm^3 were discounted from analysis, along with those CLs (†) which contained vascular contamination.

8 were below the volume threshold (20%) and 1 failed both tests (2.5%) (Table 7.3).

7.5.2 Cortical Lesions Perfusion

The mean perfusion was found to be 40±25 ml/100g/min in cortical lesions, 53±12 ml/100g/min in LNAGM and 54±8 ml/100g/min in whole of the grey matter within the ASL slice. When comparing perfusion inside the lesion to the associated LNAGM, perfusion of cortical lesions was significantly reduced by 23±9% when compared to LNAGM (p=0.013). Perfusion of cortical lesions was significantly reduced by 26±9% when compared to whole grey matter (p=0.006) (Figure 7.10).

The mean perfusion in zones 1 to 4 were 54±16, 52±13, 57±15.1 and 54±16 ml/100g/min respectively, corresponding to a reduction of perfusion in cortical lesions by 24±8%, 18±10%, 23±10% and 20±10%. The cortical lesions showed a significant reduction in perfusion compared to each zone (p=0.009, 0.028, 0.007, 0.017), however no significant difference was observed between any of the zones.

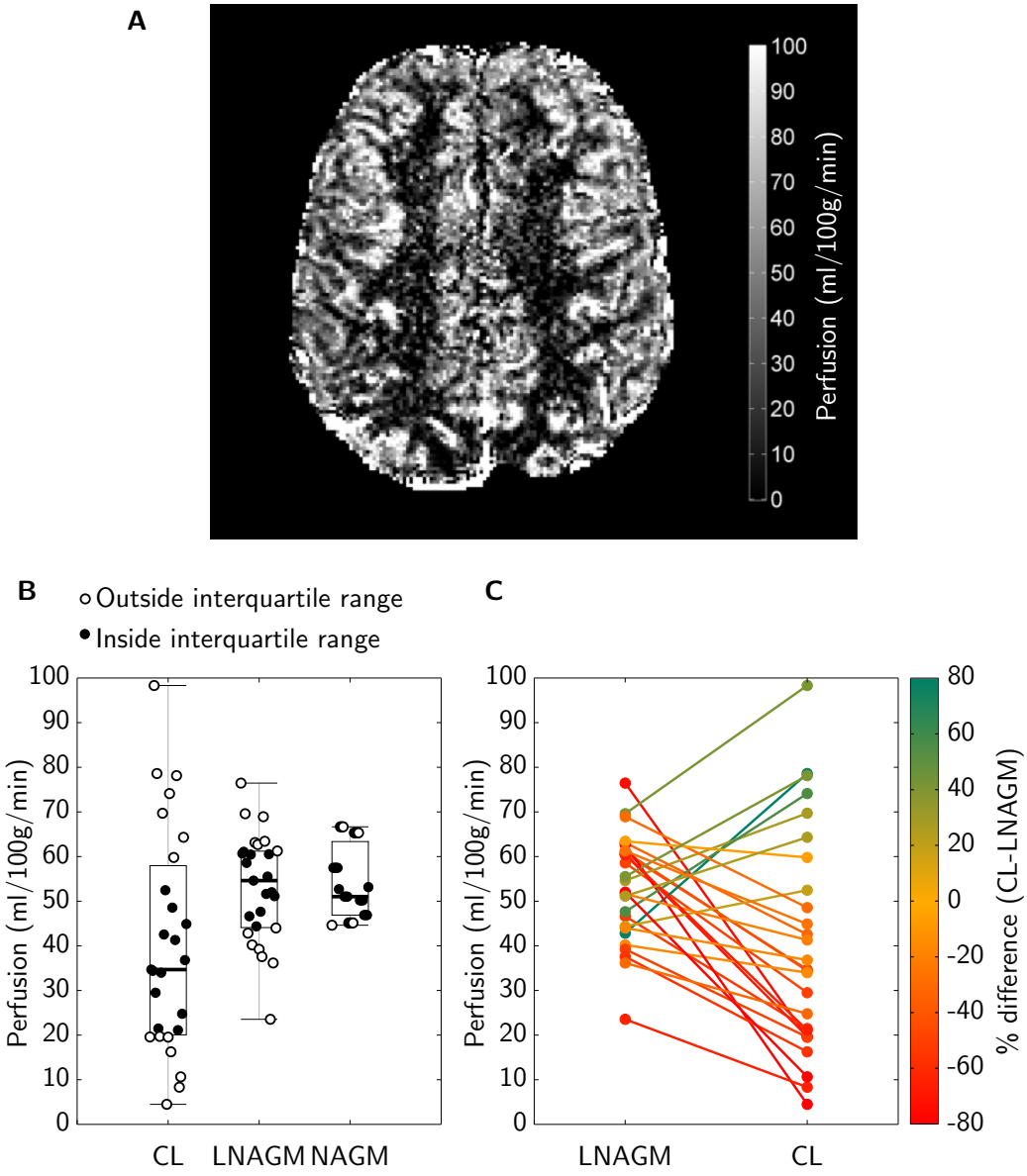


Figure 7.10: (A) Example perfusion map obtained using a bSSFP readout. (B) Boxplot illustrating perfusion within the cortical lesions, local NAGM and NAGM. (C) Plot of perfusion difference between local NAGM and CL, where the colour corresponds to the percentage difference from the CL.

7.5.3 Cortical Lesions Perfusion correlation with clinical scores

The clinical scores did not show a significant correlation with the NAGM perfusion in the 10 volunteers with usable data (MFIS: p=0.19, FSS: p=0.96 and EDSS: p=0.06). However a strong negative trend was seen between the NAGM perfusion and EDSS scores (p=0.06).

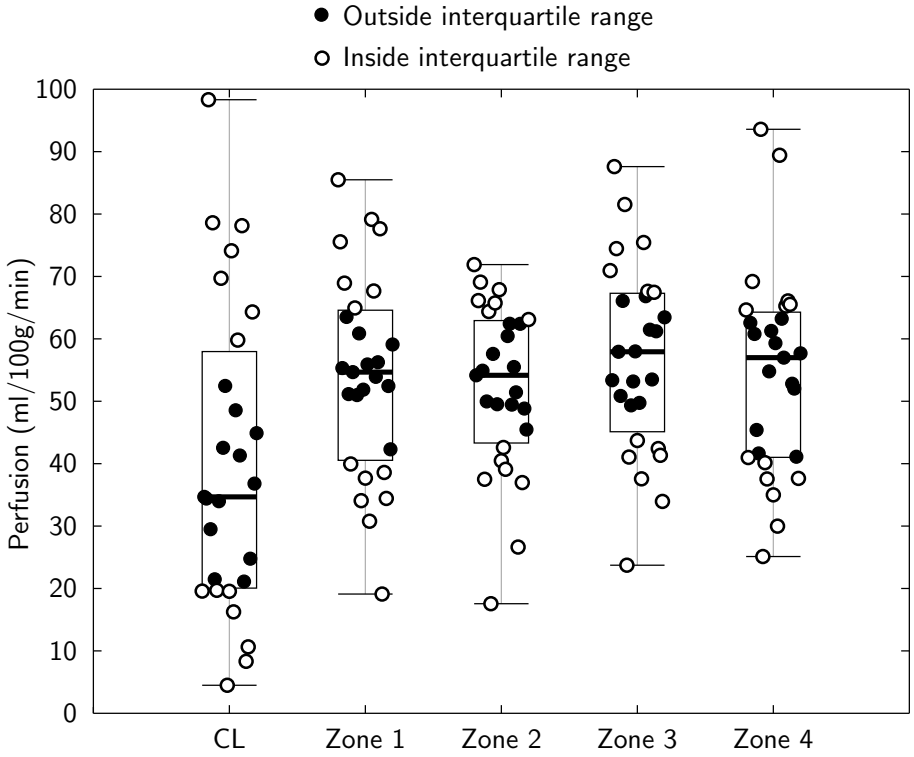


Figure 7.11: Boxplot illustrating perfusion within CLs and surrounding NAGM zones.

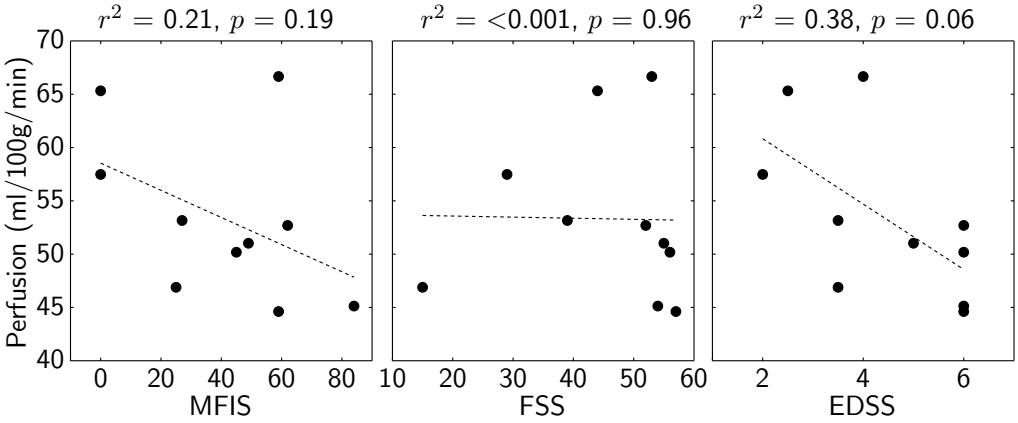


Figure 7.12: Clinical scores with perfusion.

7.6 Discussion

This is the first study to use arterial spin labelling to assess perfusion within grey matter cortical lesions in MS. This arterial spin labelling technique has been shown to be sensitive to localised perfusion deficits associated with cortical lesions, as observed in *Peruzzo et al., (2013)* [42] and *Hojjat et al., (2016)* [43]. A

summary of other studies to assess cortical lesion perfusion using DSC is shown in Table 7.4. This would allow longitudinal studies to be performed which could assess dynamic perfusion activity within the CL, which could not be performed with the use of gadolinium.

It can be seen that 73% of cortical lesions demonstrate a reduction in perfusion when compared to the local surrounding grey matter (23.2% reduction). When a paired two-tailed t-test was used to compare CL perfusion with LNAGM, the reduction was found to be significant (p=0.013). This result is in agreement with *Peruzzo et al., (2013)* [42] and *Hojjat et al., (2016)* [43] who used dynamic susceptibility contrast (DSC) to detect perfusion deficits in CLs. However, *Peruzzo et al., (2013)* detected a perfusion reduction of 45% in CLs, and *Hojjat et al., (2016)* detected a reduction in perfusion of 48% in CLs of cognitively impaired patients. A difference in perfusion reduction can be seen between the DSC and ASL techniques, which could be attributed to the different SNR and sensitivities for the two techniques. The ASL data contained vascular contamination due to the inability to suppress the vascular signal. This vascular signal may still be present in the CLs which were deemed eligible and be biasing the tissue perfusion, which may be a reason for the difference in detected perfusion reduction.

This study also detected a larger number of hyperperfused cortical lesions (27%) compared the study by *Peruzzo et al., (2013)* [42] (10%). The number of hyperperfusion lesions in the study by *Hojjat et al., (2016)* [43] was not reported. The larger fraction of hyperperfused CLs in this study could again be biased due to vascular contamination from ASL. The larger sample size of CLs assessed in *Peruzzo et al., (2013)* [42] may also provide a more accurate proportion of hyperperfusion CLs.

The perfusion changes relating to distance from cortical lesions has not previously been assessed. The perfusion inside the CLs was found to be significantly reduced to all surrounding zones, however there was no significant difference in perfusion between any of the zones. This could suggest that the damage caused by demylination in the cortex is localised and does not cause proximal damage. Alternatively, there may be proximal damage but it does not present as a perfusion reduction. The SNR of the sequence may also be

	This study	Peruzzo et al., (2013) [42]	Hojjat et al., (2016) [43]
Patients	4 PP, 1 SP, 7 RR	44 RR	39 RR
Technique	ASL	DSC	DSC
Field Strength (T)	7	1.5	3
Resolution (mm)	1.2×1.2×3	0.9×0.9×6	2.3×2.4×4
Slice Gap (mm)	N/A	1	0
Number of CLs	27	162	33
Hyperperfused CLs	27%	10%	N/A
CL perfusion compared to NAGM	-23%	-45%	-48%
Structural scan for CL identification	PSIR	DIR	PSIR

Table 7.4: Summary of MR protocols and findings of studies which have assessed cortical lesion perfusion compared to NAGM.

inefficient to detect subtle perfusion gradients within the cortex.

The whole grey matter perfusion did not show any significant correlation with the clinical scores (MFIS, FSS and EDSS), although the whole grey matter perfusion demonstrated a strong correlation with EDSS. The positioning of the single slice used to acquire ASL data was dictated by the location of the cortical lesion, meaning that the slice covered many different brain regions which varied from subject to subject. Cerebral blood flow is known to spatially vary across the head, so a single arbitrary slice is not sufficient to understand cortical perfusion as a whole. This may explain the variance in the whole grey matter perfusion values and the lack of correlation with clinical scores.

The arterial spin labelling protocol used to acquire this data had some limitations which could have affected the results. The coverage was limited to a single slice due to two factors; the time to acquire a slice and the SAR. The time to acquire a single slice using this readout was 593 ms, which would make quantifying perfusion in later slices difficult due to the decay of the blood signal. Additionally, the high SAR of this sequence also did not allow for contiguous slices, and a minimum slice gap of 1 mm would need to be

implemented. More slices could have been added either by using simultaneous multi-slice selection excitation [212] or using a FLASH acquisition, however, both come at the cost of SNR which is already limited. The single slice approach also introduces difficulties with motion correction, as only rotation about the z-axis and translation along the x-y plane can be corrected. Any data showing rotation about the x and y axis, or translation along the z-direction must be discarded. This acquisition does not allow for the suppression of vascular signals as described in Section 4.2.4.3 as bipolar gradients need to be added prior to each line of k-space. This would destroy the balanced nature of the sequences and thus the two are incompatible. Currently the bSSFP readout is not often used with arterial spin labelling, such that recommended implementations and optimised parameters have not been explored.

7.7 Conclusion

In this work, perfusion was assessed in cortical lesions and compared to surrounding grey matter in patients with Multiple Sclerosis. The spatial variance in perfusion surrounding cortical lesions was also assessed. A localised perfusion deficit was found inside cortical lesions when compared to surrounding grey matter. This perfusion deficit did not extend beyond the boundary of the cortical lesion, however and perfusion was found to be consistent within grey matter regardless of the distance from the CL. The measures of whole grey matter perfusion did not correlate with any clinical measures. The findings of this study agreed with results reported in previous literature, however this study required no exogenous contrast agent. This study has shown that arterial spin labelling at ultra high field is sufficiently sensitive to detect small localised changes to perfusion within the grey matter.

8 Conclusion

This thesis has used arterial spin labelling, phase contrast angiography, structural, and functional MRI data to investigate haemodynamic abnormalities in neurodegenerative disease, particularly in Alzheimer's Disease, Huntington's Disease and Multiple Sclerosis.

Whilst arterial spin labelling is still not used clinically for diagnosis, it has been shown to be a powerful non-invasive biomarker and excellent research tool for understanding perfusion when contrast enhanced scans cannot be used. The European Cooperation in Science and Technology (COST) Action is currently working on methods to improve and validate ASL, to allow its development into a reliable clinical tool for the diagnosis for dementia. The ultimate aim of the COST Action is to provide repeatable and robust perfusion measures from scanners of all vendors and field strengths, though the current focus is at MR field strengths of 1.5 and 3 T. In addition, a consensus has been reached as to the recommended implementation of ASL at 3 T [60], outlining the optimised parameters and planning protocols in order to normalise ASL acquisitions between studies. This chapter summarises the key findings in each of the experimental chapters, and directions for future research to follow on from these studies, with the primary focus on the implementation of methods at ultra-high field (7T).

Chapter 5 studies the structural and functional changes in Alzheimer's Disease. It is shown using ASL that haemodynamics are impaired in grey matter across the cortex in Alzheimer's Disease patients compared to age-matched healthy controls. This was displayed as a reduction in perfusion and increased transit time across the entire grey matter. It was shown that this perfusion reduction correlated with the severity of cortical thinning using the CAT12 Toolbox. In addition, a trend towards a reduction in functional connectivity, as assessed with fMRI, was observed in the Alzheimer's Disease patients in the Default Mode Network. Future work could develop an improved ASL and fMRI acquisition protocol, by utilising 3D-EPI or a simultaneous multi-slice (SMS) 2D-EPI acquisition to improve the spatial coverage of perfusion measures. The use of 3D-EPI would increase the signal-to-noise ratio (SNR), allowing fewer averages to be collected

to acquire a robust perfusion weighted image. This would be beneficial for the AD patients as the overall scan duration would be reduced.

In Chapter 6, vascular changes in Huntington's Disease (HD) were assessed. Atrophy of the striatum in HD is commonly described in the literature and was observed here using voxel-based morphometry. It was found that cerebral haemodynamics were altered across the cortex in Huntington's Disease patients compared to age-matched healthy controls, this manifests as reduced perfusion within the grey matter. A novelty of this study was to assess perfusion changes within the caudate and putamen using arterial spin labelling. A significant reduction in perfusion and a significant increase in transit time was observed in the caudate and putamen of HD patients compared to the healthy controls. In addition, an increase in arterial cerebral blood volume (aCBV) was observed in the grey matter in HD patients compared to the healthy control group. When the vascular structure itself was assessed, an increased fraction of smaller blood vessels was found, whereas the occurrence of larger vessels was lower in the HD group. A decrease in vessel density in the HD group was also observed, however this result is not supported by existing literature. A limitation of this study was the single slice coverage of the aCBV acquisition. Future work could increase the coverage of this acquisition by using a simultaneous multi-slice (SMS) 2D-EPI or 3D-EPI acquisition. When assessing vessel distributions in the brain, a time of flight (TOF) acquisition could be used as opposed to a phase contrast angiography approach used here. The recent adoption and success of this technique at 7 T [167] would allow for better understanding of vascular abnormalities at all levels of the vascular tree in HD. This would allow for confirmed improved sensitivity to the arterial side of the vascular tree, where vascular changes are most notably reported in the literature.

In the final Chapter on Multiple Sclerosis, it was found that cortical lesions contain reduced perfusion compared to surrounding normal appearing grey matter. Previous studies have demonstrated this using contrast enhanced methods, however this thesis demonstrates that high spatial resolution ASL at ultra-high field has the sensitivity to detect this reported perfusion deficit. Also assessed was the perfusion profile as a function of distance from the centre of the lesion, which demonstrated that grey matter perfusion is maintained immediately outside of the lesion boundary. The ASL protocol used a balanced

steady-state free precession (bSSFP) readout which was chosen to provide high spatial resolution and no image distortions such that it could be matched to the high resolution anatomical scans from which grey matter lesions were defined. However, this bSSFP ASL acquisition has some limitations. The ASL protocol used was limited by the spatial coverage, and the intrinsic nature of the balanced steady-state free precession (bSSFP) readout, which did not allow for vascular crushing. To increase the spatial coverage, a FLASH acquisition could be used with simultaneous multi-slice (SMS) imaging to avoid the SAR limitations which occur with the bSSFP acquisition. Despite this scheme resulting in a lower signal-to-noise ratio (SNR), the increased coverage and shorter scan duration would counter this providing increased SNR per unit time. Future work to assess baseline cortical perfusion in MS is currently under way. This study uses both dynamic susceptibility contrast (DSC) and ASL methods to assess perfusion in MS patients within the same scan session. This will allow ASL and the gold-standard DSC perfusion measures to be directly compared, and assess the validity of ASL. In addition, the same ASL protocol is being used in age-matched healthy controls to compare baseline perfusion measures with those in MS patients. The reproducibility of the ASL measures is being assessed as both MS patients and healthy controls are returning for a second scan session.

This thesis has presented original work to study the haemodynamic, functional and structural changes in neurodegenerative diseases. The methods developed here could be used to inform further studies of neurodegenerative disease at ultra-high field.

References

[1] Rabi, I.I.: On the process of space quantization. Phys. Rev. 49, 324–328 (Feb 1936)

[2] Lauterbur, P.C.: Image Formation by Induced Local Interactions: Examples Employing Nuclear Magnetic Resonance. Nature 242, 190–191 (1973)

[3] Mansfield, P.: Multi-planar image formation using nmr spin echoes. Journal of Physics C: Solid State Physics 10(3), L55 (1977)

[4] OECD: Health workforce. In: Health at a Glance 2015: OECD Indicators, pp. 79–98. Health at a Glance, OECD Publishing (nov 2015)

[5] Van Der Kolk, A.G., Hendrikse, J., Zwanenburg, J.J.M., Visser, F., Luijten, P.R.: Clinical applications of 7 T MRI in the brain. European Journal of Radiology 82(5), 708–718 (may 2013)

[6] McEvoy, L.K., Brewer, J.B.: Quantitative structural MRI for early detection of Alzheimer's disease. Expert Rev Neurother 10(11), 1675–1688 (2010)

[7] Traboulsee, A.L., Li, D.K.: The role of MRI in the diagnosis of multiple sclerosis. Adv Neurol 98, 125–146 (2006)

[8] Ogawa, S., Lee, T.M., Nayak, A.S., Glynn, P.: Oxygenation-sensitive contrast in magnetic resonance image of rodent brain at high magnetic fields. Magn Reson Med 14(1), 68–78 (1990)

[9] Babic, T.: The cholinergic hypothesis of Alzheimer's disease: a review of progress. J. Neurol. Neurosurg. Psychiatr. 67(4), 558 (1999)

[10] Sandson, T.A., O'Connor, M., Sperling, R.A., Edelman, R.R., Warach, S.: Noninvasive perfusion MRI in Alzheimer's disease: a preliminary report. Neurology 47(5), 1339–1342 (1996)

[11] Alsop, D.C., Detre, J.A., Grossman, M.: Assessment of cerebral blood flow in Alzheimer's disease by spin-labeled magnetic resonance imaging. Ann. Neurol. 47(1), 93–100 (2000)

[12] Johnson, N.A., Jahng, G.H., Weiner, M.W., Miller, B.L., Chui, H.C., Jagust, W.J., Gorno-Tempini, M.L., Schuff, N.: Pattern of cerebral hypoperfusion in Alzheimer disease and mild cognitive impairment

measured with arterial spin-labeling MR imaging: initial experience. Radiology 234(3), 851–859 (2005)

[13] Asllani, I., Habeck, C., Scarmeas, N., Borogovac, A., Brown, T.R., Stern, Y.: Multivariate and univariate analysis of continuous arterial spin labeling perfusion MRI in Alzheimer's disease. J. Cereb. Blood Flow Metab. 28(4), 725–736 (2008)

[14] Alsop, D.C., Casement, M., de Bazelaire, C., Fong, T., Press, D.Z.: Hippocampal hyperperfusion in Alzheimer's disease. Neuroimage 42(4), 1267–1274 (2008)

[15] Dai, W., Lopez, O.L., Carmichael, O.T., Becker, J.T., Kuller, L.H., Gach, H.M.: Mild cognitive impairment and alzheimer disease: patterns of altered cerebral blood flow at MR imaging. Radiology 250(3), 856–866 (2009)

[16] Fleisher, A.S., Podraza, K.M., Bangen, K.J., Taylor, C., Sherzai, A., Sidhar, K., Liu, T.T., Dale, A.M., Buxton, R.B.: Cerebral perfusion and oxygenation differences in Alzheimer's disease risk. Neurobiol. Aging 30(11), 1737–1748 (Nov 2009)

[17] Yoshiura, T., Hiwatashi, A., Noguchi, T., Yamashita, K., Ohyagi, Y., Monji, A., Nagao, E., Kamano, H., Togao, O., Honda, H.: Arterial spin labelling at 3-T MR imaging for detection of individuals with Alzheimer's disease. Eur Radiol 19(12), 2819–2825 (2009)

[18] Ding, B., Ling, H.W., Zhang, Y., Huang, J., Zhang, H., Wang, T., Yan, F.H.: Pattern of cerebral hyperperfusion in Alzheimer's disease and amnestic mild cognitive impairment using voxel-based analysis of 3D arterial spin-labeling imaging: initial experience. Clin Interv Aging 9 (2014)

[19] Binnewijzend, M.A., Kuijer, J.P., Benedictus, M.R., van der Flier, W.M., Wink, A.M., Wattjes, M.P., van Berckel, B.N., Scheltens, P., Barkhof, F.: Cerebral blood flow measured with 3D pseudocontinuous arterial spin-labeling MR imaging in Alzheimer disease and mild cognitive impairment: a marker for disease severity. Radiology 267(1), 221–230 (2013)

[20] Bron, E.E., Steketee, R.M., Houston, G.C., Oliver, R.A., Achterberg, H.C., Loog, M., van Swieten, J.C., Hammers, A., Niessen, W.J., Smits, M., Klein, S.: Diagnostic classification of arterial spin labeling and structural MRI in presenile early stage dementia. Hum Brain Mapp 35(9), 4916–4931 (2014)

[21] Xekardaki, A., Rodriguez, C., Montandon, M.L., Toma, S., Tombeur, E., Herrmann, F.R., Zekry, D., Lovblad, K.O., Barkhof, F., Giannakopoulos, P., Haller, S.: Arterial spin labeling may contribute to the prediction of cognitive deterioration in healthy elderly individuals. Radiology 274(2), 490–499 (2015)

[22] Kaneta, T., Katsuse, O., Hirano, T., Ogawa, M., Shihikura-Hino, A., Yoshida, K., Odawara, T., Hirayasu, Y., Inoue, T.: Voxel-wise correlations between cognition and cerebral blood flow using arterial spin-labeled perfusion MRI in patients with Alzheimer's disease: a cross-sectional study. BMC Neurol 17(1), 91–100 (2017)

[23] Benedictus, M.R., Leeuwis, A.E., Binnewijzend, M.A., Kuijer, J.P., Scheltens, P., Barkhof, F., van der Flier, W.M., Prins, N.D.: Lower cerebral blood flow is associated with faster cognitive decline in Alzheimer's disease. Eur Radiol 27(3), 1169–1175 (2017)

[24] Leeuwis, A.E., Benedictus, M.R., Kuijer, J.P.A., Binnewijzend, M.A.A., Hooghiemstra, A.M., Verfaillie, S.C.J., Koene, T., Scheltens, P., Barkhof, F., Prins, N.D., van der Flier, W.M.: Lower cerebral blood flow is associated with impairment in multiple cognitive domains in Alzheimer's disease. Alzheimers Dement 13(5), 531–540 (2017)

[25] Wang, L., Zang, Y., He, Y., Liang, M., Zhang, X., Tian, L., Wu, T., Jiang, T., Li, K.: Changes in hippocampal connectivity in the early stages of Alzheimer's disease: evidence from resting state fMRI. Neuroimage 31(2), 496–504 (2006)

[26] Zhang, H.Y., Wang, S.J., Xing, J., Liu, B., Ma, Z.L., Yang, M., Zhang, Z.J., Teng, G.J.: Detection of PCC functional connectivity characteristics in resting-state fMRI in mild Alzheimer's disease. Behavioural Brain Research 197(1), 103–108 (2009)

[27] Wang, K., Liang, M., Wang, L., Tian, L., Zhang, X., Li, K., Jiang, T.: Altered functional connectivity in early Alzheimer's disease: A resting-state fMRI study. Human Brain Mapping 28(10), 967–978 (2007)

[28] Zhou, J., Greicius, M.D., Gennatas, E.D., Growdon, M.E., Jang, J.Y., Rabinovici, G.D., Kramer, J.H., Weiner, M., Miller, B.L., Seeley, W.W.: Divergent network connectivity changes in behavioural variant frontotemporal dementia and Alzheimer's disease. Brain 133(5), 1352–1367

(2010)

[29] Greicius, M.D., Srivastava, G., Reiss, A.L., Menon, V.: Default-mode network activity distinguishes Alzheimer's disease from healthy aging: Evidence from functional MRI. Proceedings of the National Academy of Sciences 101(13), 4637–4642 (2004)

[30] He, Y., Wang, L., Zang, Y., Tian, L., Zhang, X., Li, K., Jiang, T.: Regional coherence changes in the early stages of Alzheimer's disease: A combined structural and resting-state functional MRI study. NeuroImage 35(2), 488–500 (2007)

[31] Liu, Y., Wang, K., YU, C., He, Y., Zhou, Y., Liang, M., Wang, L., Jiang, T.: Regional homogeneity, functional connectivity and imaging markers of Alzheimer's disease: A review of resting-state fMRI studies. Neuropsychologia 46(6), 1648–1656 (2008)

[32] MacDonald, M.E., Ambrose, C.M., Duyao, M.P., Myers, R.H., Lin, C., Srinidhi, L., Barnes, G., Taylor, S.A., James, M., Groot, N., MacFarlane, H., Jenkins, B., Anderson, M.A., Wexler, N.S., Gusella, J.F.: A novel gene containing a trinucleotide repeat that is expanded and unstable on huntington's disease chromosomes. Cell 72(6), 971 – 983 (1993)

[33] Ichise, M., Toyama, H., Fornazzari, L., Ballinger, J.R., Kirsh, J.C.: Iodine-123-IBZM dopamine D2 receptor and technetium-99m-HMPAO brain perfusion SPECT in the evaluation of patients with and subjects at risk for Huntington's disease. 34(8), 1274–1281 (aug 1993)

[34] Sax, D.S., Powsner, R., Kim, A., Tilak, S., Bhatia, R., Cupples, L.A., Myers, R.H.: Evidence of cortical metabolic dysfunction in early Huntington's disease by single-photon-emission computed tomography. Mov Disord. 11(6), 671–677 (nov 1996)

[35] Harris, G.J., Codori, A.M., Lewis, R.F., Schmidt, E., Bedi, A., Brandt, J.: Reduced basal ganglia blood flow and volume in pre-symptomatic, gene-tested persons at-risk for Huntington's disease. Brain 122(9), 1667–1678 (sep 1999)

[36] Wolf, R.C., Grön, G., Sambataro, F., Vasic, N., Wolf, N.D., Thomann, P.A., Saft, C., Landwehrmeyer, G.B., Orth, M.: Journal of Cerebral Blood Flow & Metabolism

[37] Chen, J.J., Salat, D.H., Rosas, H.D.: Complex relationships between cerebral blood flow and brain atrophy in early Huntington's disease. NeuroImage 59(2), 1043–1051 (jan 2012)

[38] Franciosi, S., Ryu, J.K., Shim, Y., Hill, A., Connolly, C., Hayden, M.R., McLarnon, J.G., Leavitt, B.R.: Age-dependent neurovascular abnormalities and altered microglial morphology in the YAC128 mouse model of Huntington disease. Neurobiology of Disease 45(1), 438–449 (2012)

[39] Cisbani, G., Freeman, T.B., Soulet, D., Saint-Pierre, M., Gagnon, D., Parent, M., Hauser, R.A., Barker, R.A., Cicchetti, F.: Striatal allografts in patients with Huntington's disease: Impact of diminished astrocytes and vascularization on graft viability. Brain 136(2), 433–443 (2013)

[40] Lin, C.Y., Hsu, Y.H., Lin, M.H., Yang, T.H., Chen, H.M., Chen, Y.C., Hsiao, H.Y., Chen, C.C., Chern, Y., Chang, C.: Neurovascular abnormalities in humans and mice with Huntington's disease. Experimental Neurology 250, 20–30 (dec 2013)

[41] Pirko, I., Lucchinetti, C.F., Sriram, S., Bakshi, R.: Gray matter involvement in multiple sclerosis. Neurology 68(9), 634–642 (feb 2007)

[42] Peruzzo, D., Castellaro, M., Calabrese, M., Veronese, E., Rinaldi, F., Bernardi, V., Favaretto, A., Gallo, P., Bertoldo, A.: Heterogeneity of cortical lesions in multiple sclerosis: an MRI perfusion study. Journal of cerebral blood flow and metabolism : official journal of the International Society of Cerebral Blood Flow and Metabolism 33(3), 457–63 (2013)

[43] Hojjat, S.P., Kincal, M., Vitorino, R., Cantrell, C.G., Feinstein, A., Zhang, L., Lee, L., O'Connor, P., Carroll, T.J., Aviv, R.I.: Cortical perfusion alteration in normal-Appearing gray matter is most sensitive to disease progression in relapsing-remitting multiple sclerosis. American Journal of Neuroradiology 37(8), 1454–1461 (2016)

[44] Pruessmann, K.P., Weiger, M., Scheidegger, M.B., Boesiger, P.: SENSE: sensitivity encoding for fast MRI. Magn Reson Med 42(5), 952–962 (Nov 1999)

[45] James, W.: The Principles of Psychology. 'Henry Holt and Company' (1890)

[46] Roy, C.S., Sherrington, C.S.: On the Regulation of the Blood-supply of the Brain. J. Physiol. (Lond.) 11(1-2), 85–158 (1890)

[47] Kety, S.S., Schmidt, C.F.: The nitrous oxide method for the quantitative determination of cerebral blood flow in man: theory, procedure and normal values. J. Clin. Invest. 27(4), 476–483 (1948)

[48] Lassen, N.A., Hoedt-Rasmussen, K., Sorensen, S.C., Skinhoj, E., Cronquist, S., Bodforss, B., Ingvar, D.H.: Regional cerebral blood flow in man determined by krypton-8. Neurology 13, 719–727 (1963)

[49] Ingvar, D.H., Risberg, J.: Influence of mental activity upon regional cerebral blood flow in man. A preliminary study. Acta Neurol. Scand., Suppl. 14, 183–186 (1965)

[50] Yamamoto, Y.L., Thompson, C.J., Meyer, E., Robertson, J.S., Feindel, W.: Dynamic positron emission tomography for study of cerebral hemodynamics in a cross section of the head using positron-emitting 68Ga-EDTA and 77Kr. J Comput Assist Tomogr 1(1), 43–56 (1977)

[51] Belliveau, J.W., Kennedy, D.N., McKinstry, R.C., Buchbinder, B.R., Weisskoff, R.M., Cohen, M.S., Vevea, J.M., Brady, T.J., Rosen, B.R.: Functional mapping of the human visual cortex by magnetic resonance imaging. Science 254(5032), 716–719 (1991)

[52] Ogawa, S., Tank, D.W., Menon, R., Ellermann, J.M., Kim, S.G., Merkle, H., Ugurbil, K.: Intrinsic signal changes accompanying sensory stimulation: functional brain mapping with magnetic resonance imaging. Proc. Natl. Acad. Sci. U.S.A. 89(13), 5951–5955 (1992)

[53] Le Bihan, D., Breton, E., Lallemand, D., Grenier, P., Cabanis, E., Laval-Jeantet, M.: MR imaging of intravoxel incoherent motions: application to diffusion and perfusion in neurologic disorders. Radiology 161(2), 401–407 (1986)

[54] Kim, S.G., Ackerman, J.J.: Quantitative determination of tumor blood flow and perfusion via deuterium nuclear magnetic resonance spectroscopy in mice. Cancer Res. 48(12), 3449–3453 (1988)

[55] Eleff, S.M., Schnall, M.D., Ligetti, L., Osbakken, M., Subramanian, V.H., Chance, B., Leigh, J.S.: Concurrent measurements of cerebral blood flow, sodium, lactate, and high-energy phosphate metabolism using 19F, 23Na, 1H, and 31P nuclear magnetic resonance spectroscopy. Magn Reson Med 7(4), 412–424 (1988)

[56] Detre, J.A., Leigh, J.S., Williams, D.S., Koretsky, A.P.: Perfusion imaging. Magn Reson Med 23(1), 37–45 (1992)

[57] Talagala, S.L., Ye, F.Q., Ledden, P.J., Chesnick, S.: Whole-brain 3D perfusion MRI at 3.0 T using CASL with a separate labeling coil. Magn Reson Med 52(1), 131–140 (2004)

[58] Li, X., Wang, D., Moeller, S., Ugurbil, K., Metzger, G.J.: Feasibility of applying MB EPI PCASL for high-resolution whole brain perfusion imaging at 7T. Proc Int Soc Mag Reson Med p. 995 (2014)

[59] Feinberg, D.A., Oshio, K.: GRASE (gradient- and spin-echo) MR imaging: a new fast clinical imaging technique. Radiology 181(2), 597–602 (1991)

[60] Alsop, D.C., Detre, J.A., Golay, X., Gunther, M., Hendrikse, J., Hernandez-Garcia, L., Lu, H., MacIntosh, B.J., Parkes, L.M., Smits, M., van Osch, M.J., Wang, D.J., Wong, E.C., Zaharchuk, G.: Recommended implementation of arterial spin-labeled perfusion MRI for clinical applications: A consensus of the ISMRM perfusion study group and the European consortium for ASL in dementia. Magn Reson Med 73(1), 102–116 (2015)

[61] Gunther, M., Bock, M., Schad, L.R.: Arterial spin labeling in combination with a look-locker sampling strategy: inflow turbo-sampling EPI-FAIR (ITS-FAIR). Magn Reson Med 46(5), 974–984 (2001)

[62] Look, D., Locker, D.R.: Time saving in measurement of nmr and epr relaxation times. Review of Scientific Instruments 41(2), 250–251 (1970)

[63] Francis, S.T., Bowtell, R., Gowland, P.A.: Modeling and optimization of Look-Locker spin labeling for measuring perfusion and transit time changes in activation studies taking into account arterial blood volume. Magn Reson Med 59(2), 316–325 (2008)

[64] Ogg, R.J., Kingsley, P.B., Taylor, J.S.: WET, a T1- and B1-insensitive water-suppression method for in vivo localized 1H NMR spectroscopy. J Magn Reson B 104(1), 1–10 (1994)

[65] Ye, F.Q., Frank, J.A., Weinberger, D.R., McLaughlin, A.C.: Noise reduction in 3D perfusion imaging by attenuating the static signal in arterial spin tagging (ASSIST). Magn Reson Med 44(1), 92–100 (2000)

[66] Garcia, D.M., Duhamel, G., Alsop, D.C.: Efficiency of inversion pulses for background suppressed arterial spin labeling. Magn Reson Med 54(2),

366–372 (2005)

[67] Hall, E.L.: Quantitative methods to assess cerebral haemodynamics. Ph.D. thesis, University of Nottingham, Sir Peter Mansfield Imaging Centre (2012)

[68] Cavusoglu, M., Pfeuffer, J., Ugurbil, K., Uludag, K.: Comparison of pulsed arterial spin labeling encoding schemes and absolute perfusion quantification. Magn Reson Imaging 27(8), 1039–1045 (2009)

[69] Kwong, K.K., Chesler, D.A., Weisskoff, R.M., Donahue, K.M., Davis, T.L., Ostergaard, L., Campbell, T.A., Rosen, B.R.: MR perfusion studies with T1-weighted echo planar imaging. Magn Reson Med 34(6), 878–887 (1995)

[70] Buxton, R.B., Frank, L.R., Wong, E.C., Siewert, B., Warach, S., Edelman, R.R.: A general kinetic model for quantitative perfusion imaging with arterial spin labeling. Magn Reson Med 40(3), 383–396 (1998)

[71] Jenkinson, M., Bannister, P., Brady, M., Smith, S.: Improved optimization for the robust and accurate linear registration and motion correction of brain images. Neuroimage 17(2), 825–841 (2002)

[72] Tan, H., Maldjian, J.A., Pollock, J.M., Burdette, J.H., Yang, L.Y., Deibler, A.R., Kraft, R.A.: A fast, effective filtering method for improving clinical pulsed arterial spin labeling MRI. J Magn Reson Imaging 29(5), 1134–1139 (2009)

[73] Maumet, C., Maurel, P., Ferre, J.C., Barillot, C.: Robust estimation of the cerebral blood flow in arterial spin labelling. Magn Reson Imaging 32(5), 497–504 (2014)

[74] Asllani, I., Borogovac, A., Brown, T.R.: Regression algorithm correcting for partial volume effects in arterial spin labeling MRI. Magn Reson Med 60(6), 1362–1371 (2008)

[75] Chalela, J.A., Alsop, D.C., Gonzalez-Atavales, J.B., Maldjian, J.A., Kasner, S.E., Detre, J.A.: Magnetic resonance perfusion imaging in acute ischemic stroke using continuous arterial spin labeling. Stroke 31(3), 680–687 (2000)

[76] Wolk, D.A., Detre, J.A.: Arterial spin labeling MRI: an emerging biomarker for Alzheimer's disease and other neurodegenerative conditions. Curr. Opin. Neurol. 25(4), 421–428 (2012)

[77] Lim, Y.M., Cho, Y.W., Shamim, S., Solomon, J., Birn, R., Luh, W.M., Gaillard, W.D., Ritzl, E.K., Theodore, W.H.: Usefulness of pulsed arterial spin labeling MR imaging in mesial temporal lobe epilepsy. Epilepsy Res. 82(2-3), 183–189 (2008)

[78] Schuff, N., Zhang, Y., Zhan, W., Lenoci, M., Ching, C., Boreta, L., Mueller, S.G., Wang, Z., Marmar, C.R., Weiner, M.W., Neylan, T.C.: Patterns of altered cortical perfusion and diminished subcortical integrity in posttraumatic stress disorder: an MRI study. Neuroimage 54 Suppl 1, S62–68 (2011)

[79] Villringer, A., Rosen, B.R., Belliveau, J.W., Ackerman, J.L., Lauffer, R.B., Buxton, R.B., Chao, Y.S., Wedeen, V.J., Brady, T.J.: Dynamic imaging with lanthanide chelates in normal brain: contrast due to magnetic susceptibility effects. Magn Reson Med 6(2), 164–174 (1988)

[80] Meier, P., Zieler, K.L.: On the theory of the indicator-dilution method for measurement of blood flow and volume. J Appl Physiol 6(12), 731–744 (1954)

[81] McDonald, R.J., McDonald, J.S., Kallmes, D.F., Jentoft, M.E., Murray, D.L., Thielen, K.R., Williamson, E.E., Eckel, L.J.: Intracranial Gadolinium Deposition after Contrast-enhanced MR Imaging. Radiology 275(3), 772–782 (2015)

[82] Kanda, T., Matsuda, M., Oba, H., Toyoda, K., Furui, S.: Gadolinium Deposition after Contrast-enhanced MR Imaging. Radiology 277(3), 924–925 (2015)

[83] Wardlaw, J.M., White, P.M.: The detection and management of unruptured intracranial aneurysms. Brain 123 (Pt 2), 205–221 (Feb 2000)

[84] Kumral, E., Kisabay, A., Atac, C.: Lesion patterns and etiology of ischemia in superior cerebellar artery territory infarcts. Cerebrovasc. Dis. 19(5), 283–290 (2005)

[85] Buxton, R.B., Frank, L.R.: A model for the coupling between cerebral blood flow and oxygen metabolism during neural stimulation. J. Cereb. Blood Flow Metab. 17(1), 64–72 (Jan 1997)

[86] Bandettini, P.A., Jesmanowicz, A., Wong, E.C., Hyde, J.S.: Processing strategies for time-course data sets in functional MRI of the human brain. Magn Reson Med 30(2), 161–173 (1993)

[87] Smith, S.M., Fox, P.T., Miller, K.L., Glahn, D.C., Fox, P.M., Mackay, C.E., Filippini, N., Watkins, K.E., Toro, R., Laird, A.R., Beckmann, C.F.: Correspondence of the brain's functional architecture during activation and rest. Proc. Natl. Acad. Sci. U.S.A. 106(31), 13040–13045 (2009)

[88] Gauthier, S., Reisberg, B., Zaudig, M., Petersen, R.C., Ritchie, K., Broich, K., Belleville, S., Brodaty, H., Bennett, D., Chertkow, H., Cummings, J.L., de Leon, M., Feldman, H., Ganguli, M., Hampel, H., Scheltens, P., Tierney, M.C., Whitehouse, P., Winblad, B.: Mild cognitive impairment. The Lancet 367(9518), 1262 – 1270 (2006)

[89] Baron, J., Chételat, G., Desgranges, B., Perchey, G., Landeau, B., de la Sayette, V., Eustache, F.: In Vivo Mapping of Gray Matter Loss with Voxel-Based Morphometry in Mild Alzheimer's Disease. NeuroImage 14(2), 298–309 (2001)

[90] Tomlinson, B., Blessed, G., Roth, M.: Observations on the brains of non-demented old people. Journal of the Neurological Sciences 7(2), 331–356 (1968)

[91] Braak, H., Braak, E.: Neuropathological stageing of Alzheimer-related changes. Acta Neuropathologica 82(4), 239–259 (1991)

[92] Delacourte, A., David, J.P., Sergeant, N., Buée, L., Wattez, A., Vermersch, P., Ghozali, F., Fallet-Bianco, C., Pasquier, F., Lebert, F., Petit, H., Di Menza, C.: The biochemical pathway of neurofibrillary degeneration in aging and Alzheimer's disease. Neurology 52(6), 1158–65 (1999)

[93] Fox, N.C., Scahill, R.I., Crum, W.R., Rossor, M.N.: Correlation between rates of brain atrophy and cognitive decline in AD. Neurology 52(8), 1687–9 (1999)

[94] Josephs, K.A., Whitwell, J.L., Ahmed, Z., Shiung, M.M., Weigand, S.D., Knopman, D.S., Boeve, B.F., Parisi, J.E., Petersen, R.C., Dickson, D.W., Jack, C.R., Jr.: Beta-amyloid burden is not associated with rates of brain atrophy. Annals of neurology 63(2), 204–12 (2008)

[95] Schott, J., Crutch, S., Frost, C., Warrington, E., Rossor, M., Fox, N.: Neuropsychological correlates of whole brain atrophy in Alzheimer's disease. Neuropsychologia 46(6), 1732–1737 (2008)

[96] Sluimer, J.D., Bouwman, F.H., Vrenken, H., Blankenstein, M.A., Barkhof, F., van der Flier, W.M., Scheltens, P.: Whole-brain atrophy rate and CSF

biomarker levels in MCI and AD: A longitudinal study. Neurobiology of Aging 31(5), 758–764 (2010)

[97] Sluimer, J.D., van der Flier, W.M., Karas, G.B., Fox, N.C., Scheltens, P., Barkhof, F., Vrenken, H.: Whole-Brain Atrophy Rate and Cognitive Decline: Longitudinal MR Study of Memory Clinic Patients. Radiology 248(2), 590–598 (2008)

[98] Cardenas, V.A., Chao, L.L., Studholme, C., Yaffe, K., Miller, B.L., Madison, C., Buckley, S.T., Mungas, D., Schuff, N., Weiner, M.W.: Brain atrophy associated with baseline and longitudinal measures of cognition. Neurobiology of aging 32(4), 572–80 (2011)

[99] Thompson, P.M., Hayashi, K.M., de Zubicaray, G.I., Janke, A.L., Rose, S.E., Semple, J., Hong, M.S., Herman, D.H., Gravano, D., Doddrell, D.M., Toga, A.W.: Mapping hippocampal and ventricular change in Alzheimer disease. NeuroImage 22(4), 1754–1766 (2004)

[100] Jack, C.R., Shiung, M.M., Gunter, J.L., O'Brien, P.C., Weigand, S.D., Knopman, D.S., Boeve, B.F., Ivnik, R.J., Smith, G.E., Cha, R.H., Tangalos, E.G., Petersen, R.C., Petersen, R.: Comparison of different MRI brain atrophy rate measures with clinical disease progression in AD. Neurology 62(4), 591–600 (2004)

[101] Morra, J.H., Tu, Z., Apostolova, L.G., Green, A.E., Avedissian, C., Madsen, S.K., Parikshak, N., Hua, X., Toga, A.W., Jack, C.R., Schuff, N., Weiner, M.W., Thompson, P.M., Alzheimer's Disease Neuroimaging Initiative, P.M., Initiative, t.A.D.N.: Automated 3D mapping of hippocampal atrophy and its clinical correlates in 400 subjects with Alzheimer's disease, mild cognitive impairment, and elderly controls. Human brain mapping 30(9), 2766–88 (2009)

[102] Ridha, B.H., Anderson, V.M., Barnes, J., Boyes, R.G., Price, S.L., Rossor, M.N., Whitwell, J.L., Jenkins, L., Black, R.S., Grundman, M., Fox, N.C.: Volumetric MRI and cognitive measures in Alzheimer disease. Journal of Neurology 255(4), 567–574 (2008)

[103] Hua, X., Lee, S., Yanovsky, I., Leow, A.D., Chou, Y.Y., Ho, A.J., Gutman, B., Toga, A.W., Jack, C.R., Bernstein, M.A., Reiman, E.M., Harvey, D.J., Kornak, J., Schuff, N., Alexander, G.E., Weiner, M.W., Thompson, P.M., Alzheimer's Disease Neuroimaging Initiative, P.M., Initiative, t.A.D.N.:

Optimizing power to track brain degeneration in Alzheimer's disease and mild cognitive impairment with tensor-based morphometry: an ADNI study of 515 subjects. NeuroImage 48(4), 668–81 (2009)

[104] Ho, A.J., Hua, X., Lee, S., Leow, A.D., Yanovsky, I., Gutman, B., Dinov, I.D., Leporé, N., Stein, J.L., Toga, A.W., Jack, C.R., Bernstein, M.A., Reiman, E.M., Harvey, D.J., Kornak, J., Schuff, N., Alexander, G.E., Weiner, M.W., Thompson, P.M., Alzheimer's Disease Neuroimaging Initiative, P.M., Initiative, t.A.D.N.: Comparing 3 T and 1.5 T MRI for tracking Alzheimer's disease progression with tensor-based morphometry. Human brain mapping 31(4), 499–514 (2010)

[105] Storandt, M., Mintun, M.A., Head, D., Morris, J.C., RL, B., DM, H.: Cognitive Decline and Brain Volume Loss as Signatures of Cerebral Amyloid-β Peptide Deposition Identified With Pittsburgh Compound B. Archives of Neurology 66(12), 176–183 (2009)

[106] Dubois, B., Feldman, H.H., Jacova, C., DeKosky, S.T., Barberger-Gateau, P., Cummings, J., Delacourte, A., Galasko, D., Gauthier, S., Jicha, G., Meguro, K., O'Brien, J., Pasquier, F., Robert, P., Rossor, M., Salloway, S., Stern, Y., Visser, P.J., Scheltens, P.: Research criteria for the diagnosis of Alzheimer's disease: revising the NINCDS-ADRDA criteria (2007)

[107] Scheltens, P., Leys, D., Barkhof, F., Huglo, D., Weinstein, H.C., Vermersch, P., Kuiper, M., Steinling, M., Wolters, E.C., Valk, J.: Atrophy of medial temporal lobes on MRI in "probable" Alzheimer's disease and normal ageing: diagnostic value and neuropsychological correlates. Journal of neurology, neurosurgery, and psychiatry 55(10), 967–72 (1992)

[108] Korf, E.S.C., Wahlund, L.O., Visser, P.J., Scheltens, P.: Medial temporal lobe atrophy on MRI predicts dementia in patients with mild cognitive impairment. Neurology 63(1), 94–100 (2004)

[109] DeCarli, C., Frisoni, G.B., Clark, C.M., Harvey, D., Grundman, M., Petersen, R.C., Thal, L.J., Jin, S., Jack, C.R., Scheltens, P.: Qualitative estimates of medial temporal atrophy as a predictor of progression from mild cognitive impairment to dementia. Arch. Neurol. 64(1), 108–115 (Jan 2007)

[110] Duara, R., Loewenstein, D.A., Potter, E., Appel, J., Greig, M.T., Urs, R., Shen, Q., Raj, A., Small, B., Barker, W., Schofield, E., Wu, Y., Potter, H.:

Medial temporal lobe atrophy on MRI scans and the diagnosis of Alzheimer disease. Neurology 71(24), 1986–92 (2008)

[111] Burton, E.J., Barber, R., Mukaetova-Ladinska, E.B., Robson, J., Perry, R.H., Jaros, E., Kalaria, R.N., O'Brien, J.T.: Medial temporal lobe atrophy on MRI differentiates Alzheimer's disease from dementia with Lewy bodies and vascular cognitive impairment: a prospective study with pathological verification of diagnosis. Brain 132(1), 195–203 (2009)

[112] Shi, F., Liu, B., Zhou, Y., Yu, C., Jiang, T.: Hippocampal volume and asymmetry in mild cognitive impairment and Alzheimer's disease: Meta-analyses of MRI studies. Hippocampus 19(11), 1055–1064 (2009)

[113] van der Flier, W.M., van Straaten, E.C.W., Barkhof, F., Ferro, J.M., Pantoni, L., Basile, A.M., Inzitari, D., Erkinjuntti, T., Wahlund, L.O., Rostrup, E., Schmidt, R., Fazekas, F., Scheltens, P., study group, L.: Medial temporal lobe atrophy and white matter hyperintensities are associated with mild cognitive deficits in non-disabled elderly people: the LADIS study. Journal of Neurology, Neurosurgery & Psychiatry 76(11), 1497–1500 (2005)

[114] Jack, C.R., Petersen, R.C., Xu, Y.C., Waring, S.C., O'Brien, P.C., Tangalos, E.G., Smith, G.E., Ivnik, R.J., Kokmen, E.: Medial temporal atrophy on mri in normal aging and very mild alzheimer's disease. Neurology 49(3), 786–794 (1997)

[115] Yoshiura, T., Hiwatashi, A., Yamashita, K., Ohyagi, Y., Monji, A., Takayama, Y., Nagao, E., Kamano, H., Noguchi, T., Honda, H.: Simultaneous measurement of arterial transit time, arterial blood volume, and cerebral blood flow using arterial spin-labeling in patients with Alzheimer disease. AJNR. American journal of neuroradiology 30(7), 1388–93 (2009)

[116] Mak, H.K.F., Chan, Q., Zhang, Z., Petersen, E.T., Qiu, D., Zhang, L., Yau, K.K.W., Chu, L.W., Golay, X.: Quantitative assessment of cerebral hemodynamic parameters by QUASAR arterial spin labeling in alzheimer's disease and cognitively normal elderly adults at 3-Tesla. Journal of Alzheimer's Disease 31(1), 33–44 (2012)

[117] Alsop, D.C., Detre, J.A.: Reduced Transit-Time Sensitivity in Noninvasive Magnetic Resonance Imaging of Human Cerebral Blood Flow. Journal of

Cerebral Blood Flow & Metabolism 16(6), 1236–1249 (1996)

[118] Sperling, R.A., Aisen, P.S., Beckett, L.A., Bennett, D.A., Craft, S., Fagan, A.M., Iwatsubo, T., Jack, C.R., Kaye, J., Montine, T.J., Park, D.C., Reiman, E.M., Rowe, C.C., Siemers, E., Stern, Y., Yaffe, K., Carrillo, M.C., Thies, B., Morrison-Bogorad, M., Wagster, M.V., Phelps, C.H.: Toward defining the preclinical stages of Alzheimer's disease: Recommendations from the National Institute on Aging-Alzheimer's Association workgroups on diagnostic guidelines for Alzheimer's disease (may 2011)

[119] Matthews, P.M., Hampshire, A.: Clinical Concepts Emerging from fMRI Functional Connectomics (aug 2016)

[120] Vemuri, P., Jones, D.T., Jack, C.R.: Resting state functional MRI in Alzheimer's Disease. Alzheimer's Research & Therapy 4(1), 2 (jan 2011)

[121] Allen, G., Barnard, H., McColl, R., Hester, A.L., Fields, J.a., Weiner, M.F., Ringe, W.K., Lipton, A.M., Brooker, M., McDonald, E., Rubin, C.D., Cullum, C.M.: Reduced hippocampal functional connectivity in Alzheimer disease. Archives of neurology 64(10), 1482–1487 (2007)

[122] Zhang, H.Y., Wang, S.J., Liu, B., Ma, Z.L., Yang, M., Zhang, Z.J., Teng, G.J.: Resting brain connectivity: changes during the progress of Alzheimer disease. Radiology 256(2), 598–606 (2010)

[123] Wu, X., Li, R., Fleisher, A.S., Reiman, E.M., Guan, X., Zhang, Y., Chen, K., Yao, L.: Altered default mode network connectivity in Alzheimer's disease-A resting functional MRI and Bayesian network study. Human Brain Mapping 32(11), 1868–1881 (2011)

[124] Grady, C.L., McIntosh, A.R., Beig, S., Keightley, M.L., Burian, H., Black, S.E.: Evidence from functional neuroimaging of a compensatory prefrontal network in Alzheimer's disease. The Journal of neuroscience : the official journal of the Society for Neuroscience 23(3), 986–93 (2003)

[125] Hafkemeijer, A., van der Grond, J., Rombouts, S.A.: Imaging the default mode network in aging and dementia. Biochimica et Biophysica Acta (BBA) - Molecular Basis of Disease 1822(3), 431–441 (2012)

[126] Folstein, M.F., Folstein, S.E., McHugh, P.R.: "Mini-mental state". A practical method for grading the cognitive state of patients for the clinician. J Psychiatr Res 12(3), 189–198 (Nov 1975)

[127] Mougin, O., Abdel-Fahim, R., Dineen, R., Pitiot, A., Evangelou, N., Gowland, P.: Imaging gray matter with concomitant null point imaging from the phase sensitive inversion recovery sequence. Magn Reson Med 76(5), 1512–1516 (2016)

[128] Hurley, A.C., Al-Radaideh, A., Bai, L., Aickelin, U., Coxon, R., Glover, P., Gowland, P.A.: Tailored RF pulse for magnetization inversion at ultrahigh field. Magn Reson Med 63(1), 51–58 (2010)

[129] Dai, W., Robson, P.M., Shankaranarayanan, A., Alsop, D.C.: Reduced resolution transit delay prescan for quantitative continuous arterial spin labeling perfusion imaging. Magn Reson Med 67(5), 1252–1265 (2012)

[130] Andersson, J.L.R., Jenkinson, M., Smith, S.: Non-linear registration, aka spatial normalisation. FMRIB technical report TR07JA2 (2010)

[131] Chappell, M., Groves, A., Whitcher, B., Woolrich, M.: Variational Bayesian Inference for a Nonlinear Forward Model. IEEE Transactions on Signal Processing 57(1), 223–236 (jan 2009)

[132] Wright, P.J., Mougin, O.E., Totman, J.J., Peters, A.M., Brookes, M.J., Coxon, R., Morris, P.E., Clemence, M., Francis, S.T., Bowtell, R.W., Gowland, P.A.: Water proton T1 measurements in brain tissue at 7, 3, and 1.5 T using IR-EPI, IR-TSE, and MPRAGE: results and optimization. MAGMA 21(1-2), 121–130 (Mar 2008)

[133] Ikonomidou, V.N., van Gelderen, P., de Zwart, J.A., Duyn, J.H.: T1 measurements at 7T with application to tissue specific imaging. Proc Int Soc Mag Reson Med p. 921 (2006)

[134] Zhang, Y., Brady, M., Smith, S.: Segmentation of brain MR images through a hidden Markov random field model and the expectation-maximization algorithm. IEEE Trans Med Imaging 20(1), 45–57 (2001)

[135] Smith, S., Brady, J.: SUSAN—a new approach to low level image processing. International journal of computer vision 23(1), 45–78 (1997)

[136] Beckmann, C., Smith, S.: Probabilistic Independent Component Analysis for Functional Magnetic Resonance Imaging. IEEE Transactions on Medical Imaging 23(2), 137–152 (2004)

[137] Filippini, N., MacIntosh, B.J., Hough, M.G., Goodwin, G.M., Frisoni, G.B., Smith, S.M., Matthews, P.M., Beckmann, C.F., Mackay, C.E.: Distinct patterns of brain activity in young carriers of the APOE- 4 allele.

Proceedings of the National Academy of Sciences 106(17), 7209–7214 (apr 2009)

[138] Winkler, A.M., Ridgway, G.R., Webster, M.A., Smith, S.M., Nichols, T.E.: Permutation inference for the general linear model. NeuroImage 92, 381–397 (may 2014)

[139] Ashford, J.W., Shan, M., Butler, S., Rajasekar, A., Schmitt, F.A.: Temporal Quantification of Alzheimer's Disease Severity: 'Time Index' Model. Dementia and Geriatric Cognitive Disorders 6(5), 269–280 (1995)

[140] Sierra-Marcos, A.: Regional Cerebral Blood Flow in Mild Cognitive Impairment and Alzheimer's Disease Measured with Arterial Spin Labeling Magnetic Resonance Imaging. International Journal of Alzheimer's Disease 2017, 1–10 (2017)

[141] Pini, L., Pievani, M., Bocchetta, M., Altomare, D., Bosco, P., Cavedo, E., Galluzzi, S., Marizzoni, M., Frisoni, G.B.: Brain atrophy in Alzheimer's Disease and aging (2016)

[142] Thirion, B., Pinel, P., Mériaux, S., Roche, A., Dehaene, S., Poline, J.B.: Analysis of a large fMRI cohort: Statistical and methodological issues for group analyses. NeuroImage 35(1), 105–120 (mar 2007)

[143] Birn, R.M., Molloy, E.K., Patriat, R., Parker, T., Meier, T.B., Kirk, G.R., Nair, V.A., Meyerand, M.E., Prabhakaran, V.: The effect of scan length on the reliability of resting-state fMRI connectivity estimates. NeuroImage 83, 550–558 (dec 2013)

[144] Birn, R.M., Diamond, J.B., Smith, M.A., Bandettini, P.A.: Separating respiratory-variation-related fluctuations from neuronal-activity-related fluctuations in fMRI. NeuroImage 31(4), 1536–1548 (jul 2006)

[145] Shmueli, K., van Gelderen, P., de Zwart, J.A., Horovitz, S.G., Fukunaga, M., Jansma, J.M., Duyn, J.H.: Low-frequency fluctuations in the cardiac rate as a source of variance in the resting-state fMRI BOLD signal. NeuroImage 38(2), 306–320 (nov 2007)

[146] Biswal, B., Zerrin Yetkin, F., Haughton, V.M., Hyde, J.S.: Functional connectivity in the motor cortex of resting human brain using echo???planar mri. Magnetic Resonance in Medicine 34(4), 537–541 (oct 1995)

[147] Lowe, M.J., Mock, B.J., Sorenson, J.A.: Functional Connectivity in Single and Multislice Echoplanar Imaging Using Resting-State Fluctuations.

NeuroImage 7(2), 119–132 (feb 1998)

[148] Drouin-Ouellet, J., Sawiak, S.J., Cisbani, G., Lagacé, M., Kuan, W.L., Saint-Pierre, M., Dury, R.J., Alata, W., St-Amour, I., Mason, S.L., Calon, F., Lacroix, S., Gowland, P.A., Francis, S.T., Barker, R.A., Cicchetti, F.: Cerebrovascular and blood-brain barrier impairments in Huntington's disease: Potential implications for its pathophysiology. Annals of Neurology 78(2), 160–177 (aug 2015)

[149] Roos, R.A., Wheelock, V., Tempkin, T., Marder, K., Nance, M., Myers, R., Zhao, H., Kayson, E., Orme, C., Shoulson, I., Aziz, N., van der Burg, J., Landwehrmeyer, G., Brundin, P., Stijnen, T., Roos, R., Arnulf, I., Nielsen, J., Lohmann, E., Schiefer, J., Wild, E., Jennum, P., Konofal, E., Walker, M., Oudiette, D., Tabrizi, S., Shoulson, I., Fahn, S., Vonsattel, J., Maat-Kievit, A., Vlis, M.V.V.D., Zoeteweij, M., Losekoot, M., van Haeringen, A., Roos, R., Decruyenaere, M., Evers-Kiebooms, G., Boogaerts, A., Philippe, K., Demyttenaere, K., Dom, R., Vandenberghe, W., Fryns, J.: Huntington's disease: a clinical review. Orphanet Journal of Rare Diseases 5(1), 40 (2010)

[150] MacDonald, M., Gines, S., Gusella, J., Wheeler, V.: Huntington's Disease. NeuroMolecular Medicine 4(1-2), 502 (2003)

[151] Khalil, H., Quinn, L., van Deursen, R., Dawes, H., Playle, R., Rosser, A., Busse, M.: What effect does a structured home-based exercise programme have on people with Huntington's disease? A randomized, controlled pilot study. Clinical rehabilitation 27(7), 646–58 (jul 2013)

[152] Rosas, H.D., Goodman, J., Chen, Y.I., Jenkins, B.G., Kennedy, D.N., Makris, N., Patti, M., Seidman, L.J., Beal, M.F., Koroshetz, W.J.: Striatal volume loss in HD as measured by MRI and the influence of CAG repeat. Neurology 57(6), 1025–8 (2001)

[153] Tabrizi, S.J., Langbehn, D.R., Leavitt, B.R., Roos, R.A., Durr, A., Craufurd, D., Kennard, C., Hicks, S.L., Fox, N.C., Scahill, R.I., Borowsky, B., Tobin, A.J., Rosas, H.D., Johnson, H., Reilmann, R., Landwehrmeyer, B., Investigators, t.T.H., Summary: Biological and clinical manifestations of Huntington's disease in the longitudinal TRACK-HD study: cross-sectional analysis of baseline data. Lancet Neurology 8, 791–801 (2009)

[154] Rosas, H.D., Koroshetz, W.J., Chen, Y.I., Skeuse, C., Vangel, M.,

Cudkowicz, M.E., Caplan, K., Marek, K., Seidman, L.J., Makris, N., Jenkins, B.G., Goldstein, J.M.: Evidence for more widespread cerebral pathology in early HD: an MRI-based morphometric analysis. Neurology 60(10), 1615–1620 (2003)

[155] Tabrizi, S.J., Scahill, R.I., Durr, A., Roos, R.A., Leavitt, B.R., Jones, R., Landwehrmeyer, G.B., Fox, N.C., Johnson, H., Hicks, S.L., Kennard, C., Craufurd, D., Frost, C., Langbehn, D.R., Reilmann, R., Stout, J.C.: Biological and clinical changes in premanifest and early stage Huntington's disease in the TRACK-HD study: The 12-month longitudinal analysis. The Lancet Neurology 10(1), 31–42 (2011)

[156] Tabrizi, S.J., Reilmann, R., Roos, R.A.C., Durr, A., Leavitt, B., Owen, G., Jones, R., Johnson, H., Craufurd, D., Hicks, S.L., Kennard, C., Landwehrmeyer, B., Stout, J.C., Borowsky, B., Scahill, R.I., Frost, C., Langbehn, D.R.: Potential endpoints for clinical trials in premanifest and early Huntington's disease in the TRACK-HD study: Analysis of 24 month observational data. The Lancet Neurology 11(1), 42–53 (2012)

[157] Tabrizi, S.J., Scahill, R.I., Owen, G., Durr, A., Leavitt, B.R., Roos, R.A., Borowsky, B., Landwehrmeyer, B., Frost, C., Johnson, H., Craufurd, D., Reilmann, R., Stout, J.C., Langbehn, D.R.: Predictors of phenotypic progression and disease onset in premanifest and early-stage Huntington's disease in the TRACK-HD study: Analysis of 36-month observational data. The Lancet Neurology 12(7), 637–649 (2013)

[158] Paulsen, J.S., Hayden, M., Stout, J.C., Langbehn, D.R., Aylward, E., Ross, C.A., Guttman, M., Nance, M., Kieburtz, K., Oakes, D., Shoulson, I., Kayson, E., Johnson, S., Penziner, E., Predict-HD Investigators of the Huntington Study Group: Preparing for preventive clinical trials: the Predict-HD study. Archives of neurology 63(6), 883–90 (2006)

[159] Paulsen, J.S., Langbehn, D.R., Stout, J.C., Aylward, E., Ross, C.a., Nance, M., Guttman, M., Johnson, S., MacDonald, M., Beglinger, L.J., Duff, K., Kayson, E., Biglan, K., Shoulson, I., Oakes, D., Hayden, M.: Detection of Huntington's disease decades before diagnosis: the Predict-HD study. Journal of neurology, neurosurgery, and psychiatry 79(8), 874–880 (2008)

[160] Harris, G.J., Aylward, E.H., Peyser, C.E., Pearlson, G.D., Brandt, J., Roberts-Twillie, J.V., Barta, P.E., Folstein, S.E.: Single photon emission

computed tomographic blood flow and magnetic resonance volume imaging of basal ganglia in Huntington's disease 53(4), 316–324 (1996)

[161] Harris, G.J., Pearlson, G.D., Peyser, C.E., Aylward, E.H., Roberts, J., Barta, P.E., Chase, G.A., Folstein, S.E.: Putamen volume reduction on magnetic resonance imaging exceeds caudate changes in mild Huntington's disease. Annals of Neurology 31(1), 69–75 (1992)

[162] Aylward, E.H., Codori, a.M., Barta, P.E., Pearlson, G.D., Harris, G.J., Brandt, J.: Basal ganglia volume and proximity to onset in presymptomatic Huntington disease. (1996)

[163] Rosas, H.D., Liu, a.K., Hersch, S., Glessner, M., Ferrante, R.J., Salat, D.H., van der Kouwe, a., Jenkins, B.G., Dale, a.M., Fischl, B.: Neurology

[164] Rosas, H.D., Salat, D.H., Lee, S.Y., Zaleta, A.K., Pappu, V., Fischl, B., Greve, D., Hevelone, N., Hersch, S.M.: Cerebral cortex and the clinical expression of Huntington's disease: Complexity and heterogeneity. Brain 131(4), 1057–1068 (2008)

[165] Hua, J., Unschuld, P.G., Margolis, R.L., Van Zijl, P.C.M., Ross, C.A.: Elevated arteriolar cerebral blood volume in prodromal Huntington's disease. Movement Disorders 29(3), 396–401 (mar 2014)

[166] Johnson, E.B., Rees, E.M., Labuschagne, I., Durr, A., Leavitt, B.R., Roos, R.A., Reilmann, R., Johnson, H., Hobbs, N.Z., Langbehn, D.R., Stout, J.C., Tabrizi, S.J., Scahill, R.I., Axelson, E., Bechtel, N., Van Bogaard, S.J., Bohlen, S., Callaghan, J., Campbell, C., Campbell, M., Cash, D., Coleman, A., Craufurd, D., Santos, R.D., Decolongon, J., Dumas, E., Fox, N., Frost, C., Van der Grond, J., T'Hart, E., Hicks, S., Hobbs, N., Jauffret, C., Jones, R., Justo, D., Kennard, C., Lahiri, N., Landwehmeyer, B., Lehericy, S., Malone, I., Marelli, C., Milchman, C., Nigaud, K., Owen, G., Pepple, T., Queller, S., Read, J., Say, M., Sturrock, A., Valabrègue, R., Wang, C.: The impact of occipital lobe cortical thickness on cognitive task performance: An investigation in Huntington's Disease. Neuropsychologia (Pt A), 138–146 (dec)

[167] Benjamin, P., Viessmann, O., Mackinnon, A.D., Jezzard, P., Markus, H.S.: 7 Tesla MRI in cerebral small vessel disease (jul 2015)

[168] Society, M.: MS in the UK. MS Society (Jan 2016)

[169] Ascherio, A., Munger, K.L., Simon, K.C.: Vitamin D and multiple sclerosis (jun 2010)

[170] Ge, Y., Kister, I., Chawl, S., Sinnecker, T., Herbert, J., Paul, F., Wuerfel, J.: Cortical lesions of multiple sclerosis: Signal, morphological and vascular abnormalities at ultra high field (7t) mri (April 2015)

[171] Bakshi, R., Ariyaratana, S., Benedict, R.H., Jacobs, L.: Fluid-attenuated inversion recovery magnetic resonance imaging detects cortical and juxtacortical multiple sclerosis lesions. Archives of neurology 58(5), 742–748 (2001)

[172] Sethi, V., Yousry, T.a., Muhlert, N., Ron, M., Golay, X., Wheeler-Kingshott, C., Miller, D.H., Chard, D.T.: Improved detection of cortical MS lesions with phase-sensitive inversion recovery MRI. Journal of Neurology, Neurosurgery & Psychiatry 83(9), 877–882 (2012)

[173] Turetschek, K., Wunderbaldinger, P., Bankier, A.A., Zontsich, T., Graf, O., Mallek, R., Hittmair, K.: Double inversion recovery imaging of the brain: Initial experience and comparison with fluid attenuated inversion recovery imaging. Magnetic Resonance Imaging 16(2), 127–135 (1998)

[174] Geurts, J.J.G., Pouwels, P.J.W., Uitdehaag, B.M.J., Polman, C.H., Barkhof, F., Castelijns, J.A.: Intracortical lesions in multiple sclerosis: improved detection with 3D double inversion-recovery MR imaging. Radiology 236(1), 254–260 (2005)

[175] Kilsdonk, I.D., Jonkman, L.E., Klaver, R., Van Veluw, S.J., Zwanenburg, J.J., Kuijer, J.P., Pouwels, P.J., Twisk, J.W., Wattjes, M.P., Luijten, P.R., Barkhof, F., Geurts, J.J.: Increased cortical grey matter lesion detection in multiple sclerosis with 7 T MRI: A post-mortem verification study. Brain 139(5), 1472–1481 (2016)

[176] Tallantyre, E.C., Morgan, P.S., Dixon, J.E., Al-Radaideh, A., Brookes, M.J., Morris, P.G., Evangelou, N.: 3 Tesla and 7 Tesla MRI of multiple sclerosis cortical lesions. Journal of magnetic resonance imaging : JMRI 32(4), 971–977 (sep 2010)

[177] Geurts, J.J.G., Bö, L., Pouwels, P.J.W., Castelijns, J.A., Polman, C.H., Barkhof, F.: Cortical lesions in multiple sclerosis: Combined postmortem MR imaging and histopathology. American Journal of Neuroradiology 26(3), 572–577 (2005)

[178] Calabrese, M., Agosta, F., Rinaldi, F., Mattisi, I., Grossi, P., Favaretto, A., Atzori, M., Bernardi, V., Barachino, L., Rinaldi, L., Perini, P., Gallo, P., Filippi, M.: Cortical Lesions and Atrophy Associated With Cognitive Impairment in Relapsing-Remitting Multiple Sclerosis. Archives of Neurology 66(9), 726–731 (sep 2009)

[179] Lazeron, R.H., Langdon, D.W., Filippi, M., van Waesberghe, J.H., Stevenson, V.L., Boringa, J.B., Origgi, D., Thompson, A.J., Falautano, M., Polman, C.H., Barkhof, F.: Neuropsychological impairment in multiple sclerosis patients: the role of (juxta)cortical lesion on FLAIR 6(4), 280–285 (2000)

[180] Sokic, D.V., Stojsavljevic, N., Drulovic, J., Dujmovic, I., Mesaros, S., Ercegovac, M., Peric, V., Dragutinovic, G., Levic, Z.: Seizures in multiple sclerosis. Epilepsia 42(1), 72–9 (jan 2001)

[181] Spatt, J., Chaix, R., Mamoli, B.: Epileptic and non-epileptic seizures in multiple sclerosis (2001)

[182] Feinstein, A., Roy, P., Lobaugh, N., Feinstein, K., O'Connor, P., Black, S.: Structural brain abnormalities in multiple sclerosis patients with major depression. Neurology 62(4), 586–590 (2004)

[183] Law, M., Saindane, A.M., Ge, Y., Babb, J.S., Johnson, G., Mannon, L.J., Herbert, J., Grossman, R.I.: Microvascular abnormality in relapsing-remitting multiple sclerosis: perfusion MR imaging findings in normal-appearing white matter. Radiology 231(1), 645–652 (2004)

[184] Wuerfel, J., Bellmann-Strobl, J., Brunecker, P., Aktas, O., McFarland, H., Villringer, A., Zipp, F.: Changes in cerebral perfusion precede plaque formation in multiple sclerosis: A longitudinal perfusion MRI study. Brain 127(1), 111–119 (2004)

[185] Inglese, M., Park, S.j., Johnson, G., Babb, J.S., Miles, L., Jaggi, H., Herbert, J., Grossman, R.I.: Deep gray matter perfusion in multiple sclerosis: dynamic susceptibility contrast perfusion magnetic resonance imaging at 3 T. Archives of neurology 64(2), 196–202 (2007)

[186] Ge, Y., Law, M., Johnson, G., Herbert, J., Babb, J.S., Mannon, L.J., Grossman, R.I.: Dynamic susceptibility contrast perfusion MR imaging of multiple sclerosis lesions: characterizing hemodynamic impairment and

inflammatory activity. AJNR American journal of neuroradiology 26(July), 1539–1547 (2005)

[187] Adhya, S., Johnson, G., Herbert, J., Jaggi, H., Babb, J.S., Grossman, R.I., Inglese, M.: Pattern of hemodynamic impairment in multiple sclerosis: Dynamic susceptibility contrast perfusion MR imaging at 3.0 T. NeuroImage 33(4), 1029–1035 (2006)

[188] Inglese, M., Adhya, S., Johnson, G., Babb, J.S., Miles, L., Jaggi, H., Herbert, J., Grossman, R.I.: Perfusion magnetic resonance imaging correlates of neuropsychological impairment in multiple sclerosis. Journal of cerebral blood flow and metabolism : official journal of the International Society of Cerebral Blood Flow and Metabolism 28(1), 164–171 (2008)

[189] Varga, A.W., Johnson, G., Babb, J.S., Herbert, J., Grossman, R.I., Inglese, M.: White matter hemodynamic abnormalities precede sub-cortical gray matter changes in multiple sclerosis. Journal of the Neurological Sciences 282(1-2), 28–33 (2009)

[190] Saindane, A.M., Law, M., Ge, Y., Johnson, G., Babb, J.S., Grossman, R.I.: Correlation of Diffusion Tensor and Dynamic Perfusion MR Imaging Metrics in Normal- Appearing Corpus Callosum: Support for Primary Hypoperfusion in Multiple Sclerosis. American Journal of Neuroradiology 28, 767–772 (2007)

[191] Ingrisch, M., Morhard, D., Sourbron, S., Gerdes, L., Kümpfel, T., Hohlfeld, R., Reiser, M., Glaser, C.: Measuring perfusion and permeability in multiple sclerosis: dynamic contrast-enhanced MRI in 3D at 3T. Proceedings 17th Scientific Meeting, International Society for Magnetic Resonance in Medicine Honolulu, 1157 (2009)

[192] Zamboni, P., Galeotti, R., Menegatti, E., Malagoni, A.M., Tacconi, G., Dall'ara, S., Bartolomei, I., Salvi, F.: Chronic cerebrospinal venous insufficiency in patients with multiple sclerosis. Journal of Neurology, Neurosurgery, and Psychiatry 80(4), 392–399 (2009)

[193] Rashid, W., Parkes, L.M., Ingle, G.T., Chard, D.T., Toosy, A.T., Altmann, D.R., Symms, M.R., Tofts, P.S., Thompson, A.J., Miller, D.H.: Abnormalities of cerebral perfusion in multiple sclerosis. Journal of neurology, neurosurgery, and psychiatry 75(9), 1288–93 (2004)

[194] Amann, M., Achtnichts, L., Hirsch, J.G., Naegelin, Y., Gregori, J., Weier,

K., Thöni, A., Mueller-Lenke, N., Radue, E.W., Günther, M., Kappos, L., Gass, A.: 3D GRASE arterial spin labelling reveals an inverse correlation of cortical perfusion with the white matter lesion volume in MS. Multiple sclerosis (Houndmills, Basingstoke, England) 18(11), 1570–6 (2012)

[195] Debernard, L., Melzer, T.R., Van Stockum, S., Graham, C., Wheeler-Kingshott, C.A., Dalrymple-Alford, J.C., Miller, D.H., Mason, D.F.: Reduced grey matter perfusion without volume loss in early relapsing-remitting multiple sclerosis. Journal of neurology, neurosurgery, and psychiatry 85(5), 544–51 (2014)

[196] Ota, M., Sato, N., Nakata, Y., Ito, K., Kamiya, K., Maikusa, N., Ogawa, M., Okamoto, T., Obu, S., Noda, T., Araki, M., Yamamura, T., Kunugi, H.: Abnormalities of cerebral blood flow in multiple sclerosis: A pseudocontinuous arterial spin labeling MRI study. Magnetic Resonance Imaging 31(6), 990–995 (2013)

[197] Steen, C., D'haeseleer, M., Hoogduin, J.M., Fierens, Y., Cambron, M., Mostert, J.P., Heersema, D.J., Koch, M.W., De Keyser, J.: Cerebral white matter blood flow and energy metabolism in multiple sclerosis. Multiple sclerosis (Houndmills, Basingstoke, England) 19(10), 1282–9 (2013)

[198] Haselhorst, R., Kappos, L., Bilecen, D., Scheffler, K., Möri, D., Radü, E.W., Seelig, J.: Dynamic susceptibility contrast MR imaging of plaque development in multiple sclerosis: Application of an extended blood-brain barrier leakage correction. Journal of Magnetic Resonance Imaging 11(5), 495–505 (2000)

[199] Moll, N.M., Rietsch, A.M., Thomas, S., Ransohoff, A.J., Lee, J.C., Fox, R., Chang, A., Ransohoff, R.M., Fisher, E.: Multiple sclerosis normal-appearing white matter: Pathology-imaging correlations. Annals of Neurology 70(5), 764–773 (nov 2011)

[200] Kanda, T., Ishii, K., Kawaguchi, H., Kitajima, K., Takenaka, D.: High signal intensity in the dentate nucleus and globus pallidus on unenhanced T1-weighted MR images: relationship with increasing cumulative dose of a gadolinium-based contrast material. Radiology 270(3), 834–41 (2014)

[201] Radbruch, A., Weberling, L.D., Kieslich, P.J., Eidel, O., Burth, S., Kickingereder, P., Heiland, S., Wick, W., Schlemmer, H.P., Bendszus, M.: Gadolinium Retention in the Dentate Nucleus and Globus Pallidus

Is Dependent on the Class of Contrast Agent. Radiology 275(3), 150337 (2015)

[202] Pitt, D., Boster, A., Pei, W., Wohleb, E., Jasne, A., Zachariah, C.R., Rammohan, K., Knopp, M.V., Schmalbrock, P.: Imaging cortical lesions in multiple sclerosis with ultra-high-field magnetic resonance imaging. Archives of neurology 67(7), 812–818 (jul 2010)

[203] Zuo, Z., Wang, R., Zhuo, Y., Xue, R., St. Lawrence, K.S., Wang, D.J.J.: Turbo-FLASH Based Arterial Spin Labeled Perfusion MRI at 7 T. PLoS ONE 8(6), e66612 (jun 2013)

[204] Wang, Y., Moeller, S., Li, X., Vu, A.T., Krasileva, K., Ugurbil, K., Yacoub, E., Wang, D.J.: Simultaneous multi-slice Turbo-FLASH imaging with CAIPIRINHA for whole brain distortion-free pseudo-continuous arterial spin labeling at 3 and 7T. NeuroImage 113, 279–288 (jun 2015)

[205] Stafford, R.B., Woo, M.K., Oh, S.H., Dolui, S., Zhao, T., Kim, Y.B., Detre, J.A., Cho, Z.H., Lee, J.: An actively decoupled dual transceiver coil system for continuous ASL at 7 T. International Journal of Imaging Systems and Technology 26(2), 106–115 (jun 2016)

[206] Pfeuffer, J., Adriany, G., Shmuel, A., Yacoub, E., Van De Moortele, P.F., Hu, X., Ugurbil, K.: Perfusion-based high-resolution functional imaging in the human brain at 7 Tesla. Magnetic resonance in medicine : official journal of the Society of Magnetic Resonance in Medicine / Society of Magnetic Resonance in Medicine 47(5), 903–11 (2002)

[207] Gowland, P.A., Leach, M.O.: A simple method for the restoration of signal polarity in multi-image inversion recovery sequences for measuring T1 (mar 1991)

[208] Hou, P., Hasan, K.M., Sitton, C.W., Wolinsky, J.S., Narayana, P.A.: American Journal of Neuroradiology (6), 1432–1438

[209] Park, H.W., Cho, M.H., Cho, Z.H.: Real-value representation in inversion-recovery NMR imaging by use of a phase-correction method. Magnetic Resonance in Medicine 3(1), 15–23 (1986)

[210] Marques, J.P., Kober, T., Krueger, G., van der Zwaag, W., Van de Moortele, P.F., Gruetter, R.: MP2RAGE, a self bias-field corrected sequence for improved segmentation and T1-mapping at high field. NeuroImage 49(2), 1271–1281 (jan 2010)

[211] Blockley, N.P., Jiang, L., Gardener, A.G., Ludman, C.N., Francis, S.T., Gowland, P.A.: Field strength dependence of R1 and R2* relaxivities of human whole blood to ProHance, vasovist, and deoxyhemoglobin. Magnetic Resonance in Medicine 60(6), 1313–1320 (dec 2008)

[212] Barth, M., Breuer, F., Koopmans, P.J., Norris, D.G., Poser, B.A.: Simultaneous multislice (SMS) imaging techniques (jan 2016)